

DRAFT: UNCLASSIFIED



ARL-TR-XXXX • UNDEFINED



A Dodecahedral Model for Alveoli: Interim Report

by Alan D. Freed, Shahla Zamani, Sandipan Paul and John D. Clayton

Approved for public release; distribution is unlimited.

DRAFT: UNCLASSIFIED

DRAFT: UNCLASSIFIED

NOTICES

Disclaimers

The findings in this report are not to be construed as an official Department of the Army position unless so designated by other authorized documents.

Citation of manufacturer's or trade names does not constitute an official endorsement or approval of the use thereof.

Destroy this report when it is no longer needed. Do not return it to the originator.

DRAFT: UNCLASSIFIED

DRAFT: UNCLASSIFIED

ARL-TR-XXXX • UNDEFINED



A Dodecahedral Model for Alveoli: Interim Report

by A.D. Freed, S. Zamani, S. Pual and J.D. Clayton
Weapons and Materials Research Directorate, CCDC Army Research Laboratory

Approved for public release; distribution is unlimited.

DRAFT: UNCLASSIFIED

DRAFT: UNCLASSIFIED

REPORT DOCUMENTATION PAGE				Form Approved OMB No. 0704-0188
<p>Public reporting burden for this collection of information is estimated to average 1 hour per response, including the time for reviewing instructions, searching existing data sources, gathering and maintaining the data needed, and completing and reviewing the collection information. Send comments regarding this burden estimate or any other aspect of this collection of information, including suggestions for reducing the burden, to Department of Defense, Washington Headquarters Services, Directorate for Information Operations and Reports (0704-0188), 1215 Jefferson Davis Highway, Suite 1204, Arlington, VA 22202-4302. Respondents should be aware that notwithstanding any other provision of law, no person shall be subject to any penalty for failing to comply with a collection of information if it does not display a currently valid OMB control number.</p>				
PLEASE DO NOT RETURN YOUR FORM TO THE ABOVE ADDRESS.				
1. REPORT DATE (DD-MM-YYYY) DRAFT: July 13, 2020	2. REPORT TYPE Unknown Report Type	3. DATES COVERED (From - To) June 2019–June 2020		
4. TITLE AND SUBTITLE A Dodecahedral Model for Alveoli: Interim Report		5a. CONTRACT NUMBER 5b. GRANT NUMBER 5c. PROGRAM ELEMENT NUMBER		
6. AUTHOR(S) Alan D. Freed, Shahla Zamani, Sandipan Paul and John D. Clayton		5d. PROJECT NUMBER 5e. TASK NUMBER 5f. WORK UNIT NUMBER		
7. PERFORMING ORGANIZATION NAME(S) AND ADDRESS(ES) US Army Combat Capabilities Development Command Army Research Laboratory ATTN: FCDD-RLW-PC Aberdeen Proving Ground, MD 21005-5066		8. PERFORMING ORGANIZATION REPORT NUMBER ARL-TR-XXXX		
9. SPONSORING/MONITORING AGENCY NAME(S) AND ADDRESS(ES)		10. SPONSOR/MONITOR'S ACRONYM(S) 11. SPONSOR/MONITOR'S REPORT NUMBER(S)		
12. DISTRIBUTION/AVAILABILITY STATEMENT Approved for public release; distribution is unlimited.				
13. SUPPLEMENTARY NOTES primary authors' emails: < afreed@tamu.edu > and < john.d.clayton1.civ@mail.mil >.				
14. ABSTRACT Write abstract here.				
15. SUBJECT TERMS				
16. SECURITY CLASSIFICATION OF:		17. LIMITATION OF ABSTRACT UU	18. NUMBER OF PAGES 207	19a. NAME OF RESPONSIBLE PERSON 19b. TELEPHONE NUMBER (Include area code)
a. REPORT Unclassified	b. ABSTRACT Unclassified	c. THIS PAGE Unclassified		

DRAFT: UNCLASSIFIED

Contents

List of Figures viii

List of Tables xiii

Acknowledgments xv

1 Introduction **1**

1.1. Problem Statement 2

1.2. Approach 6

1.3. Organization 8

2 Dodecahedra: A Model for Alveoli **10**

2.1. Co-ordinate Indexing 11

2.2. Geometric Properties of a Regular Pentagon 15

2.3. Geometric Properties of a Regular Dodecahedron 16

2.4. Dimensions of Human Alveoli 17

2.5. Geometric Properties for Irregular Pentagons and Dodecahedra 17

2.6. Indexing Scheme for Dodecahedra 19

2.7. Co-Ordinate Systems for Chordal Fibers and Pentagonal Membranes 21

3 Kinematics **23**

3.1. 1D Chords 23

DRAFT: UNCLASSIFIED

3.1.1 Shape Functions for Interpolating a Rod	23
3.1.2 Deformation Gradient for a Rod	24
3.2.2D Triangles	24
3.2.1 Shape Functions for Interpolating a Triangle	24
3.3.2D Irregular Pentagons	25
3.3.1 Wachspress' Shape Functions for Interpolating an Irregular Pentagon	25
3.3.2 First Derivatives of the Shape Functions	28
3.3.3 Second Derivatives of the Shape Functions	29
3.3.4 Deformation Gradient for an Irregular Pentagon	31
3.3.5 Compatibility Conditions	32
3.3.6 Gram-Schmidt Decomposition of the Deformation Gradient	34
3.3.6.1 QR Factorization of \mathbf{F}	35
3.3.6.2 Dilemma	36
3.3.6.3 Remedy	37
3.3.7 Thermodynamic Strains and Strain Rates	40
3.3.7.1 Stretch Rates	40
3.4.3D Irregular Dodecahedra	41
3.4.1 Shape Functions for Interpolating an Irregular Tetrahedron	41
3.4.1.1 Deformation Gradient for an Irregular Tetrahedron	42
3.4.2 QR Factorization of \mathbf{F}	43
3.4.3 Thermodynamic Strains and Strain Rates	44
3.4.3.1 Stretch Rates	45
3.5. Code Verification: Kinematics	46
3.5.1 Isotropic Motions	47
3.5.1.1 Geometric vs. Thermodynamic Strains	47
3.5.2 Isochoric Motions	48
3.5.2.1 Geometric Strains	49
3.5.2.2 Thermodynamic Strains	51
3.5.3 Co-ordinate Pivoting	53

3.5.4 Compatible Membrane Deformations	57
4 Constitutive Theory	61
4.1. Green Thermoelastic Solids: Uniform Motions in 1D, 2D & 3D	62
4.1.1 Constitutive Equations	63
4.1.2 Material Response Functions	65
4.1.3 Thermoelastic Models for Modeling Alveoli: Uniform Motions	67
4.2. Green Thermoelastic Membranes: Non-Uniform Motions	69
4.2.1 General Constitutive Equations	70
4.2.2 Material Response Functions	71
4.2.3 Constitutive Equations Governing a Thermoelastic Membrane	73
4.2.3.1 The Poisson Effect	74
4.3. Green Thermoelastic Solids: Non-Uniform Motions	75
4.3.1 Constitutive Equations	76
4.3.2 Material Properties	79
4.3.3 Constitutive Equations Governing a Thermoelastic Solid	80
4.3.3.1 The Poisson Effect	81
4.4. Modeling an Alveolus	82
4.4.1 Constraints/Assumptions for Alveoli Subjected to Shock Waves	82
4.4.2 Modeling Septal Chords Subjected to Shock Waves	84
4.4.3 Modeling Alveolar Septa Subjected to Shock Waves	87
4.4.4 Modeling an Alveolar Volume Subjected to Shock Waves	92
4.4.4.1 Alveoli Filled with Air	92
4.4.4.2 Alveoli Filled with Fluid	93
4.5. Finite Element Implementation of Constitutive Equations	94
4.5.1 1D Formulation	95
4.5.2 2D Formulation	96
4.5.3 3D Formulation	98

4.6. Code Verification and Capabilities of the Constitutive Equations	99
---	----

5 Numerical Integrators 107

5.1. ODE Solvers	107
5.1.1 PECE Solver for First-Order ODEs	107
5.1.1.1 Start-Up Algorithm	108
5.1.1.2 Two-Step ODE Solver	108
5.1.2 A Relevant Example	109
5.1.3 PECE Solver for Second-Order ODEs	110
5.1.3.1 Start-Up Algorithm	111
5.1.3.2 Two-Step ODE Solver	111
5.1.4 A Relevant Example	112
5.2. Quadrature Rules for Spatial Integration	113
5.2.1 Gauss Integration Along a Rod	113
5.2.2 Multi-Dimensional Integration	114
5.2.3 Gauss Integration of a Triangle	115
5.2.4 Gauss Integration of a Pentagon	116
5.2.5 Gauss Integration of a Tetrahedron	117
5.3. Interpolation: Nodal Points \mapsto Gauss Points Extrapolation: Gauss Points \mapsto Nodal Points	118
5.3.1 Self-Consistent Interpolation/Extrapolation Procedures for Rods	121
5.3.2 Self-Consistent Interpolation/Extrapolation Procedures for Triangles	122
5.3.3 Self-Consistent Interpolation/Extrapolation Procedures for Tetrahedra	123
5.3.4 Self-Consistent Interpolation/Extrapolation Procedures for Pentagons	124
5.4. Converting Nodal Stresses into Nodal Forces	126

6 Variational Formulation 127

6.1. Mass Matrix	129
------------------	-----

DRAFT: UNCLASSIFIED

6.1.1 Mass Matrices for a Chord	130
6.1.1.1 Assemble Mass Matrices for the Septal Chords	131
6.1.2 Mass Matrices for a Pentagon	132
6.1.2.1 Assemble Mass Matrices for the Alveolar Septa	133
6.1.3 Mass Matrices for a Tetrahedron	133
6.1.3.1 Assemble Tetrahedral Mass Matrices to Get Mass Matrix for an Alveolar Sac	135
6.2. Stiffness Matrix	136
6.2.1 Stiffness Matrix for Chord	138
6.2.2 Stiffness Matrix for Pentagon	141
6.2.3 Stiffness Matrix for a tetrahedron	147
6.3. Force Vector	157
6.3.1 Force Vector for a Chord	158
6.3.2 Force Vector for a Pentagon	158
6.3.3 Force Vector for a Tetrahedron	159
7.1. References	161
Appendix A. Implicit Elasticity	170

List of Figures

Fig. 1	Finite element analysis done using LS-Dyna to model shock waves traversing a cross-sectional slice of a human torso. Material models from the LS-Dyna library of available models were used. ³	3
Fig. 2	A medical drawing of the respiratory system. ³	4
Fig. 3	Lungs excised from animals (most likely ovine) who expired from injuries caused by a blast. ⁴	4
Fig. 4	SEM photographs from a sectioned rat lung. The alveolar diameter in rat lung is about one quarter the alveolar diameter in human lung.	6
Fig. 5	All images were from Tsokos <i>et al.</i> ¹⁵	7
Fig. 6	Geometric representations for a dodecahedron.	11
Fig. 7	A regular pentagon inscribed within the unit circle establishes its natural co-ordinate system with co-ordinates (ξ, η) described in Eqn. (4), and whose origin is located at its centroid. Vertices are numbered counterclockwise with the uppermost vertex being labeled 1.	15
Fig. 8	Alveolar diameters in human lung.	18
Fig. 9	The co-ordinate system of a chord $(\vec{e}_1, \vec{e}_2, \vec{e}_3)$ relative to the co-ordinate system of its dodecahedron $(\vec{E}_1, \vec{E}_2, \vec{E}_3)$ with origins located at their respective centroids that are offset by a translation χ . These describe a mapping $[\{\vec{e}_1\}\{\vec{e}_2\}\{\vec{e}_3\}] = [\{\vec{E}_1\}\{\vec{E}_2\}\{\vec{E}_3\}][\mathbf{Q}]$ where \mathbf{Q} is an orthogonal rotation. The tangent base vector \vec{e}_1 aligns with the axis of this chord. The normal base vector \vec{e}_2 is coaxial with a line segment drawn from the origin out to the chordal axis such that $\vec{e}_1 \cdot \vec{e}_2 = 0$, while the binormal base vector is given by the cross product $\vec{e}_3 = \vec{e}_1 \times \vec{e}_2$.	21
Fig. 10	The co-ordinate system of a pentagon $(\vec{e}_1, \vec{e}_2, \vec{e}_3)$ relative to the co-ordinate system of its dodecahedron $(\vec{E}_1, \vec{E}_2, \vec{E}_3)$ with origins located at their respective centroids that are offset by a translation χ . These describe a mapping $[\{\vec{e}_1\}\{\vec{e}_2\}\{\vec{e}_3\}] = [\{\vec{E}_1\}\{\vec{E}_2\}\{\vec{E}_3\}][\mathbf{Q}]$ where \mathbf{Q} is an orthogonal rotation. Base vector \vec{e}_1 is coaxial to a line segment that connects two vertices which locate a pair of shoulders in a pentagon, viz., vertices 2 and 5 in Fig. 7. Base vector \vec{e}_2 is coaxial with a line segment drawn from the head of this pentagon, i.e., vertex 1 in Fig. 7, down to its base such that $\vec{e}_1 \cdot \vec{e}_2 = 0$. Base vector $\vec{e}_3 = \vec{e}_1 \times \vec{e}_2$ is the outward normal to this surface.	22
Fig. 11	Wachspress shape functions for a pentagon, in this case, shape function N_1 .	29

Fig. 12 Physical attributes of a planar deformation: a and b represent elongations, while $g = \tan \phi$ denotes the magnitude of shear. They are measured in a physical frame of reference with unit base vectors (\vec{g}_1, \vec{g}_2) where \vec{g}_1 embeds in the material.	35
Fig. 13 The left graphic designates a reference configuration while the right two graphics designate deformed configurations, both in basis (\vec{g}_1, \vec{g}_2) . The top graphic associates with the motion of Eqn. (37a), while the bottom graphic associates with the motion of Eqn. (37b).....	37
Fig. 14 A general description for homogeneous planar deformation, where $x, y \in \mathbb{R}_+$ and $\alpha, \beta \in \mathbb{R}$. Shears α and β are drawn in their positive sense.	38
Fig. 15 Response of a dodecahedron exposed to an isotropic motion of dilatation. The abscissa is the control variable and the ordinates are response variables. The right graphic plots the areal response of the pentagons $\xi = \ln \sqrt{A/A_0}$, while the left graphic plots the axial response of the chords $e = \ln(L/L_0)$. Both are plotted against the volumetric response of the dodecahedron $\Xi = \ln \sqrt[3]{V/V_0}$. Here V denotes dodecahedral volume, A denotes pentagonal area, and L denotes chordal length, all being evaluated in the current state, whose reference values are V_0, A_0 and L_0 .	47
Fig. 16 Response of a dodecahedron exposed to a far-field isotropic motion of dilatation. The abscissa is the control variable and the ordinates are response variables. The right graphic plots the three thermodynamic strains, as they apply to a pentagon, while the left graphic plots the geometric strain of a pentagon.....	48
Fig. 17 Response of a dodecahedron exposed to far-field motions of pure and simple shears. Note that the ordinate is $\times 10^{-15}$ and machine precision is $\sim 2.2 \times 10^{-16}$	49
Fig. 18 Response of a dodecahedron exposed to far-field pure-shear motions in the sense of Treloar: ⁶¹ $a = \ell$, $b = 1/\ell$ and $c = 1$ in the top images; $a = 1$, $b = \ell$ and $c = 1/\ell$ in the middle images; and $a = 1/\ell$, $b = 1$ and $c = \ell$ in the bottom images, with ℓ denoting an elongation of extrusion. In all six graphic images, the relevant (controlled) motion of the far-field pure shear is plotted along the abscissa. In each image pair, the right graphic presents pentagonal dilations, while the left graphic presents chordal elongations. Only unique responses are plotted; repetitions are not.....	50
Fig. 19 Response of a dodecahedron exposed to far-field simple-shear motions. In all six graphic images, the relevant (controlled) motion of simple shear is plotted along the abscissa. In each image pair, the right graphic presents pentagonal dilations, while the left graphic presents chordal elongations. Only unique responses are plotted; repetitions are not. Responses in the 13 plane differ from those of the 12 and 23 planes.	52

- Fig. 20 Same boundary conditions as in Fig. 18. Pentagonal areas were used to compute dilation in Fig. 18. The shape functions of Wachspress were used to compute dilation here. The uniform response in the right column of Fig. 18 and in the left column above are the same, providing additional assurance that the code has been correctly implemented. The squeeze response shown in the center column is the same for all three orientations of far-field pure shear, i.e., this response is isotropic. The right column has ordinates scaled by 10^{-14} implicating that there is no effective simple shear response occurring within any pentagonal surface of the dodecahedron whenever it is subjected to a far-field motion of pure shear..... 54
- Fig. 21 Same boundary conditions as in Fig. 19. Pentagonal areas were used to compute dilation in Fig. 19. The shape functions of Wachspress were used to compute dilation here. The uniform response in the right column of Fig. 19 and in the left column above are the same, providing additional assurance that the code has been correctly implemented. Like the dilational responses of the left column, the squeeze responses of the center column are the same in the 12 and 23 planes, but differ in the 13 plane. In all cases, the simple shear response of any pentagonal plane is proportional to that of the far-field shear imposed, further substantiating the code's implementation. The shear response of the septal membranes is isotropic..... 55
- Fig. 22 A far-field shear of γ_{23} is imposed on the dodecahedron. Pentagons 1 and 8 exhibit the plotted response. The top set of figures result whenever the pivoting strategy of Section 3.3.6.3 is used, while the bottom set of figures result whenever no pivoting strategy is employed. The dilation (left graphs) and squeeze (center graphs) responses are not effected by pivoting, only shear (right graphs) is effected. Pivoting maintains a linear shear response under a far-field shearing of the dodecahedron, as desired. 56
- Fig. 23 A far-field shear of γ_{23} is imposed on the dodecahedron. Pentagons 3 and 10 exhibit the plotted response. The top set of figures result whenever the pivoting strategy of Section 3.3.6.3 is used, while the bottom set of figures result whenever no pivoting strategy is employed. The dilation (left graphs) and squeeze (center graphs) responses are not effected by pivoting, only shear (right graphs) is effected. Pivoting maintains a linear shear response under a far-field shearing of the dodecahedron, as desired. 56

- Fig. 24 Planar compatibility requires $F_{11,2} = F_{12,1}$ and $F_{22,1} = F_{21,2}$ where the left-hand sides of these formulae are plotted as the abscissæ and the right-hand sides are plotted as the ordinates. For compatibility, the response ought to lie along the 45° diagonal, which is drawn in red over the range of $\pm 10^{-15}$ where machine precision is about 2.2×10^{-16} . Here the motion is one of uniform dilatation out to 100% strain. 57
- Fig. 25 Planar compatibility requires $F_{11,2} = F_{12,1}$ and $F_{22,1} = F_{21,2}$ where the left-hand sides of these formulae are plotted as the abscissæ and the right-hand sides are plotted as the ordinates. For compatibility, the response ought to lie along the 45° diagonal, which is drawn in red over the range of $\pm 10^{-15}$ where machine precision is about 2.2×10^{-16} . Here the motion is one of pure shear out to 100% strain with elongation occurring in the 1-direction, contraction occurring in the 2 direction, while the 3-direction is held fixed. These results pertain to pentagon 5: nodes 15, 5, 12, 11, 1, cf. Fig. 6 and Table 3. The top row of figures is the best response (at Gauss point 7, cf. Fig. 32) while the bottom row of figures is the worst response (at Gauss point 5). 59
- Fig. 26 Planar compatibility requires $F_{11,2} = F_{12,1}$ and $F_{22,1} = F_{21,2}$ where the left-hand sides of these formulae are plotted as the abscissæ and the right-hand sides are plotted as the ordinates. For compatibility, the response ought to lie along the 45° diagonal, which is drawn in red over the range of $\pm 10^{-15}$ where machine precision is about 2.2×10^{-16} . Here the motion is one of simple shear out to 100% strain, shearing along 1-2 planes in the 1-direction. These results pertain to pentagon 5: nodes 15, 5, 12, 11, 1, cf. Fig. 6 and Table 3. The top row of figures is the best response (at Gauss point 7, cf. Fig. 32) while the bottom row of figures is the worst response (at Gauss point 5). 60
- Fig. 27 Typical histograms for alveolar chord diameters constructed using the statistics reported in Table 4. Their tails weigh heavy at the larger diameters, because their distributions are normal in the square root of their diameters. These two histograms are virtually identical. 85
- Fig. 28 Typical stress/strain (left column) and entropy/strain (right column) response curves for collagen fibers loaded *in vivo* to 5% strain. The top row presents their absolute responses, while the bottom row presents their relative responses. A reference fiber length, whereat strain is arbitrarily set to zero, has been selected to associate with half the available stretch that can be attributed to molecular reconfiguration. 100

DRAFT: UNCLASSIFIED

- Fig. 29 Stress/strain (left column), entropy density/strain (center column), and local truncation error/strain (right column) curves for collagen using the material parameters listed in Table 5, which are described in terms of probability distributions. The top row is for strains out to 10%, the second row is for strains out to 20%, the third row is for strains out to 30%, and the fourth row is for strains out to 40%. There were no fiber failures in those that were stretched out to 10% and 20% strain. Six of the thirty fibers failed in those stretched out to 30% strain, while twenty eight of the thirty fibers failed for those stretched out to 40% strain. The local truncation errors plotted here associate with the PECE integrator presented in Eqn. (95) of Part 5 using 75 steps of integration, with errors less than 10^{-10} set at 10^{-10} . The reported truncation errors never exceeded 0.001% 102
- Fig. 30 Relative force/strain (left column), relative nominal stress/strain (center column), and relative entropy/strain (right column) curves for septal chords comprised of individual collagen and elastin fibers whose material parameters are listed in Table 5, which are described in terms of probability distributions. The top row is for strains out to 10%, the second row is for strains out to 20%, the third row is for strains out to 30%, and the fourth row is for strains out to 40%. There were no fiber failures in those that were stretched out to 10% and 20% strain. Six of the thirty collagen fibers failed in those stretched out to 30% strain with none of the elastin fibers failing, while twenty nine of the thirty collagen fibers failed for those stretched out to 40% strain, again, with none of the elastin fibers failing..... 103
- Fig. 31 Membrane response from thirty numerical experiments whose constitutive behavior is described by Eqns. (71 & 82) using the parameters listed in Table 6. The first column gives the $(s^\pi - s_0^\pi, \xi)$ conjugate pair response, the second column gives the $(s^\sigma - s_0^\sigma, \varepsilon)$ conjugate pair response, while the third column gives the $(s^\tau - s_0^\tau, \gamma)$ conjugate pair response. The first row represents a dilation experiment described by Eqn. (93a), the second row represents a pure shear experiment described by Eqn. (93b), while the third row represents a simple shear experiment described by Eqn. (93c). During these numerical experiments, eight membranes ruptured under dialation, while none ruptured during these pure and simple shear experiments..... 105
- Fig. 32 Locations of generalized, Gaussian, quadrature nodes for the 3rd (left) and 5th (right) degree integration methods presented in Table 9. Vertex 1 is located at the top of the pentagon, cf. Fig. 7, while the coordinate origin is located at its centroid (node 1 in the right figure). It is readily apparent that these quadrature rules are not symmetric. 117

List of Tables

Table 1	Natural co-ordinates for the vertices of a regular dodecahedron, as labeled in Fig. 6(b) according to Eqn. (7).....	19
Table 2	Vertices that locate the endpoints of septal chords in a dodecahedron, as labeled in Fig. 6(b).	20
Table 3	Vertices that locate the corners of regular pentagonal surfaces in a regular dodecahedron, and the chords that connect them. They are indexed counterclockwise when viewed looking from the outside in, and labeled according to Fig. 6(b). The apex for each pentagon resides at the peak of the hipped roof-line for that pentagon. This turns out to be important..	20
Table 4	Mean and standard deviations in variance for the square root of septal chord diameters \sqrt{D} reported by Sabin <i>et al.</i> ⁴¹ These septal chords are comprised of collagen and elastin fibers that act independent of one another, and therefore, they are considered to be loaded in parallel with one another.....	84
Table 5	Physical properties for hydrated collagen and elastin fibers. Collagen denatures at around 60°C, ⁸⁸ i.e., above this temperature collagen will shrink rapidly—an effect not modeled here.	88
Table 6	The elastic properties reported here are for visceral pleura taken from Freed <i>et al.</i> ⁵² and parenchyma taken from Saraf et al., ⁶⁹ divided by 10 to adjust for septal thickness vs. basement membrane thickness. The thermophysical properties lie between that of water and collagen, weighted towards that of water, and evaluated at body temperature.....	90
Table 7	Gauss quadrature weights and nodes for integrating over a line in its natural co-ordinate system ξ . These weights sum to 2, which is the span of its natural co-ordinate. We note that $\sqrt{3}/3 \approx 0.577350269189626$ and that $\sqrt{15}/25 \approx 0.774596669241483$	114
Table 8	Symmetric weights and nodes for Gauss quadratures that integrate over a triangle in its natural co-ordinate system (ξ, η) , where $0 \leq \xi \leq 1$ and $0 \leq \eta \leq 1 - \xi$. These weights sum to $1/2$, which is the area of a triangle when evaluated in its natural co-ordinate system.....	115
Table 9	Gauss quadrature weights and nodes (a.k.a., cubature rules) for integrating over a regular pentagon in its natural co-ordinate system (ξ, η) . These weights sum to the area of a pentagon inscribing an unit circle, the formula for which is given in Eqn. (6).	116

DRAFT: UNCLASSIFIED

Table 10 Symmetric weights and nodes for Gauss quadratures that integrate over a tetrahedron in its natural co-ordinate system (ξ, η, ζ) , where $0 \leq \xi \leq 1 - \eta - \zeta$, $0 \leq \eta \leq 1 - \zeta$ and $0 \leq \zeta \leq 1$. These weights sum to $1/6$, which is the volume of a tetrahedron measured in its natural co-ordinate system.....	119
Table 11 A Gauss quadrature rule for integrating functions over the lengths of rods. It approximates $\int_{-1}^1 f(\xi) d\xi$ using two quadrature points. The weights of quadrature sum to its length because $L = \int_{-1}^1 d\xi = 2$. This quadrature rule is from Christoffel. It integrates polynomials along a line exactly up through second order.	122
Table 12 A Gauss quadrature rule for integrating functions over the areas of triangles. It approximates $\int_0^1 \int_0^{1-\xi} f(\xi, \eta) d\eta d\xi$ using three quadrature points. The weights of quadrature sum to its area because $A = \int_0^1 \int_0^{1-\xi} d\eta d\xi = 1/2$. This quadrature rule is from Strang. It integrates polynomials over a triangular region exactly up through second order.	123
Table 13 A Gauss quadrature rule for integrating functions over the volumes of tetrahedra. It approximates $\int_0^1 \int_0^{1-\xi} \int_0^{1-\xi-\eta} f(\xi, \eta, \zeta) d\zeta d\eta d\xi$ using four quadrature points. The weights of quadrature sum to its volume because $V = \int_0^1 \int_0^{1-\xi} \int_0^{1-\xi-\eta} d\zeta d\eta d\xi = 1/6$. This quadrature rule is from Keast. It integrates polynomials over a tetrahedral region exactly up through second order. As a point of reference, the centroid has co-ordinates $(1/4, 1/4, 1/4)$	124
Table 14 Generalized, Gaussian, weights and nodes for integrating over a triangle in its natural co-ordinate system.	160

DRAFT: UNCLASSIFIED

Acknowledgments

Prof. Alan D. Freed acknowledges support of a Joint Faculty Appointment with the U.S. Army Combat Capabilities Development Command (CCDC) Army Research Laboratory. Shahla Zamani and Sandipan Pual acknowledge support from a grant funded by the CCDC Army Research Laboratory. John D. Clayton acknowledges support of the CCDC Army Research Laboratory. Prof. J.N. Reddy was the PI for that part of this project performed at Texas A&M University by Shahla Zamani and Sandipan Paul. Dr. M. Kleinberger was the Cooperative Agreement Manager (CAM) and Dr. John D. Clayton was the Technical Manager (TM) for this contract at the CCDC Army Research Laboratory.

Part 1

Introduction

Injuries that occur after blast waves impact a soldier wearing Personal Protective Equipment (PPE) or that occur after non-penetrating ballistic projectiles impact a soldier wearing PPE are referred to as Behind Armor Blunt Trauma (BABT). The kinetic energy from such impacts is absorbed by a soldier's PPE, and by the bony and soft tissues of the soldier beneath. Standards have been written by which PPE's have been designed to since 1972. Verification is through experiments where, typically, a suit of body armor is placed over a 'body' subjected to a ballistic impact from a projectile fired by a weapon, all in accordance with a standard. Current practice is to use clay (usually Roma Plastilina No. 1 clay) as a surrogate for the human body in these tests. A principle objective of an internal Army Research Laboratory–Weapons and Materials Research Directorate (ARL-WMRD) project, *Modeling Large Deformations and Stress Wave Mechanics in Soft Biological Tissue*, is to develop accurate material models for the human body that are also efficient in their finite element implementation, thereby facilitating the study BABT for design of PPE. This is a 6.1 research project whose hand-off to a 6.2 development team at project's end will aid Army engineers in their design of improved PPE by allowing them to run in-silico BABT tests to complement their actual in-field experiments.

The ARL-WMRD *Modeling Large Deformations and Stress Wave Mechanics in Soft Biological Tissue* project has three primary objectives: *i*) new material models, *ii*) new experiments, and *iii*) new trauma metrics. Lung has been selected as the soft tissue of interest for this study. What are sought are models and metrics whose parameters are physical and unique, and whose numeric implementation will be efficient and stable. Continuum thermodynamic models for lung tissue and a trauma metric are being developed (Clayton & Freed^{1,2} and this document). The work done under this sub-project, *A Dodecahedral Model for Alveoli*, complements its parent project, *Modeling Large Deformations and Stress Wave Mechanics in Soft Biological Tissue*, with regards to the first and third objectives of this ARL-WMRD program. The models being developed are expected to be improvements over those currently supplied by LS-Dyna in their materials library that, e.g., have been used

to study shock waves traversing a human torso not wearing body armor, cf. Fig. 1.

BABT occurs at the microscopic level of alveoli, which make up the parenchyma, i.e., the spongy tissue of lung that comprises around 90% of lung by volume, cf. Fig. 2, there being some 500 million alveoli in a typical lung. Most damage occurs just beneath the visceral pleural, as seen in Fig. 3, and is thought to be a consequence of the large disparity in wave speeds between solid tissues ($\sim 1,500$ m/s) and the spongy parenchyma ($\sim 30\text{-}40$ m/s).⁴ The objective of this work is to develop a mechanistic multi-scale model capable of describing the deformation and damage that occur at an alveolar level, caused by a shock wave traveling through the parenchyma, induced through either a blast or a ballistic impact to a soldier's PPE. In-silico experiments done using this microscopic model are to be used to 'inform' our macroscopic model in those areas where actual lung experiments are difficult if not impossible to perform.

1.1. Problem Statement

Pulmonary contusion is one of the most common thoracic soft-tissue injuries caused by blunt trauma, with a mortality rate of 10-25%.⁵ Damage to lungs is the main cause of morbidity following high-level blast exposures.⁶ Lung laceration is also common and debilitating.⁷ Existing constitutive models for lung tissue were developed from limited static test data, e.g., Fung, Vawter *et al.*⁸⁻¹⁰ These models, and others developed since then, omit relevant physics pertinent to blast and ballistic impacts required to assess BABT. They also require cumbersome optimization protocols to fit non-unique parameter sets,^{11,12} and/or are not validated against independent data.¹³ Better lung models suitable for dynamic analysis are needed so that the Army can design improved PPE to better protect their soldiers.

The primary objective of the ARL-WMRD project *Modeling Large Deformations and Stress Wave Mechanics in Soft Biological Tissue* is to develop such models for deformation and damage/injury assessment. These are continuum models derived from thermodynamics that utilize internal state variables to account for the irreversible aspects of response.^{1,2} Models (both macroscopic and microscopic) are specifically sought whose parameters are physical and whose parameterization is straightforward. Characterization of the parameters in a model requires experimental data. This presents an enormous challenge, one that is being addressed in the ARL-WMRD project through other university collaborators.

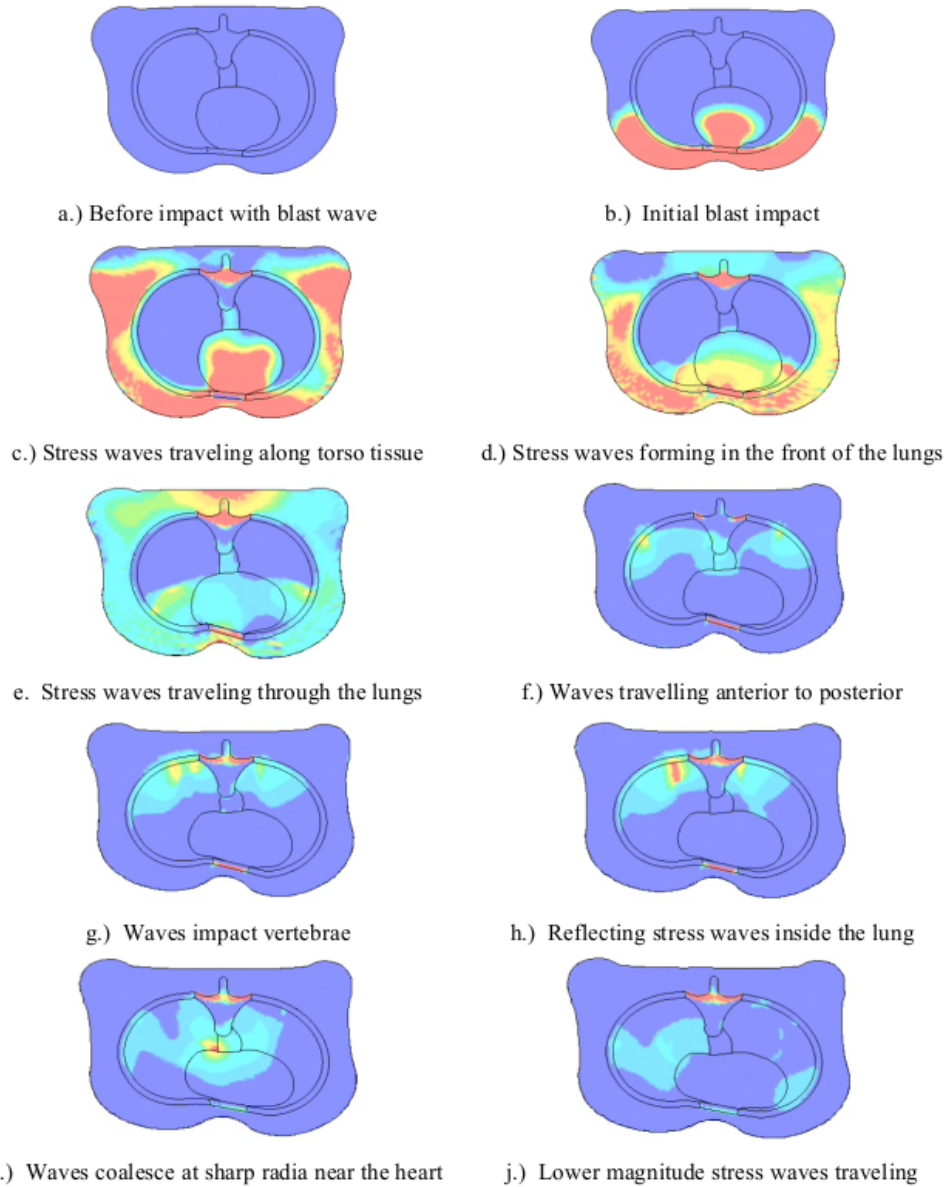


Fig. 1 Finite element analysis done using LS-Dyna to model shock waves traversing a cross-sectional slice of a human torso. Material models from the LS-Dyna library of available models were used.³

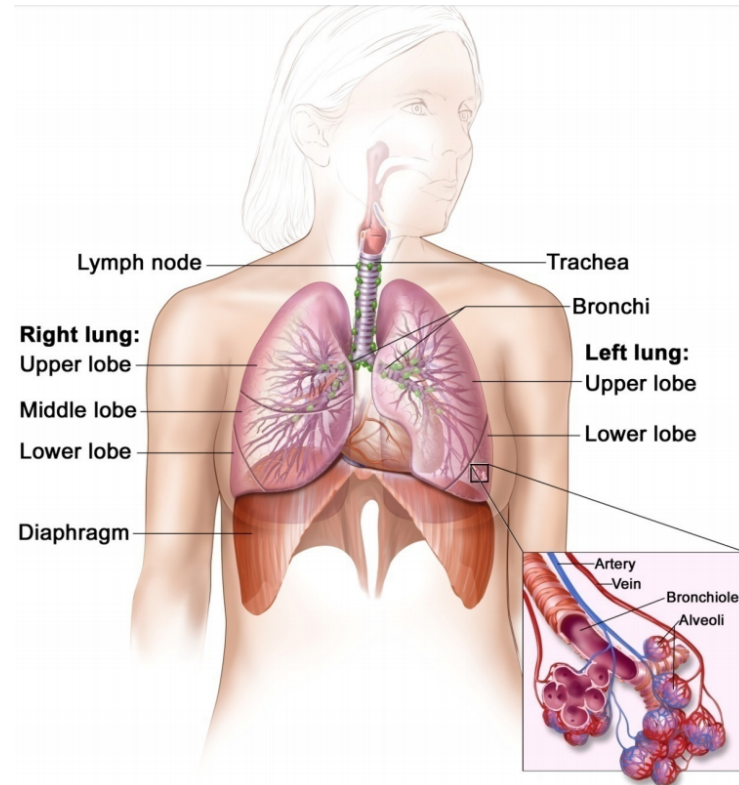


Fig. 2 A medical drawing of the respiratory system.³



Fig. 3 Lungs excised from animals (most likely ovine) who expired from injuries caused by a blast.⁴

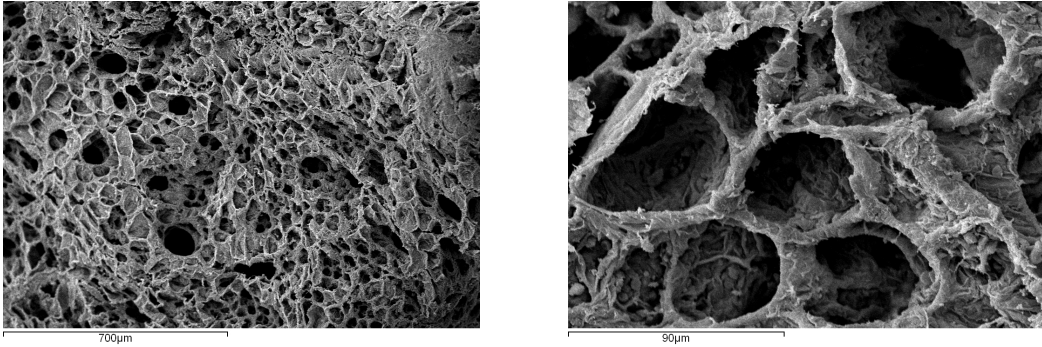
DRAFT: UNCLASSIFIED

Performing experiments for the purpose of model characterization is extremely difficult when it comes to modeling lung. Lung is a structure; parenchyma is a material. Therefore, one would normally choose to test the parenchyma, and from these data extract one's model parameters but, because of its spongy nature, we are challenged to do so in a physically meaningful way. Consequently, one typically tests whole lungs, or lobes thereof, and from these structural experiments we are tasked to extract material parameters through an inverse analysis. An alternative approach whereby one could, in principle, acquire parameters for the continuum models being developed at ARL-WMRD would be to homogenize a microscopic structural response for the alveoli of parenchyma. The work presented here addresses this approach in our modeling of deformation, damage and injury in alveolar structures.

Our approach is also advantageous for understanding the influence of microstructure on the higher-scale continuum properties. Curve fitting to macroscopic data alone does not provide such insight. This multi-scale approach can also be used to determine properties for regimes (stress-strain-strain rate histories) that cannot be reached experimentally, due to limitations in testing facilities, capabilities, or sufficient animal tissue availability.

The narrative that follows seeks to develop two material models for lung: one for mechanical deformation and the other for damage/injury/trauma. Models are sought whose parameters have physical interpretation. Ideally, they will enhance our understanding of the deformation and damage mechanisms at play during BABT. Specifically, they will describe how alveoli respond to pressure-waves and/or shear-waves as these wave fronts pass through them. This modeling will be accomplished by constructing a multi-scale model connecting the parenchyma (macro) and alveolar (micro) levels. In-silico experiments could then be done on the alveolar structural model, whose homogenized response could serve as an aid in the characterization of ARL's continuum models. These ARL-WMRD models are being designed to perform efficiently in their implementation into finite element codes. This will allow for BABT analyses to be done during the design of future PPE with an ultimate goal of saving soldiers' lives.

The primary purpose of this work is to provide a microscopic model for lung tissue that can be used as an aid in the parameterization of a macroscopic model for lung that will be reasonably accurate yet efficient to run in full torso finite element



(a) Magnification at 100X. This is Fig. 5 in Freed *et al.*¹⁴

(b) Magnification at 750X. This is Fig. 7 in Freed *et al.*¹⁴

Fig. 4 SEM photographs from a sectioned rat lung. The alveolar diameter in rat lung is about one quarter the alveolar diameter in human lung.

analyses to study BABT.

1.2. Approach

Figure 4 shows micrographs from a rat lung taken at different magnifications. In the lower-resolution image one sees numerous alveoli that became exposed because of the sectioning process. Also present are several alveolar ducts that connect the individual alveoli with the bronchial tree. In the higher-resolution image we observe the faceted structure of these alveoli, wherein one can see the septal chords and membranes, the latter being traversed by capillaries through which gas exchange occurs. Gas exchange will not be modeled here.

Alveolar geometry is modeled here as a dodecahedron, i.e., a soccer-ball like structure comprised of twelve pentagonal facets bordered by thirty septal cords that are connected at twenty vertices. Each vertex links three neighboring cords of the alveolus with a fourth chord from a neighboring alveolus. BABT can occur through multiple mechanisms, e.g., tearing of septal cords and/or alveolar membranes, and in more severe cases, rupturing of capillaries can also happen causing interstitial fluids and blood to leak into neighboring alveoli, all illustrated in Fig. 5. Our dodecahedral model for alveoli is capable of capturing these trauma events.

Conjecture. *A microscopic strain field, measured at the scale of alveoli, is the same as its macroscopic strain field in which it resides, measured at the scale of parenchyma. The motion is affine, and the local motion is homogeneous.*

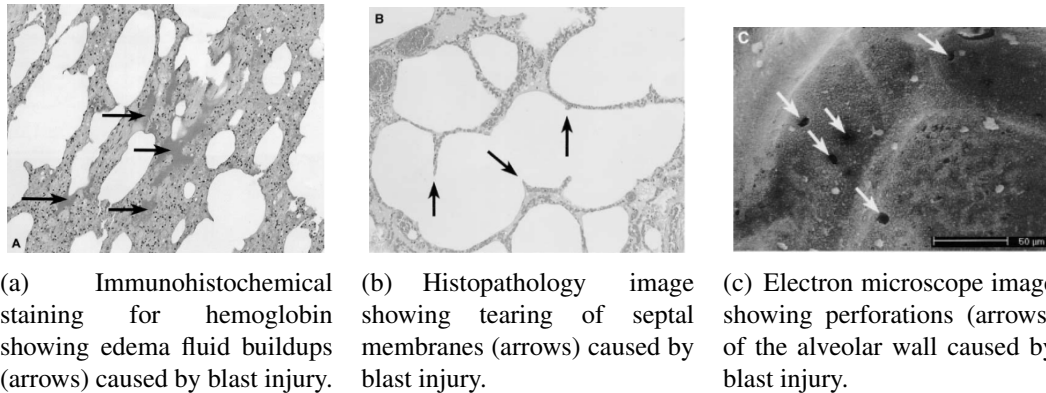


Fig. 5 All images were from Tsokos *et al.*¹⁵

This hypothesis was tested and confirmed in an experimental study done by Butler *et al.*¹⁶ where they used light scattering to study changes in geometry of the septal planes in alveoli, from which they concluded: “the microscopic strain field does not differ significantly from the macroscopic field.” We employ this hypothesis by taking the deformation gradient from, say, a Gauss point in a finite element model of lung, e.g., from a Gauss point associated with Fig. 1, and imposing it as a far-field deformation onto our dodecahedral model of an alveolus. From this kinematic input we arrive at an upper bound on the macroscopic stress/stiffness response, akin to a Voigt approximation, through a homogenization of the microscopic forces created within our structural model for an alveolus.

The authors of a review article on alveolar strain finished by writing:

“In general, computational mechanics approaches to determine function in a healthy or diseased lung have proven to be useful in explaining or measuring observations that are not captured by imaging modalities. However, for these models to fully explain complex physiological mechanical events, appropriate mechanical properties, boundary conditions, and mechanical loads must be identified. Moreover, validation of such computational models, which is an essential component of any computational mechanics approach, remains to be a challenge in the analysis of soft tissue mechanics.”

Roan & Waters [17, pg. L633]

In this research we set out to develop a constitutive framework for alveolar mechanics, fully cognizant of the aforementioned challenges. Our objectives are different

DRAFT: UNCLASSIFIED

from those of prior studies in alveolar mechanics in that we seek to describe the response/injury of a human lung that has been subjected to a stress wave propagating across the thorax region caused by an impact from either a blunt object or a blast wave. Consequently, some important aspects in the modeling of a breathing lung are thought to be less impactful here, e.g., the effect of surfactant in keeping alveoli from collapsing at the end of expiration.

As a foundation, we adopt the guideline:

“Constitutive equations are phenomenological. They are regarded as empirical by experimenters, and axiomatic by mathematicians. In biomechanics, we often try to derive them on the basis of microstructure . . . in order to gain a better understanding, or to get some guidance to the mathematical form.”

Y.-C. Fung [18, pg. 431]

The approach adopted here is to use the geometry of a dodecahedron as a *microscopic* mechanical model for alveoli, whose far-field response to mechanical stimuli, in accordance with our Conjecture on pg. 6, will be used to inform the development of a *macroscopic* mechanical model for parenchyma,^{1,2} the predominant tissue in lung. This is deemed necessary because of the complex porous structure of parenchyma, as compared with the homogeneous structure of rubbery elastic solids whose theories have historically been employed to model parenchyma.^{8,9,19,20} The ARL-WMRD continuum (macroscopic) model for parenchyma¹ will be implemented into finite element codes by others on our team with an end objective of providing a numerical tool that can be used by Army engineers in their efforts to develop improved and more effective designs for a soldier’s PPE.

1.3. Organization

This document is organized in the following manner. Part 2 introduces the dodecahedron as a model for alveoli. Its geometric properties are derived in detail with regards to its three geometric features: 1D septal chords, 2D septal membranes, and 3D volume. Part 3 develops the kinematics required for us to model a deforming dodecahedron, again focusing on the 1D chords, 2D membranes, and the 3D volume within, including the shape functions needed for interpolating each geometry. Part 4 derives constitutive models suitable for describing the thermo-mechanical response for the structural constituents of an alveolus: its septal chords, its permeable

DRAFT: UNCLASSIFIED

membranes, and its volume. Part 5 presents numerical methods used for solving first-order parabolic and second-order hyperbolic, ordinary, differential equations (ODEs), and for solving spatial integrations along a bar, across a pentagon, and throughout a tetrahedron using Gaussian quadrature schemes designed for each geometry. Part 6 describes a variational formulation used to create our structural model for an alveolus, which consists of three models: one comprised of septal chords, another comprised of septal membranes, and the third comprised of alveolar volume. All interpolate their stresses to the vertices where the forces from each are summed and homogenized for return to the macroscopic solver. Constitutive equations suitable for modeling biological tissues are derived from thermodynamics using the theory of implicit elasticity presented in App. A.

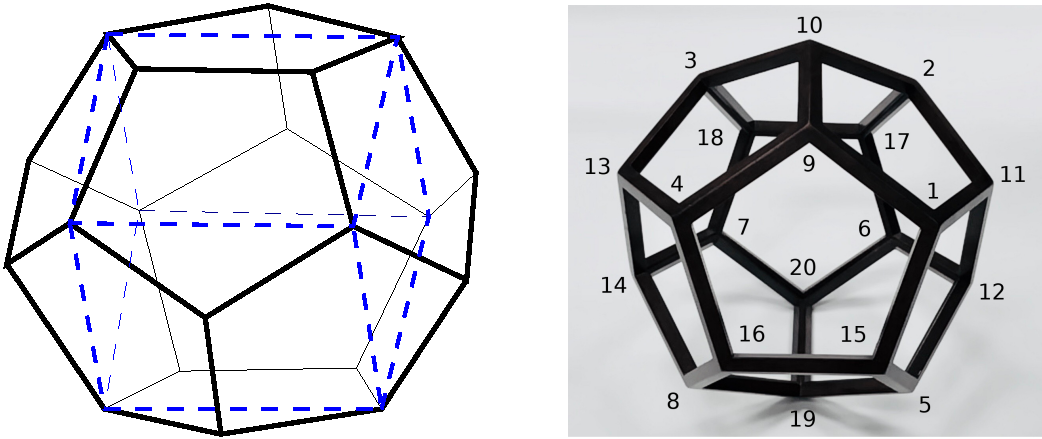
Part 2

Dodecahedra: A Model for Alveoli

Typical alveoli are fourteen sided polyhedra with one face normally being open as a mouth to an alveolar duct, and whose septal membranes typically become flat at transpulmonary pressures as low as 2 cm H₂O.²¹ To capture the microstructural features of lung, researchers have modeled both alveoli and alveolar ducts, as seen in Fig. 4; we only address alveoli here. Three different geometric shapes are typically employed when modeling an alveolus: a dodecahedron introduced by Frankus & Lee²² in 1974, a rhombic dodecahedron introduced by de Ryk, Thiesse, Namati & McLennan²³ in 2007, and a truncated octahedron, i.e., a tetrakaidecahedron, introduced by Dale, Matthews & Schroter²⁴ in 1980. The dodecahedron and rhombic dodecahedron are both twelve sided polyhedra with faces being pentagons and rhombuses, respectively. A tetrakaidecahedron is a pair of pyramids stacked bottom to bottom, forming an octahedron, whose six points are then removed. The end result is a fourteen sided polyhedron with six faces that are squares and eight faces that are hexagons, where like shapes have like dimensions.

The tetrakaidecahedron and rhombic dodecahedron are both volume filling. This property is preferred whenever one sets out to construct assemblages of alveoli to build a microstructural model that is to be solved numerically via a finite element method. The purpose of such an exercise is to homogenize the response of an alveolar assembly up to the macroscopic level, i.e., the level of a continuum mass point, a.k.a., the parenchyma.^{23–29} Such a finite element model can serve as a representative volume element (RVE) for parenchyma.

The dodecahedron is an isotropic structure, or very nearly so as we shall show, and is nearly volume filling.³⁰ It becomes a preferred geometry whenever a single alveolus is to be used as the RVE of homogenization, and from which closed form solutions have been derived.^{14,30–32} Here isotropy of the microstructure ensures an isotropic macro response. Parenchyma, as a tissue, is isotropic;^{20,33,34} whereas, lung, as an organ, is a complex, heterogeneous structure.^{35,36} This distinction has, from time-to-time, been forgotten.³⁷



(a) A cube is contained within a dodecahedron, with one of its five possible orientations being displayed. Atop each face of the cube resides four pentagonal sub-areas that form the shape of a hipped roof line.

(b) Vertices 1 through 8 are located at the corners of such a cube. The centroid for the cube is also the centroid for the dodecahedron. Vertices 9 through 20 are corners of the hipped roof lines residing above each face of the cube.

Fig. 6 Geometric representations for a dodecahedron.

For the reasons stated above, a dodecahedron, with vertices labeled according to Fig. 6(b), is the geometric structure selected for use in this study. The question of how one assigns a co-ordinate system to a dodecahedron is discussed first. Given this co-ordinate system, vertices of a dodecahedron are then assigned from which its septal chords and septal membranes are readily established.

2.1. Co-ordinate Indexing

An orthonormal set of base vectors $(\vec{i}, \vec{j}, \vec{k})$ is assigned to a dodecahedron whose origin resides at its centroid and whose directions align with a set of far-field base vectors used for reference in one's finite element model of a lung. The question is: How does one orient the indexing scheme of Fig. 6 against this basis? Alternatively: How can one describe a mapping $(\vec{i}, \vec{j}, \vec{k}) \mapsto (\vec{E}_1, \vec{E}_2, \vec{E}_3)$ wherein an orthonormal set of base vectors $(\vec{E}_1, \vec{E}_2, \vec{E}_3)$ is to serve as a reference basis for our alveolar dodecahedron to which the indexing scheme presented in Fig. 6 applies?

Given that a finite element model for lung exists, then a deformation gradient \mathbf{F} can be made available at any mass point therein whereat an alveolus of interest resides. The components of this deformation gradient are F_{ij} , $i, j = 1, 2, 3$, when evaluated in the co-ordinate frame $(\vec{i}, \vec{j}, \vec{k})$, which is the co-ordinate frame of the finite element analysis. A Gram-Schmidt (or **QR**) decomposition of a non-singular

3×3 matrix results in a tangent vector \vec{g}_1 and normal vector $\vec{g}_1 \times \vec{g}_2$ that remain invariant under transformations of the triangular matrix \mathbf{R} .³⁸ These convected base vectors $(\vec{g}_1, \vec{g}_2, \vec{g}_3)$ rotate out of basis $(\vec{E}_1, \vec{E}_2, \vec{E}_3)$ via a Gram rotation.³⁹ Given this geometric information, Paul, Rajagopal & Freed⁴⁰ were able to provide an answer to the above question of co-ordinate frame selection.

Their approach begins by establishing the extent of transverse shear crossing each of the co-ordinate directions $(\vec{i}, \vec{j}, \vec{k})$, as quantified by

$$\mathcal{G}_1 = \frac{\sqrt{F_{21}^2 + F_{31}^2}}{F_{11}}, \quad \mathcal{G}_2 = \frac{\sqrt{F_{12}^2 + F_{32}^2}}{F_{22}}, \quad \mathcal{G}_3 = \frac{\sqrt{F_{13}^2 + F_{23}^2}}{F_{33}} \quad (1)$$

where \mathcal{G}_i is a measure of the shear deformation cutting across the i^{th} direction. Unit vector \vec{E}_1 is selected as that direction from the set $\{\vec{i}, \vec{j}, \vec{k}\}$ which possesses minimal transverse shear. Once selected, there are two possible planes that contain base vector \vec{E}_1 , and the one selected whose normal is to be $\vec{E}_1 \times \vec{E}_2$ is that plane with the least amount of in-plane shear, which can be determined by taking appropriate dot products between column vectors $\mathbf{f}_i = \{F_{1i} \ F_{2i} \ F_{3i}\}^T$, $i = 1, 2, 3$. Vector \mathbf{f}_i has elements taken from the i^{th} column of matrix F_{ij} , which represents the deformation gradient \mathbf{F} evaluated in $(\vec{i}, \vec{j}, \vec{k})$. Their strategy is summarized in Alg. 1.

Algorithm 1 inputs a deformation gradient \mathbf{F} whose components F_{ij} are evaluated in the co-ordinate system $(\vec{i}, \vec{j}, \vec{k})$ associated with, in our case, a finite element model for lung. The algorithm outputs an orthogonal matrix \mathbf{P} that re-indexes the components of deformation gradient F_{ij} into an equivalent form where $\mathbf{F} = \mathcal{F}_{ij} \vec{E}_i \otimes \vec{E}_j$. It is this re-indexed matrix \mathcal{F}_{ij} that is to be subjected to Gram-Schmidt factorization, which is discussed later in Part 3.

There are six cases that can arise. Their associated orthogonal matrices are

$$\begin{aligned} [\mathbf{P}_1] &= \begin{bmatrix} 1 & 0 & 0 \\ 0 & 1 & 0 \\ 0 & 0 & 1 \end{bmatrix} & [\mathbf{P}_2] &= \begin{bmatrix} 1 & 0 & 0 \\ 0 & 0 & 1 \\ 0 & 1 & 0 \end{bmatrix} & [\mathbf{P}_3] &= \begin{bmatrix} 0 & 1 & 0 \\ 1 & 0 & 0 \\ 0 & 0 & 1 \end{bmatrix} \\ [\mathbf{P}_4] &= \begin{bmatrix} 0 & 0 & 1 \\ 1 & 0 & 0 \\ 0 & 1 & 0 \end{bmatrix} & [\mathbf{P}_5] &= \begin{bmatrix} 0 & 1 & 0 \\ 0 & 0 & 1 \\ 1 & 0 & 0 \end{bmatrix} & [\mathbf{P}_6] &= \begin{bmatrix} 0 & 0 & 1 \\ 0 & 1 & 0 \\ 1 & 0 & 0 \end{bmatrix} \end{aligned} \quad (2a)$$

Algorithm 1: Pivoting of the co-ordinate system.

Input: Deformation gradient \mathbf{F} with components F_{ij} expressed in $(\vec{i}, \vec{j}, \vec{k})$.

if $\mathcal{G}_1 \leq \mathcal{G}_2$ and $\mathcal{G}_1 \leq \mathcal{G}_3$ **then**

if $f_1 \cdot f_2 \leq f_1 \cdot f_3$ **then**
 $[\mathcal{F}_1] = [\mathbf{P}_1]^T [\mathbf{F}] [\mathbf{P}_1] : [\mathcal{F}] = [\mathcal{F}_1], [\mathbf{P}] = [\mathbf{P}_1],$
 $\therefore (\vec{i}, \vec{j}, \vec{k}) \mapsto (\vec{\mathbf{E}}_1, \vec{\mathbf{E}}_2, \vec{\mathbf{E}}_3)$

else
 $[\mathcal{F}_2] = [\mathbf{P}_2]^T [\mathbf{F}] [\mathbf{P}_2] : [\mathcal{F}] = [\mathcal{F}_2], [\mathbf{P}] = [\mathbf{P}_2],$
 $\therefore (\vec{i}, \vec{j}, \vec{k}) \mapsto (\vec{\mathbf{E}}_1, \vec{\mathbf{E}}_3, \vec{\mathbf{E}}_2)$

else if $\mathcal{G}_2 \leq \mathcal{G}_1$ and $\mathcal{G}_2 \leq \mathcal{G}_3$ **then**

if $f_1 \cdot f_2 \leq f_2 \cdot f_3$ **then**
 $[\mathcal{F}_3] = [\mathbf{P}_3]^T [\mathbf{F}] [\mathbf{P}_3] : [\mathcal{F}] = [\mathcal{F}_3], [\mathbf{P}] = [\mathbf{P}_3],$
 $\therefore (\vec{i}, \vec{j}, \vec{k}) \mapsto (\vec{\mathbf{E}}_2, \vec{\mathbf{E}}_1, \vec{\mathbf{E}}_3)$

else
 $[\mathcal{F}_4] = [\mathbf{P}_4]^T [\mathbf{F}] [\mathbf{P}_4] : [\mathcal{F}] = [\mathcal{F}_4], [\mathbf{P}] = [\mathbf{P}_4],$
 $\therefore (\vec{i}, \vec{j}, \vec{k}) \mapsto (\vec{\mathbf{E}}_2, \vec{\mathbf{E}}_3, \vec{\mathbf{E}}_1)$

else

if $f_1 \cdot f_3 \leq f_2 \cdot f_3$ **then**
 $[\mathcal{F}_5] = [\mathbf{P}_5]^T [\mathbf{F}] [\mathbf{P}_5] : [\mathcal{F}] = [\mathcal{F}_5], [\mathbf{P}] = [\mathbf{P}_5],$
 $\therefore (\vec{i}, \vec{j}, \vec{k}) \mapsto (\vec{\mathbf{E}}_3, \vec{\mathbf{E}}_1, \vec{\mathbf{E}}_2)$

else
 $[\mathcal{F}_6] = [\mathbf{P}_6]^T [\mathbf{F}] [\mathbf{P}_6] : [\mathcal{F}] = [\mathcal{F}_6], [\mathbf{P}] = [\mathbf{P}_6],$
 $\therefore (\vec{i}, \vec{j}, \vec{k}) \mapsto (\vec{\mathbf{E}}_3, \vec{\mathbf{E}}_2, \vec{\mathbf{E}}_1)$

Output: Deformation gradient \mathbf{F} with components \mathcal{F}_{ij} expressed in $(\vec{\mathbf{E}}_1, \vec{\mathbf{E}}_2, \vec{\mathbf{E}}_3)$, as re-indexed by the orthogonal matrix $[\mathbf{P}]$.

whose affiliated components for the re-indexed deformation gradient are

$$\begin{aligned} [\mathcal{F}_1] &= \begin{bmatrix} F_{11} & F_{12} & F_{13} \\ F_{21} & F_{22} & F_{23} \\ F_{31} & F_{32} & F_{33} \end{bmatrix} & [\mathcal{F}_2] &= \begin{bmatrix} F_{11} & F_{13} & F_{12} \\ F_{31} & F_{33} & F_{32} \\ F_{21} & F_{23} & F_{22} \end{bmatrix} & [\mathcal{F}_3] &= \begin{bmatrix} F_{22} & F_{21} & F_{23} \\ F_{12} & F_{11} & F_{13} \\ F_{32} & F_{31} & F_{33} \end{bmatrix} \\ [\mathcal{F}_4] &= \begin{bmatrix} F_{22} & F_{23} & F_{21} \\ F_{32} & F_{33} & F_{31} \\ F_{12} & F_{13} & F_{11} \end{bmatrix} & [\mathcal{F}_5] &= \begin{bmatrix} F_{33} & F_{31} & F_{32} \\ F_{13} & F_{11} & F_{12} \\ F_{23} & F_{21} & F_{22} \end{bmatrix} & [\mathcal{F}_6] &= \begin{bmatrix} F_{33} & F_{32} & F_{31} \\ F_{23} & F_{22} & F_{21} \\ F_{13} & F_{12} & F_{11} \end{bmatrix} \end{aligned} \tag{2b}$$

where case 1 is the default case whose operator \mathbf{P}_1 is the identity tensor.

All vectors \mathbf{V} with components V_i evaluated in $(\vec{\mathbf{E}}_1, \vec{\mathbf{E}}_2, \vec{\mathbf{E}}_3)$ will rotate into $(\vec{\mathbf{i}}, \vec{\mathbf{j}}, \vec{\mathbf{k}})$ with components V_i according to the map

$$V_i = P_{ij} V_j \quad \text{or inversely} \quad V_i = P_{ji} V_j \tag{3a}$$

while all tensors \mathbf{T} with components T_{ij} evaluated in $(\vec{\mathbf{E}}_1, \vec{\mathbf{E}}_2, \vec{\mathbf{E}}_3)$ will rotate into $(\vec{\mathbf{i}}, \vec{\mathbf{j}}, \vec{\mathbf{k}})$ with components T_{ij} according to the map

$$T_{ij} = P_{ik} T_{k\ell} P_{j\ell} \quad \text{or inversely} \quad T_{ij} = P_{ki} T_{k\ell} P_{\ell j} \tag{3b}$$

where the latter appears in Alg. 1 with regards to components of the deformation gradient.

From this point onward, it is assumed that base vectors $(\vec{\mathbf{E}}_1, \vec{\mathbf{E}}_2, \vec{\mathbf{E}}_3)$ are known, and that they serve as the reference basis for our alveolar analysis.

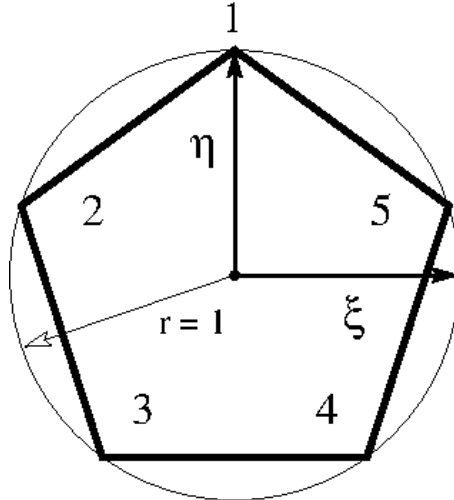


Fig. 7 A regular pentagon inscribed within the unit circle establishes its natural co-ordinate system with co-ordinates (ξ, η) described in Eqn. (4), and whose origin is located at its centroid. Vertices are numbered counterclockwise with the uppermost vertex being labeled 1.

2.2. Geometric Properties of a Regular Pentagon

Figure 7 presents a regular pentagon drawn in its natural co-ordinate system with co-ordinates designated as (ξ, η) . Vertices of such a pentagon are placed at

$$\xi = \cos \left(\frac{2(k-1)\pi}{5} + \frac{\pi}{2} \right) \quad \eta = \sin \left(\frac{2(k-1)\pi}{5} + \frac{\pi}{2} \right) \quad k = 1, 2, \dots, 5 \quad (4)$$

wherein k denotes the vertex number, as assigned in Fig. 7. These vertices inscribe a pentagon within the unit circle.

Lengths of the five chords in a regular pentagon, when measured in its natural co-ordinate system, are all

$$L^p = 2 \cos(\omega) \approx 1.176 \quad (5)$$

while the area of this pentagon is

$$A^p = \frac{5}{4} \tan(\omega) L^p{}^2 = 5 \sin(\omega) \cos(\omega) \approx 2.378 \quad (6)$$

where area of the unit circle that inscribes this pentagon is $\pi r^2 \approx 3.142$, $r = 1$. The inside angles of a regular pentagon all measure $2\omega = 108^\circ$. All approximations are truncated at four significant figures.

2.3. Geometric Properties of a Regular Dodecahedron

Like the pentagon considered above, which inscribes the unit circle, here we consider a dodecahedron that inscribes the unit sphere. Let this geometry be described in its natural co-ordinate system with co-ordinates (ξ, η, ζ) whose origin is located at its centroid, the center of the sphere. The twenty vertices of this dodecahedron, all of which touch the unit sphere, are placed at

$$\begin{array}{ccc} \xi & \eta & \zeta \\ \hline \pm 1/\sqrt{3} & \pm 1/\sqrt{3} & \pm 1/\sqrt{3} \\ \pm \phi/\sqrt{3} & \pm 1/\sqrt{3}\phi & 0 \\ 0 & \pm \phi/\sqrt{3} & \pm 1/\sqrt{3}\phi \\ \pm 1/\sqrt{3}\phi & 0 & \pm \phi/\sqrt{3} \end{array} \quad (7)$$

where $\phi = (1 + \sqrt{5})/2 \approx 1.618$, which is also known as the golden ratio.

Lengths of the thirty chords in a regular dodecahedron, when measured in its natural co-ordinate system, are all

$$L^d = \frac{2}{\sqrt{3}\phi} \approx 0.7136 \quad (8)$$

while the volume of such a dodecahedron is

$$V^d = \frac{40}{3\sqrt{3}\phi^3} \tan^2(\omega) \sin(\omega) \approx 2.785 \quad (9)$$

where volume of the unit sphere that inscribes the dodecahedron is $\frac{4}{3}\pi r^3 \approx 4.189$, $r = 1$.

The scale factor to map between the natural co-ordinates of a pentagon, defined in Eq. (4), with those of a dodecahedron, defined in Eq. (7), is

$$\frac{L^p}{R^p} = \frac{L^d}{R_d^p} \quad \text{or} \quad R_d^p = \frac{R^p L^d}{L^p} = \frac{L^d}{L^p} = \frac{1}{\sqrt{3}\phi \cos(\omega)} \approx 0.6071 \quad (10)$$

because $R^p = 1$, with scale factor R_d^p being the radius that inscribes a pentagon on the surface of a dodecaheron that itself inscribes an unit sphere.

2.4. Dimensions of Human Alveoli

Septal chord length $L(D)$, expressed as a function of alveolar diameter D , can be estimated by considering the areal projection of a dodecahedron onto a plane that contains one of its pentagonal faces, which leads to

$$L = \frac{D}{\tan(\omega)(1 + \cos(\alpha))} \approx \frac{D}{2.685}, \quad (11)$$

where $\alpha = \pi/10 = 18^\circ$. (There are twenty, equal, pie-shaped wedges that comprise this projected area.) This is an average of the shortest and longest distances across this plane of projection. Alveolar diameter D is a property that can be measured in histological studies of parenchyma.

To dimension the alveoli of human lung, Sabin, Fung & Tremer⁴¹ measured the mean diameter across an individual alveolus, viz., D of Eq. (11), sectioned from human lungs that were fixed at three different pressures. Samples were taken from nine lungs extracted postmortem from individuals between 16 to 89 years of age.* At a transpulmonary pressure of 4 cm H₂O, the mean alveolar diameter was $D = 191 \pm 86 \mu\text{m}$ determined from a sampling size of 1423; at a pressure of 10 cm H₂O, $D = 202 \pm 88 \mu\text{m}$ determined from a sampling size of 1296; and at a pressure of 14 cm H₂O, $D = 235 \pm 99 \mu\text{m}$ determined from a sampling size of 1083. These data are plotted in Fig. 8. All reported and drawn error bounds pertain to plus/minus one standard deviation in error.

2.5. Geometric Properties for Irregular Pentagons and Dodecahedra

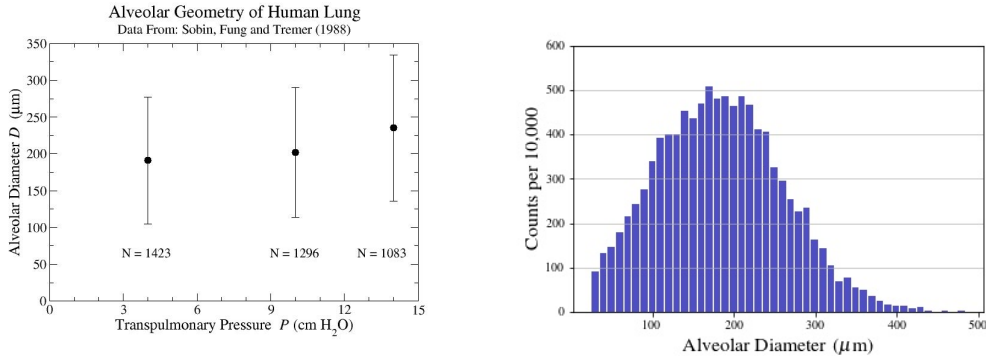
Formulæ (6 & 9) only apply for regular pentagons and dodecahedra evaluated in their respective natural co-ordinate systems. For irregular dodecahedra, the areas of its irregular pentagons are calculated via†

$$A = \frac{1}{2} \sum_{i=1}^5 (x_i y_{i+1} - x_{i+1} y_i) \quad (12)$$

where $x_6 \Leftarrow x_1$ and $y_6 \Leftarrow y_1$. In order for the predicted area to be positive when using this formula, it is necessary that the vertices (x_i, y_i) index counterclockwise,

*Sabin *et al.*⁴¹ also documented an age effect in these data that has been averaged over here, i.e., ignored.

†Bourke, P., “Polygons, Meshes.” <http://paulbourke.net/geometry/>.



(a) Mean and standard deviations for alveolar diameters in human lung.⁴¹ (b) A typical histogram for these statistics, truncated at alveolar diameters below 24 μm .

Fig. 8 Alveolar diameters in human lung.

as drawn in Fig. 7. The centroid of this pentagon has co-ordinates[†]

$$c_x = \frac{1}{6A} \sum_{i=1}^5 (x_i + x_{i+1})(x_i y_{i+1} - x_{i+1} y_i) \quad (13a)$$

$$c_y = \frac{1}{6A} \sum_{i=1}^5 (y_i + y_{i+1})(x_i y_{i+1} - x_{i+1} y_i) \quad (13b)$$

wherein the vertex co-ordinates x_i and y_i are quantified in a 2D pentagonal frame of reference, e.g., as established later in Fig. 10.

To compute the volume of an irregular dodecahedron, use the formula^{*}

$$288 V_{tet}^2 = \begin{vmatrix} 0 & 1 & 1 & 1 & 1 \\ 1 & 0 & \ell_{12}^2 & \ell_{13}^2 & \ell_{14}^2 \\ 1 & \ell_{21}^2 & 0 & \ell_{23}^2 & \ell_{24}^2 \\ 1 & \ell_{31}^2 & \ell_{32}^2 & 0 & \ell_{34}^2 \\ 1 & \ell_{41}^2 & \ell_{42}^2 & \ell_{43}^2 & 0 \end{vmatrix} \quad (14)$$

to calculate each of the 60 individual tetrahedral volumes that collectively fill the volume of an irregular dodecahedron. Here ℓ_{ij} is the length of that tetrahedral edge with vertices i and j ; $i, j = 1, 2, 3, 4$; $i \neq j$; with $\ell_{ij} = \ell_{ji}$.

^{*}Colins, K. D., “Cayley-Menger Determinant.” From MathWorld—A Wolfram Web Resource, created by Eric W. Weisstein. <http://mathworld.wolfram.com/CayleyMengerDeterminant.html>.

Vertex	ξ	η	ζ	Vertex	ξ	η	ζ
1	$1/\sqrt{3}$	$1/\sqrt{3}$	$1/\sqrt{3}$	11	$\phi/\sqrt{3}$	$1/\sqrt{3}\phi$	0
2	$1/\sqrt{3}$	$1/\sqrt{3}$	$-1/\sqrt{3}$	12	$\phi/\sqrt{3}$	$-1/\sqrt{3}\phi$	0
3	$-1/\sqrt{3}$	$1/\sqrt{3}$	$-1/\sqrt{3}$	13	$-\phi/\sqrt{3}$	$1/\sqrt{3}\phi$	0
4	$-1/\sqrt{3}$	$1/\sqrt{3}$	$1/\sqrt{3}$	14	$-\phi/\sqrt{3}$	$-1/\sqrt{3}\phi$	0
5	$1/\sqrt{3}$	$-1/\sqrt{3}$	$1/\sqrt{3}$	15	$1/\sqrt{3}\phi$	0	$\phi/\sqrt{3}$
6	$1/\sqrt{3}$	$-1/\sqrt{3}$	$-1/\sqrt{3}$	16	$-1/\sqrt{3}\phi$	0	$\phi/\sqrt{3}$
7	$-1/\sqrt{3}$	$-1/\sqrt{3}$	$-1/\sqrt{3}$	17	$1/\sqrt{3}\phi$	0	$-\phi/\sqrt{3}$
8	$-1/\sqrt{3}$	$-1/\sqrt{3}$	$1/\sqrt{3}$	18	$-1/\sqrt{3}\phi$	0	$-\phi/\sqrt{3}$
9	0	$\phi/\sqrt{3}$	$1/\sqrt{3}\phi$	19	0	$-\phi/\sqrt{3}$	$1/\sqrt{3}\phi$
10	0	$\phi/\sqrt{3}$	$-1/\sqrt{3}\phi$	20	0	$-\phi/\sqrt{3}$	$-1/\sqrt{3}\phi$

Table 1 Natural co-ordinates for the vertices of a regular dodecahedron, as labeled in Fig. 6(b) according to Eqn. (7).

2.6. Indexing Scheme for Dodecahedra

In order to implement the dodecahedron as a geometric model for an alveolar sac, as suggested by the images in Fig. 4, it first becomes necessary to introduce a labeling strategy. Such a scheme is arbitrary, but once chosen it enables an analysis to be put forward. The labeling scheme adopted in this work is illustrated in the Fig. 6(b).

The co-ordinates positioning the twenty vertices of a regular dodecahedron in its natural frame of reference are presented in Table 1. According to the labeling scheme of Fig. 6(b), the thirty chords of a dodecahedron are given vertex assignments according to Table 2, while its twelve pentagons are given vertex assignments according to Table 3.

The sixty tetrahedra that fill the volume of the dodecahedron contain vertices according to the following strategy. Beginning with pentagon 1 and sequencing to pentagon 12, two of the four vertices come from a side of the pentagon in question with the remaining two vertices being the centroid for the associated pentagon and the centroid for the dodecahedron, i.e., the co-ordinate origin. From Table 3, tetrahedron 1 contains vertices 11 and 2 of pentagon 1, tetrahedron 2 contains vertices 2 and 10, tetrahedron 3 contains vertices 10 and 9, tetrahedron 4 contains vertices 9 and 1, tetrahedron 5 contains vertices 1 and 11, tetrahedron 6 contains vertices 10 and 2 from pentagon 2, etc.

Chord	Vertices	Chord	Vertices	Chord	Vertices
1	9, 10	11	17, 18	21	7, 18
2	1, 9	12	3, 18	22	7, 14
3	2, 10	13	4, 16	23	13, 14
4	3, 10	14	15, 16	24	8, 14
5	4, 9	15	1, 15	25	8, 16
6	1, 11	16	5, 15	26	5, 19
7	2, 11	17	5, 12	27	6, 20
8	3, 13	18	11, 12	28	7, 20
9	4, 13	19	6, 12	29	8, 19
10	2, 17	20	6, 17	30	19, 20

Table 2 Vertices that locate the endpoints of septal chords in a dodecahedron, as labeled in Fig. 6(b).

Pentagon	Vertices	Chords
1	11, 2, 10, 9, 1	6, 7, 3, 1, 2
2	10, 2, 17, 18, 3	4, 3, 10, 11, 12
3	13, 4, 9, 10, 3	8, 9, 5, 1, 4
4	9, 4, 16, 15, 1	2, 5, 13, 14, 15
5	15, 5, 12, 11, 1	15, 16, 17, 18, 6
6	17, 2, 11, 12, 6	20, 10, 7, 18, 19
7	18, 7, 14, 13, 3	12, 21, 22, 23, 8
8	16, 4, 13, 14, 8	25, 13, 9, 23, 24
9	12, 5, 19, 20, 6	19, 17, 26, 30, 27
10	14, 7, 20, 19, 8	24, 22, 28, 30, 29
11	20, 7, 18, 17, 6	27, 28, 21, 11, 20
12	19, 5, 15, 16, 8	29, 26, 16, 14, 25

Table 3 Vertices that locate the corners of regular pentagonal surfaces in a regular dodecahedron, and the chords that connect them. They are indexed counterclockwise when viewed looking from the outside in, and labeled according to Fig. 6(b). The apex for each pentagon resides at the peak of the hipped roof-line for that pentagon. This turns out to be important.

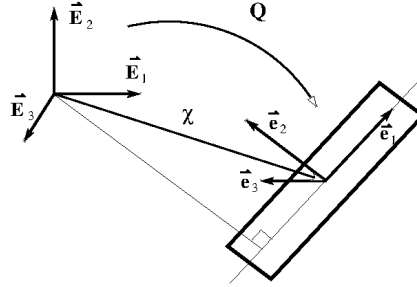


Fig. 9 The co-ordinate system of a chord ($\vec{e}_1, \vec{e}_2, \vec{e}_3$) relative to the co-ordinate system of its dodecahedron ($\vec{E}_1, \vec{E}_2, \vec{E}_3$) with origins located at their respective centroids that are offset by a translation χ . These describe a mapping $[\{\vec{e}_1\}\{\vec{e}_2\}\{\vec{e}_3\}] = [\{\vec{E}_1\}\{\vec{E}_2\}\{\vec{E}_3\}][Q]$ where Q is an orthogonal rotation. The tangent base vector \vec{e}_1 aligns with the axis of this chord. The normal base vector \vec{e}_2 is coaxial with a line segment drawn from the origin out to the chordal axis such that $\vec{e}_1 \cdot \vec{e}_2 = 0$, while the binormal base vector is given by the cross product $\vec{e}_3 = \vec{e}_1 \times \vec{e}_2$.

2.7. Co-Ordinate Systems for Chordal Fibers and Pentagonal Membranes

The dodecahedron used to model an alveolus is considered to be regular in its ‘natural’ configuration, with a capability of being irregular in its reference configuration, and certainly becoming irregular after deformation. The co-ordinate frame of its natural state is taken to have its origin positioned at the centroid of this regular dodecahedron, i.e., at the centroid of its enclosed cube (cf. Fig. 6) or, equivalently, at the origin of that unit sphere for which the dodecahedron inscribes, as presented in Table 1. We denote the base vectors associated with this frame of reference as $(\vec{E}_1, \vec{E}_2, \vec{E}_3)$, assigned according to Section 2.1. There are two other co-ordinate systems with relevance to our analysis: those for the chordal fibers, and those for the pentagonal membranes.

The local co-ordinate system of a chordal fiber is presented in Fig. 9, while the local co-ordinate system of a pentagonal membrane is presented in Fig. 10. Both co-ordinate systems are denoted as $(\vec{e}_1, \vec{e}_2, \vec{e}_3)$ and each rotates out of the reference co-ordinate system $(\vec{E}_1, \vec{E}_2, \vec{E}_3)$ via its own orthogonal tensor Q .

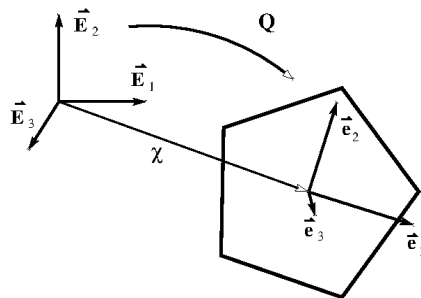


Fig. 10 The co-ordinate system of a pentagon ($\vec{e}_1, \vec{e}_2, \vec{e}_3$) relative to the co-ordinate system of its dodecahedron ($\vec{E}_1, \vec{E}_2, \vec{E}_3$) with origins located at their respective centroids that are offset by a translation χ . These describe a mapping $[\{\vec{e}_1\}\{\vec{e}_2\}\{\vec{e}_3\}] = [\{\vec{E}_1\}\{\vec{E}_2\}\{\vec{E}_3\}][Q]$ where Q is an orthogonal rotation. Base vector \vec{e}_1 is coaxial to a line segment that connects two vertices which locate a pair of shoulders in a pentagon, viz., vertices 2 and 5 in Fig. 7. Base vector \vec{e}_2 is coaxial with a line segment drawn from the head of this pentagon, i.e., vertex 1 in Fig. 7, down to its base such that $\vec{e}_1 \cdot \vec{e}_2 = 0$. Base vector $\vec{e}_3 = \vec{e}_1 \times \vec{e}_2$ is the outward normal to this surface.

Part 3

Kinematics

The irregular dodecahedron used here as a model for alveoli describes a 3D structure composed of thirty 1D rods (the septal chords) joined at twenty nodes (the vertices) that collectively circumscribe twelve 2D pentagonal membranes (the alveolar septa) that in turn envelop an alveolar sac whose volume is represented using sixty tetrahedra. To be able to describe the overall mechanical response of this 3D dodecahedral structure, it is conjectured to be sufficient to know the individual mechanical responses of its 1D septal chords, its 2D septal membranes, and the 3D void within. Their relevant kinematics are presented here, along with the shape functions used for interpolation and their descriptions of deformation via stretch, using Laplace stretch⁴² as our chosen kinematic field.

3.1. 1D Chords

The stretch of a rod under extension is a ratio of its lengths. Specifically, $\lambda := L/L_0$ where L and L_0 are its current and reference lengths, respectively, whose strain and strain rate are taken to be $e = \ln \lambda$ and $de = \lambda^{-1}d\lambda$. This is often referred to as a logarithmic, natural or true strain. Consequently, the kinematic analysis of a chord is trivial.

3.1.1 Shape Functions for Interpolating a Rod

A two-noded alveolar chord has shape functions N_i , $i = 1, 2$, that, when evaluated in its natural co-ordinate system where $-1 \leq \xi \leq 1$, describe a matrix with elements

$$\mathbf{N} = \begin{bmatrix} N_1 & N_2 \end{bmatrix} = \begin{bmatrix} \frac{1}{2}(1 - \xi) & \frac{1}{2}(1 + \xi) \end{bmatrix} \quad (15a)$$

that interpolate vector fields according to

$$\mathbf{x}(\xi) = \sum_{i=1}^2 N_i(\xi) \mathbf{x}_i, \quad \mathbf{u}(\xi) = \sum_{i=1}^2 N_i(\xi) \mathbf{u}_i \quad (15b)$$

etc., and whose spatial gradients are

$$N_{1,\xi} = -\frac{1}{2} \quad \text{and} \quad N_{2,\xi} = \frac{1}{2} \quad (15c)$$

wherein ξ is the natural co-ordinate. Components x_i and $u_i := x_i - x_{0i}$ are their global co-ordinates and displacements, respectively, located at the two nodes of a chord evaluated in the co-ordinate frame $(\vec{\mathbf{e}}_1, \vec{\mathbf{e}}_2, \vec{\mathbf{e}}_3)$ of Fig. 9 with the chordal axis lying in the $\vec{\mathbf{e}}_1$ direction.

3.1.2 Deformation Gradient for a Rod

The deformation gradient in this case is simply

$$\begin{aligned} \mathbf{F}(\xi) &= 1 + \frac{\partial \mathbf{u}}{\partial \xi} \left(\frac{\partial \mathbf{x}_0}{\partial \xi} \right)^{-1} = 1 + \sum_{i=1}^2 N_{i,\xi} u_i \left(\sum_{i=1}^2 N_{i,\xi} x_{0i} \right)^{-1} \\ &= 1 + \frac{u_2 - u_1}{x_{02} - x_{01}} \vec{\mathbf{e}}_1 \otimes \vec{\mathbf{e}}_1 = \frac{x_2 - x_1}{x_{02} - x_{01}} \vec{\mathbf{e}}_1 \otimes \vec{\mathbf{e}}_1 \end{aligned} \quad (16)$$

which is uniform over the length of a chord, i.e., it is independent of ξ .

3.2. 2D Triangles

Triangular elements are needed in a support capacity in order to construct our alevolar model; specifically, the four surfaces of a tetrahedron are triangles. What is required of them is a capability to compute the traction acting across such a surface through integration. This requires knowledge of their shape functions and quadrature rules, the latter topic being discussed in Part 5.

3.2.1 Shape Functions for Interpolating a Triangle

The shape functions for a triangle expressed in terms of its natural co-ordinates (ξ, η) , where $0 \leq \xi \leq 1$ and $0 \leq \eta \leq 1 - \xi$, are given by

$$N_1 = 1 - \xi - \eta \quad N_2 = \xi \quad N_3 = \eta \quad (17a)$$

with gradients of

$$N_{1,\xi} = -1 \quad N_{2,\xi} = 1 \quad N_{3,\xi} = 0 \quad (17\text{b})$$

$$N_{2,\eta} = -1 \quad N_{2,\eta} = 0 \quad N_{3,\eta} = 1 \quad (17\text{c})$$

so that the area of a triangle in its natural co-ordinates is $\frac{1}{2}$.

No further kinematics are required from triangular elements in our analysis.

3.3. 2D Irregular Pentagons

The kinematics of an irregular pentagon, on the other hand, are not trivial. Shape functions are required from which deformation gradients can then be constructed. Once a deformation gradient is in hand, the state of stretch occurring within a pentagon can finally be derived. Several possible decompositions of the deformation gradient are possible, i.e., stretch is not unique in 2D (nor in 3D). Here we employ the Laplace stretch.⁴³

3.3.1 Wachspress' Shape Functions for Interpolating an Irregular Pentagon

The idea here is to model each pentagonal face of the dodecahedron with exactly one pentagonal finite element. Five constant-strain triangles were originally considered, but their accuracy was found to be wanting when compared with that of a single pentagonal element whenever deformation becomes non-uniform. There was no difference between them whenever the deformation was an uniform dilation.

In 1975, Wachspress^{44,45} derived a set of shape functions N_i that are capable of interpolating convex polyhedra. His shape functions take on the form of rational polynomials, viz., $N_i = A_i/B$ where A_i and B are polynomials. In contrast, classic isoparametric elements are constructed from polynomial shape functions.⁴⁶ For the Wachspress shape functions of a pentagon, the A_i are cubic polynomials, while B is a quadratic polynomial.

Let us consider a convex pentagonal domain Ω defined over \mathbb{R}^2 whose vertices have global co-ordinates of

$$(x_1, y_1), (x_2, y_2), (x_3, y_3), (x_4, y_4), (x_5, y_5)$$

when evaluated in the pentagonal co-ordinate system $(\vec{\mathbf{e}}_1, \vec{\mathbf{e}}_2)$ of Fig. 10, with $\vec{\mathbf{e}}_3$ being an outward normal to the pentagon. Associated with this set of global co-ordinates is a set of local or natural co-ordinates

$$(\xi_1, \eta_1), (\xi_2, \eta_2), (\xi_3, \eta_3), (\xi_4, \eta_4), (\xi_5, \eta_5)$$

that describe a mapping or interpolation of

$$\begin{aligned} x(\xi, \eta) &= \sum_{i=1}^5 N_i(\xi, \eta) x_i & \text{or} & & x(\xi) &= \sum_{i=1}^5 N_i(\xi) x_i \\ y(\xi, \eta) &= \sum_{i=1}^5 N_i(\xi, \eta) y_i \end{aligned} \quad (18)$$

which relate natural co-ordinates $\xi \equiv (\xi, \eta)$ to global co-ordinates $\mathbf{x} \equiv (x, y)$, where $\mathbf{x}_i \equiv (x_i, y_i)$ are nodal co-ordinates at the i^{th} vertex, with i indexing counter-clockwise around a pentagon according to Fig. 7. Displacement $\mathbf{u}(\mathbf{x}) := \mathbf{x} - \mathbf{x}_0$, with reference co-ordinates $\mathbf{x}_0 \equiv (x_0, y_0)$, also obeys this mapping

$$\begin{aligned} u(\xi, \eta) &= \sum_{i=1}^5 N_i(\xi, \eta) u_i & \text{or} & & \mathbf{u}(\xi) &= \sum_{i=1}^5 N_i(\xi) \mathbf{u}_i \\ v(\xi, \eta) &= \sum_{i=1}^5 N_i(\xi, \eta) v_i \end{aligned} \quad (19)$$

whose co-ordinates $\mathbf{u}_i \equiv (u_i, v_i)$ designate the nodal displacements.

Shape functions $N_i(\xi) \equiv N_i(\xi, \eta)$ are interpolation functions that place any position P with local co-ordinates $\xi \equiv (\xi, \eta) \in \bar{\Omega}$, where $\bar{\Omega} := \Omega \cup \partial\Omega$, into their global co-ordinates $\mathbf{x} \equiv (x, y)$. The shape functions of Wachspress^{44,45} possess the following properties:⁴⁷

1. Partition of unity: $\sum_{i=1}^5 N_i(\xi) = 1, \quad 0 \leq N_i(\xi) \leq 1$.
2. Interpolate nodal data: $N_i(\xi_j) = \Xi_{ij}$.
3. Linear completeness: $\sum_{i=1}^5 N_i(\xi) \mathbf{x}_i = \mathbf{x}$.
4. For $\xi \in \Omega$, $N_i(\xi)$ is C^∞ , but for $\xi \in \partial\Omega$, $N_i(\xi)$ is C^0 , i.e., interpolation is linear along an edge (or chord) connecting two neighboring vertices.

For interpolating a convex, planar, pentagonal shape, the shape functions of Wachspress have polynomials of order three in their numerators, and another polynomial

DRAFT: UNCLASSIFIED

of order two in their denominators; specifically, we write them here as

$$N_{i+1}(\xi, \eta) = \kappa_i A_i(\xi, \eta)/B(\xi, \eta), \quad i = 1, 2, \dots, 5 \quad (20a)$$

with scaling factors κ_i , where $N_1 \Leftarrow N_6$, whose numerators and denominator for interpolating a pentagon are evaluated via

$$\begin{aligned} A_i(\xi, \eta) &= \alpha_{0i} + \alpha_{1i}\xi + \alpha_{2i}\eta + \alpha_{3i}\xi^2 + \alpha_{4i}\xi\eta + \alpha_{5i}\eta^2 \\ &\quad + \alpha_{6i}\xi^3 + \alpha_{7i}\xi^2\eta + \alpha_{8i}\xi\eta^2 + \alpha_{9i}\eta^3 \end{aligned} \quad (20b)$$

$$B(\xi, \eta) = \beta_0 + \beta_1\xi + \beta_2\eta + \beta_3\xi^2 + \beta_4\xi\eta + \beta_5\eta^2 \quad (20c)$$

where coefficients in the numerator, i.e., A_i , differ with index i , while those in the denominator, viz., $B := \sum_{i=1}^5 A_i$, are the same for all five shape functions.

We apply the construction technique of Dasgupta⁴⁸ to compute the shape functions of Wachspress for an irregular convex pentagon. Consider a chord c_i that connects vertex $\xi_{i-1} = (\xi_{i-1}, \eta_{i-1})$ with vertex $\xi_i = (\xi_i, \eta_i)$ via a straight line segment such that $\ell_i = 0$ with $\ell_i := 1 - a_i\xi - b_i\eta$ wherein

$$a_i = \frac{\eta_i - \eta_{i-1}}{\xi_{i-1}\eta_i - \xi_i\eta_{i-1}} \quad (21a)$$

$$b_i = \frac{\xi_{i-1} - \xi_i}{\xi_{i-1}\eta_i - \xi_i\eta_{i-1}} \quad (21b)$$

for which Dasgupta derived the following set of constraints

$$\kappa_i = \kappa_{i-1} \left(\frac{a_{i+1}(\xi_{i-1} - \xi_i) + b_{i+1}(\eta_{i-1} - \eta_i)}{a_{i-1}(\xi_i - \xi_{i-1}) + b_{i-1}(\eta_i - \eta_{i-1})} \right) \quad (21c)$$

with recursion starting at $\kappa_1 := 1$. Coefficients κ_i enforce property 4 listed above.

With this information in hand, we derived rational polynomials describing Wachspress' shape functions for a pentagon specified in Eqn. (20) in terms of parameters

a_i , b_i and κ_i . The polynomial coefficients for the A_i in Eqn. (20b) have values of

$$\alpha_{0i} = 1 \quad (22a)$$

$$\alpha_{1i} = -(a_{i+1} + a_{i+2} + a_{i+3}) \quad (22b)$$

$$\alpha_{2i} = -(b_{i+1} + b_{i+2} + b_{i+3}) \quad (22c)$$

$$\alpha_{3i} = a_{i+1}a_{i+2} + a_{i+2}a_{i+3} + a_{i+3}a_{i+1} \quad (22d)$$

$$\alpha_{4i} = a_{i+1}(b_{i+2} + b_{i+3}) + a_{i+2}(b_{i+1} + b_{i+3}) + a_{i+3}(b_{i+1} + b_{i+2}) \quad (22e)$$

$$\alpha_{5i} = b_{i+1}b_{i+2} + b_{i+2}b_{i+3} + b_{i+3}b_{i+1} \quad (22f)$$

$$\alpha_{6i} = -a_{i+1}a_{i+2}a_{i+3} \quad (22g)$$

$$\alpha_{7i} = -(a_{i+1}a_{i+2}b_{i+3} + a_{i+1}b_{i+2}a_{i+3} + b_{i+1}a_{i+2}a_{i+3}) \quad (22h)$$

$$\alpha_{8i} = -(a_{i+1}b_{i+2}b_{i+3} + b_{i+1}a_{i+2}b_{i+3} + b_{i+1}b_{i+2}a_{i+3}) \quad (22i)$$

$$\alpha_{9i} = -b_{i+1}b_{i+2}b_{i+3} \quad (22j)$$

which differ for each shape function via index $i = 1, 2, \dots, 5$, while the polynomial coefficients for B in Eqn. (20c) have values of

$$\beta_i = \sum_{j=1}^5 \alpha_{ij} \kappa_j, \quad i = 0, 1, \dots, 5 \quad (23)$$

which are the same for all five shape functions. Sums over the four cubic terms in Eqn. (22) all vanish—a byproduct of Wachspress’ formulation. In the above formulæ, an index count of $i \equiv 0 \implies i = 5$, while index counts of $i \equiv 6 \implies i = 1$, $i \equiv 7 \implies i = 2$ and $i \equiv 8 \implies i = 3$. Shape function N_1 is illustrated in Fig. 11, with like images applying for the other four shape functions.

3.3.2 First Derivatives of the Shape Functions

The first derivatives of Wachspress’ shape functions for a pentagon are

$$N_{i+1,\xi}(\xi, \eta) = \kappa_i N_{i,\xi}(\xi, \eta) / B^2(\xi, \eta) \quad (24a)$$

$$N_{i+1,\eta}(\xi, \eta) = \kappa_i N_{i,\eta}(\xi, \eta) / B^2(\xi, \eta) \quad (24b)$$

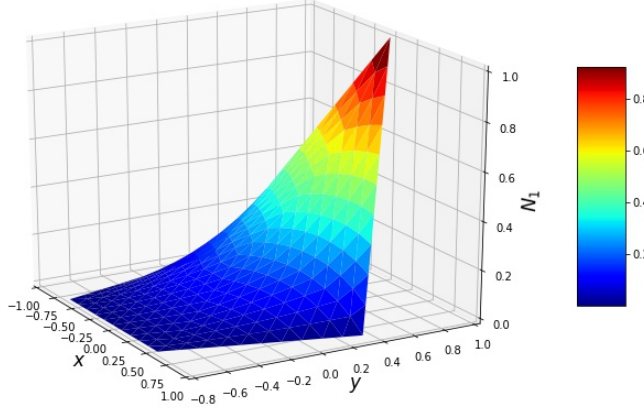


Fig. 11 Wachspress shape functions for a pentagon, in this case, shape function N_1 .

where $N_{i+1,\xi}(\xi, \eta) = \partial N_{i+1}(\xi, \eta)/\partial\xi$ and $N_{i+1,\eta}(\xi, \eta) = \partial N_{i+1}(\xi, \eta)/\partial\eta$ with

$$\mathcal{N}_{i,\xi}(\xi, \eta) = B(\xi, \eta)A_{i,\xi}(\xi, \eta) - B_{,\xi}(\xi, \eta)A_i(\xi, \eta) \quad (24c)$$

$$\mathcal{N}_{i,\eta}(\xi, \eta) = B(\xi, \eta)A_{i,\eta}(\xi, \eta) - B_{,\eta}(\xi, \eta)A_i(\xi, \eta) \quad (24d)$$

which contain the polynomials

$$A_{i,\xi}(\xi, \eta) = \alpha_{1i} + 2\alpha_{3i}\xi + \alpha_{4i}\eta + 3\alpha_{6i}\xi^2 + 2\alpha_{7i}\xi\eta + \alpha_{8i}\eta^2 \quad (24e)$$

$$A_{i,\eta}(\xi, \eta) = \alpha_{2i} + \alpha_{4i}\xi + 2\alpha_{5i}\eta + \alpha_{7i}\xi^2 + 2\alpha_{8i}\xi\eta + 3\alpha_{9i}\eta^2 \quad (24f)$$

$$B_{,\xi}(\xi, \eta) = \beta_1 + 2\beta_3\xi + \beta_4\eta \quad (24g)$$

$$B_{,\eta}(\xi, \eta) = \beta_2 + \beta_4\xi + 2\beta_5\eta \quad (24h)$$

from which the deformation and displacement gradients are constructed.

3.3.3 Second Derivatives of the Shape Functions

The second derivatives of these shape functions, which we used to test the compat-

DRAFT: UNCLASSIFIED

ibility conditions of this element, are described by

$$N_{i+1,\xi\xi} = \kappa_i \mathfrak{N}_{i,\xi\xi}(\xi, \eta) / B^3(\xi, \eta) \quad (25a)$$

$$N_{i+1,\xi\eta} = \kappa_i \mathfrak{N}_{i,\xi\eta}(\xi, \eta) / B^3(\xi, \eta) \quad (25b)$$

$$N_{i+1,\eta\xi} = \kappa_i \mathfrak{N}_{i,\eta\xi}(\xi, \eta) / B^3(\xi, \eta) \quad (25c)$$

$$N_{i+1,\eta\eta} = \kappa_i \mathfrak{N}_{i,\eta\eta}(\xi, \eta) / B^3(\xi, \eta) \quad (25d)$$

where $N_{i+1,\xi\eta}(\xi, \eta) = \partial^2 N_{i+1}(\xi, \eta) / \partial \xi \partial \eta$, etc., and where

$$\mathfrak{N}_{i,\xi\xi}(\xi, \eta) = B(\xi, \eta) \mathcal{N}_{i,\xi\xi}(\xi, \eta) - 2B_{,\xi}(\xi, \eta) \mathcal{N}_{i,\xi}(\xi, \eta) \quad (25e)$$

$$\mathfrak{N}_{i,\xi\eta}(\xi, \eta) = B(\xi, \eta) \mathcal{N}_{i,\xi\eta}(\xi, \eta) - 2B_{,\xi}(\xi, \eta) \mathcal{N}_{i,\eta}(\xi, \eta) \quad (25f)$$

$$\mathfrak{N}_{i,\eta\xi}(\xi, \eta) = B(\xi, \eta) \mathcal{N}_{i,\eta\xi}(\xi, \eta) - 2B_{,\eta}(\xi, \eta) \mathcal{N}_{i,\xi}(\xi, \eta) \quad (25g)$$

$$\mathfrak{N}_{i,\eta\eta}(\xi, \eta) = B(\xi, \eta) \mathcal{N}_{i,\eta\eta}(\xi, \eta) - 2B_{,\eta}(\xi, \eta) \mathcal{N}_{i,\eta}(\xi, \eta) \quad (25h)$$

wherein

$$\mathcal{N}_{i,\xi\xi}(\xi, \eta) = B(\xi, \eta) A_{i,\xi\xi}(\xi, \eta) - B_{,\xi\xi}(\xi, \eta) A_i(\xi, \eta) \quad (25i)$$

$$\begin{aligned} \mathcal{N}_{i,\xi\eta}(\xi, \eta) &= B(\xi, \eta) A_{i,\xi\eta}(\xi, \eta) + B_{,\xi}(\xi, \eta) A_{i,\eta}(\xi, \eta) \\ &\quad - B_{,\eta}(\xi, \eta) A_{i,\xi}(\xi, \eta) - B_{,\xi\eta}(\xi, \eta) A_i(\xi, \eta) \end{aligned} \quad (25j)$$

$$\begin{aligned} \mathcal{N}_{i,\eta\xi}(\xi, \eta) &= B(\xi, \eta) A_{i,\eta\xi}(\xi, \eta) + B_{,\eta}(\xi, \eta) A_{i,\xi}(\xi, \eta) \\ &\quad - B_{,\xi}(\xi, \eta) A_{i,\eta}(\xi, \eta) - B_{,\eta\xi}(\xi, \eta) A_i(\xi, \eta) \end{aligned} \quad (25k)$$

$$\mathcal{N}_{i,\eta\eta}(\xi, \eta) = B(\xi, \eta) A_{i,\eta\eta}(\xi, \eta) - B_{,\eta\eta}(\xi, \eta) A_i(\xi, \eta) \quad (25l)$$

which contain polynomials

$$A_{i,\xi\xi}(\xi, \eta) = 2\alpha_{3i} + 6\alpha_{6i}\xi + 2\alpha_{7i}\eta \quad (25m)$$

$$A_{i,\xi\eta}(\xi, \eta) = \alpha_{4i} + 2\alpha_{7i}\xi + 2\alpha_{8i}\eta \quad (25n)$$

$$A_{i,\eta\xi}(\xi, \eta) = 2\alpha_{5i} + 2\alpha_{8i}\xi + 6\alpha_{9i}\eta \quad (25o)$$

$$B_{,\xi\xi}(\xi, \eta) = 2\beta_3 \quad (25p)$$

$$B_{,\xi\eta}(\xi, \eta) = \beta_4 \quad (25q)$$

$$B_{,\eta\xi}(\xi, \eta) = 2\beta_5 \quad (25r)$$

with $A_{i,\xi\eta}(\xi, \eta) = A_{i,\eta\xi}(\xi, \eta)$ and $B_{,\xi\eta}(\xi, \eta) = B_{,\eta\xi}(\xi, \eta)$.

3.3.4 Deformation Gradient for an Irregular Pentagon

Derivatives of displacement (u, v) taken with respect to the local co-ordinates (ξ, η) described in terms of gradients of the shape functions $N_{i,\xi}(\xi, \eta)$ and $N_{i,\eta}(\xi, \eta)$ of a pentagon have components

$$\begin{bmatrix} \partial u / \partial \xi & \partial u / \partial \eta \\ \partial v / \partial \xi & \partial v / \partial \eta \end{bmatrix} = \begin{bmatrix} \sum_{i=1}^5 N_{i,\xi}(\xi, \eta) u_i & \sum_{i=1}^5 N_{i,\eta}(\xi, \eta) u_i \\ \sum_{i=1}^5 N_{i,\xi}(\xi, \eta) v_i & \sum_{i=1}^5 N_{i,\eta}(\xi, \eta) v_i \end{bmatrix} \quad (26a)$$

where $u := x - x_0$ and $v := y - y_0$. Gradients of the global co-ordinates (x_0, y_0) evaluated in a reference state taken with respect to the local co-ordinates (ξ, η) have components

$$\begin{bmatrix} \partial x_0 / \partial \xi & \partial x_0 / \partial \eta \\ \partial y_0 / \partial \xi & \partial y_0 / \partial \eta \end{bmatrix} = \begin{bmatrix} \sum_{i=1}^5 N_{i,\xi}(\xi, \eta) x_{0i} & \sum_{i=1}^5 N_{i,\eta}(\xi, \eta) x_{0i} \\ \sum_{i=1}^5 N_{i,\xi}(\xi, \eta) y_{0i} & \sum_{i=1}^5 N_{i,\eta}(\xi, \eta) y_{0i} \end{bmatrix} \quad (26b)$$

wherein (x_{0i}, y_{0i}) are the reference global co-ordinates at the i^{th} vertex, while gradients of the global co-ordinates (x, y) evaluated in the current state taken with respect to the local co-ordinates (ξ, η) have components

$$\begin{bmatrix} \partial x / \partial \xi & \partial x / \partial \eta \\ \partial y / \partial \xi & \partial y / \partial \eta \end{bmatrix} = \begin{bmatrix} \sum_{i=1}^5 N_{i,\xi}(\xi, \eta) x_i & \sum_{i=1}^5 N_{i,\eta}(\xi, \eta) x_i \\ \sum_{i=1}^5 N_{i,\xi}(\xi, \eta) y_i & \sum_{i=1}^5 N_{i,\eta}(\xi, \eta) y_i \end{bmatrix} \quad (26c)$$

whose transpose establishes the Jacobian matrix

$$\mathbf{J} := \begin{bmatrix} \partial x / \partial \xi & \partial y / \partial \xi \\ \partial x / \partial \eta & \partial y / \partial \eta \end{bmatrix} = \begin{bmatrix} \sum_{i=1}^5 N_{i,\xi}(\xi, \eta) x_i & \sum_{i=1}^5 N_{i,\xi}(\xi, \eta) y_i \\ \sum_{i=1}^5 N_{i,\eta}(\xi, \eta) x_i & \sum_{i=1}^5 N_{i,\eta}(\xi, \eta) y_i \end{bmatrix} \quad (26d)$$

wherein (x_i, y_i) are the current global co-ordinates at the i^{th} vertex.

From the above matrices, one can construct the deformation gradient $\mathbf{F} = \partial \mathbf{x} / \partial \mathbf{x}_0 = \mathbf{I} + \partial \mathbf{u} / \partial \mathbf{x}_0$ for an irregular pentagon via

$$\begin{aligned} \mathbf{F}(\xi, \eta) &= \begin{bmatrix} F_{11}(\xi, \eta) & F_{12}(\xi, \eta) \\ F_{21}(\xi, \eta) & F_{22}(\xi, \eta) \end{bmatrix} \\ &= \begin{bmatrix} 1 & 0 \\ 0 & 1 \end{bmatrix} + \begin{bmatrix} \partial u / \partial \xi & \partial u / \partial \eta \\ \partial v / \partial \xi & \partial v / \partial \eta \end{bmatrix} \begin{bmatrix} \partial x_0 / \partial \xi & \partial x_0 / \partial \eta \\ \partial y_0 / \partial \xi & \partial y_0 / \partial \eta \end{bmatrix}^{-1} \end{aligned} \quad (27a)$$

whose inverse is

$$\mathbf{F}^{-1}(\xi, \eta) = \frac{1}{F_{11}(\xi, \eta)F_{22}(\xi, \eta) - F_{21}(\xi, \eta)F_{12}(\xi, \eta)} \begin{bmatrix} F_{22}(\xi, \eta) & -F_{12}(\xi, \eta) \\ -F_{21}(\xi, \eta) & F_{11}(\xi, \eta) \end{bmatrix} \quad (27b)$$

while its associated displacement gradient $\mathbf{G} = \partial \mathbf{u} / \partial \mathbf{x}$ is given by

$$\mathbf{G}(\xi, \eta) = \begin{bmatrix} G_{11}(\xi, \eta) & G_{12}(\xi, \eta) \\ G_{21}(\xi, \eta) & G_{22}(\xi, \eta) \end{bmatrix} = \begin{bmatrix} \partial u / \partial \xi & \partial u / \partial \eta \\ \partial v / \partial \xi & \partial v / \partial \eta \end{bmatrix} \begin{bmatrix} \partial x / \partial \xi & \partial x / \partial \eta \\ \partial y / \partial \xi & \partial y / \partial \eta \end{bmatrix}^{-1} \quad (28)$$

which is not invertible, in general. All are evaluated in the 12 plane belonging to a co-ordinate system $(\vec{\mathbf{e}}_2, \vec{\mathbf{e}}_2, \vec{\mathbf{e}}_3)$ that orients this pentagon, with $\vec{\mathbf{e}}_3$ being normal to its surface, as illustrated in Fig. 10. The deformation and displacement gradients are two, fundamental, kinematic fields commonly used in the construction of constitutive equations.

3.3.5 Compatibility Conditions

To ensure that a deformation is compatible, and therefore integrable, it follows that the curl of its deformation gradient must be zero.⁴⁹ This condition is trivially satisfied for the shape functions that we use for 1D chords, 2D triangles, and 3D tetrahedra. However, for the Wachspress shape function used to interpolate pentagons, this needs to be verified. Vanishing of the curl of \mathbf{F} results in two constraint equations for the planar case, they being

$$F_{11,2} = F_{12,1} \quad \text{and} \quad F_{22,1} = F_{21,2} \quad (29)$$

whose spatial derivatives associate with the $(\vec{\mathbf{e}}_1, \vec{\mathbf{e}}_2)$ co-ordinate frame.

From Eqn. (27), it follows that the spatial derivatives of the deformation gradient

are

$$\begin{aligned}
 \mathbf{F}_{,1}(\xi, \eta) &= \frac{\partial}{\partial x_0} \begin{bmatrix} F_{11}(\xi, \eta) & F_{12}(\xi, \eta) \\ F_{21}(\xi, \eta) & F_{22}(\xi, \eta) \end{bmatrix} \\
 &= \frac{\partial \xi}{\partial x_0} \left(\frac{\partial}{\partial \xi} \begin{bmatrix} \partial u / \partial \xi & \partial u / \partial \eta \\ \partial v / \partial \xi & \partial v / \partial \eta \end{bmatrix} \right) \begin{bmatrix} \partial x_0 / \partial \xi & \partial x_0 / \partial \eta \\ \partial y_0 / \partial \xi & \partial y_0 / \partial \eta \end{bmatrix}^{-1} - \begin{bmatrix} \partial u / \partial \xi & \partial u / \partial \eta \\ \partial v / \partial \xi & \partial v / \partial \eta \end{bmatrix} \\
 &\quad \times \begin{bmatrix} \partial x_0 / \partial \xi & \partial x_0 / \partial \eta \\ \partial y_0 / \partial \xi & \partial y_0 / \partial \eta \end{bmatrix}^{-1} \frac{\partial}{\partial \xi} \left(\begin{bmatrix} \partial x_0 / \partial \xi & \partial x_0 / \partial \eta \\ \partial y_0 / \partial \xi & \partial y_0 / \partial \eta \end{bmatrix} \right) \begin{bmatrix} \partial x_0 / \partial \xi & \partial x_0 / \partial \eta \\ \partial y_0 / \partial \xi & \partial y_0 / \partial \eta \end{bmatrix}^{-1} \Bigg) \\
 \end{aligned} \tag{30a}$$

and

$$\begin{aligned}
 \mathbf{F}_{,2}(\xi, \eta) &= \frac{\partial}{\partial y_0} \begin{bmatrix} F_{11}(\xi, \eta) & F_{12}(\xi, \eta) \\ F_{21}(\xi, \eta) & F_{22}(\xi, \eta) \end{bmatrix} \\
 &= \frac{\partial \eta}{\partial y_0} \left(\frac{\partial}{\partial \eta} \begin{bmatrix} \partial u / \partial \xi & \partial u / \partial \eta \\ \partial v / \partial \xi & \partial v / \partial \eta \end{bmatrix} \right) \begin{bmatrix} \partial x_0 / \partial \xi & \partial x_0 / \partial \eta \\ \partial y_0 / \partial \xi & \partial y_0 / \partial \eta \end{bmatrix}^{-1} - \begin{bmatrix} \partial u / \partial \xi & \partial u / \partial \eta \\ \partial v / \partial \xi & \partial v / \partial \eta \end{bmatrix} \\
 &\quad \times \begin{bmatrix} \partial x_0 / \partial \xi & \partial x_0 / \partial \eta \\ \partial y_0 / \partial \xi & \partial y_0 / \partial \eta \end{bmatrix}^{-1} \frac{\partial}{\partial \eta} \left(\begin{bmatrix} \partial x_0 / \partial \xi & \partial x_0 / \partial \eta \\ \partial y_0 / \partial \xi & \partial y_0 / \partial \eta \end{bmatrix} \right) \begin{bmatrix} \partial x_0 / \partial \xi & \partial x_0 / \partial \eta \\ \partial y_0 / \partial \xi & \partial y_0 / \partial \eta \end{bmatrix}^{-1} \Bigg) \\
 \end{aligned} \tag{30b}$$

wherein

$$\frac{\partial}{\partial \xi} \begin{bmatrix} \partial u / \partial \xi & \partial u / \partial \eta \\ \partial v / \partial \xi & \partial v / \partial \eta \end{bmatrix} = \begin{bmatrix} \sum_{i=1}^5 N_{i,\xi\xi}(\xi, \eta) u_i & \sum_{i=1}^5 N_{i,\xi\eta}(\xi, \eta) u_i \\ \sum_{i=1}^5 N_{i,\xi\xi}(\xi, \eta) v_i & \sum_{i=1}^5 N_{i,\xi\eta}(\xi, \eta) v_i \end{bmatrix} \tag{31a}$$

$$\frac{\partial}{\partial \eta} \begin{bmatrix} \partial u / \partial \xi & \partial u / \partial \eta \\ \partial v / \partial \xi & \partial v / \partial \eta \end{bmatrix} = \begin{bmatrix} \sum_{i=1}^5 N_{i,\eta\xi}(\xi, \eta) u_i & \sum_{i=1}^5 N_{i,\eta\eta}(\xi, \eta) u_i \\ \sum_{i=1}^5 N_{i,\eta\xi}(\xi, \eta) v_i & \sum_{i=1}^5 N_{i,\eta\eta}(\xi, \eta) v_i \end{bmatrix} \tag{31b}$$

and

$$\frac{\partial}{\partial \xi} \begin{bmatrix} \partial x_0 / \partial \xi & \partial x_0 / \partial \eta \\ \partial y_0 / \partial \xi & \partial y_0 / \partial \eta \end{bmatrix} = \begin{bmatrix} \sum_{i=1}^5 N_{i,\xi\xi}(\xi, \eta) x_{0i} & \sum_{i=1}^5 N_{i,\xi\eta}(\xi, \eta) x_{0i} \\ \sum_{i=1}^5 N_{i,\xi\xi}(\xi, \eta) y_{0i} & \sum_{i=1}^5 N_{i,\xi\eta}(\xi, \eta) y_{0i} \end{bmatrix} \tag{31c}$$

$$\frac{\partial}{\partial \eta} \begin{bmatrix} \partial x_0 / \partial \xi & \partial x_0 / \partial \eta \\ \partial y_0 / \partial \xi & \partial y_0 / \partial \eta \end{bmatrix} = \begin{bmatrix} \sum_{i=1}^5 N_{i,\eta\xi}(\xi, \eta) x_{0i} & \sum_{i=1}^5 N_{i,\eta\eta}(\xi, \eta) x_{0i} \\ \sum_{i=1}^5 N_{i,\eta\xi}(\xi, \eta) y_{0i} & \sum_{i=1}^5 N_{i,\eta\eta}(\xi, \eta) y_{0i} \end{bmatrix} \tag{31d}$$

with $\partial \xi / \partial x_0$ and $\partial \eta / \partial y_0$ effectively being scaling factors that we take to be de-

scribed as a ratio of septal chord lengths; specifically, let

$$\frac{\partial \xi}{\partial x_0} \approx \frac{\partial \eta}{\partial y_0} \approx \frac{L(\xi, \eta)}{L_0(x, y)} = \frac{\cos(\omega)}{\sqrt{A_0/5 \tan(\omega)}} \quad (32)$$

where $L(\xi, \eta)$ is the septal length of a pentagonal edge in its natural configuration, as drawn in Fig. 7, while $L_0(x, y)$ is the actual, alveolar, septal length with $A_0(x, y)$ being the area of an alveolar septum in its reference state. This formula follows from Eqns. (5 & 6).

We study compatibility only for the purpose of assessing applicability in our choice of selecting Wachspress shape functions. Otherwise, it is not required in our modeling of an alveolus via a dodecahedron.

3.3.6 Gram-Schmidt Decomposition of the Deformation Gradient

To describe kinematics of a planar membrane, an upper-triangular Gram-Schmidt decomposition of the deformation gradient \mathbf{F} is used in lieu of the symmetric polar decomposition that is commonly adopted.^{43,50–53} McLellan^{38,54} was the first to propose a triangular decomposition of \mathbf{F} , to prove its uniqueness and existence, and to establish many of its physical properties. This idea has been rediscovered several times since then, e.g.,^{50,55,56} A thorough history of the **QR** (Gram-Schmidt) decomposition has been written by Leon, Björck & Gander,⁵⁷ with a brief history regarding its application to kinematics being given in Freed *et al.*⁴³

A Gram-Schmidt factorization of the deformation gradient \mathbf{F} is written here as $\mathbf{F} = \mathcal{R}\mathcal{U}$, where the rotation \mathcal{R} is orthogonal, and where the Laplace stretch \mathcal{U} is upper-triangular.^{43*} This triangular measure of stretch possesses an inherent property in two space: the direction aligned with the rotated 1-axis, denoted as \vec{g}_1 , remains invariant under transformation \mathcal{U} ,³⁸ i.e., it is a material vector in a neighborhood surrounding that particle whereat \mathbf{F} is evaluated.³⁹ This property has some interesting ramifications addressed in Section 3.3.6.2.

*The **QR** rotation \mathcal{R} and stretch \mathcal{U} tensors are distinct from those that arise from a polar decomposition of a deformation gradient, typically denoted as \mathbf{R} and \mathbf{U} , as found in any, modern, continuum mechanics text. McLellan^{38,54} introduced the Laplace stretch in 1976, which he denoted as \mathbf{H} , while Srinivasa⁵⁰ denoted it as $\tilde{\mathbf{F}}$ in his 2012 paper.

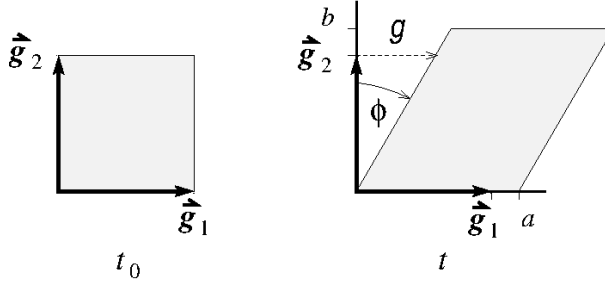


Fig. 12 Physical attributes of a planar deformation: a and b represent elongations, while $g = \tan \phi$ denotes the magnitude of shear. They are measured in a physical frame of reference with unit base vectors (\vec{g}_1, \vec{g}_2) where \vec{g}_1 embeds in the material.

3.3.6.1 QR Factorization of \mathbf{F}

The 2×2 deformation gradient associated with a planar membrane has a Gram-Schmidt decomposition expressed in terms of four physical attributes. Three of these attributes describe deformation. They are defined as⁵²

$$a = \sqrt{F_{11}^2 + F_{21}^2}, \quad b = \frac{F_{11}F_{22} - F_{12}F_{21}}{\sqrt{F_{11}^2 + F_{21}^2}}, \quad g = \frac{F_{11}F_{12} + F_{22}F_{21}}{F_{11}^2 + F_{21}^2} \quad (33)$$

thereby populating Laplace stretch \mathcal{U} and its inverse \mathcal{U}^{-1} with components

$$\mathcal{U} = \begin{bmatrix} a & ag \\ 0 & b \end{bmatrix} \quad \text{and} \quad \mathcal{U}^{-1} = \begin{bmatrix} 1/a & -g/b \\ 0 & 1/b \end{bmatrix} \quad (34)$$

where a and b are the principal elongations (ratios of current lengths to reference lengths) and g is the extent of in-plane shear, as measured in a co-ordinate frame (\vec{g}_1, \vec{g}_2) illustrated in Fig. 12. It is worth pointing out that the components of Laplace stretch, viz., \mathcal{U}_{ij} , are evaluated in the reference co-ordinate system (\vec{e}_1, \vec{e}_2) of the pentagon, as $\mathbf{F} = F_{ij} \vec{e}_i \otimes \vec{e}_j$, but their physical interpretations arise in the Gram rotated co-ordinate system (\vec{g}_1, \vec{g}_2) .

Orthogonal tensor $\mathcal{R} = [\vec{g}_1 \mid \vec{g}_2] = \delta_{ij} \vec{g}_i \otimes \vec{e}_j = \mathcal{R}_{ij} \vec{e}_i \otimes \vec{e}_j$ rotates the reference co-ordinate axes (\vec{e}_1, \vec{e}_2) into a physical co-ordinate system (\vec{g}_1, \vec{g}_2) through an angle θ , which is the fourth physical attribute arising from a **QR** factorization of \mathbf{F} . This angle of rotation describes a proper orthogonal matrix, specifically

$$\mathcal{R} = \begin{bmatrix} \cos \theta & -\sin \theta \\ \sin \theta & \cos \theta \end{bmatrix} \quad (35)$$

with

$$\sin \theta = \frac{F_{21}}{\sqrt{F_{11}^2 + F_{21}^2}}, \quad \cos \theta = \frac{F_{11}}{\sqrt{F_{11}^2 + F_{21}^2}} \quad \therefore \quad \theta = \tan^{-1} \left(\frac{F_{21}}{F_{11}} \right) \quad (36)$$

where a positive angle θ corresponds with a counterclockwise rotation of physical axes ($\vec{\mathbf{g}}_1, \vec{\mathbf{g}}_2$) about reference axes ($\vec{\mathbf{e}}_1, \vec{\mathbf{e}}_2$).

From the four independent components of a planar deformation gradient F_{ij} come three deformation attributes, i.e., a, b and g , and one rotational attribute, i.e., θ .

3.3.6.2 Dilemma

Until recently, there has been a tacit assumption in prior applications of Gram-Schmidt factorizations of \mathbf{F} that the physical base vectors ($\vec{\mathbf{g}}_1, \vec{\mathbf{g}}_2$) always satisfy a geometric condition whereby the physical 1-direction $\vec{\mathbf{g}}_1$ rotates out of the reference 1-direction $\vec{\mathbf{e}}_1$, but this need not always be the case. Physical vector $\vec{\mathbf{g}}_1$ could equally likely rotate out of the 2-direction $\vec{\mathbf{e}}_2$ of the reference frame. At issue is not: How the physical base vectors orient in space? That is managed by Gram's procedure. Rather, at issue is: How do the physical base vectors index with respect to the reference base vectors? This topic is addressed in Section 2.1 for the 3D case; below we address it for the 2D case.

To illustrate the concern, consider two deformation histories, as drawn in Fig. 13, each of which describes a simple shear taking place in the plane of a membrane. In one case shear occurs in the 1-direction, while in the other case shear occurs in the 2-direction. There are no elongations in either deformation. These motions lead to Gram-Schmidt factorizations of the deformation gradient, when following the protocol of Eqns. (33–36), that are described by

$$\mathbf{F} = \begin{bmatrix} 1 & \gamma \\ 0 & 1 \end{bmatrix} \implies \mathcal{R} = \begin{bmatrix} 1 & 0 \\ 0 & 1 \end{bmatrix}, \quad \mathcal{U} = \begin{bmatrix} 1 & \gamma \\ 0 & 1 \end{bmatrix} \quad (37a)$$

and

$$\mathbf{F} = \begin{bmatrix} 1 & 0 \\ \gamma & 1 \end{bmatrix} \implies \begin{cases} \mathcal{R} = \frac{1}{\sqrt{1+\gamma^2}} \begin{bmatrix} 1 & -\gamma \\ \gamma & 1 \end{bmatrix} \\ \mathcal{U} = \begin{bmatrix} \sqrt{1+\gamma^2} & \gamma \\ 0 & 1/\sqrt{1+\gamma^2} \end{bmatrix} \end{cases} \quad (37b)$$

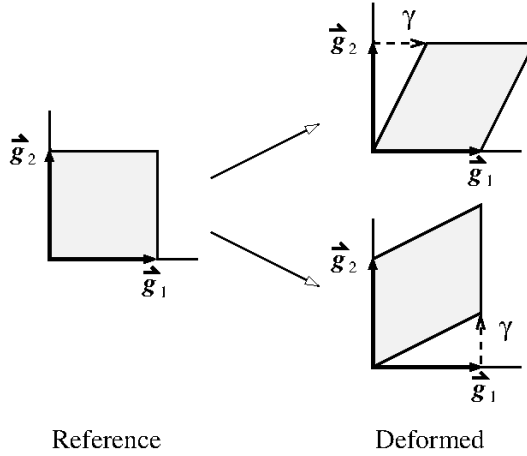


Fig. 13 The left graphic designates a reference configuration while the right two graphics designate deformed configurations, both in basis (\vec{g}_1, \vec{g}_2) . The top graphic associates with the motion of Eqn. (37a), while the bottom graphic associates with the motion of Eqn. (37b).

respectively, where we see that shear \mathcal{U}_{12} has the same physical interpretation in both cases, viz., γ , but elongations \mathcal{U}_{11} and \mathcal{U}_{22} do not, viz., $\mathcal{U}_{11} = 1$ and $\mathcal{U}_{22} = 1$ in Eqn. (37a), whereas $\mathcal{U}_{11} = \sqrt{1 + \gamma^2}$ and $\mathcal{U}_{22} = 1/\sqrt{1 + \gamma^2}$ for the motion described in Eqn. (37b). Consequently, two geometric interpretations are produced for just one physical mode of deformation. This cannot be!

The only difference between the motions that lead to the two deformation gradients presented in Eqn. (37) is one's choice for labeling the co-ordinate directions. Matrix operations of row and column pivoting, taken from linear algebra, allow one to transform the lower-triangular form of Eqn. (37b) into an upper-triangular form like Eqn. (37a); hence, producing an unified physical interpretation for both shearing motions, and thereby providing a means for establishing a remedy to this dilemma.

3.3.6.3 Remedy

For 2D membranes, there are only two co-ordinate re-indexings that are possible (for 3D solids there are six, cf. Section 2.1). The default is no re-indexing at all, in which case

$$[\mathbf{P}] = [\mathbf{P}_0] := \begin{bmatrix} 1 & 0 \\ 0 & 1 \end{bmatrix} \quad \Rightarrow \quad \begin{bmatrix} \mathcal{F}_{11} & \mathcal{F}_{12} \\ \mathcal{F}_{21} & \mathcal{F}_{22} \end{bmatrix} := \begin{bmatrix} F_{11} & F_{12} \\ F_{21} & F_{22} \end{bmatrix} \quad (38a)$$

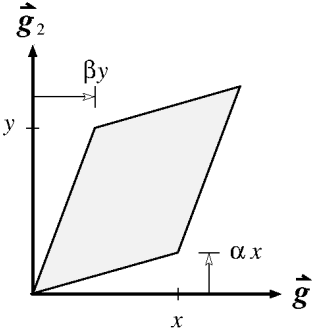


Fig. 14 A general description for homogeneous planar deformation, where $x, y \in \mathbb{R}_+$ and $\alpha, \beta \in \mathbb{R}$. Shears α and β are drawn in their positive sense.

while in the second case there is a re-indexing specified by

$$[\mathbf{P}] = [\mathbf{P}_1] := \begin{bmatrix} 0 & 1 \\ 1 & 0 \end{bmatrix} \quad \Rightarrow \quad \begin{bmatrix} \mathcal{F}_{11} & \mathcal{F}_{12} \\ \mathcal{F}_{21} & \mathcal{F}_{22} \end{bmatrix} := \begin{bmatrix} F_{22} & F_{21} \\ F_{12} & F_{11} \end{bmatrix} \quad (38b)$$

where components $\mathcal{F}_{ij} = P_{ki} F_{k\ell} P_{\ell j}$ are the components to be used in the Gram-Schmidt factorization presented in Section 3.3.6.1, see also Section 2.1, and where $\mathbf{P} \in \{\mathbf{P}_0, \mathbf{P}_1\}$ is orthogonal, i.e., $\mathbf{P}\mathbf{P}^T = \mathbf{P}^T\mathbf{P} = \mathbf{I}$ with $\det \mathbf{P} = \pm 1$; specifically, $\det \mathbf{P}_0 = +1$ while $\det \mathbf{P}_1 = -1$.

The challenge in implementing such a strategy is to determine when to switch from \mathbf{P}_0 (case 1) to \mathbf{P}_1 (case 2), or back again, viz., from \mathbf{P}_1 to \mathbf{P}_0 . Continuity in the physical fields of deformation (a, b, g) must be satisfied in order for such a change in co-ordinate frame to be physically meaningful. To this end, it is useful to represent the components of a planar deformation gradient as

$$\begin{bmatrix} \mathcal{F}_{11} & \mathcal{F}_{12} \\ \mathcal{F}_{21} & \mathcal{F}_{22} \end{bmatrix} = \begin{cases} \text{case 1 : } & \begin{bmatrix} F_{11} & F_{12} \\ F_{21} & F_{22} \end{bmatrix} = \begin{bmatrix} x & \beta y \\ \alpha x & y \end{bmatrix} \\ \text{case 2 : } & \begin{bmatrix} F_{22} & F_{21} \\ F_{12} & F_{11} \end{bmatrix} = \begin{bmatrix} y & \alpha x \\ \beta y & x \end{bmatrix} \end{cases} \quad (39)$$

where $x = F_{11}$ and $y = F_{22}$ are elongations, while ratios $\alpha = F_{21}/F_{11}$ and $\beta = F_{12}/F_{22}$ are magnitudes of shear, as illustrated in Fig. 14.

The physical attributes for Laplace stretch, as they pertain to the two cases in Eqn. (38), written in terms of components F_{ij} from $\mathbf{F} = F_{ij} \vec{\mathbf{e}}_i \otimes \vec{\mathbf{e}}_j$ as defined

in Eqn. (39), are respectively given by

$$\tilde{a} = x\sqrt{1 + \alpha^2} \quad \hat{a} = y\sqrt{1 + \beta^2} \quad (40a)$$

$$\tilde{b} = y(1 - \alpha\beta) / \sqrt{1 + \alpha^2} \quad \hat{b} = x(1 - \alpha\beta) / \sqrt{1 + \beta^2} \quad (40b)$$

$$\tilde{g} = y(\alpha + \beta) / x(1 + \alpha^2) \quad \hat{g} = x(\alpha + \beta) / y(1 + \beta^2) \quad (40c)$$

$$\tilde{\theta} = \tan^{-1}(-\alpha) \quad \hat{\theta} = \tan^{-1}(-\beta) \quad (40d)$$

where attributes in the left column apply to case 1 (i.e., Eqn. 38a) while those in the right column apply to case 2 (viz., Eqn. 38b). The actual set of physical attributes $\{a, b, g, \theta\}$ that are to be used when quantifying Laplace stretch and its inverse, according to Eqn. (34), are then selected via the strategy

$$\text{if } |\tilde{g}| \geq |\hat{g}| : \quad \{\tilde{a}, \tilde{b}, \tilde{g}, \tilde{\theta}\} \mapsto \{a, b, g, \theta\} \quad (41a)$$

$$\text{else } |\tilde{g}| \leq |\hat{g}| : \quad \{\hat{a}, \hat{b}, \hat{g}, \hat{\theta}\} \mapsto \{a, b, g, \theta\} \quad (41b)$$

where it is easily verified that $\tilde{a} = \hat{a}$ and $\tilde{b} = \hat{b}$ whenever $\tilde{g} = \hat{g}$; consequently, the physical attributes of deformation a, b, g remain continuous across a co-ordinate switch, however, the angle of co-ordinate rotation θ will not be continuous across such a switch between co-ordinate frames, as they represent rotations out of different co-ordinate directions. A like statement applies in the 3D case whenever one uses the re-indexing scheme presented in Section 2.1, i.e., the physical attributes of Laplace stretch remain continuous across a re-indexing of one's co-ordinate frame.

The above strategy returns matrices for the rotation and Laplace stretch described in Eqn. (37a) for both deformation gradients presented in Eqn. (37). The dilemma is remedied. Laplace stretch, as remedied, therefore has an unique physical interpretation. Co-ordinate re-indexing ensures that the invariant properties of Laplace stretch³⁸ are adhered to.

The above protocol is the 2D version of the 3D version presented in Section 2.1. It is easier to understand what is happening in the 2D case, which is why more detail is presented here. It may certainly happen that even when the 3D co-ordinates are re-indexed, there may be one or more of the twelve pentagons whose 2D co-ordinates need to be re-indexed, too.

There are three kinematic variables that describe deformation in a planar membrane:

elongation ratios a and b and simple shear g . These variables will vary both temporally and spatially throughout a pentagon whenever Wachspress' shape functions are used.

3.3.7 Thermodynamic Strains and Strain Rates

In terms of the above physical attributes for stretch, i.e., a , b and g , and their reference values, viz., a_0 , b_0 and g_0 , one can define a set of strain attributes derived from thermodynamics, specifically⁵⁸

$$\xi := \ln \left(\sqrt{\frac{a}{a_0} \frac{b}{b_0}} \right) \quad d\xi = \frac{1}{2} \left(\frac{da}{a} + \frac{db}{b} \right) \quad (42a)$$

$$\varepsilon := \ln \left(\sqrt{\frac{a}{a_0} \frac{b_0}{b}} \right) \quad d\varepsilon = \frac{1}{2} \left(\frac{da}{a} - \frac{db}{b} \right) \quad (42b)$$

$$\gamma := g - g_0 \quad d\gamma = dg \quad (42c)$$

whose rates are exact differentials, i.e., they are independent of path—a tacit requirement from thermodynamics.⁵⁹ Here ξ denotes dilation (uniform areal stretch), ε denotes squeeze (pure shear), and γ denotes (simple) shear.

3.3.7.1 Stretch Rates

The following approximations for stretch rates were derived by Freed & Zamani.³⁹ From these, the various strain rates listed in Eqn. (42) can be established.

A forward difference formula is used to approximate rates in the reference configuration for the various stretch attributes, as obtained from $d\mathcal{U}_0 = (\mathcal{U}_1 - \mathcal{U}_0)/dt + \mathcal{O}(dt)$ that, neglecting higher-order terms, produces

$$da_0 = \frac{a_1 - a_0}{dt}, \quad db_0 = \frac{b_1 - b_0}{dt}, \quad dg_0 = \frac{a_1}{a_0} \left(\frac{g_1 - g_0}{dt} \right) \quad (43)$$

where $dt = t_1 - t_0$ is the applied time step. A backward difference formula $d\mathcal{U}_1 = (\mathcal{U}_1 - \mathcal{U}_0)/dt + \mathcal{O}(dt)$ is used to estimate rates for the various stretch attributes at the end of its first integration step that, neglecting higher-order terms, give

$$da_1 = \frac{a_1 - a_0}{dt}, \quad db_1 = \frac{b_1 - b_0}{dt}, \quad dg_1 = \frac{a_0}{a_1} \left(\frac{g_1 - g_0}{dt} \right). \quad (44)$$

Curiously, there is a distinction in how the shear rates are approximated at the two nodes for this first interval of integration.

Equations (43 & 44) are first-order approximations for these derivatives. Second-order approximations can be established whenever $n > 0$ provided the stepsize for step $[n, n + 1]$ equals the stepsize for step $[n - 1, n]$, where state $n = 0$ associates with an initial condition. The backward difference formula $d\mathcal{U}_{n+1} = (3\mathcal{U}_{n+1} - 4\mathcal{U}_n + \mathcal{U}_{n-1})/2dt + \mathcal{O}((dt)^2)$ then produces rates for the stretch attributes of

$$\begin{aligned} da_{n+1} &= \frac{3a_{n+1} - 4a_n + a_{n-1}}{2dt} \\ db_{n+1} &= \frac{3b_{n+1} - 4b_n + b_{n-1}}{2dt} \\ dg_{n+1} &= \frac{2a_n}{a_{n+1}} \left(\frac{g_{n+1} - g_n}{dt} \right) - \frac{a_{n-1}}{a_{n+1}} \left(\frac{g_{n+1} - g_{n-1}}{2dt} \right) \end{aligned} \quad (45)$$

which require stretch attributes a_{n-1} , b_{n-1} and g_{n-1} to be stored in a finite element setting.

3.4. 3D Irregular Dodecahedra

The primary kinematic variables needed to describe the deformation of an irregular dodecahedron used as a model for an alveolar sac are its volume V (see Section 2.5) and the differential change in volume dV , with the former following from Eq. (14) and the latter coming from a suitable finite difference formula. Whenever the material filling an alveolar sac is air (its normal healthy condition), no further breakdown of these kinematics is required.

However, whenever an alveolar sac is filled with fluid (blood, interstitial fluids, plem, etc.) this fluid can be expected to behave solid-like in the face of a passing shock wave. In this situation, non-uniform measures for strain (i.e., shears) can be expected to arise.

3.4.1 Shape Functions for Interpolating an Irregular Tetrahedron

The shape functions associated with the four vertices of a tetrahedron N_i , $i = 1, 2, 3, 4$, are defined as follows

$$N_1 = 1 - \xi - \eta - \zeta, \quad N_2 = \xi, \quad N_3 = \eta, \quad N_4 = \zeta \quad (46a)$$

where ξ , η and ζ represent natural co-ordinates with $0 \leq \xi \leq 1$, $0 \leq \eta \leq 1 - \xi$ and $0 \leq \zeta \leq 1 - \xi - \eta$. Gradients of these shape functions are

$$\begin{aligned} N_{1,\xi} &= -1, & N_{1,\eta} &= -1, & N_{1,\zeta} &= -1 \\ N_{2,\xi} &= 1, & N_{2,\eta} &= 0, & N_{2,\zeta} &= 0 \\ N_{3,\xi} &= 0, & N_{3,\eta} &= 1, & N_{3,\zeta} &= 0 \\ N_{4,\xi} &= 0, & N_{4,\eta} &= 0, & N_{4,\zeta} &= 1 \end{aligned} \quad (46b)$$

and consequently the deformation gradient will be constant throughout its volume, like the deformation gradients used for chords and triangles.

3.4.1.1 Deformation Gradient for an Irregular Tetrahedron

The deformation gradient for a volume element is constructed from

$$\mathbf{F}(\xi, \eta, \zeta) = \begin{bmatrix} 1 & 0 & 0 \\ 0 & 1 & 0 \\ 0 & 0 & 1 \end{bmatrix} + \begin{bmatrix} \partial u / \partial \xi & \partial u / \partial \eta & \partial u / \partial \zeta \\ \partial v / \partial \xi & \partial v / \partial \eta & \partial v / \partial \zeta \\ \partial w / \partial \xi & \partial w / \partial \eta & \partial w / \partial \zeta \end{bmatrix} \begin{bmatrix} \partial x_0 / \partial \xi & \partial x_0 / \partial \eta & \partial x_0 / \partial \zeta \\ \partial y_0 / \partial \xi & \partial y_0 / \partial \eta & \partial y_0 / \partial \zeta \\ \partial z_0 / \partial \xi & \partial z_0 / \partial \eta & \partial z_0 / \partial \zeta \end{bmatrix}^{-1} \quad (47)$$

such that, for the four-node tetrahedron considered here, one has

$$\begin{bmatrix} \partial u / \partial \xi & \partial u / \partial \eta & \partial u / \partial \zeta \\ \partial v / \partial \xi & \partial v / \partial \eta & \partial v / \partial \zeta \\ \partial w / \partial \xi & \partial w / \partial \eta & \partial w / \partial \zeta \end{bmatrix} = \begin{bmatrix} \sum_{i=1}^4 N_{i,\xi} u_i & \sum_{i=1}^4 N_{i,\eta} u_i & \sum_{i=1}^4 N_{i,\zeta} u_i \\ \sum_{i=1}^4 N_{i,\xi} v_i & \sum_{i=1}^4 N_{i,\eta} v_i & \sum_{i=1}^4 N_{i,\zeta} v_i \\ \sum_{i=1}^4 N_{i,\xi} w_i & \sum_{i=1}^4 N_{i,\eta} w_i & \sum_{i=1}^4 N_{i,\zeta} w_i \end{bmatrix} \\ = \begin{bmatrix} u_2 - u_1 & u_3 - u_1 & u_4 - u_1 \\ v_2 - v_1 & v_3 - v_1 & v_4 - v_1 \\ w_2 - w_1 & w_3 - w_1 & w_4 - w_1 \end{bmatrix} \quad (48a)$$

whose nodal displacements $\mathbf{u}_i := \mathbf{x}_i - \mathbf{x}_{0i}$, $i = 1, 2, 3, 4$, have components of $\mathbf{u}_i = u_i \vec{\mathbf{E}}_1 + v_i \vec{\mathbf{E}}_2 + w_i \vec{\mathbf{E}}_3$, when evaluated in the reference co-ordinate frame $(\vec{\mathbf{E}}_1, \vec{\mathbf{E}}_2, \vec{\mathbf{E}}_3)$ of our dodecahedron, with $u_i := x_i - x_{0i}$, $v_i := y_i - y_{0i}$ and $w_i := z_i - z_{0i}$, and where

$$\begin{aligned} \begin{bmatrix} \partial x_0 / \partial \xi & \partial x_0 / \partial \eta & \partial x_0 / \partial \zeta \\ \partial y_0 / \partial \xi & \partial y_0 / \partial \eta & \partial y_0 / \partial \zeta \\ \partial z_0 / \partial \xi & \partial z_0 / \partial \eta & \partial z_0 / \partial \zeta \end{bmatrix} &= \begin{bmatrix} \sum_{i=1}^4 N_{i,\xi} x_{0i} & \sum_{i=1}^4 N_{i,\eta} x_{0i} & \sum_{i=1}^4 N_{i,\zeta} x_{0i} \\ \sum_{i=1}^4 N_{i,\xi} y_{0i} & \sum_{i=1}^4 N_{i,\eta} y_{0i} & \sum_{i=1}^4 N_{i,\zeta} y_{0i} \\ \sum_{i=1}^4 N_{i,\xi} z_{0i} & \sum_{i=1}^4 N_{i,\eta} z_{0i} & \sum_{i=1}^4 N_{i,\zeta} z_{0i} \end{bmatrix} \\ &= \begin{bmatrix} x_{02} - x_{01} & x_{03} - x_{01} & x_{04} - x_{01} \\ y_{02} - y_{01} & y_{03} - y_{01} & y_{04} - y_{01} \\ z_{02} - z_{01} & z_{03} - z_{01} & z_{04} - z_{01} \end{bmatrix} \quad (48b) \end{aligned}$$

whose initial nodal positions are $\mathbf{x}_{0i} = x_{0i} \vec{\mathbf{E}}_1 + y_{0i} \vec{\mathbf{E}}_2 + z_{0i} \vec{\mathbf{E}}_3$ at vertex i . This matrix is invertible, because the four vertices of a tetrahedron are distinct. The Jacobian matrix is given by

$$\begin{aligned} \mathbf{J} := \begin{bmatrix} \partial x / \partial \xi & \partial y / \partial \xi & \partial z / \partial \xi \\ \partial x / \partial \eta & \partial y / \partial \eta & \partial z / \partial \eta \\ \partial x / \partial \zeta & \partial y / \partial \zeta & \partial z / \partial \zeta \end{bmatrix} &= \begin{bmatrix} \sum_{i=1}^4 N_{i,\xi} x_i & \sum_{i=1}^4 N_{i,\xi} y_i & \sum_{i=1}^4 N_{i,\xi} z_i \\ \sum_{i=1}^4 N_{i,\eta} x_i & \sum_{i=1}^4 N_{i,\eta} y_i & \sum_{i=1}^4 N_{i,\eta} z_i \\ \sum_{i=1}^4 N_{i,\zeta} x_i & \sum_{i=1}^4 N_{i,\zeta} y_i & \sum_{i=1}^4 N_{i,\zeta} z_i \end{bmatrix} \\ &= \begin{bmatrix} x_2 - x_1 & y_2 - y_1 & z_2 - z_1 \\ x_3 - x_1 & y_3 - y_1 & z_3 - z_1 \\ x_4 - x_1 & y_4 - y_1 & z_4 - z_1 \end{bmatrix} \quad (48c) \end{aligned}$$

whose determinant is used in integrations. The current nodal positions have components $\mathbf{x}_i = x_i \vec{\mathbf{E}}_1 + y_i \vec{\mathbf{E}}_2 + z_i \vec{\mathbf{E}}_3$, $i = 1, 2, 3, 4$, in the dodecahedral frame $(\vec{\mathbf{E}}_1, \vec{\mathbf{E}}_2, \vec{\mathbf{E}}_3)$. The Jacobian matrix is invertible, because the four vertices of a tetrahedron are distinct.

3.4.2 QR Factorization of \mathbf{F}

The re-indexed deformation gradient presented in Section 2.1 has a Gram-Schmidt decomposition that we denote as $\mathbf{F} = \mathcal{R}\mathcal{U}$ whose components are an orthogonal rotation matrix $\mathcal{R} = [\vec{\mathbf{g}}_1 \mid \vec{\mathbf{g}}_2 \mid \vec{\mathbf{g}}_3] = \delta_{ij} \vec{\mathbf{g}}_i \otimes \vec{\mathbf{E}}_j = \mathcal{R}_{ij} \vec{\mathbf{E}}_i \otimes \vec{\mathbf{E}}_j$ and an upper-triangular matrix $\mathcal{U} = \mathcal{U}_{ij} \vec{\mathbf{E}}_i \otimes \vec{\mathbf{E}}_j$ called Laplace stretch,⁴³ both evaluated in the reference co-ordinate frame $(\vec{\mathbf{E}}_1, \vec{\mathbf{E}}_2, \vec{\mathbf{E}}_3)$, so that $\mathbf{F} = \mathcal{F}_{ij} \vec{\mathbf{E}}_i \otimes \vec{\mathbf{E}}_j = \mathcal{R}_{ik} \mathcal{U}_{kj} \vec{\mathbf{E}}_i \otimes \vec{\mathbf{E}}_j$, and therefore $\mathcal{F}_{ij} = \mathcal{R}_{ik} \mathcal{U}_{kj}$.

The components of Laplace stretch \mathcal{U}_{ij} are readily gotten through a Cholesky factorization of the right Cauchy-Green deformation tensor $\mathbf{C} = \mathcal{C}_{ij} \vec{\mathbf{E}}_i \otimes \vec{\mathbf{E}}_j$ with tensor components $\mathcal{C}_{ij} = \mathcal{F}_{ki} \mathcal{F}_{kj}$ that relate to their physical attributes via⁵⁸

$$\mathcal{U} = \begin{bmatrix} a & a\gamma & a\beta \\ 0 & b & b\alpha \\ 0 & 0 & c \end{bmatrix} \quad \text{with inverse} \quad \mathcal{U}^{-1} = \begin{bmatrix} 1/a & -\gamma/b & -(\beta - \alpha\gamma)/c \\ 0 & 1/b & -\alpha/c \\ 0 & 0 & 1/c \end{bmatrix} \quad (49)$$

with tensor components \mathcal{U}_{ij} being evaluated according to formulæ⁵⁰

$$\begin{aligned} \mathcal{U}_{11} &= \sqrt{\mathcal{C}_{11}} & \mathcal{U}_{12} &= \mathcal{C}_{12}/\mathcal{U}_{11} & \mathcal{U}_{13} &= \mathcal{C}_{13}/\mathcal{U}_{11} \\ \mathcal{U}_{21} &= 0 & \mathcal{U}_{22} &= \sqrt{\mathcal{C}_{22} - \mathcal{U}_{12}^2} & \mathcal{U}_{23} &= (\mathcal{C}_{23} - \mathcal{U}_{12}\mathcal{U}_{13})/\mathcal{U}_{22} \\ \mathcal{U}_{31} &= 0 & \mathcal{U}_{32} &= 0 & \mathcal{U}_{33} &= \sqrt{\mathcal{C}_{33} - \mathcal{U}_{13}^2 - \mathcal{U}_{23}^2} \end{aligned} \quad (50)$$

implying that the physical attributes for Laplace stretch can be evaluated via

$$a := \mathcal{U}_{11}, \quad b := \mathcal{U}_{22}, \quad c := \mathcal{U}_{33}, \quad \alpha := \frac{\mathcal{U}_{23}}{\mathcal{U}_{22}}, \quad \beta := \frac{\mathcal{U}_{13}}{\mathcal{U}_{11}}, \quad \gamma := \frac{\mathcal{U}_{12}}{\mathcal{U}_{11}} \quad (51)$$

where a, b and c are three, orthogonal, elongation ratios, and where α, β and γ are three, orthogonal, simple shears, with $a_0, b_0, c_0, \alpha_0, \beta_0$ and γ_0 denoting their values in some reference state. The elongations must be positive, whereas the shears may be of either sign. Collectively, they constitute a complete set of physical attributes for describing stretch from which constitutive equations can then be constructed.

No eigenvalue/eigenvector analysis is required to acquire either the stretch components or their attributes when using this technique.⁵⁰ The eigenvalues and eigenvectors of the triangular Laplace stretch equate with the eigenvalues and eigenvectors of the symmetric polar stretch *only* in an absence of shear.⁵⁵ Laplace stretch associates with the geometric description of a cube deforming into a parallelepiped; whereas, polar stretch associates with the geometric description of a sphere deforming into an ellipsoid. They are distinct measures of stretch.

3.4.3 Thermodynamic Strains and Strain Rates

In terms of the above physical attributes for stretch, one can define an useful set of

strain attributes derived from thermodynamics, specifically⁵⁸

$$\Xi := \ln \left(\sqrt[3]{\frac{a}{a_0} \frac{b}{b_0} \frac{c}{c_0}} \right) \quad d\Xi = \frac{1}{2} \left(\frac{da}{a} + \frac{db}{b} + \frac{dc}{c} \right) \quad (52a)$$

$$\varepsilon_1 := \ln \left(\sqrt[3]{\frac{a}{a_0} \frac{b_0}{b}} \right) \quad d\varepsilon_1 = \frac{1}{3} \left(\frac{da}{a} - \frac{db}{b} \right) \quad (52b)$$

$$\varepsilon_2 := \ln \left(\sqrt[3]{\frac{b}{b_0} \frac{c_0}{c}} \right) \quad d\varepsilon_2 = \frac{1}{3} \left(\frac{db}{b} - \frac{dc}{c} \right) \quad (52c)$$

$$\gamma_1 := \alpha - \alpha_0 \quad d\gamma_1 = d\alpha \quad (52d)$$

$$\gamma_2 := \beta - \beta_0 \quad d\gamma_2 = d\beta \quad (52e)$$

$$\gamma_3 := \gamma - \gamma_0 \quad d\gamma_3 = d\gamma \quad (52f)$$

whose rates are exact differentials, i.e., they are independent of path—a tacit requirement from thermodynamics.⁵⁹ Here Ξ represents dilatation, ε_1 is a squeeze in the 12 plane, and ε_2 is a squeeze in the 23-plane, while γ_1 is a shear in the 23 plane, γ_2 is a shear in the 13 plane, and γ_3 is a shear in the 12 plane, which are three, orthonormal, simple shearing motions. There is a third squeeze, too, viz., $\varepsilon_3 = -\varepsilon_1 - \varepsilon_2$, but it is not an independent descriptor of strain.

3.4.3.1 Stretch Rates

The following approximations for stretch rates were derived by Freed & Zamani.³⁹ From these, the various strain rates listed in Eqn. (52) can be established.

A forward difference formula is used to approximate rates in the reference configuration for the various stretch attributes, as obtained from $d\mathcal{U}_0 = (\mathcal{U}_1 - \mathcal{U}_0)/dt + \mathcal{O}(dt)$. Neglecting higher-order terms, this produces

$$\begin{aligned} da_0 &= \frac{a_1 - a_0}{dt} & d\alpha_0 &= \frac{b_1}{b_0} \left(\frac{\alpha_1 - \alpha_0}{dt} \right) \\ db_0 &= \frac{b_1 - b_0}{dt} & d\beta_0 &= \frac{a_1}{a_0} \left(\frac{\beta_1 - \beta_0}{dt} \right) \\ dc_0 &= \frac{c_1 - c_0}{dt} & d\gamma_0 &= \frac{a_1}{a_0} \left(\frac{\gamma_1 - \gamma_0}{dt} \right). \end{aligned} \quad (53)$$

A backward difference formula $d\mathcal{U}_1 = (\mathcal{U}_1 - \mathcal{U}_0)/dt + \mathcal{O}(dt)$ is used to estimate rates for the various stretch attributes at the end of its first integration step, from

which it follows that

$$\begin{aligned} da_1 &= \frac{a_1 - a_0}{dt} & d\alpha_1 &= \frac{b_0}{b_1} \left(\frac{\alpha_1 - \alpha_0}{dt} \right) \\ db_1 &= \frac{b_1 - b_0}{dt} & d\beta_1 &= \frac{a_0}{a_1} \left(\frac{\beta_1 - \beta_0}{dt} \right) \\ dc_1 &= \frac{c_1 - c_0}{dt} & d\gamma_1 &= \frac{a_0}{a_1} \left(\frac{\gamma_1 - \gamma_0}{dt} \right). \end{aligned} \quad (54)$$

Curiously, there is a distinction in how the shear rates are approximated at the two nodes belonging to this first interval of integration.

Equations (53 & 54) are first-order approximations for these derivatives. Second-order approximations can be established whenever $n > 0$ provided the stepsize for step $[n, n + 1]$ equals the stepsize for step $[n - 1, n]$, where state $n = 0$ associates with an initial condition. The backward difference formula $d\mathcal{U}_{n+1} = (3\mathcal{U}_{n+1} - 4\mathcal{U}_n + \mathcal{U}_{n-1})/2dt + \mathcal{O}((dt)^2)$ produces differential stretch rates of

$$\begin{aligned} da_{n+1} &= \frac{3a_{n+1} - 4a_n + a_{n-1}}{2dt} \\ db_{n+1} &= \frac{3b_{n+1} - 4b_n + b_{n-1}}{2dt} \\ dc_{n+1} &= \frac{3c_{n+1} - 4c_n + c_{n-1}}{2dt} \\ d\alpha_{n+1} &= 2 \frac{b_n}{b_{n+1}} \left(\frac{\alpha_{n+1} - \alpha_n}{dt} \right) - \frac{b_{n-1}}{b_{n+1}} \left(\frac{\alpha_{n+1} - \alpha_{n-1}}{2dt} \right) \\ d\beta_{n+1} &= 2 \frac{a_n}{a_{n+1}} \left(\frac{\beta_{n+1} - \beta_n}{dt} \right) - \frac{a_{n-1}}{a_{n+1}} \left(\frac{\beta_{n+1} - \beta_{n-1}}{2dt} \right) \\ d\gamma_{n+1} &= 2 \frac{a_n}{a_{n+1}} \left(\frac{\gamma_{n+1} - \gamma_n}{dt} \right) - \frac{a_{n-1}}{a_{n+1}} \left(\frac{\gamma_{n+1} - \gamma_{n-1}}{2dt} \right) \end{aligned} \quad (55)$$

which require data to be stored for the previous state associated with step $n - 1$.

3.5. Code Verification: Kinematics

The thermodynamic conjugate pairs of Freed *et al.*^{52,53,58} result in the following geometric/thermodynamic strain measures for our dodecahedral model: for 1D rods, an axial strain $e = \ln(L/L_0)$; for 2D membranes, a dilation $\xi = \ln \sqrt{ab/a_0 b_0} = \ln \sqrt{A/A_0}$, a squeeze (or pure shear) $\varepsilon = \ln \sqrt{ab_0/a_0 b} = \ln \sqrt{\Gamma/\Gamma_0}$, and a (simple) shear $\gamma = g - g_0$; and for 3D dodecahedra, a dilatation $\Xi = \ln \sqrt[3]{V/V_0}$ and, for those cases where the medium within an alveolar sac can support non-uniform

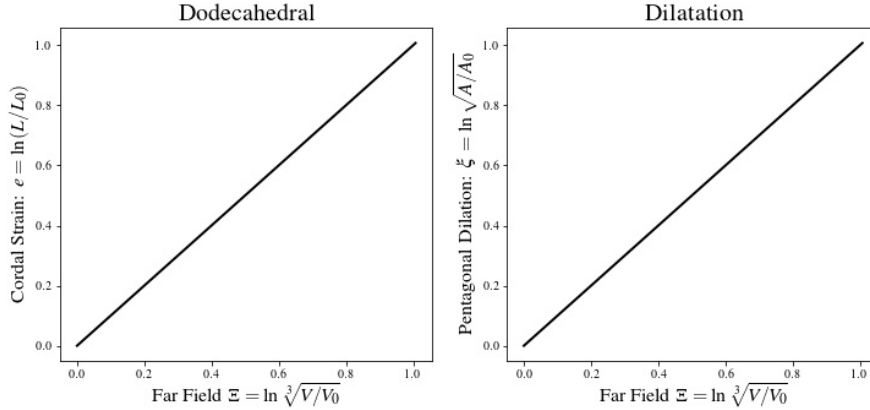


Fig. 15 Response of a dodecahedron exposed to an isotropic motion of dilatation. The abscissa is the control variable and the ordinates are response variables. The right graphic plots the areal response of the pentagons $\xi := \ln \sqrt{A/A_0}$, while the left graphic plots the axial response of the chords $e := \ln(L/L_0)$. Both are plotted against the volumetric response of the dodecahedron $\Xi := \ln \sqrt[3]{V/V_0}$. Here V denotes dodecahedral volume, A denotes pentagonal area, and L denotes chordal length, all being evaluated in the current state, whose reference values are V_0 , A_0 and L_0 .

stresses, two squeezes $\varepsilon_1 = \ln \sqrt[3]{ab_0/a_0b}$ and $\varepsilon_2 = \ln \sqrt[3]{bc_0/b_0c}$ plus three shears $\gamma_1 = \alpha - \alpha_0$, $\gamma_2 = \beta - \beta_0$ and $\gamma_3 = \gamma - \gamma_0$.

3.5.1 Isotropic Motions

Imposing the uniform far-field motion of a volumetric expansion onto our dodecahedral model results in a dodecahedral dilatation ($\Xi := \ln \sqrt[3]{V/V_0}$) that equals its pentagonal dilation ($\xi := \ln \sqrt{A/A_0}$) that equals its chordal strain ($e := \ln(L/L_0)$). These three strain measures follow from the 3-mode thermodynamic theory of Freed *et al.*,^{52,53} as presented above. Other choices for strain measures do not result in one-to-one relationships when exposed to an isotropic motion like those observed here. This is a particularly useful result in that it establishes a meaningful scaling in terms of strains between the three dimensions, cf. Fig. 15. It also provides for a verification of the numerical implementation of our dodecahedral model.

3.5.1.1 Geometric vs. Thermodynamic Strains

There are two types of strain measures that one can use to quantify deformation within a pentagon of a dodecahedron: geometric and thermodynamic. For the uniform far-field motion of volumetric expansion, only a thermodynamic strain known as dilation, i.e., $\xi = \ln \sqrt{ab/a_0b_0}$, varies with the motion, and its response equals

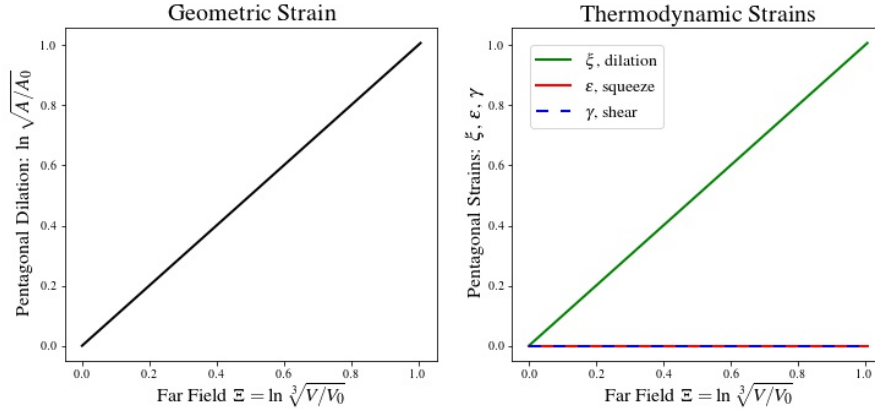


Fig. 16 Response of a dodecahedron exposed to a far-field isotropic motion of dilatation. The abscissa is the control variable and the ordinates are response variables. The right graphic plots the three thermodynamic strains, as they apply to a pentagon, while the left graphic plots the geometric strain of a pentagon.

that of the geometric strain $\ln \sqrt{A/A_0}$, see Fig. 16. Also present in this graph is an observation that the thermodynamic strains for squeeze ε and shear γ do not contribute under motions of pure dilatation, as expected. This further verifies the numerical implementation of our dodecahedral model.

To put this into perspective, we compare with studies done by multiple investigators where ratios of alveolar surface area, viz., A/A_0 , have been measured in rat, rabbit, guinea pig, and cat, cf. Roan & Waters [17, Table 1]. These experiments considered ranges that went as low as 25% and as high as 100% of total lung capacity. Taking statistics of their tabulation produced results of: $A/A_0 = 1.47 \pm 0.44$ during inflation and $A/A_0 = 1.18 \pm 0.14$ during deflation, which correspond to a $\xi = \ln \sqrt{A/A_0} = 0.19 \pm 0.18$ for inflation and a $\xi = \ln \sqrt{A/A_0} = 0.08 \pm 0.07$ for deflation. These areal strain values coincide with chordal strains of $e = \ln(L/L_0) = 0.13$ measured in vivo around the periphery of an alveolus in rat lung, as reported by Perlman & Bhattachary.⁶⁰ Our kinematics have been verified well past these physiologic ranges, viz., for dilatations up to 100% logarithmic strain.

3.5.2 Isochoric Motions

The motions of pure and simple shears are volume preserving. Imposing these shears as far-field motions onto our dodecahedral model produced the results displayed in Fig. 17. For a simple shear, the numerical model is in error by about

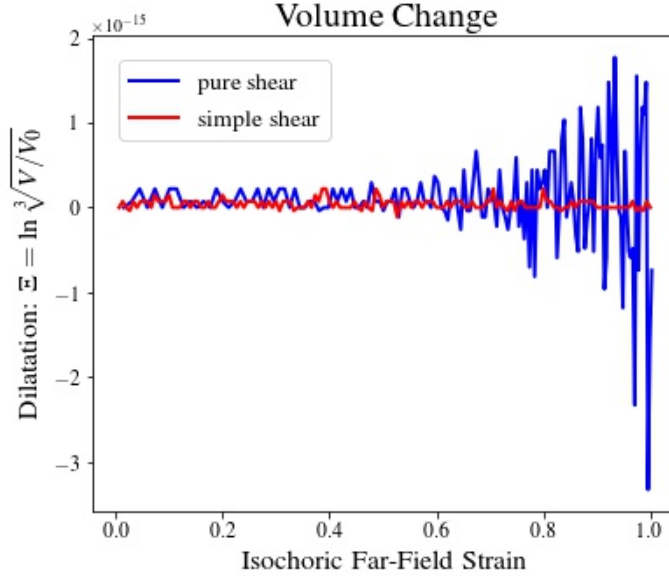


Fig. 17 Response of a dodecahedron exposed to far-field motions of pure and simple shears. Note that the ordinate is $\times 10^{-15}$ and machine precision is $\sim 2.2 \times 10^{-16}$.

machine precision, i.e., $\epsilon_m \approx 2.2 \times 10^{-16}$, for strains up to 100%, while for pure shear (a special case of squeeze in 3D) the model is in error by about machine precision for strains up to of about 60%, after which the error increases up to about $10\epsilon_m$ at strains around 100%. This further verifies the numerical implementation of our dodecahedral model.

3.5.2.1 Geometric Strains

How the thirty chords and the twelve irregular pentagons deform under far-field motions of pure shear is displayed in Fig. 18. Figure 17 demonstrates that the overall response of a dodecahedron is isochoric during pure shear. Regardless, Fig. 18 demonstrates that the individual chordal and pentagonal constituents deform in a non-homogeneous manner, where the strains have been calculated as geometric changes in dodecahedral shape. This result agrees with *in vivo* observations made by Perlman & Bhattacharya⁶⁰ where confocal microscopy was used to image a breathing rat lung.

For the chords, there are six independent responses for dodecahedral motions of pure shear: two chords each for three of these lines, and eight chords each for the remaining three curves present in the left images of Fig. 18. For pentagons, there

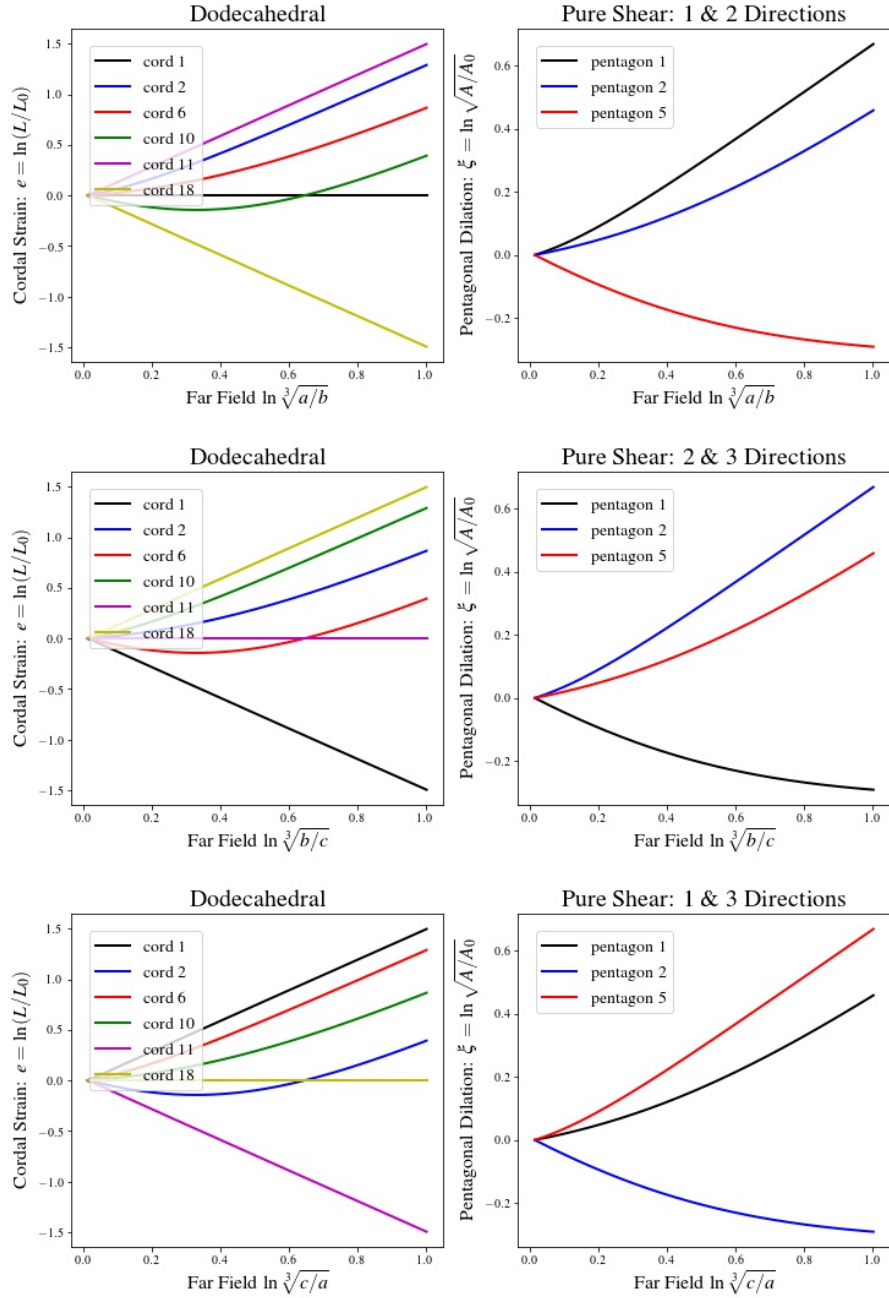


Fig. 18 Response of a dodecahedron exposed to far-field pure-shear motions in the sense of Treloar:⁶¹ $a = \ell$, $b = 1/\ell$ and $c = 1$ in the top images; $a = 1$, $b = \ell$ and $c = 1/\ell$ in the middle images; and $a = 1/\ell$, $b = 1$ and $c = \ell$ in the bottom images, with ℓ denoting an elongation of extrusion. In all six graphic images, the relevant (controlled) motion of the far-field pure shear is plotted along the abscissa. In each image pair, the right graphic presents pentagonal dilations, while the left graphic presents chordal elongations. Only unique responses are plotted; repetitions are not.

are three independent responses with four pentagons responding according to each curve shown in the right images. Although different chords and pentagons deform differently when sheared in different directions, their collective responses are the same regardless of the far-field direction being sheared. Consequently, the local geometric response of a dodecahedron is isotropic under the far-field motions of pure shear.

How the thirty chords and the twelve irregular pentagons deform under far-field motions of simple shear is displayed in Fig. 19. Figure 17 demonstrates that the overall response of a dodecahedron is isochoric during a far-field simple shear. Figure 19 demonstrates that the individual chordal and pentagonal constituents deform in a non-homogeneous manner during simple shears, like they do for pure shears. However, unlike pure shears whose collective chordal and pentagonal responses remain isotropic, here they diverge slightly from isotropy under motions of simple shear. Simple shears in the 12 and 23 planes have the same collective response; whereas, simple shear in the 13 plane has a slightly different response.

Figures 15–19 show that a dodecahedron is (nearly, but not completely) isotropic in its kinematic response, as measured by the geometric strains $e = \ln(L/L_0)$, $\xi = \ln \sqrt{A/A_0}$ and $\Xi = \ln \sqrt[3]{V/V_0}$. Furthermore, even though a far-field deformation is homogeneous, in accordance with our Conjecture on pg. 6, the local deformations within the individual constituents of an alveolus will typically be heterogeneous, which agrees with imaging data.⁶⁰

3.5.2.2 Thermodynamic Strains

Addressing the septal response, modeled here as a set of twelve irregular pentagons per alveolus, we desire to come to a determination regarding how to best model the deformation occurring within these alveolar septa. In the section above we investigated the geometric response of alveolar septa via the strain measure $\ln \sqrt{A/A_0}$, which quantifies dilation.

The thermodynamic strains arising from a Gram-Schmidt factorization of the deformation gradient put forward in Section 3.3 specify three strain measures pertinent to a membrane: dilation $\xi = \ln \sqrt{ab/a_0 b_0}$, squeeze $\varepsilon = \ln \sqrt{ab_0/a_0 b}$ and shear $\gamma = g - g_0$, where elongations a and b and magnitude of shear g are illustrated in Fig. 12. Of these, dilation is an uniform response, while squeeze and shear describe non-uniform responses. To acquire them requires knowing the deformation

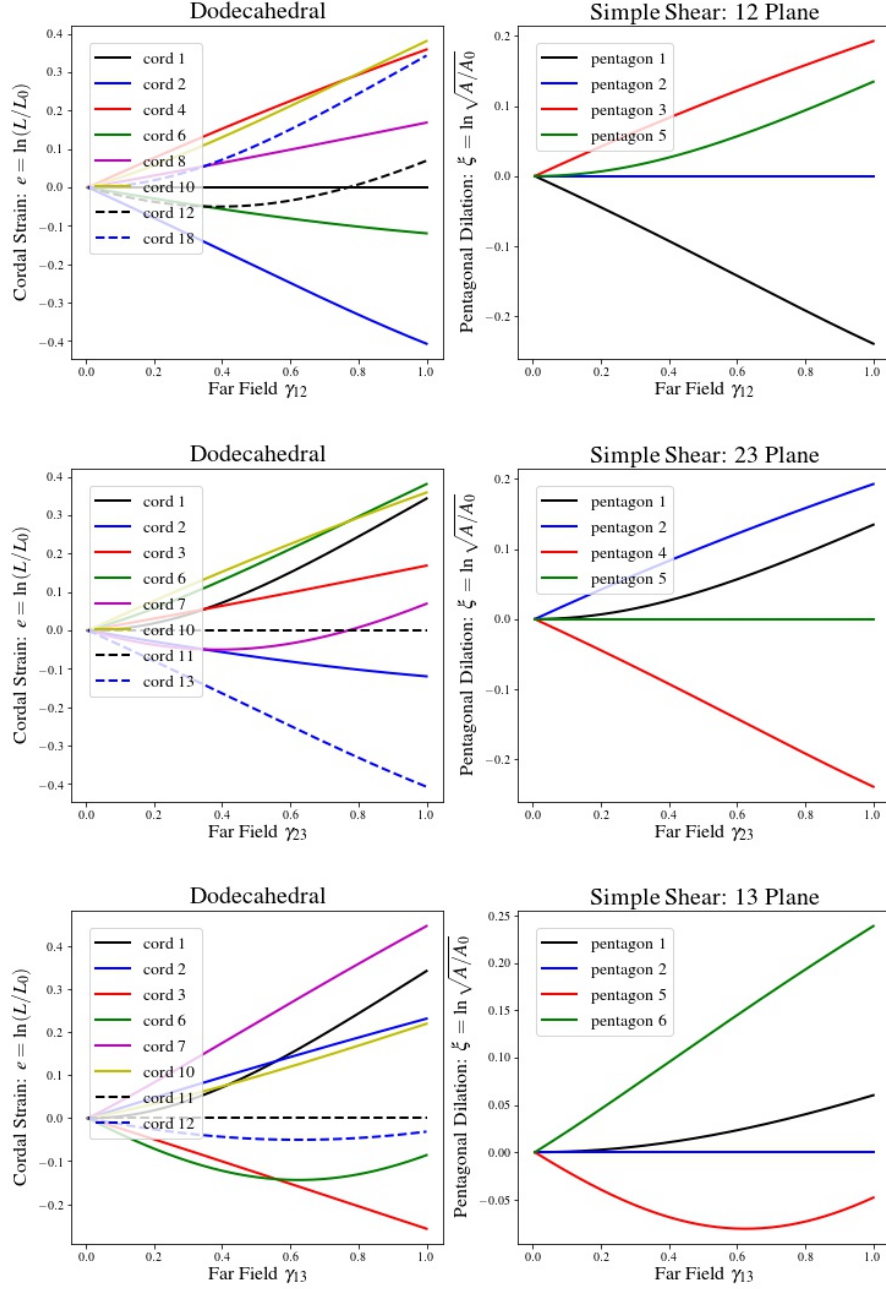


Fig. 19 Response of a dodecahedron exposed to far-field simple-shear motions. In all six graphic images, the relevant (controlled) motion of simple shear is plotted along the abscissa. In each image pair, the right graphic presents pentagonal dilations, while the left graphic presents chordal elongations. Only unique responses are plotted; repetitions are not. Responses in the 13 plane differ from those of the 12 and 23 planes.

gradient.

The curves in Figs. 18 & 19 were obtained from geometric measures for chordal strain $\ln(L/L_0)$ and areal dilation $\ln\sqrt{A/A_0}$. They were computed under separate far-field conditions of pure and simple shears. The curves in Figs. 20 & 21 were obtained from thermodynamic measures for membrane strain under the same far-field deformations. The strains of dilation ξ , squeeze ε , and shear γ were computed in accordance with Section 3.3 using deformation gradients gotten from the pentagonal shape functions of Wachspress⁴⁴ discussed in Section 3.3.*

Figures 18–21 allow us to conclude that if septal dilation were the only mode of planar deformation thought to cause a mechanical response, then knowledge of the geometric strain $\xi = \ln\sqrt{A/A_0}$ would be adequate; there would be no need to introduce a separate finite-element discretization of the septal planes for acquiring their deformation gradients. However, if the non-uniform responses of squeeze ε and shear γ are thought to contribute to the overall mechanical response of these membranes, then the shape functions of Wachspress^{44,45} ought to be used for acquiring the deformation gradient within a septal plane. We found, but do not present figures to support this observation, that constant-strain triangles are not accurate enough for our application. Strains derived from Wachspress shape functions are inhomogeneous; consequently, the deformation gradient will need to be evaluated at each Gauss point of integration within a pentagon, cf. Section 5.2.

3.5.3 Co-ordinate Pivoting

The pivoting strategy of Section 3.3.6.3 used to address the physical dilemma of Section 3.3.6.2 did not engage often during our assessment of the code, but it did arise at least twice with effects illustrated in Figs. 22 & 23. Here one can see that there is a clear effect on the shear response within four pentagonal planes; however, no change is observed to have occurred in either the dilation or squeeze responses, as expected. It is not always possible to know when or where a co-ordinate relabeling ought to occur; consequently, the algorithm put forward in Section 3.3.6.3 is deemed necessary.

*Five constant-strain triangles were also used to quantify the deformation gradient for each pentagonal surface at its centroid—the common vertex to all five triangles. This approach provided accurate descriptions for uniform strain, i.e., dilation ξ , but not for the two non-uniform strains, viz., squeeze ε and shear γ ; hence, our preference to use Wachspress shape functions for alveolar planes.

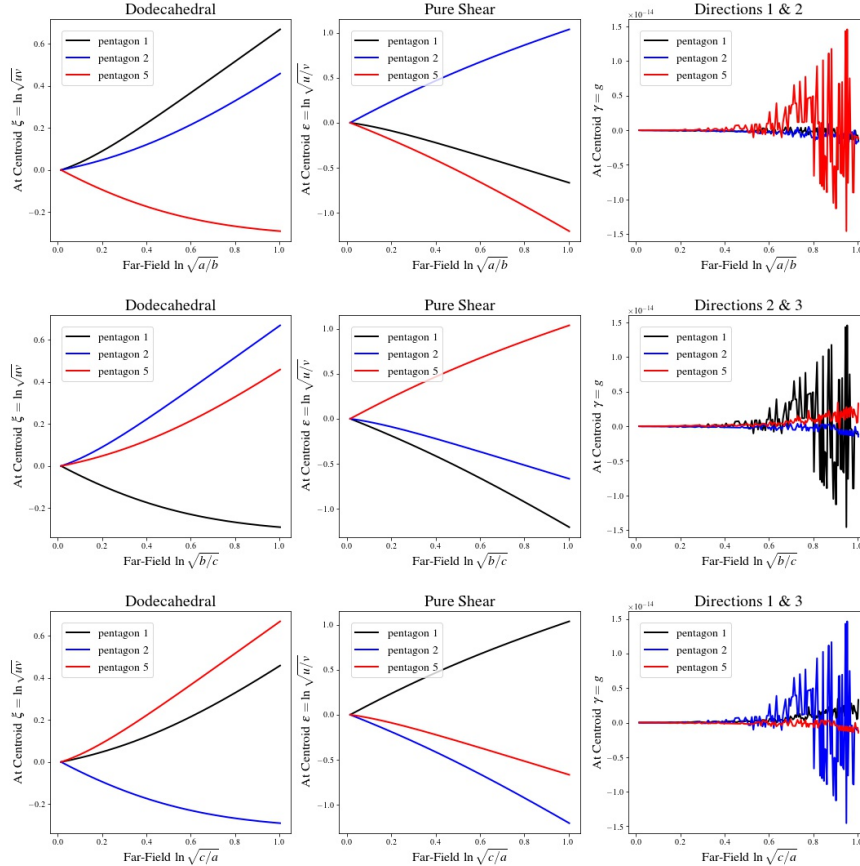


Fig. 20 Same boundary conditions as in Fig. 18. Pentagonal areas were used to compute dilation in Fig. 18. The shape functions of Wachspress were used to compute dilation here. The uniform response in the right column of Fig. 18 and in the left column above are the same, providing additional assurance that the code has been correctly implemented. The squeeze response shown in the center column is the same for all three orientations of far-field pure shear, i.e., this response is isotropic. The right column has ordinates scaled by 10^{-14} implicating that there is no effective simple shear response occurring within any pentagonal surface of the dodecahedron whenever it is subjected to a far-field motion of pure shear.

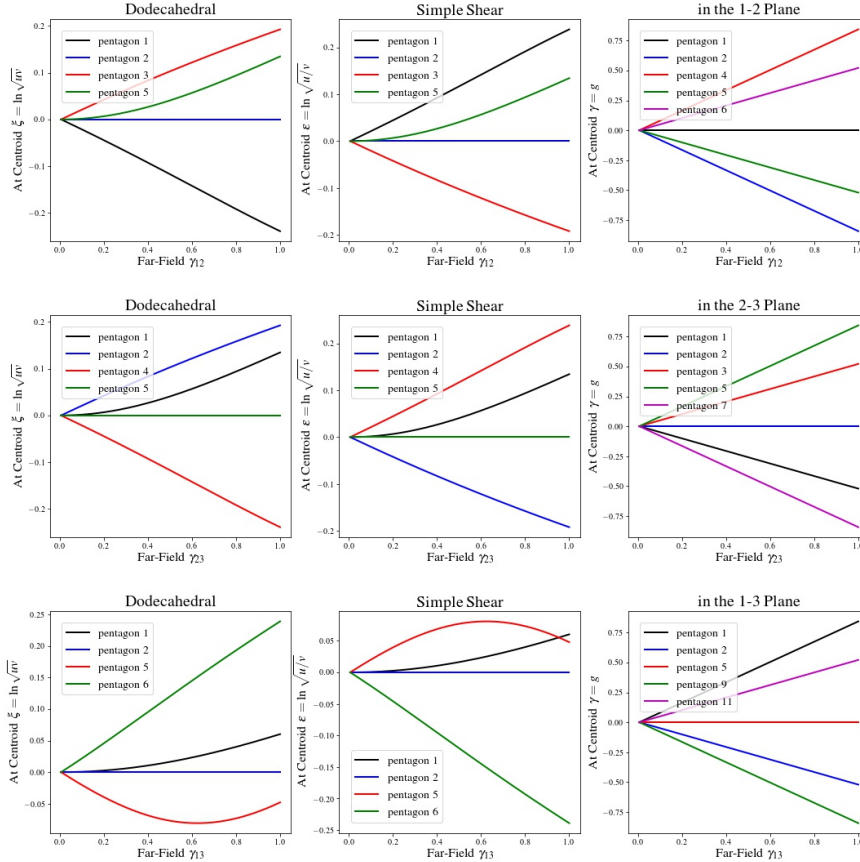


Fig. 21 Same boundary conditions as in Fig. 19. Pentagonal areas were used to compute dilation in Fig. 19. The shape functions of Wachspress were used to compute dilation here. The uniform response in the right column of Fig. 19 and in the left column above are the same, providing additional assurance that the code has been correctly implemented. Like the dilational responses of the left column, the squeeze responses of the center column are the same in the 12 and 23 planes, but differ in the 13 plane. In all cases, the simple shear response of any pentagonal plane is proportional to that of the far-field shear imposed, further substantiating the code's implementation. The shear response of the septal membranes is isotropic.

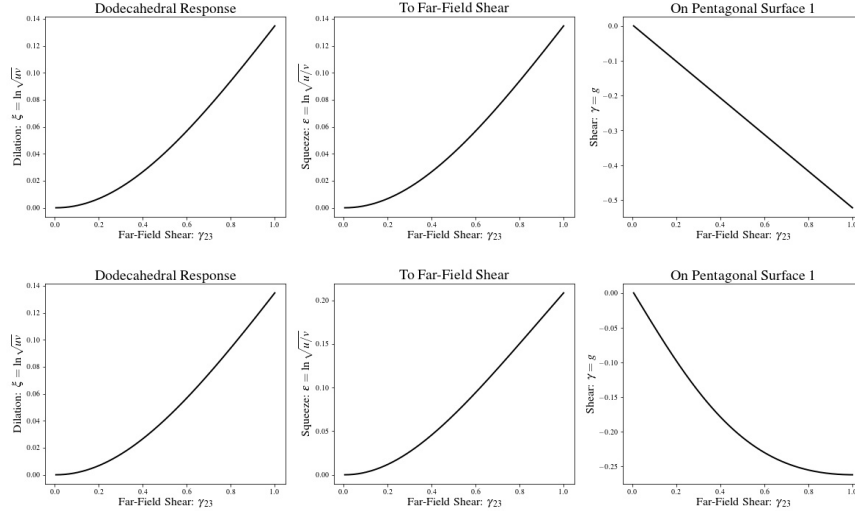


Fig. 22 A far-field shear of γ_{23} is imposed on the dodecahedron. Pentagons 1 and 8 exhibit the plotted response. The top set of figures result whenever the pivoting strategy of Section 3.3.6.3 is used, while the bottom set of figures result whenever no pivoting strategy is employed. The dilation (left graphs) and squeeze (center graphs) responses are not effected by pivoting, only shear (right graphs) is effected. Pivoting maintains a linear shear response under a far-field shearing of the dodecahedron, as desired.

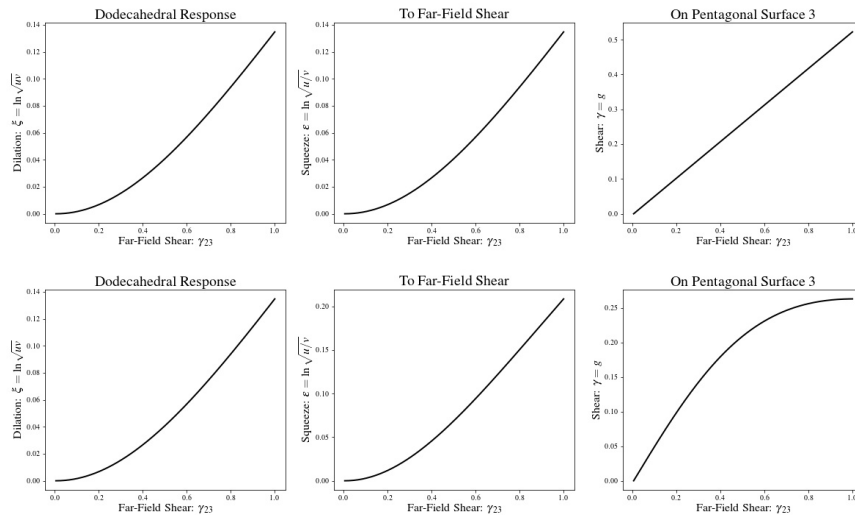


Fig. 23 A far-field shear of γ_{23} is imposed on the dodecahedron. Pentagons 3 and 10 exhibit the plotted response. The top set of figures result whenever the pivoting strategy of Section 3.3.6.3 is used, while the bottom set of figures result whenever no pivoting strategy is employed. The dilation (left graphs) and squeeze (center graphs) responses are not effected by pivoting, only shear (right graphs) is effected. Pivoting maintains a linear shear response under a far-field shearing of the dodecahedron, as desired.

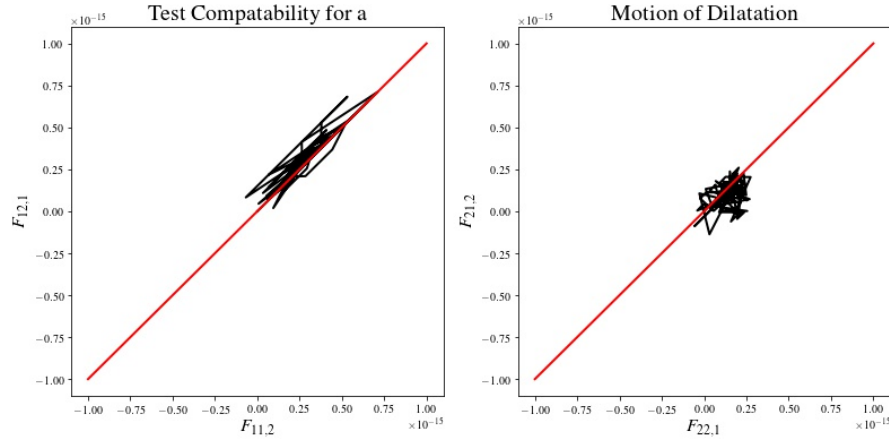


Fig. 24 Planar compatibility requires $F_{11,2} = F_{12,1}$ and $F_{22,1} = F_{21,2}$ where the left-hand sides of these formulæ are plotted as the abscissæ and the right-hand sides are plotted as the ordinates. For compatibility, the response ought to lie along the 45° diagonal, which is drawn in red over the range of $\pm 10^{-15}$ where machine precision is about 2.2×10^{-16} . Here the motion is one of uniform dilatation out to 100% strain.

3.5.4 Compatible Membrane Deformations

For a deformation to be compatible, and therefore integrable, the curl of its deformation gradient must vanish, viz., $\text{curl}(\mathbf{F}) = \mathbf{0}$.⁴⁹ Equation (29) provides constraint equations for the compatibility of planar motions, e.g., septal planes of an alveolus. Here we test to make sure that these conditions are satisfied within the pentagonal planes of our alveolar dodecahedron, assuming that the shape functions of Wachspress apply.

Figure 24 presents the compatibility response at the centroid of a typical pentagonal plane during the uniform expansion of a regular dodecahedron out to 100% strain. Theoretically, all four derivatives should be zero for this motion. Actually, their values are on the order of machine precision. Most importantly, whenever they are not zero, they lie along the 45° diagonal, thereby verifying compatibility in the case of a dilatation.

Similarly, Figs. 25 & 26 present typical responses for testing compatibility during far-field pure shear (Fig. 25) and simple shear (Fig. 26) deformations. In both cases, one of the four pentagons around the girth of the dodecahedron (viz., #5) has been selected, as both modes of deformation are activated in this pentagon. In both cases, errors are typically less than ten times machine precision, thereby verifying

DRAFT: UNCLASSIFIED

compatibility in the cases of squeeze and shear.

This collective set of graphs, Figs. 24–26, investigate the constraint of compatibility in terms of the three fundamental modes of deformation: dilatation, squeeze and shear. These figures verify that the constraint of compatibility is satisfied when using the pentagonal shape functions of Wachspress^{44,45} in our dodecahedral model, as errors are typically less than ten times machine precision. This has been verified out to deformations that are at least three times those of their normal physiologic range.

Our kinematic analysis of a dodecaheron has been verified both theoretically and numerically.

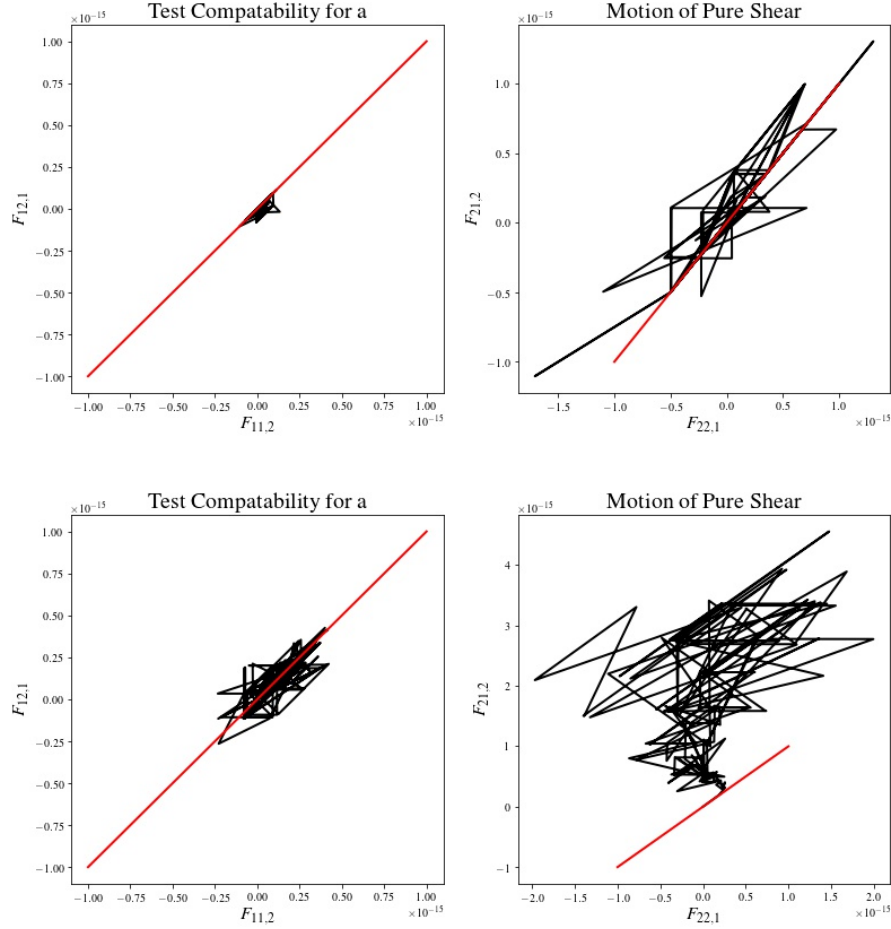


Fig. 25 Planar compatibility requires $F_{11,2} = F_{12,1}$ and $F_{22,1} = F_{21,2}$ where the left-hand sides of these formulæ are plotted as the abscissæ and the right-hand sides are plotted as the ordinates. For compatibility, the response ought to lie along the 45° diagonal, which is drawn in red over the range of $\pm 10^{-15}$ where machine precision is about 2.2×10^{-16} . Here the motion is one of pure shear out to 100% strain with elongation occurring in the 1-direction, contraction occurring in the 2 direction, while the 3-direction is held fixed. These results pertain to pentagon 5: nodes 15, 5, 12, 11, 1, cf. Fig. 6 and Table 3. The top row of figures is the best response (at Gauss point 7, cf. Fig. 32) while the bottom row of figures is the worst response (at Gauss point 5).

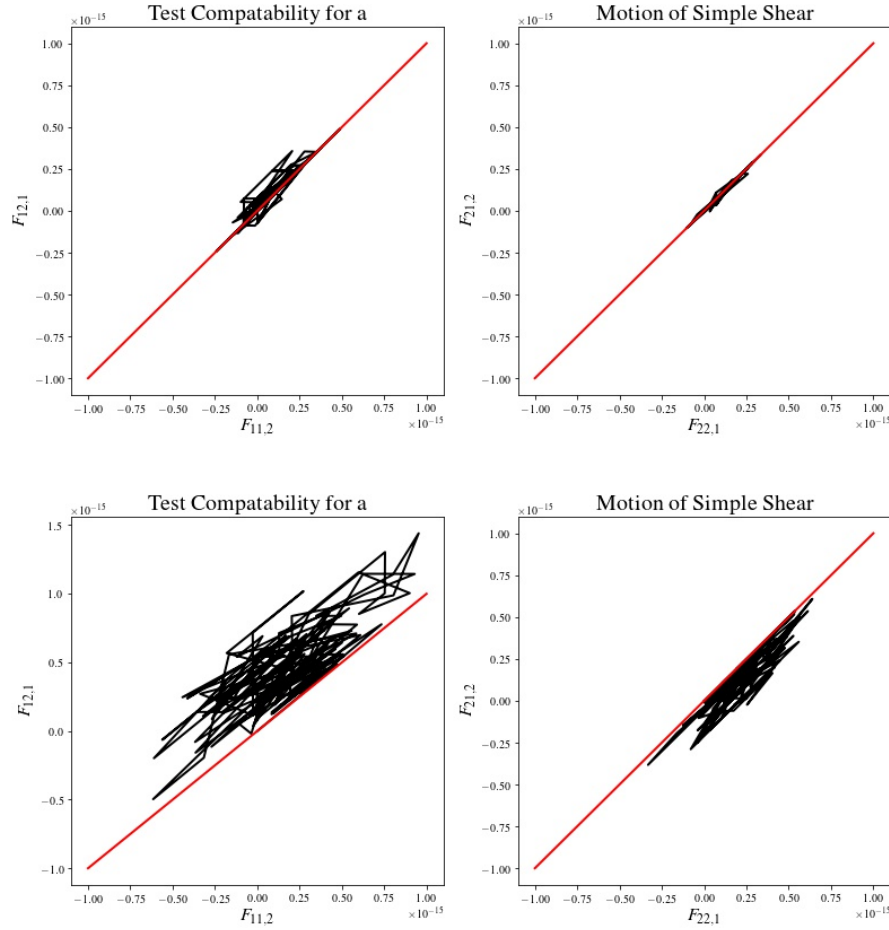


Fig. 26 Planar compatibility requires $F_{11,2} = F_{12,1}$ and $F_{22,1} = F_{21,2}$ where the left-hand sides of these formulae are plotted as the abscissæ and the right-hand sides are plotted as the ordinates. For compatibility, the response ought to lie along the 45° diagonal, which is drawn in red over the range of $\pm 10^{-15}$ where machine precision is about 2.2×10^{-16} . Here the motion is one of simple shear out to 100% strain, shearing along 1-2 planes in the 1-direction. These results pertain to pentagon 5: nodes 15, 5, 12, 11, 1, cf. Fig. 6 and Table 3. The top row of figures is the best response (at Gauss point 7, cf. Fig. 32) while the bottom row of figures is the worst response (at Gauss point 5).

Part 4

Constitutive Theory

Roan & Waters¹⁷ and Suki *et al.*^{62,63} have both written extensive review articles on the mechanics of parenchyma. They have provided detailed information about the structural constituents of alveoli. And they have discussed their influence on the overall mechanical response of parenchyma. Of particular relevance, from a mechanics perspective, are the constituent building blocks of alveolar tissue: collagen (types I and III, predominantly), elastin, proteoglycans and other structural proteins, surfactant, and cells (epithelial and endothelial, predominantly). These constituents are assembled in such a manner so as to produce a variety of alveolar sub-structures that are essentially 1D (alveolar chords), 2D (alveolar septa) and 3D (alveolar sacs) in their geometric construction.

A dodecahedron is used here as a geometric model for an alveolus,²² cf. Figs. 4 & 6. This model is comprised of: thirty 1D rods that represent alveolar chords, twelve 2D membranes that represent alveolar septa, considered here to be pentagonal in shape, and one 3D cavity filled with air (or fluid in the case of a contusion caused by injury, or of an edema caused by disease) whose geometry is considered to be dodecahedral in shape. The thermoelastic constitutive equations presented here for spatial chords and membranes are derived in App. A. Elastic behavior is sufficient for our intended application of studying alveoli subjected to traveling waves.

We recall from our kinematic study of a dodecahedron that the geometric strains (i.e., $e := \ln(L/L_0)$ for the elongation of septal chords, $\xi := \ln \sqrt{A/A_0}$ for the dilation of septal membranes, and $\Xi := \ln \sqrt[3]{V/V_0}$ for the dilatation of alveolar volume) are equivalent to one another under motions of uniform expansion/compression. These three, geometric, strain measures also exist as thermodynamic strains, each associating with a distinct and unique conjugate stress.^{53,58}

Constitutive equations are a derived consequence from physical laws governing thermodynamic processes. Here we derive constitutive equations applicable for modeling 1D thermoelastic fibers (alveolar chords), 2D thermoelastic membranes (alveolar septa), and 3D thermoelastic volumes (alveolar sacs). In Section 4.1, we

assume that the motions are uniform in their spatial dimension. Later, in Sections 4.2 & 4.3, the non-uniform motions of squeeze and shear are included into our thermodynamic framework for membranes and volumes, respectively. Section 4.4 pulls these results together, sufficient for the intended purpose of modeling the three structural facets that comprise an alveolous. Specifically, all geometric entities (alveolar chords, alveolar septa, and alveolar sacs) are now described in terms of stresses (dyne/cm^2) instead of their intensive thermodynamic forces (force, surface tension, and stress). This is done to facilitate implementation of these models into code, and to facilitate interpretations of their results by engineers and scientists. The chapter closes with a discussion of their implementation into finite elements in Section 4.5 along with a set of examples created to verify our code in Section 4.6. The biologic constitutive equations presented in this part are derived in App. A from an implicit theory of elasticity.

4.1. Green Thermoelastic Solids: Uniform Motions in 1D, 2D & 3D

Combining the First and Second Laws of Thermodynamics governing uniform, reversible, adiabatic processes results in the following three formulae, one per dimension; they are

$$\text{In 1 Dimension:} \quad dU = \theta d\eta + \frac{1}{\rho_{1D}} F dL/L \quad (56a)$$

$$\text{In 2 Dimensions:} \quad dU = \theta d\eta + \frac{1}{\rho_{2D}} T dA/A \quad (56b)$$

$$\text{In 3 Dimensions:} \quad dU = \theta d\eta - \frac{1}{\rho_{3D}} P dV/V \quad (56c)$$

wherein U is an internal energy density ($\text{erg/g} = \text{dyne.cm/g}$), which is a function of state, θ is a temperature in Kelvin ($273 + {}^\circ\text{C}$), η is an entropy density (erg/g.K), L is a length of line (cm), A is an area of surface (cm^2), V is a volume of space (cm^3), F is a force (dyne), T is a surface tension (dyne/cm), and P is a pressure ($\text{dyne}/\text{cm}^2 = \text{barye}$), whereas the mass densities ρ_{1D} (g/cm), ρ_{2D} (g/cm^2) and ρ_{3D} (g/cm^3) associate with a reference state of per unit length, or per unit area, or per unit volume, as appropriate. Pressure P is assigned to be positive whenever a body undergoes hydrostatic compression, as is classically assigned. However, per accepted practice in continuum mechanics, the sign of pressure may flip back and forth depending upon what pressure we are talking about in lung mechanics, e.g., it is common to refer to transpulmonary pressures as being positive (not negative). Typically, the trace of stress is positive for this measure of pressure.

4.1.1 Constitutive Equations

Because the internal energy density U is a state function, its differential rate of change describes a Pfaffian form⁵⁹ out of which the following constitutive formulæ are readily obtained

$$\text{In 1D: } \theta = \partial_\eta U(\eta, \ln(L/L_0)) \quad F = \rho_{1D} \partial_{\ln(L/L_0)} U(\eta, \ln(L/L_0)) \quad (57a)$$

$$\text{In 2D: } \theta = \partial_\eta U(\eta, \ln(A/A_0)) \quad T = \rho_{2D} \partial_{\ln(A/A_0)} U(\eta, \ln(A/A_0)) \quad (57b)$$

$$\text{In 3D: } \theta = \partial_\eta U(\eta, \ln(V/V_0)) \quad -P = \rho_{3D} \partial_{\ln(V/V_0)} U(\eta, \ln(V/V_0)) \quad (57c)$$

where strains are logarithms of dimension-appropriate stretches. As a matter of convenience, we adopt the notation $\partial_\eta U := \partial U / \partial \eta$, etc. Employing the geometric strains of Part 3, viz., $e := \ln(L/L_0)$, $\xi := \ln \sqrt{A/A_0}$ and $\Xi := \ln \sqrt[3]{V/V_0}$ with differential rates of $de = L^{-1} dL$, $d\xi = \frac{1}{2} A^{-1} dA$ and $d\Xi = \frac{1}{3} V^{-1} dV$, these constitutive equations take on the following simpler form

$$\text{In 1D: } \theta = \partial_\eta U(\eta, e) \quad F = \rho_{1D} \partial_e U(\eta, e) \quad (58a)$$

$$\text{In 2D: } \theta = \partial_\eta U(\eta, \xi) \quad \pi = \rho_{2D} \partial_\xi U(\eta, \xi) \quad (58b)$$

$$\text{In 3D: } \theta = \partial_\eta U(\eta, \Xi) \quad \Pi = \rho_{3D} \partial_\Xi U(\eta, \Xi) \quad (58c)$$

wherein $\pi := 2T$ and $\Pi := -3P$ are the measures for surface tension and pressure that we use in this work. We find it useful to use this negative measure for pressure because the transpulmonary pressure in lung, under normal physiologic conditions, is typically negative; hence, Π would be positive in its specification of transpulmonary pressure. The above constitutive equations describe Green thermoelastic solids of specified dimension undergoing uniform motions in adiabatic enclosures.

We consider response variables for temperature and force/surface-tension/pressure to be C^1 functions of state; therefore, the internal energy U is a C^2 function of state in a Green thermoelastic solid undergoing uniform adiabatic motions (cf. Weinhold⁶⁴ and Gilmore⁶⁵). Under these conditions of smoothness, one can differentiate Eqn. (58), thereby producing the following collection of coupled, partial, differen-

tial equations

$$\text{In 1D: } \begin{Bmatrix} d\theta \\ dF \end{Bmatrix} = \begin{bmatrix} \partial_{\eta\eta} U & \partial_{\eta e} U \\ \rho_{1D} \partial_{e\eta} U & \rho_{1D} \partial_{ee} U \end{bmatrix} \begin{Bmatrix} d\eta \\ de \end{Bmatrix} \quad (59a)$$

$$\text{In 2D: } \begin{Bmatrix} d\theta \\ d\pi \end{Bmatrix} = \begin{bmatrix} \partial_{\eta\eta} U & \partial_{\eta\xi} U \\ \rho_{2D} \partial_{\xi\eta} U & \rho_{2D} \partial_{\xi\xi} U \end{bmatrix} \begin{Bmatrix} d\eta \\ d\xi \end{Bmatrix} \quad (59b)$$

$$\text{In 3D: } \begin{Bmatrix} d\theta \\ d\Pi \end{Bmatrix} = \begin{bmatrix} \partial_{\eta\eta} U & \partial_{\eta\Xi} U \\ \rho_{3D} \partial_{\Xi\eta} U & \rho_{3D} \partial_{\Xi\Xi} U \end{bmatrix} \begin{Bmatrix} d\eta \\ d\Xi \end{Bmatrix} \quad (59c)$$

where mixed partial derivatives obey $\partial_{e\eta} U = \partial^2 U / \partial e \partial \eta = \partial^2 U / \partial \eta \partial e = \partial_{\eta e} U$, etc., that in the thermodynamics literature are referred to as Maxwell's relations; they are also known as Sylvester's criteria for the integrability of a Pfaffian form.

Exchanging cause and effect between entropy and temperature in Eqn. (59) gives
In 1D:

$$\begin{Bmatrix} d\eta \\ dF \end{Bmatrix} = \begin{bmatrix} \theta / \partial_{\eta\eta} U & -\partial_{\eta e} U / \partial_{\eta\eta} U \\ \rho_{1D} \theta \partial_{e\eta} U / \partial_{\eta\eta} U & \rho_{1D} (\partial_{ee} U - \partial_{e\eta} U \cdot \partial_{\eta e} U / \partial_{\eta\eta} U) \end{bmatrix} \begin{Bmatrix} \theta^{-1} d\theta \\ de \end{Bmatrix} \quad (60a)$$

In 2D:

$$\begin{Bmatrix} d\eta \\ d\pi \end{Bmatrix} = \begin{bmatrix} \theta / \partial_{\eta\eta} U & -\partial_{\eta\xi} U / \partial_{\eta\eta} U \\ \rho_{2D} \theta \partial_{\xi\eta} U / \partial_{\eta\eta} U & \rho_{2D} (\partial_{\xi\xi} U - \partial_{\xi\eta} U \cdot \partial_{\eta\xi} U / \partial_{\eta\eta} U) \end{bmatrix} \begin{Bmatrix} \theta^{-1} d\theta \\ d\xi \end{Bmatrix} \quad (60b)$$

In 3D:

$$\begin{Bmatrix} d\eta \\ d\Pi \end{Bmatrix} = \begin{bmatrix} \theta / \partial_{\eta\eta} U & -\partial_{\eta\Xi} U / \partial_{\eta\eta} U \\ \rho_{3D} \theta \partial_{\Xi\eta} U / \partial_{\eta\eta} U & \rho_{3D} (\partial_{\Xi\Xi} U - \partial_{\Xi\eta} U \cdot \partial_{\eta\Xi} U / \partial_{\eta\eta} U) \end{bmatrix} \begin{Bmatrix} \theta^{-1} d\theta \\ d\Xi \end{Bmatrix} \quad (60c)$$

where we recall that $de = L^{-1} dL$, $d\xi = \frac{1}{2} A^{-1} dA$ and $d\Xi = \frac{1}{3} V^{-1} dV$, so that we have logarithmic rates describing both components in each of the right-hand vectors above. Here we adopt the independent variables of a Helmholtz free energy, namely temperature and strain, but we do not employ his potential, preferring to retain the internal energy potential so as to ensure a proper incorporation of Maxwell's constraint.

Constitutive equations (59 & 60) take on the form of a hypo-elastic material model,⁶⁶ which is ideal for numerical implementation whenever one uses solution techniques like those presented in Part 5.

4.1.2 Material Response Functions

Experiments are performed for the purpose of characterizing material behavior. In mechanics, we relate measured material properties to gradients and curvatures of thermodynamic potentials, out of which material models are constructed. Experiments are typically done to quantify the following material properties, defined here as tangents to response curves, and selected per a material's physical dimension.

In 1D:

$$C_F := \frac{d\eta}{\theta^{-1} d\theta} \Big|_{dF=0} \quad \alpha_F := \frac{L^{-1} dL}{\theta^{-1} d\theta} \Big|_{dF=0} \quad E_\theta := \frac{dF}{L^{-1} dL} \Big|_{d\theta=0} \quad (61a)$$

In 2D:

$$C_T := \frac{d\eta}{\theta^{-1} d\theta} \Big|_{dT=0} \quad \alpha_T := \frac{A^{-1} dA}{\theta^{-1} d\theta} \Big|_{dT=0} = 2\alpha_F \quad M_\theta := \frac{dT}{A^{-1} dA} \Big|_{d\theta=0} \quad (61b)$$

In 3D:

$$C_P := \frac{d\eta}{\theta^{-1} d\theta} \Big|_{dP=0} \quad \alpha_P := \frac{V^{-1} dV}{\theta^{-1} d\theta} \Big|_{dP=0} = 3\alpha_F \quad K_\theta := \frac{-dP}{V^{-1} dV} \Big|_{d\theta=0} \quad (61c)$$

whose analogs as secant functions are defined in App. A.

The various thermal strain coefficients α_F , α_T , α_P are, however, distinct from one another. Even though each is dimensionless, each is defined with respect to its own physical dimension. Nevertheless, because $\ln(L/L_0) = \frac{1}{2}\ln(A/A_0) = \frac{1}{3}\ln(V/V_0)$, it follows that $\alpha_T = 2\alpha_F$ and $\alpha_P = 3\alpha_F$, so there is really just one thermal strain coefficient, i.e., α_F , that, hereafter, is denoted as α_t where the subscript 't' denotes *tangent**. It is noteworthy to point out that what one typically refers to as the coefficient of thermal expansion, i.e., α (1/K), is distinct from the thermal strain coefficient, viz., α_t (dimensionless); specifically, $\alpha_t = \alpha\theta_0$ for small temperature excursions, cf. App. A.

The various specific heats C_F , C_T , C_P (erg/g.K) are distinct, yet essentially, they are equivalent as each is defined per unit mass, insensitive to dimension. They are evaluated at a fixed thermodynamic force, which does depend upon dimension. Here-

*In App. A, subscript 't' is used to denote *tangent*; whereas, subscript 's' is used to denote *secant*, e.g., $dF = E_t de$ whereas $F = E_s e$. Here, the defined material properties are tangent properties. Secant properties, and their definitions, can be found in App. A. Both secant and tangent moduli are needed by the variational formulation put forward in Part 6.

after, we will denote the tangent response to specific heat as C_t that, in App. A, is shown to relate to the secant version of specific heat C_s via

$$1\text{D:} \quad C_t = C_s - \alpha_s \frac{F - F_0}{\rho_{1D}\theta} \quad (62\text{a})$$

$$2\text{D:} \quad C_t = C_s - \alpha_s \frac{\pi - \pi_0}{\rho_{2D}\theta} \quad (62\text{b})$$

$$3\text{D:} \quad C_t = C_s - \alpha_s \frac{\Pi - \Pi_0}{\rho_{3D}\theta} \quad (62\text{c})$$

where C_s is the density of specific heat at constant pressure that one typically finds tabulated in the literature. Usually, the secant and tangent versions for the thermal strain coefficient are equivalent, i.e., $\alpha_s \equiv \alpha_t$. Here F_0 , π_0 and Π_0 are the force, surface tension, and pressure associated with some specified reference state, i.e., it is in this state where their conjugate strains are assigned to zero, viz., $e_0 = 0$, $\xi_0 = 0$ and $\Xi_0 = 0$ even though $F_0 \neq 0$, $\pi_0 \neq 0$ and $\Pi_0 \neq 0$, in general.

The various tangent moduli E_θ , M_θ and K_θ are also distinct. They have different dimensions. Material property E_θ is a modulus of extension (dyne); material property M_θ is a modulus of dilation (dyne/cm); and material property K_θ is a modulus of dilatation (dyne/cm²), a.k.a. the bulk modulus, with each modulus being measured at a fixed temperature. Shear moduli are discussed later in Sections 4.2 & 4.3. The above material properties are gradients. They constitute tangents to their associated physical response curves, and as such, are denoted hereafter as E_t , M_t and K_t . Consequently, they need not be of constant value throughout state space, like a Hookean material would suppose them to be. In other words, the secant and tangent moduli need not be the same in any given state. This is an important characteristic for the hypo-elastic constructions of Eqns. (59 or 60), as they pertain to our application.

In terms of the material properties given in Eqn. (61), of which there are three per dimension, the internal energy density has three curvatures that associate with it. For 1D materials:

$$\partial_{\eta\eta}U = \frac{\rho_{1D}\theta^2}{\rho_{1D}C_t\theta - \alpha_t^2 E_t} \quad (63\text{a})$$

$$\partial_{ee}U = \frac{C_t E_t \theta}{\rho_{1D}C_t\theta - \alpha_t^2 E_t} \quad (63\text{b})$$

$$\partial_{\eta e}U \equiv \partial_{e\eta}U = \frac{-\alpha_t E_t \theta}{\rho_{1D}C_t\theta - \alpha_t^2 E_t} \quad (63\text{c})$$

For 2D materials:

$$\partial_{\eta\eta}U = \frac{\rho_{2D}\theta^2}{\rho_{2D}C_t\theta - 4\alpha_t^2M_t} \quad (63d)$$

$$\partial_{\xi\xi}U = \frac{4C_tM_t\theta}{\rho_{2D}C_t\theta - 4\alpha_t^2M_t} \quad (63e)$$

$$\partial_{\eta\xi}U \equiv \partial_{\xi\eta}U = \frac{-4\alpha_tM_t\theta}{\rho_{2D}C_t\theta - 4\alpha_t^2M_t} \quad (63f)$$

For 3D materials (cf. Weinhold⁶⁴ and Gilmore⁶⁵):

$$\partial_{\eta\eta}U = \frac{\rho_{3D}\theta^2}{\rho_{3D}C_t\theta - 9\alpha_t^2K_t} \quad (63g)$$

$$\partial_{\Xi\Xi}U = \frac{9C_tK_t\theta}{\rho_{3D}C_t\theta - 9\alpha_t^2K_t} \quad (63h)$$

$$\partial_{\eta\Xi}U \equiv \partial_{\Xi\eta}U = \frac{-9\alpha_tK_t\theta}{\rho_{3D}C_t\theta - 9\alpha_t^2K_t} \quad (63i)$$

These materials constants are constrained by thermodynamics in that

$$0 < E_t < \frac{\rho_{1D}C_t\theta}{\alpha_t^2}, \quad 0 < M_t < \frac{\rho_{2D}C_t\theta}{4\alpha_t^2}, \quad 0 < K_t < \frac{\rho_{3D}C_t\theta}{9\alpha_t^2} \quad (64)$$

which ensure that their respective thermodynamic Jacobians cannot become singular. Singularities can and do occur, e.g., during a phase change in a crystal,^{54,65} but such processes are not expected to arise in our application.

4.1.3 Thermoelastic Models for Modeling Alveoli: Uniform Motions

We now write down our constitutive formulæ for quantifying uniform responses in thermoelastic solids of 1, 2 and 3 dimensions. They are thermoelastic constitutive equations (60) with Helmholtz variables expressed in terms of the material properties defined in Eqn. (61) assigned to the internal energy density U according to

Eqn. (63), with outcomes of:

$$\text{For 1D: } \begin{Bmatrix} d\eta \\ dF \end{Bmatrix} = \begin{bmatrix} C_t - \alpha_t^2 E_t / \rho\theta & \alpha_t E_t / \rho\theta \\ -\alpha_t E_t & E_t \end{bmatrix} \begin{Bmatrix} \theta^{-1} d\theta \\ de \end{Bmatrix} \quad (65a)$$

$$\text{For 2D: } \begin{Bmatrix} d\eta \\ d\pi \end{Bmatrix} = \begin{bmatrix} C_t - 4\alpha_t^2 M_t / \rho\theta & 4\alpha_t M_t / \rho\theta \\ -4\alpha_t M_t & 4M_t \end{bmatrix} \begin{Bmatrix} \theta^{-1} d\theta \\ d\xi \end{Bmatrix} \quad (65b)$$

$$\text{For 3D: } \begin{Bmatrix} d\eta \\ d\Pi \end{Bmatrix} = \begin{bmatrix} C_t - 9\alpha_t^2 K_t / \rho\theta & 9\alpha_t K_t / \rho\theta \\ -9\alpha_t K_t & 9K_t \end{bmatrix} \begin{Bmatrix} \theta^{-1} d\theta \\ d\Xi \end{Bmatrix} \quad (65c)$$

where we simplify our expressions by suppressing the dimension for which mass density applies. This is considered to be understood. There are four material properties for each dimension (e.g., for 1D materials they are: ρ , C_t , α_t and E_t) with the latter three being tangent properties defined according to Eqn. (61).

The upper-left element in each matrix of Eqn. (65) represents a heat capacity evaluated at constant strain—a material property not easily measured. Whereas, the specific heat evaluated at constant pressure (viz., the C_s found in the 11 matrix component of these tangent moduli, as established in Eqn. 62) is more amenable to experiments, and is the property that one typically finds in published data tables.

Constitutive equations (65a–65c), derived here from the First and Second Laws of Thermodynamics, describe thermoelastic materials undergoing uniform motions through adiabatic processes. They present themselves as hypo-elastic material models,⁶⁶ which are often preferred for incorporating constitutive equations into finite element packages.

Equation (65) has cause and effect variables that are appropriate for our multiscale application. In this process, a localization procedure pulls the temperature θ and deformation gradient \mathbf{F} taken from the parenchyma scale (e.g., Gauss points in a finite element grid of lung) down to the level of an alveolar scale (in our modeling, a dodecahedron). Differential strain rates $d\mathcal{U} \cdot \mathcal{U}^{-1}$ are then constructed through appropriate finite difference formulæ, where \mathcal{U} denotes the Laplace stretch.⁴³ These continuum rates are then mapped into our local thermodynamic rates, with alveolar entropy and stress following from a numerical integration of the above constitutive equations. These constitutive equations apply to the various facets of our dodecahedral model for an alveolar sac through a finite element discretization. Afterwards, an homogenization procedure takes the updated alveolar entropy and nodal trac-

tions, and pushes them up to the continuum level as averaged parenchymal entropy and parenchymal stresses.

4.2. Green Thermoelastic Membranes: Non-Uniform Motions

The First and Second Laws of Thermodynamics governing a reversible adiabatic process are described by the formula $dU = \theta d\eta + \frac{1}{\rho} dW$, where dW is the mechanical power expended by stressing a material element of mass density ρ . For the case of a 2D planar membrane, a mass density of $\rho \Leftarrow \rho_{2D}$ applies, with its change in mechanical work being expressed as^{42,52,53}

$$dW = \text{tr} \left(\begin{bmatrix} \mathcal{S}_{11} & \mathcal{S}_{12} \\ \mathcal{S}_{21} & \mathcal{S}_{22} \end{bmatrix} \begin{bmatrix} a^{-1} da & (a/b) dg \\ 0 & b^{-1} db \end{bmatrix} \right) = \pi d\xi + \sigma d\varepsilon + \tau d\gamma \quad (66a)$$

wherein \mathcal{S}_{ij} are the components of a surface tension evaluated in the co-ordinate frame of a membrane. (In Section 4.5 they will be converted into components of the Eulerian Kirchhoff stress and the Lagrangian, second, Piola-Kirchhoff stress.)

Equation (66a) conjectures that the First and Second Laws of Thermodynamics can be expressed as a differential equation known as a Pfaffian form that, in this case, looks like

$$dU = \theta d\eta + \frac{1}{\rho} (\pi d\xi + \sigma d\varepsilon + \tau d\gamma) \quad (66b)$$

where $\{\pi, \sigma, \tau\}$ describes a set of intensive scalar-valued stresses whose thermodynamic conjugates $\{\xi, \varepsilon, \gamma\}$ describe a set of extensive scalar-valued strains. This contrasts with the classic approach, where the work done is decomposed into a scalar-valued isotropic part and a tensor-valued deviatoric part. The above thermodynamic strains are defined in Section 3.3.6.1, while their conjugate stresses, and how they relate to the tensor components of stress, are discussed in Section 4.5.

Conjugate pair (ξ, π) describes a dilation $2 d\xi \Leftarrow A^{-1} dA$ caused by a surface tension $\pi \Leftarrow 2T$ where $\xi := \ln \sqrt{A/A_0}$ and $\pi := \mathcal{S}_{11} + \mathcal{S}_{22}$. This pair describes the uniform contribution to stress power discussed in Section 4.1. Pair (ε, σ) describes a squeeze ε (or pure shear) caused by a normal-stress difference $\sigma := \mathcal{S}_{11} - \mathcal{S}_{22}$. And pair (γ, τ) describes an in-plane shear γ caused by a shear stress τ . Collectively, pairs (ε, σ) and (γ, τ) account for any non-uniform contributions to stress power, i.e., contributions from other than uniform dilation. These pairs are quantified in

Section 4.4.

4.2.1 General Constitutive Equations

Because a change in the internal energy dU governing a reversible adiabatic process is described by an exact differential,⁵⁹ with $U(\eta, \xi, \varepsilon, \gamma)$ in the case of a planar membrane, it follows that a constitutive response for a Green thermoelastic membrane is described by

$$\begin{aligned}\theta &= \partial_\eta U(\eta, \xi, \varepsilon, \gamma) & \pi &= \rho \partial_\xi U(\eta, \xi, \varepsilon, \gamma) \\ \sigma &= \rho \partial_\varepsilon U(\eta, \xi, \varepsilon, \gamma) & \tau &= \rho \partial_\gamma U(\eta, \xi, \varepsilon, \gamma).\end{aligned}\tag{67}$$

Considering each intensive variable, viz., θ , π , σ and τ , to be at least a C^1 function of the set of extensive variables $(\eta, \xi, \varepsilon, \gamma)$, thereby implies that the internal energy U is at least a C^2 function of state. Therefore, the constitutive expressions in Eqn. (67) can be recast into the following system of differential equations

$$\begin{Bmatrix} d\theta \\ d\pi \\ d\sigma \\ d\tau \end{Bmatrix} = \begin{bmatrix} \partial_{\eta\eta} U & \partial_{\eta\xi} U & \partial_{\eta\varepsilon} U & \partial_{\eta\gamma} U \\ \rho \partial_{\xi\eta} U & \rho \partial_{\xi\xi} U & \rho \partial_{\xi\varepsilon} U & \rho \partial_{\xi\gamma} U \\ \rho \partial_{\varepsilon\eta} U & \rho \partial_{\varepsilon\xi} U & \rho \partial_{\varepsilon\varepsilon} U & \rho \partial_{\varepsilon\gamma} U \\ \rho \partial_{\gamma\eta} U & \rho \partial_{\gamma\xi} U & \rho \partial_{\gamma\varepsilon} U & \rho \partial_{\gamma\gamma} U \end{bmatrix} \begin{Bmatrix} d\eta \\ d\xi \\ d\varepsilon \\ d\gamma \end{Bmatrix} \tag{68}$$

whose upper-left 2×2 sub-matrix also appears in Eqn. (59b), which governs the uniform contribution of a response. The above 4×4 matrix describes the full non-uniform response permissible by a Green thermoelastic membrane undergoing an adiabatic process.

For our application, it is reasonable to assume that the presence of a non-uniform planar motion will not cause an uniform planar response. Said differently, it is reasonable to assume that pure ε and simple γ shears will not effect a change in either temperature θ or surface tension π . As such, $\partial_{\eta\varepsilon} U = \partial_{\eta\gamma} U = \partial_{\xi\varepsilon} U = \partial_{\xi\gamma} U = 0$, and Eqn. (68) simplifies to

$$\begin{Bmatrix} d\theta \\ d\pi \\ d\sigma \\ d\tau \end{Bmatrix} = \begin{bmatrix} \partial_{\eta\eta} U & \partial_{\eta\xi} U & 0 & 0 \\ \rho \partial_{\xi\eta} U & \rho \partial_{\xi\xi} U & 0 & 0 \\ 0 & 0 & \rho \partial_{\varepsilon\varepsilon} U & \rho \partial_{\varepsilon\gamma} U \\ 0 & 0 & \rho \partial_{\gamma\varepsilon} U & \rho \partial_{\gamma\gamma} U \end{bmatrix} \begin{Bmatrix} d\eta \\ d\xi \\ d\varepsilon \\ d\gamma \end{Bmatrix}$$

with $\partial_{\varepsilon\eta}U = \partial_{\gamma\eta}U = \partial_{\varepsilon\xi}U = \partial_{\gamma\xi}U = 0$ following because of Maxwell's relationships. Furthermore, it is considered that the pure and simple shear responses act independently, too, so that $\partial_{\gamma\varepsilon}U = \partial_{\varepsilon\gamma}U = 0$.^{*} Converting the above internal energy formulation into its Helmholtz equivalent produces two uncoupled matrix equations; they are,

$$\begin{Bmatrix} d\eta \\ d\pi \end{Bmatrix} = \begin{bmatrix} \theta/\partial_{\eta\eta}U & -\partial_{\eta\xi}U/\partial_{\eta\eta}U \\ \rho\theta \partial_{\xi\eta}U/\partial_{\eta\eta}U & \rho(\partial_{\xi\xi}U - \partial_{\xi\eta}U \cdot \partial_{\eta\xi}U/\partial_{\eta\eta}U) \end{bmatrix} \begin{Bmatrix} \theta^{-1} d\theta \\ d\xi \end{Bmatrix} \quad (69a)$$

where both $\theta^{-1} d\theta$ and $d\xi = \frac{1}{2}A^{-1} dA$ are logarithmic rates, and

$$\begin{Bmatrix} d\sigma \\ d\tau \end{Bmatrix} = \rho \begin{bmatrix} \partial_{\varepsilon\varepsilon}U & 0 \\ 0 & \partial_{\gamma\gamma}U \end{bmatrix} \begin{Bmatrix} d\varepsilon \\ d\gamma \end{Bmatrix} \quad (69b)$$

where $d\varepsilon = \Gamma^{-1} d\Gamma$ is also logarithmic in structure, while $d\gamma = dg$ is linear in its deformation field. All diagonal based strains are logarithmic, while all off-diagonal based strains are linear in our conjugate pair approach. The result is a general theoretical structure for a Green thermoelastic membrane appropriate for our application.

Note: The uniform response (Eqn. 69a) and the non-uniform response (Eqn. 69b) are, by supposition, decoupled in this constitutive construction. There is experimental evidence that the bulk and shear moduli of parenchyma both depend upon transpulmonary pressure.^{67,68} It is conjectured that this is a structural effect of alveolar geometry; it is not a characteristic of the constituents that comprise an alveolus. As such, we do not couple the uniform and non-uniform responses in the constitutive framework of Eqn. (69) at this time in order that we may test this conjecture.

4.2.2 Material Response Functions

The material model put forward here for a thermoelastic membrane has a mass density per unit area of ρ and five material properties that appear as tangent functions: a specific heat C_t at constant tension, a lineal thermal strain coefficient α_t at constant tension, an areal modulus M_t at constant temperature, a squeeze modulus N_t at

*There is a second-order coupling that can exist between the modes of squeeze and shear in a 3D solid. It is the Poynting effect,⁵³ but this effect is thought not to arise to a level of significance in a 2D membrane.

constant shear, and a shear modulus G_t at constant squeeze. The density of specific heat C_t is defined as

$$C_t := \frac{d\eta}{\theta^{-1} d\theta} \Big|_T = \frac{d\eta}{\theta^{-1} d\theta} \Big|_\pi \quad (70a)$$

where θ is temperature, η is entropy density, and $\pi = \mathcal{S}_{11} + \mathcal{S}_{22} = 2T$ is the surface tension acting in a membrane. C_t is commonly referred to in the literature as the specific heat at constant pressure. The lineal thermal strain coefficient α_t is defined as

$$\alpha_t := \frac{L^{-1} dL}{\theta^{-1} d\theta} \Big|_T = \frac{1}{2} \frac{A^{-1} dA}{\theta^{-1} d\theta} \Big|_T = \frac{d\xi}{\theta^{-1} d\theta} \Big|_\pi \quad (70b)$$

which is a dimensionless material property. Here $A = ab$ denotes a relative area with $\xi = \ln \sqrt{A/A_0}$ being the areal strain, a.k.a. dilation. This property is not the thermal expansion coefficient commonly used in the literature, which has dimensions of reciprocal temperature, cf. App. A. The associated, uniform, areal modulus M_t is defined as

$$M_t := \frac{dT}{A^{-1} dA} \Big|_\theta = \frac{d\frac{1}{2}(\mathcal{S}_{11} + \mathcal{S}_{22})}{A^{-1} dA} \Big|_\theta = \frac{1}{4} \frac{d\pi}{d\xi} \Big|_\theta \quad (70c)$$

which is the 2D version of a 3D bulk modulus. A new modulus introduced by Freed *et al.*,⁵² which they call the in-plane squeeze modulus N_t , is defined as

$$N_t := \frac{dN_1}{\Gamma^{-1} d\Gamma} \Big|_g = \frac{d(\mathcal{S}_{11} - \mathcal{S}_{22})}{\Gamma^{-1} d\Gamma} \Big|_g = \frac{1}{2} \frac{d\sigma}{d\varepsilon} \Big|_\gamma \quad (70d)$$

where $\sigma = \mathcal{S}_{11} - \mathcal{S}_{22}$ is a normal-stress difference, often denoted as N_1 in the polymers literature, and where $\Gamma = a/b$ is the stretch of squeeze with $\varepsilon = \ln \sqrt{\Gamma/\Gamma_0}$ being the strain of squeeze, while $\gamma = g - g_0$ determines the shear strain. Finally, an in-plane shear modulus G_t is defined as

$$G_t := \frac{1}{\Gamma} \frac{d\mathcal{S}_{21}}{dg} \Big|_\Gamma = \frac{d\tau}{d\gamma} \Big|_\varepsilon \quad (70e)$$

where $\tau := \Gamma \mathcal{S}_{21}$ establishes the shear stress, recalling that $\varepsilon = \ln(\Gamma/\Gamma_0)$.

4.2.3 Constitutive Equations Governing a Thermoelastic Membrane

It is the Gibbs free-energy potential (viz., $\mathcal{G}(\theta, \pi, \sigma, \tau) = U - \theta\eta - \pi\xi - \sigma\varepsilon - \tau\gamma$, which exchanges cause and effect with that of the internal energy $U(\eta, \xi, \varepsilon, \gamma)$), that is most easily expressed in terms of the above material properties, cf. App. A; specifically,

$$\begin{Bmatrix} d\eta \\ d\xi \\ d\varepsilon \\ d\gamma \end{Bmatrix} = - \begin{bmatrix} \partial_{\theta\theta}\mathcal{G} & \partial_{\theta\pi}\mathcal{G} & 0 & 0 \\ \rho\partial_{\pi\theta}\mathcal{G} & \rho\partial_{\pi\pi}\mathcal{G} & 0 & 0 \\ 0 & 0 & \rho\partial_{\sigma\sigma}\mathcal{G} & 0 \\ 0 & 0 & 0 & \rho\partial_{\tau\tau}\mathcal{G} \end{bmatrix} \begin{Bmatrix} d\theta \\ d\pi \\ d\sigma \\ d\tau \end{Bmatrix}$$

where $\partial_{\theta\pi}\mathcal{G} = \partial_{\pi\theta}\mathcal{G}$ from Maxwell's constraint. Incorporating the material property definitions put forward in Eqn. (70) into the above differential equation leads to

$$\begin{Bmatrix} d\eta \\ d\xi \\ d\varepsilon \\ d\gamma \end{Bmatrix} = \begin{bmatrix} C_t & \alpha_t/\rho\theta & 0 & 0 \\ \alpha_t & 1/4M_t & 0 & 0 \\ 0 & 0 & 1/2N_t & 0 \\ 0 & 0 & 0 & 1/G_t \end{bmatrix} \begin{Bmatrix} \theta^{-1}d\theta \\ d\pi \\ d\sigma \\ d\tau \end{Bmatrix}$$

where gradients $\partial\eta/\partial\theta$, $\partial\xi/\partial\theta$ and $\partial\pi/\partial\xi$ relate to the material properties through $\partial_{\theta\theta}\mathcal{G} = \partial\eta/\partial\theta$, $\rho\partial_{\pi\theta}\mathcal{G} = \partial\xi/\partial\theta = \rho\partial_{\theta\pi}\mathcal{G}$ and $\rho\partial_{\pi\pi}\mathcal{G} = \partial\xi/\partial\pi = (\partial\pi/\partial\xi)^{-1}$. The upper-left 2×2 sub-matrix, which describes the uniform contribution to a response, can be rearranged to read as

$$\begin{Bmatrix} d\eta \\ d\pi \end{Bmatrix} = \begin{bmatrix} C_t - 4\alpha_t^2 M / \rho\theta & 4\alpha_t M / \rho\theta \\ -4\alpha_t M & 4M \end{bmatrix} \begin{Bmatrix} \theta^{-1}d\theta \\ d\xi \end{Bmatrix} \quad (71a)$$

where $M = M_t(\theta, \xi, \pi)$, while the non-uniform or shear response of Eqn. (69b) is given quite simply by

$$\begin{Bmatrix} d\sigma \\ d\tau \end{Bmatrix} = \begin{bmatrix} 2N & 0 \\ 0 & G \end{bmatrix} \begin{Bmatrix} d\varepsilon \\ d\gamma \end{Bmatrix} \quad (71b)$$

where $N = N_t(\varepsilon, \sigma)$ and $G = G_t(\gamma, \tau)$. Collectively, moduli M_t , N_t and G_t describe the mechanical response of a thermoelastic membrane. These moduli can depend upon both stress and strain, in accordance with the implicit theory of elasticity presented in App. A.

4.2.3.1 The Poisson Effect

The areal modulus M_t is ideally determined from an equibiaxial experiment. Assuming knowledge of its value, then given the following definition for an areal Poisson's ratio

$$\nu := -\frac{db/b}{da/a}$$

it immediately follows that the squeeze modulus N_t can be determined from an uniaxial experiment where traction is applied along that axis from which elongation a is measured; specifically,

$$N_t = 2M_t \frac{1 - \nu}{1 + \nu} \quad \text{given that } S_{11} \neq 0 \quad \text{and} \quad S_{21} = S_{22} = 0$$

provided that the temperature θ is held constant. Consequently, $\frac{2}{3}M_t \leq N_t \leq 2M_t$ follows provided that $0 \leq \nu \leq \frac{1}{2}$, so the squeeze modulus N_t is observed to play an analogous role as the shear modulus μ found in the classical theory of elasticity.

If one were to consider such a membrane as having uniform thickness h that varies with deformation so as to preserve its volume, then $\nu = \frac{1}{2}$ and Eqn. (71b) would become

$$\begin{Bmatrix} d\sigma \\ d\tau \end{Bmatrix} = \begin{bmatrix} 4M_t/3 & 0 \\ 0 & G_t \end{bmatrix} \begin{Bmatrix} d\varepsilon \\ d\gamma \end{Bmatrix} \quad (71c)$$

which is a useful result, as now there are just two moduli to establish through experiments, viz., M_t and G_t .

Note: The conjugate pair approach presented here allows for a distinct shear modulus G that can take on any positive value. This is important because shear experiments done on soft tissues, which, unfortunately, are few in number, tend to produce shear moduli that are many orders in magnitude smaller than their bulk moduli, e.g., in parenchyma their ratio is $K/G \approx 10^4$ (150 MPa vs. 10–54 kPa).⁶⁹ Classically, such a result has been used to argue that a material can be modeled, to a reasonable approximation, as being ideally incompressible—a 3D notion. The idea of modeling parenchyma as an incompressible material is in complete opposition with its true physiologic nature. Such an assumption is no longer necessary to make when adopting the conjugate pair approach adopted here and elsewhere.^{1,2,42,43,52,53,58}

4.3. Green Thermoelastic Solids: Non-Uniform Motions

The First and Second Laws of Thermodynamics governing a reversible adiabatic process done on a 3D body result in the formula $dU = \theta d\eta + \frac{1}{\rho} dW$, where dW is the mechanical power expended by stressing a body with mass density ρ , specifically^{42,52,53}

$$\begin{aligned} dW &= \text{tr} \left(\begin{bmatrix} \mathcal{S}_{11} & \mathcal{S}_{12} & \mathcal{S}_{13} \\ \mathcal{S}_{21} & \mathcal{S}_{22} & \mathcal{S}_{23} \\ \mathcal{S}_{31} & \mathcal{S}_{32} & \mathcal{S}_{33} \end{bmatrix} \begin{bmatrix} a^{-1} da & (a/b) d\gamma & (a/c)(d\beta - \alpha d\gamma) \\ 0 & b^{-1} db & (b/c) d\alpha \\ 0 & 0 & c^{-1} dc \end{bmatrix} \right) \\ &= \Pi d\Xi + \sum_{i=1}^3 (\sigma_i d\varepsilon_i + \tau_i d\gamma_i) \end{aligned} \quad (72a)$$

which is subject to constraints $\sigma_3 = -(\sigma_1 + \sigma_2)$ and $d\varepsilon_3 = -(d\varepsilon_1 + d\varepsilon_2)$. Consequently, six of the seven conjugate pairs in this formulation are independent, as one ought to expect. Stress components \mathcal{S}_{ij} can be either rotated into the Kirchhoff stress of an Eulerian frame, or they can be pulled back into the second Piola-Kirchhoff stress of a Lagrangian frame, as established in Section 4.5.

The above expression conjectures that the thermodynamics of a 3D elastic solid contained within the confines of an adiabatic enclosure can be described by the Pfaffian equation

$$dU = \theta d\eta + \frac{1}{\rho} \left(\Pi d\Xi + \sum_{i=1}^2 \sigma_i d\varepsilon_i + (\sigma_1 + \sigma_2)(d\varepsilon_1 + d\varepsilon_2) + \sum_{i=1}^3 \tau_i d\gamma_i \right) \quad (72b)$$

where stresses $\{\Pi, \sigma_1, \sigma_2, \tau_1, \tau_2, \tau_3\}$ describe a set of independent, scalar-valued, intensive variables, and where strains $\{\Xi, \varepsilon_1, \varepsilon_2, \gamma_1, \gamma_2, \gamma_3\}$ describe a set of independent, scalar-valued, extensive variables. This contrasts with the classic approach where the work done decomposes into a scalar-valued isotropic part and a tensor-valued deviatoric part. A direct consequence of adopting a triangular construction for strain rate is that the pure- and simple-shear contributions of a deviatoric response can be further separated into independent scalar contributions that are nearly orthogonal to one another; whereas, they remain coupled into one tensor field whenever a symmetric construction for strain rate is adopted, which is standard practice today. The above thermodynamic strains are defined in Section 3.4.1.1, while their conjugate stresses and how they relate to commonly used stress tensors is discussed

later in Section 4.5.

4.3.1 Constitutive Equations

Because a change in the internal energy dU governing a reversible adiabatic process is described by an exact differential,⁵⁹ with $U(\eta, \Xi, \varepsilon_1, \varepsilon_2, \gamma_1, \gamma_2, \gamma_3)$ in three space, it necessarily follows that a constitutive response for a Green thermoelastic solid is governed by a constitutive equation for temperature⁵⁸

$$\theta = \partial_\eta U(\eta, \Xi, \varepsilon_1, \varepsilon_2, \gamma_1, \gamma_2, \gamma_3) \quad (73a)$$

a constitutive equation for pressure

$$\Pi = \rho \partial_\Xi U(\eta, \Xi, \varepsilon_1, \varepsilon_2, \gamma_1, \gamma_2, \gamma_3) \quad (73b)$$

two constitutive equations for the normal-stress differences

$$\begin{Bmatrix} \sigma_1 \\ \sigma_2 \end{Bmatrix} = \frac{1}{3} \begin{bmatrix} 2 & -1 \\ -1 & 2 \end{bmatrix} \begin{Bmatrix} \rho \partial_{\varepsilon_1} U(\eta, \Xi, \varepsilon_1, \varepsilon_2, \gamma_1, \gamma_2, \gamma_3) \\ \rho \partial_{\varepsilon_2} U(\eta, \Xi, \varepsilon_1, \varepsilon_2, \gamma_1, \gamma_2, \gamma_3) \end{Bmatrix} \quad (73c)$$

and three constitutive equations for the shear stresses

$$\tau_1 = \rho \partial_{\gamma_1} U(\eta, \Xi, \varepsilon_1, \varepsilon_2, \gamma_1, \gamma_2, \gamma_3) \quad (73d)$$

$$\tau_2 = \rho \partial_{\gamma_2} U(\eta, \Xi, \varepsilon_1, \varepsilon_2, \gamma_1, \gamma_2, \gamma_3) \quad (73e)$$

$$\tau_3 = \rho \partial_{\gamma_3} U(\eta, \Xi, \varepsilon_1, \varepsilon_2, \gamma_1, \gamma_2, \gamma_3) \quad (73f)$$

where the coupled expressions for the two squeeze stresses in Eqn. (73c) arise from the energetic contribution

$$\partial_{\varepsilon_1} U d\varepsilon_1 + \partial_{\varepsilon_2} U d\varepsilon_2 = \sigma_1 d\varepsilon_1 + \sigma_2 d\varepsilon_2 + (\sigma_1 + \sigma_2)(d\varepsilon_1 + d\varepsilon_2)$$

that incorporates constraints $\sigma_3 = -(\sigma_1 + \sigma_2)$ and $d\varepsilon_3 = -(d\varepsilon_1 + d\varepsilon_2)$ into the work done, viz., $\sigma_3 d\varepsilon_3$ does work, and as such, conjugate pair $(\sigma_3, \varepsilon_3)$ has an influence on constitutive response, even though they are not independent variables.

Considering each, independent, intensive variable, i.e., $\theta, \Pi, \sigma_1, \sigma_2, \tau_1, \tau_2, \tau_3$, to be a C^1 function of each, independent, extensive variable, viz., $\eta, \Xi, \varepsilon_1, \varepsilon_2, \gamma_1, \gamma_2, \gamma_3$, then the internal energy U must be a C^2 function of state, and the constitutive ex-

DRAFT: UNCLASSIFIED

pressions in Eqn. (73) can be recast into the following system of differential equations

$$\begin{Bmatrix} d\theta \\ d\Pi \\ d\sigma_1 \\ d\sigma_2 \\ d\tau_1 \\ d\tau_2 \\ d\tau_3 \end{Bmatrix} = \begin{bmatrix} \partial_{\eta\eta}U & \partial_{\eta\Xi}U & \partial_{\eta\varepsilon_1}U & \partial_{\eta\varepsilon_2}U & \partial_{\eta\gamma_1}U & \partial_{\eta\gamma_2}U & \partial_{\eta\gamma_3}U \\ \rho\partial_{\Xi\eta}U & \rho\partial_{\Xi\Xi}U & \rho\partial_{\Xi\varepsilon_1}U & \rho\partial_{\Xi\varepsilon_2}U & \rho\partial_{\Xi\gamma_1}U & \rho\partial_{\Xi\gamma_2}U & \rho\partial_{\Xi\gamma_3}U \\ \rho M_{1\eta} & \rho M_{1\Xi} & \rho M_{1\varepsilon_1} & \rho M_{1\varepsilon_2} & \rho M_{1\gamma_1} & \rho M_{1\gamma_2} & \rho M_{1\gamma_3} \\ \rho M_{2\eta} & \rho M_{2\Xi} & \rho M_{2\varepsilon_1} & \rho M_{2\varepsilon_2} & \rho M_{2\gamma_1} & \rho M_{2\gamma_2} & \rho M_{2\gamma_3} \\ \rho\partial_{\gamma_1\eta}U & \rho\partial_{\gamma_1\Xi}U & \rho\partial_{\gamma_1\varepsilon_1}U & \rho\partial_{\gamma_1\varepsilon_2}U & \rho\partial_{\gamma_1\gamma_1}U & \rho\partial_{\gamma_1\gamma_2}U & \rho\partial_{\gamma_1\gamma_3}U \\ \rho\partial_{\gamma_2\eta}U & \rho\partial_{\gamma_2\Xi}U & \rho\partial_{\gamma_2\varepsilon_1}U & \rho\partial_{\gamma_2\varepsilon_2}U & \rho\partial_{\gamma_2\gamma_1}U & \rho\partial_{\gamma_2\gamma_2}U & \rho\partial_{\gamma_2\gamma_3}U \\ \rho\partial_{\gamma_3\eta}U & \rho\partial_{\gamma_3\Xi}U & \rho\partial_{\gamma_3\varepsilon_1}U & \rho\partial_{\gamma_3\varepsilon_2}U & \rho\partial_{\gamma_3\gamma_1}U & \rho\partial_{\gamma_3\gamma_2}U & \rho\partial_{\gamma_3\gamma_3}U \end{bmatrix} \begin{Bmatrix} d\eta \\ d\Xi \\ d\varepsilon_1 \\ d\varepsilon_2 \\ d\gamma_1 \\ d\gamma_2 \\ d\gamma_3 \end{Bmatrix} \quad (74)$$

whose upper-left 2×2 sub-matrix also appears in Eqn. (59c), which governs the uniform contribution of a response. The squeeze response of Eqn. (73c) associates with tangent moduli that are defined accordingly

$$M_{1\eta} = \frac{1}{3}(2\partial_{\varepsilon_1\eta}U - \partial_{\varepsilon_2\eta}U) \quad M_{2\eta} = \frac{1}{3}(2\partial_{\varepsilon_2\eta}U - \partial_{\varepsilon_1\eta}U) \quad (75a)$$

$$M_{1\Xi} = \frac{1}{3}(2\partial_{\varepsilon_1\Xi}U - \partial_{\varepsilon_2\Xi}U) \quad M_{2\Xi} = \frac{1}{3}(2\partial_{\varepsilon_2\Xi}U - \partial_{\varepsilon_1\Xi}U) \quad (75b)$$

$$M_{1\varepsilon_1} = \frac{1}{3}(2\partial_{\varepsilon_1\varepsilon_1}U - \partial_{\varepsilon_2\varepsilon_1}U) \quad M_{2\varepsilon_1} = \frac{1}{3}(2\partial_{\varepsilon_2\varepsilon_1}U - \partial_{\varepsilon_1\varepsilon_1}U) \quad (75c)$$

$$M_{1\varepsilon_2} = \frac{1}{3}(2\partial_{\varepsilon_1\varepsilon_2}U - \partial_{\varepsilon_2\varepsilon_2}U) \quad M_{2\varepsilon_2} = \frac{1}{3}(2\partial_{\varepsilon_2\varepsilon_2}U - \partial_{\varepsilon_1\varepsilon_2}U) \quad (75d)$$

$$M_{1\gamma_1} = \frac{1}{3}(2\partial_{\varepsilon_1\gamma_1}U - \partial_{\varepsilon_2\gamma_1}U) \quad M_{2\gamma_1} = \frac{1}{3}(2\partial_{\varepsilon_2\gamma_1}U - \partial_{\varepsilon_1\gamma_1}U) \quad (75e)$$

$$M_{1\gamma_2} = \frac{1}{3}(2\partial_{\varepsilon_1\gamma_2}U - \partial_{\varepsilon_2\gamma_2}U) \quad M_{2\gamma_2} = \frac{1}{3}(2\partial_{\varepsilon_2\gamma_2}U - \partial_{\varepsilon_1\gamma_2}U) \quad (75f)$$

$$M_{1\gamma_3} = \frac{1}{3}(2\partial_{\varepsilon_1\gamma_3}U - \partial_{\varepsilon_2\gamma_3}U) \quad M_{2\gamma_3} = \frac{1}{3}(2\partial_{\varepsilon_2\gamma_3}U - \partial_{\varepsilon_1\gamma_3}U) \quad (75g)$$

so that, collectively, Eqns. (74 & 75) describe the full non-uniform response permissible by a Green thermoelastic solid expressed as a hypo-elastic material undergoing an adiabatic process.

As in the case of membranes, it is reasonable to assume that the presence of a non-uniform motion will not cause an uniform response. For our application, it is also reasonable to assume that there is no coupling between the modes of squeeze and shear.* Furthermore, it is assumed that there is no coupling betwixt the two independent squeeze modes, nor between the three independent shear modes. Consequently, all mixed partial derivatives that associate with a non-uniform response

*The Poynting effect is a second-order effect that couples squeeze and shear.⁵³ It is assumed that such a coupling does not play a contributing role in the current application, and can therefore be neglected.

are taken to be zero, and therefore Eqns. (74 & 75) simplify to

$$\begin{aligned} & \left\{ d\theta \quad d\Pi \quad d\sigma_1 \quad d\sigma_2 \quad d\tau_1 \quad d\tau_2 \quad d\tau_3 \right\}^\top \\ = & \begin{bmatrix} \partial_{\eta\eta}U & \partial_{\eta\Xi}U & 0 & 0 & 0 & 0 & 0 \\ \rho\partial_{\Xi\eta}U & \rho\partial_{\Xi\Xi}U & 0 & 0 & 0 & 0 & 0 \\ 0 & 0 & \rho\frac{2}{3}\partial_{\varepsilon_1\varepsilon_1}U & -\rho\frac{1}{3}\partial_{\varepsilon_2\varepsilon_2}U & 0 & 0 & 0 \\ 0 & 0 & -\rho\frac{1}{3}\partial_{\varepsilon_1\varepsilon_1}U & \rho\frac{2}{3}\partial_{\varepsilon_2\varepsilon_2}U & 0 & 0 & 0 \\ 0 & 0 & 0 & 0 & \rho\partial_{\gamma_1\gamma_1}U & 0 & 0 \\ 0 & 0 & 0 & 0 & 0 & \rho\partial_{\gamma_2\gamma_2}U & 0 \\ 0 & 0 & 0 & 0 & 0 & 0 & \rho\partial_{\gamma_3\gamma_3}U \end{bmatrix} \begin{Bmatrix} d\eta \\ d\Xi \\ d\varepsilon_1 \\ d\varepsilon_2 \\ d\gamma_1 \\ d\gamma_2 \\ d\gamma_3 \end{Bmatrix} \end{aligned}$$

where what may appear as being a coupling between $d\sigma_1$ and $d\sigma_2$ is actually a consequence arising from the two constraint equations $d\sigma_3 = -(d\sigma_1 + d\sigma_2)$ and $d\varepsilon_3 = -(d\varepsilon_1 + d\varepsilon_2)$.

The above system of equations can be rewritten as three independent systems of differential equations; specifically, the first differential matrix equation is

$$\begin{Bmatrix} d\theta \\ d\Pi \end{Bmatrix} = \begin{bmatrix} \partial_{\eta\eta}U & \partial_{\eta\Xi}U \\ \rho\partial_{\Xi\eta}U & \rho\partial_{\Xi\Xi}U \end{bmatrix} \begin{Bmatrix} d\eta \\ d\Xi \end{Bmatrix}$$

that when rewritten in terms of Helmholtz state variables becomes

$$\begin{Bmatrix} d\eta \\ d\Pi \end{Bmatrix} = \begin{bmatrix} \theta/\partial_{\eta\eta}U & -\partial_{\eta\Xi}U/\partial_{\eta\eta}U \\ \rho\theta\partial_{\Xi\eta}U/\partial_{\eta\eta}U & \rho(\partial_{\Xi\Xi}U - \partial_{\Xi\eta}U \cdot \partial_{\eta\Xi}U/\partial_{\eta\eta}U) \end{bmatrix} \begin{Bmatrix} \theta^{-1} d\theta \\ d\Xi \end{Bmatrix} \quad (76a)$$

recalling that $d\Xi = \frac{1}{3}V^{-1}dV$, plus a full matrix equation that governs the squeeze response

$$\begin{Bmatrix} d\sigma_1 \\ d\sigma_2 \end{Bmatrix} = \frac{\rho}{3} \begin{bmatrix} 2\partial_{\varepsilon_1\varepsilon_1}U & -\partial_{\varepsilon_2\varepsilon_2}U \\ -\partial_{\varepsilon_1\varepsilon_1}U & 2\partial_{\varepsilon_2\varepsilon_2}U \end{bmatrix} \begin{Bmatrix} d\varepsilon_1 \\ d\varepsilon_2 \end{Bmatrix} \quad (76b)$$

and a diagonal matrix equation that governs the shear response

$$\begin{Bmatrix} d\tau_1 \\ d\tau_2 \\ d\tau_3 \end{Bmatrix} = \rho \begin{bmatrix} \partial_{\gamma_1\gamma_1}U & 0 & 0 \\ 0 & \partial_{\gamma_2\gamma_2}U & 0 \\ 0 & 0 & \partial_{\gamma_3\gamma_3}U \end{bmatrix} \begin{Bmatrix} d\gamma_1 \\ d\gamma_2 \\ d\gamma_3 \end{Bmatrix} \quad (76c)$$

to which we now seek a description when expressed in terms of a set of specified material properties.

4.3.2 Material Properties

The material model put forward here is for a general thermoelastic solid with mass density ρ that has, at most, eight material properties/functions: a specific heat C_t and a lineal thermal strain coefficient α_t , both evaluated at constant pressure, a bulk modulus K_t evaluated at constant temperature, two squeeze moduli N_1 and N_2 evaluated at constant shear, and three shear moduli G_1 , G_2 and G_3 evaluated at constant squeeze. The specific heat C_t density is defined as

$$C_t := \frac{d\eta}{\theta^{-1} d\theta} \Big|_P = \frac{d\eta}{\theta^{-1} d\theta} \Big|_{\Pi} \quad (77a)$$

where θ is temperature, η is entropy density, and $\Pi := \mathcal{S}_{11} + \mathcal{S}_{22} + \mathcal{S}_{33} =: -3P$ is negative pressure. The lineal thermal strain coefficient α_t is defined as

$$\alpha_t := \frac{L^{-1} dL}{\theta^{-1} d\theta} \Big|_P = \frac{1}{3} \frac{V^{-1} dV}{\theta^{-1} d\theta} \Big|_P = \frac{d\Xi}{\theta^{-1} d\theta} \Big|_{\Pi} \quad (77b)$$

where $V = abc$ denotes a relative volume with $\Xi = \ln \sqrt[3]{V/V_0}$ being volumetric strain, a.k.a. dilatation. Note: the above definition for thermal strain, which is dimensionless, is *not* equivalent to the coefficient for thermal expansion commonly used in mechanics, which has units of reciprocal temperature, cf. App. A. The associated bulk modulus K_t is defined as

$$K_t := - \frac{dP}{V^{-1} dV} \Big|_{\theta} = \frac{1}{9} \frac{d\Pi}{d\Xi} \Big|_{\theta} \quad (77c)$$

that together with C_t and α_t describe the uniform response. Considering transpulmonary pressure, $P < 0$ under normal physiologic conditions, so $\Pi > 0$, not $P < 0$, is the more intuitive measure for working with the trace of stress when describing transpulmonary pressure.

The non-uniform response is described in terms of two in-plane squeeze moduli N_1 and N_2 that are defined as

$$N_1 := \frac{d(\mathcal{S}_{11} - \mathcal{S}_{22})}{\Gamma_1^{-1} d\Gamma_1} \Big|_{\Gamma_2} = \frac{1}{3} \frac{d\sigma_1}{d\varepsilon_1} \Big|_{\varepsilon_2} \quad (77d)$$

$$N_2 := \frac{d(\mathcal{S}_{22} - \mathcal{S}_{33})}{\Gamma_2^{-1} d\Gamma_2} \Big|_{\Gamma_1} = \frac{1}{3} \frac{d\sigma_2}{d\varepsilon_2} \Big|_{\varepsilon_1} \quad (77e)$$

where $\sigma_1 := \mathcal{S}_{11} - \mathcal{S}_{22}$ and $\sigma_2 := \mathcal{S}_{22} - \mathcal{S}_{33}$ are commonly referred to as the first and second normal-stress differences, respectively, in the polymers literature, with $\Gamma_1 := a/b$ and $\Gamma_2 := b/c$ being their conjugate squeeze stretches, and with $\varepsilon_1 = \ln \sqrt[3]{\Gamma_1/\Gamma_{10}}$ and $\varepsilon_2 = \ln \sqrt[3]{\Gamma_2/\Gamma_{20}}$ being their conjugate squeeze strains. Finally, there are three in-plane shear moduli G_1 , G_2 and G_3 that are defined as

$$G_1 := \Gamma_2 \left. \frac{d\mathcal{S}_{32}}{d\gamma_1} \right|_{\Gamma_2} \quad (77f)$$

$$G_2 := \Gamma_1 \Gamma_2 \left. \frac{d\mathcal{S}_{31}}{d\gamma_2} \right|_{\Gamma_1 \Gamma_2} \quad (77g)$$

$$G_3 := \Gamma_1 \left. \frac{d\mathcal{S}_{21}}{d\gamma_3} \right|_{\Gamma_1, \gamma_1, \tau_2} \quad (77h)$$

where $\tau_1 := \Gamma_2 \mathcal{S}_{32}$, $\tau_2 := \Gamma_1 \Gamma_2 \mathcal{S}_{31}$ and $\tau_3 := \Gamma_1 \mathcal{S}_{21} - \alpha \tau_2$ quantify the three shear stresses, with $\gamma_1 := \alpha - \alpha_0$, $\gamma_2 := \beta - \beta_0$ and $\gamma_3 := \gamma - \gamma_0$ being their respective shear strains.

A material is said to be ‘isotropic’ in our constitutive framework if its squeeze moduli can be described via a single material function, i.e., $N_1 = N_t(\sigma_1, \varepsilon_1)$ and $N_2 = N_t(\sigma_2, \varepsilon_2)$, and if its shear moduli can be described via a single material function, viz., $G_1 = G_t(\tau_1, \gamma_1)$, $G_2 = G_t(\tau_2, \gamma_2)$ and $G_3 = G_t(\tau_3, \gamma_3)$. In other words, the two squeeze response curves may have different tangents at any given moment, but these tangents are evaluated from the same material function for squeeze. A like statement applies to shear. In this regard, parenchyma is isotropic. An isotropic thermoelastic solid, in our approach, is characterized by its mass density ρ along with five, tangent, material properties: C_t , α_t , K_t , N_t and G_t where subscript ‘ t ’ denotes that these are tangent properties (vs. secant properties, which are discussed in App. A). This notion of isotropy is different from that of classical theory, where only four material properties apply: a specific heat, a coefficient for thermal expansion, a bulk modulus, and a shear modulus.

4.3.3 Constitutive Equations Governing a Thermoelastic Solid

In terms of the material properties put forward in Eqn. (77), the uniform response

of the thermoelastic solid given in Eqn. (76a) takes on the form of

$$\begin{Bmatrix} d\eta \\ d\Pi \end{Bmatrix} = \begin{bmatrix} C_t - 9\alpha^2 K/\rho\theta & 9\alpha K/\rho\theta \\ -9\alpha K & 9K \end{bmatrix} \begin{Bmatrix} \theta^{-1} d\theta \\ d\Xi \end{Bmatrix}, \quad \alpha = \alpha_t \quad K = K_t(\theta, \Pi, \Xi) \quad (78a)$$

while the non-uniform squeeze response is described by

$$\begin{Bmatrix} d\sigma_1 \\ d\sigma_2 \end{Bmatrix} = \frac{3}{2} \begin{bmatrix} 2N_1 & -N_2 \\ -N_1 & 2N_2 \end{bmatrix} \begin{Bmatrix} d\varepsilon_1 \\ d\varepsilon_2 \end{Bmatrix}, \quad \begin{aligned} N_1 &= N_t(\sigma_1, \varepsilon_1) \\ N_2 &= N_t(\sigma_2, \varepsilon_2) \end{aligned} \quad (78b)$$

and the non-uniform shear response is described by

$$\begin{Bmatrix} d\tau_1 \\ d\tau_2 \\ d\tau_3 \end{Bmatrix} = \begin{bmatrix} G_1 & 0 & 0 \\ 0 & G_2 & 0 \\ 0 & 0 & G_3 \end{bmatrix} \begin{Bmatrix} d\gamma_1 \\ d\gamma_2 \\ d\gamma_3 \end{Bmatrix}, \quad \begin{aligned} G_1 &= G_t(\tau_1, \gamma_1) \\ G_2 &= G_t(\tau_2, \gamma_2) \\ G_3 &= G_t(\tau_3, \gamma_3) \end{aligned} \quad (78c)$$

which is the general form for a thermoelastic solid that we shall use going forward. These moduli are expressed as depending upon both stress and strain, in accordance with the implicit theory of elasticity presented in App. A.

4.3.3.1 The Poisson Effect

Assuming that the bulk modulus K_t is known, then the squeeze modulus N_t for an isotropic material can be determined from a single uniaxial experiment by measuring its Poisson response via

$$\nu := -\frac{db/b}{da/a} = -\frac{dc/c}{da/a}$$

from which it follows that

$$N_t = 3K_t \frac{1 - 2\nu}{1 + \nu} \quad \text{provided that } S_{11} \neq 0 \quad \text{and} \quad S_{22} = S_{33} = 0$$

where temperature θ has been held constant. Consequently, $N_t = 2\mu$ where μ is the shear modulus from the classical theory of elasticity. On the other hand, our shear modulus G_t is distinct from the shear modulus μ employed by the classical theory of elasticity where strains and rotations are infinitesimal in extent—an assumption not imposed by our approach.

4.4. Modeling an Alveolus

To facilitate the numeric implementation of our models, and to facilitate interpretations of their results by engineers and scientists whom will use our framework, this section converts all fields defined in 1D and 2D into their 3D analogs; specifically, forces and surface tensions are converted into stresses, all moduli will now have units of stress, all thermal strain coefficients associate with linear expansions, and all mass densities relate mass to volume.

Only one-third of the cross-sectional area of an alveolar chord, and only one-half of the wall thickness of an alveolar septum associate with any given dodecahedron.³⁰ Specifically, a third of the total force carried by a septal fiber belongs with the given alveolus, with the remaining two-thirds of the transmitted force belonging to its two adjoining alveoli. Likewise, only half of the surface traction carried along a septal membrane belongs with the given alveolus, with the other half of its surface traction belonging to its adjacent alveoli. Like statements apply for their entropies.

About 75% of the acting transpulmonary pressure (the difference between pleural and alveolar pressures) is carried by the alveolar structure, with the remaining 25% being carried by the pleural membrane encasing the lung.⁷⁰

4.4.1 Constraints/Assumptions for Alveoli Subjected to Shock Waves

Because the primary purpose for the alveolar model being constructed here is to better understand alveolar behavior as a shock wave passes over it, there are certain assumptions that we impose upon our model that under normal or different physiologic conditions might otherwise not apply.

First: An alveolus is considered to be an adiabatic pressure vessel in which air and heat cannot move into or out of as a shock wave passes over it, simply because the wave speed is too fast. There is insufficient time for these transport phenomena to occur. This relates to the ‘closed-cell’ approximation used by Clayton & Freed² in the dynamic loading of their continuum model for parenchyma.

Second: The tissues that comprise lung are viscoelastic^{21,71} mixtures of collagen, elastin, cells, and the ground substance.^{17,63} Whenever a lung is subjected to a shock wave there is insufficient time for the viscous characteristics in a viscoelastic re-

DRAFT: UNCLASSIFIED

sponse to manifest themselves; therefore, the overall response is glassy elastic. Furthermore, even though we could construct a mixture theory for modeling an alveolar membrane, it would be challenging to establish the boundary conditions, nor would we be able to construct the necessary experiments to parameterize it; consequently, an isotropic, elastic, homogeneous continuum is assumed for modeling the planar septa.

Third: Temperature remains continuous in a jump across the kinematic discontinuity caused by a shock wave traveling through a compressible gas.⁷² As such, temperature is taken to be continuous across the spatial discontinuity of a shock wave traveling through parenchyma, too. However, temperature can change both in front of and behind a traveling wave, where the alveolar sac first compresses and then expands. Throughout this excursion, the overall process is taken to be adiabatic, in accordance with the first assumption.

Fourth: The air/membrane interface of an alveolus is lined with a surfactant, which is a thin bi-lipid film that has a significant role to play during normal lung function. This film reduces alveolar surface tension to help avert total lung collapse at maximum exhale.⁷³ Even so, some alveoli still collapse, getting re-recruited during a later breath. Models have been proposed for both surfactant⁷⁴ and alveolar recruitment,⁷⁵ but these effects are not included here as they are not thought to play a significant role in lung mechanics when a lung becomes subjected to a shock wave.

Fifth: Matsuda *et al.*⁷⁶ found the diameters of collagen and elastin fibers that circumscribe an alveolar mouth to be about 5-7 times larger than those of their septal chords. The alveolar mouth, with its thicker fibers and open face that attach an alveolus to an alveolar duct, is modeled here as a phantom face, viz., with fibers sized like any of the other eleven pentagonal elements comprising a dodecahedron, and a twelfth phantom face placed where an alveolar mouth would otherwise reside.¹⁴ Kimmel & Budiansky supported this conjecture via a private communication they had with Prof. T. A. Wilson, after which Kimmel & Budiansky wrote:³²

“Professor T. A. Wilson notes that the present model does not take explicit account of either alveolar openings or their fibrous boundaries. Wilson suggests that the elastic resistance of the ring boundaries tends to make up for the missing surface tension in the holes, so that neglect of both effects may be self-compensating.”

transpulmonary pressure	4 cm H ₂ O		
Age	15–35	36–45	> 65
collagen: \sqrt{D} , (μm) ^{1/2}	0.952 \pm 0.242	0.958 \pm 0.255	1.045 \pm 0.270
elastin: \sqrt{D} , (μm) ^{1/2}	0.957 \pm 0.239	0.970 \pm 0.213	1.093 \pm 0.274
transpulmonary pressure	14 cm H ₂ O		
Age	15–35	36–45	> 65
collagen: \sqrt{D} , (μm) ^{1/2}	0.955 \pm 0.246	0.994 \pm 0.237	1.054 \pm 0.279
elastin: \sqrt{D} , (μm) ^{1/2}	0.956 \pm 0.237	0.988 \pm 0.263	1.079 \pm 0.281

Table 4 Mean and standard deviations in variance for the square root of septal chord diameters \sqrt{D} reported by Sabin *et al.*⁴¹ These septal chords are comprised of collagen and elastin fibers that act independent of one another, and therefore, they are considered to be loaded in parallel with one another.

This conjecture of Kimmel & Budiansky, along with the experimental findings of Matsuda *et al.*, provide a pathway by which one can scale the surface traction carried by a single alveolar membrane with that of the chords that envelope it. In other words, this provides an avenue for parameterizing the membrane model in an otherwise void of relevant experimental data needed to estimate its parameters.

Sixth: Alveolar surfaces are modeled as membranes, not plates, and therefore are assumed to have no out-of-plane bending stiffness. This is in concert with our assumption that the septal chords are modeled as rods, not beams, because of their slenderness ratio. Furthermore, these septa tend to be flat because there are roughly equal pressures acting on both sides of these membranes, thereby eliminating curvature, which is the driving force behind out-of-plane bending²¹ and, we surmise, also helps to suppress wrinkling.

4.4.2 Modeling Septal Chords Subjected to Shock Waves

Alveoli are biologic structures constructed of septal chords that circumscribe alveolar membranes that envelope an alveolar sac whereat gas exchange occurs. These chords are comprised of individual collagen and elastin fibers loaded in parallel.^{41,76} The extent of elastic energy stored within a chord will depend upon the diameters D^c and D^e and length L of these individual fibers.* Let superscript ‘ c ’ denote col-

*Sabin *et al.*⁴¹ considered that the stored energy of chords also depends upon their curvature, which they measured and quantified, i.e., they considered these chords to be beams. However, with a slenderness ratio of $\bar{L}/\bar{D} = 102 \pm 12$, which we obtained from analyzing their data, it is reasonable to model them as rods, not beams. Consequently, the dodecahedral truss used as an alveolar model

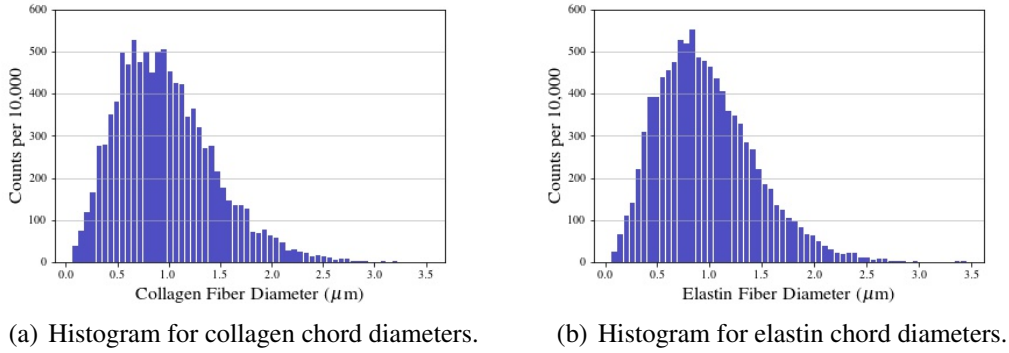


Fig. 27 Typical histograms for alveolar chord diameters constructed using the statistics reported in Table 4. Their tails weigh heavy at the larger diameters, because their distributions are normal in the square root of their diameters. These two histograms are virtually identical.

lagen, and superscript ‘*e*’ denote elastin. Sabin *et al.*⁴¹ determined that the square root of their diameters \sqrt{D} distribute normally, with a mean $\bar{D}^{1/2}$ and standard deviation $\sigma_{\sqrt{D}}$ that also depend upon age and transpulmonary pressure, as presented in Table 4 and illustrated in Fig. 27.

The collagen and elastin fibers that make up a septal chord have the same length L , they experience the same strain e , and they exist at the same temperature θ ; therefore, we employ Eqn. (65a) as the governing constitutive equation to describe their mechanical behaviors; specifically, for the collagen fiber in an alveolar chord

$$\begin{Bmatrix} d\eta^c \\ ds^c \end{Bmatrix} = \begin{bmatrix} C_t^c - (\alpha_t^c)^2 E^c / \rho^c \theta & \alpha_t^c E^c / \rho^c \theta \\ -\alpha_t^c E^c & E^c \end{bmatrix} \begin{Bmatrix} \theta^{-1} d\theta \\ L^{-1} dL \end{Bmatrix} \quad (79a)$$

where $E^c = E_t^c(\theta, e, s^c)$, and for the elastin fiber in an alveolar chord

$$\begin{Bmatrix} d\eta^e \\ ds^e \end{Bmatrix} = \begin{bmatrix} C_t^e - (\alpha_t^e)^2 E^e / \rho^e \theta & \alpha_t^e E^e / \rho^e \theta \\ -\alpha_t^e E^e & E^e \end{bmatrix} \begin{Bmatrix} \theta^{-1} d\theta \\ L^{-1} dL \end{Bmatrix} \quad (79b)$$

where $E^e = E_t^e(\theta, e, s^e)$, and where η^c and η^e are the entropy densities (erg/g.K) for collagen and elastin; $s^c := \lambda F^c / A_0^c$ and $s^e := \lambda F^e / A_0^e$ are the chordal stresses (barye = dyne/cm²) carried by the collagen and elastin fibers, wherein $\lambda = L/L_0$ is the fiber stretch, A_0^c and A_0^e are their traction-free cross-sectional areas (cm²), and F^c and F^e are the forces (dyne) they transmit. Parameters C_t^c and C_t^e are their

is considered to be a pinned truss, not a rigid truss, thereby greatly simplifying the boundary value problem.

DRAFT: UNCLASSIFIED

specific heats at constant pressure (erg/g.K), α_t^c and α_t^e are their lineal thermal strain coefficients, E^c and E^e are their elastic moduli (dyne/cm² = erg/cm³), and ρ^c and ρ^e are their mass densities (g/cm³). These differential equations are subject to initial conditions considered to be $s_0^c = s^c|_{L=L_0}$, $s_0^e = s^e|_{L=L_0}$, $\eta^c = \eta_0^c$ and $\eta^e = \eta_0^e$, where η_0^c and η_0^e are their respective entropy densities at rest. *In vivo*, s_0^c and s_0^e are positive valued, cf. App. A; whereas, *ex vivo*, s_0^c and s_0^e would be zero valued.

The actual force and entropy of an individual septal chord in our alveolar model is taken to be one third of a fiber's calculated values, as determined by Eqn. (79), because each alveolar chord is typically shared between three adjoining alveoli; consequently,

$$F^f = (A_0^c s^c + A_0^e s^e)/3\lambda \quad \text{and} \quad S^f = (\rho^c V_0^c \eta^c + \rho^e V_0^e \eta^e)/3 \quad (80)$$

where F^f (dyne) is a third of the fiber's force carried by a septal chord, and S^f (erg/K) is a third of the fiber's entropy.

Collagen is a fiber comprised of numerous, long, slender, wavy filaments whose waviness, known as crimp, straightens under sufficient deformation.^{77,78} Elastin is a linked fiber network, much like an elastomer, whose filaments between crosslinks rotate to align with an axis of loading under sufficient deformation.^{79,80} Consequently, collagen and elastin both recruit constituent filaments with increasing deformation into an overall, load-bearing, fiber response. The internal energies of collagen and elastin may therefore be thought of as being comprised of a molecular configuration energy and a mechanical strain energy. As such, both collagen and elastin are modeled as Freed-Rajagopal biologic fibers, which are described in terms of two such internal energies. Their model is derived from the theory of implicit elasticity, cf. App. A. According to their model, Eqn. (A-7), tangent compliances for collagen and elastin, pertinent to the hypo-elastic constitutive formulation of Eqn. (79), are described by

$$\frac{1}{E_t^c(\theta, s^c, e)} = \frac{e_{1_{\max}}^c - e_1^c}{E_1^c e_{1_{\max}}^c + 2(s^c - s_0^c)} + \frac{1}{E_2^c} \quad (81a)$$

$$\frac{1}{E_t^e(\theta, s^e, e)} = \frac{e_t^e - e_1^e}{E_1^e e_t^e + 2(s^e - s_0^e)} + \frac{1}{E_2^e} \quad (81b)$$

whose internal strains are established from

$$e_1^c = e - \alpha_t^c \ln \left(\frac{\theta}{\theta_0} \right) - \frac{s^c - s_0^c}{E_2^c} \quad (81c)$$

$$e_1^e = e - \alpha_t^e \ln \left(\frac{\theta}{\theta_0} \right) - \frac{s^e - s_0^e}{E_2^e} \quad (81d)$$

with θ_0 being body temperature, i.e., 310 K. Material constants E_1^c and E_2^c are the two asymptotic moduli for collagen that bound its response, i.e., $E_1^c \leq E_t^c \leq E_2^c$, while E_1^e and E_2^e are the two asymptotic moduli for elastin that bound its response, viz., $E_1^e \leq E_t^e \leq E_2^e$, both having units of stress (barye = dyne/cm²), with $e_{1_{\max}}^c$ and $e_{2_{\max}}^e$ being their respective transition strains (see their derivation in App. A), i.e., they are the limiting/maximum states of internal conformation strain. Collagen fibers are considered to fracture whenever the strain of stretching molecular bonds exceeds $e_f^c := s_f^c/E_2^c$, where s_f^c is the fracture stress. In contrast, elastin fibers are assumed to remain intact. (Elastin ruptures at strains in excess of 250%, which vastly exceeds the strain range that alveoli are exposed to.)

Moduli $E_t^c = E_1^c E_2^c / (E_1^c + E_2^c)$ and $E_t^e = E_1^e E_2^e / (E_1^e + E_2^e)$ are considered to apply for stresses less than their respective reference stress, viz., for $s^c < s_0^c$ or $s^e < s_0^e$, to which we assign values of $s_0^c = \frac{1}{2} E_1^c e_{1_{\max}}^c$ and $s_0^e = \frac{1}{2} E_1^e e_{1_{\max}}^e$. At these reference stresses, L is set to L_0 and therefore strain $e = 0$. This is done to help ensure a stable numerical implementation, as long slender rods readily buckle under compressive loads—a phenomenon not modeled here. Prestressing fibers is also nature’s way of ensuring their structural integrity.

Material properties needed to model septal chords are listed in Tables 4 & 5. From Eqn. (64), these elastic moduli are bound from above by Eqn. (64) implying that $E_{\max}^c = 2.25 \times 10^{12}$ barye (dyne/cm²) and $E_{\max}^e = 1.7 \times 10^{12}$ barye. We therefore observe that E_2^c and E_2^e are about 10^5 times smaller than E_{\max}^c and E_{\max}^e , which seems reasonable for *in vivo* fibers. This theoretical upper bound for a collagen molecule is about 100 times greater than what have been measured by testing collagen fibrils under ideal laboratory conditions.⁸⁹ Like results have been found for metals.

4.4.3 Modeling Alveolar Septa Subjected to Shock Waves

The thermoelastic response of a planar membrane used to model alveolar septa, as

Collagen		
Parameter	Value	Reference
ρ^c [g/cm ³]	1.34	Fels ⁸¹
η_0^c [erg/g.K]	3.7×10^7	Kanagy ⁸²
C_p^c [erg/g.K]	1.7×10^7	Weir ⁸³
$\alpha_s^c = \alpha_t^c$	0.056	estimated from TLC $\approx 30\%$
$e_{1,\max}^c$	0.09 ± 0.018	
e_f^c	0.25 ± 0.025	
E_1^c [barye]	$5.0 \pm 1.0 \times 10^5$	
E_2^c [barye]	$5.0 \pm 0.5 \times 10^7$	
s_0^e [barye]	$E_1^c e_{1,\max}^c / 2$	assumption
Elastin		
Parameter	Value	Reference
ρ^e [g/cm ³]	1.31	Lillie & Gosline ⁸⁴
η_0^e [erg/g.K]	3.4×10^7	Shadwick & Gosline ⁸⁵
C_p^e [erg/g.K]	4.2×10^7	Kakivaya & Hoeve ⁸⁶
$\alpha_s^e = \alpha_t^e$	0.1	Lillie & Gosline ⁸⁴
$e_{1,\max}^e$	0.4 ± 0.08	Shadwick & Gosline ⁸⁵
E_1^e [barye]	$2.3 \pm 0.3 \times 10^6$	Urry [80, Fig. 18]
E_2^e [barye]	$1.0 \pm 0.1 \times 10^7$	Lillie & Gosline [87, Fig. 5]
s_0^e [barye]	$E_1^e e_{1,\max}^e / 2$	assumption

Table 5 Physical properties for hydrated collagen and elastin fibers. Collagen denatures at around 60°C,⁸⁸ i.e., above this temperature collagen will shrink rapidly—an effect not modeled here.

DRAFT: UNCLASSIFIED

described in Eqn. (71), is governed by the following pair of differential equations. The first set of ODEs establishes the uniform response of a membrane, as described in Eqn. (71a), viz.,

$$\begin{Bmatrix} d\eta \\ ds^\pi \end{Bmatrix} = \begin{bmatrix} C_t - 4\alpha_t^2 M / \rho\theta & 4\alpha_t M / \rho\theta \\ -4\alpha_t M & 4M \end{bmatrix} \begin{Bmatrix} \theta^{-1} d\theta \\ d\xi \end{Bmatrix}, \quad M = M_t(\theta, s^\pi, \xi)$$

where $s^\pi := \pi/h$ has units of stress (dyne/cm²) with h denoting height or thickness of the spetal membrane. Assuming the volume of a septal membrane remains constant, thickness would obey $h = h_0 \exp(-2\xi)$ with h_0 being its reference thickness. Tangent modulus M is an areal equivalent of the bulk modulus. The second set of ODEs establishes the non-uniform response of a membrane, as described in Eqn. (71b), viz.,

$$\begin{Bmatrix} ds^\sigma \\ ds^\tau \end{Bmatrix} = \begin{bmatrix} 2N & 0 \\ 0 & G \end{bmatrix} \begin{Bmatrix} d\varepsilon \\ d\gamma \end{Bmatrix}, \quad N = N_t(s^\sigma, \varepsilon) \quad G = G_t(s^\tau, \gamma)$$

where $s^\sigma := \sigma/h$ and $s^\tau := \tau/h$ also have units of stress (dyne/cm²). Modulus N is the squeeze (pure shear) tangent modulus, while modulus G is the (simple) shear tangent modulus. These moduli are distinct; however, moduli M and N relate to one another through Poisson's response, cf. Eqn. (71c). How this is handled for biologic tissues is addressed below.

From a mechanics perspective, we know a great deal more about alveolar chords than we know about alveolar septa. More judgment will therefore be required in our construction and parameterization of a material model for alveolar membranes.

A typical alveolar septum is 4-5 μm thick.⁶³ They are comprised of an outside layer of epithelial cells that encase capillaries made of endothelial cells along with a basement membrane that is composed of unorganized collagen and elastin filaments, plus proteoglycans and other extracellular proteins. This basement membrane, roughly at mid-plane in an alveolar septum, has a width of about 0.5 μm .¹⁷ Inertial forces generated by these membranes are to be based upon a membrane thickness of $\sim 5 \mu\text{m}$ with an approximate density of water, while the structural forces that they carry are to be based upon a basement membrane thickness of $\sim 0.5 \mu\text{m}$.

It is not known how much of the mechanical load is actually carried by the cells in

DRAFT: UNCLASSIFIED

Property	Value
ρ [g/cm ³]	1.1
η_0 [erg/g.K]	5.0×10^6
C_p [erg/g.K]	2.1×10^7
α_t	0.037
$\xi_{1\max}$	0.24 ± 0.24
ξ_f	0.2
M_1 [barye]	$1.0 \pm 0.1 \times 10^4$
M_2 [barye]	$3.0 \pm 0.1 \times 10^6$
s_0^π [barye]	$M_1 \xi_{1\max} / 2$
$\varepsilon_{1\max}$	$\xi_{1\max} / 4$
N_1 [barye]	$2M_1 / 3$
N_2 [barye]	$5M_2 / 4$
$\gamma_{1\max}$	$3\xi_{1\max} / 2$
G_1 [barye]	$M_1 / 25$
G_2 [barye]	$M_2 / 25$

Table 6 The elastic properties reported here are for visceral pleura taken from Freed *et al.*⁵² and parenchyma taken from Saraf *et al.*,⁶⁹ divided by 10 to adjust for septal thickness vs. basement membrane thickness. The thermophysical properties lie between that of water and collagen, weighted towards that of water, and evaluated at body temperature.

an alveolar septum vs. the extracellular basement membrane they encase, but it is generally thought that this basement membrane carries the majority of the load.⁶³ Therefore, by diminishing the moduli that are appropriate for describing a basement membrane with thickness $\sim 0.5 \mu\text{m}$ by a factor of 10, one gets estimates for effective septal moduli that are applicable when modeling a whole septal membrane with thickness $\sim 5 \mu\text{m}$. We employ the model parameters specified in Table 6, which are based upon this assumption.

Collagen and elastin appear as thin filaments randomly oriented and somewhat uniformly dispersed throughout a basement membrane, unlike the strongly aligned fibers that appear in septal chords. Furthermore, there are a large number of proteins throughout these septa. Consequently, for our purposes, we model this collective ensemble of tissue and structure types as a homogeneous isotropic membrane modeled after the Freed-Rajagopal biologic fiber⁹⁰ that we have extended to mem-

branes in App. A, specifically

$$\frac{1}{M_t(\theta, \xi, s^\pi)} = \frac{\xi_{1\max} - \xi_1}{M_1 \xi_{1\max} + \frac{1}{2}(s^\pi - s_0^\pi)} + \frac{1}{M_2} \quad \xi_1 = \xi - \alpha_t \ln \left(\frac{\theta}{\theta_0} \right) - \frac{s^\pi - s_0^\pi}{4M_2} \quad (82a)$$

$$\frac{1}{N_t(\varepsilon, s^\sigma)} = \frac{\operatorname{sgn}(\varepsilon_1) \varepsilon_{1\max} - \varepsilon_1}{N_1 \operatorname{sgn}(\varepsilon_1) \varepsilon_{1\max} + s^\sigma} + \frac{1}{N_2} \quad \varepsilon_1 = \varepsilon - \frac{s^\sigma}{2N_2} \quad (82b)$$

and

$$\frac{1}{G_t(\gamma, s^\tau)} = \frac{\operatorname{sgn}(\gamma_1) \gamma_{1\max} - \gamma_1}{G_1 \operatorname{sgn}(\gamma_1) \gamma_{1\max} + 2s^\tau} + \frac{1}{G_2} \quad \gamma_1 = \gamma - \frac{s^\tau}{G_2} \quad (82c)$$

where compliant, initial, tangent moduli M_1 , N_1 and G_1 and stiff, terminal, tangent moduli M_2 , N_2 and G_2 bound their respective responses so that $M_1 \leq M_t \leq M_2$, $N_1 \leq N_t \leq N_2$ and $G_1 \leq G_t \leq G_2$, with a gradual transition between their asymptotic bounds occurring around strains $\xi_{1\max}$, $\varepsilon_{1\max}$ and $\gamma_{1\max}$, with membrane failure or rupture being considered to only occur in the dilation mode whenever $\xi > \xi_f$.

Whenever $s^\pi < s_0^\pi$, modulus M_t is assigned a value of $M_t = M_1 M_2 / (M_1 + M_2)$ that is the tangent modulus at reference stress s_0^π , which we take to be $\frac{1}{2} M_1 \xi_{1\max}$. Negative surface tensions cause wrinkling of a membrane surface, which is not addressed here. In contrast, the squeeze N_t and shear G_t moduli maintain applicability whenever their arguments become negative valued. This is handled via the sign function introduced in Eqns. (82b & 82c).

In Section 4.2.3.1 it was determined that $N = \frac{2}{3}M$ whenever Poisson's ratio ν is a half. Imposing this constraint of incompressibility is straightforward for Hookean materials, but it is not as obvious for biologic materials. Examining the data of Freed *et al.*⁵² for the pleural membrane, it seems reasonable to apply this proportionality factor to the limiting moduli, viz., it was found that $N_1 \approx \frac{2}{3}M_1$ and $N_2 \approx \frac{2}{3}M_2$. However, the transition strains were not found to obey this scaling; rather, $\varepsilon_t \approx \frac{1}{4}\xi_t$. Regarding the shear response of parenchyma, we use the bounds reported by Saraf *et al.*⁶⁹ for setting G_1 and G_2 , while using the transition strain γ_t reported in Freed *et al.*⁵² for muscle tissue. Clearly, there is a need for experiments to provide better estimates for these material properties.

Finite element technology is used to interpolate the entropy and these stresses, integrated at the Gauss points, to entropies and forces at the vertices of a pentagon,

cf. Part 6. The actual entropies and forces interpolated to these nodes are halved, because each septal plane belongs to two adjoining alveoli.

4.4.4 Modeling an Alveolar Volume Subjected to Shock Waves

Alveoli are connected to bronchial trees via alveolar ducts. Under normal conditions, air moves in and out of the alveoli via these ducts. However, when subjected to a stress wave passing over an alveolus, there is no time for the transport of air to take place. Hence, we can consider the air (and heat) within an alveolus to become ‘trapped’, and the pressure to be uniform therein. The governing thermodynamic process is therefore adiabatic. It is under this condition that we model the volumetric response of an alveolar sac.

4.4.4.1 Alveoli Filled with Air

Considering the water saturated air within an alveolus to be an ideal gas, then⁹¹

$$PV = nR\theta \quad \text{or} \quad \frac{PV}{\theta} = \frac{P_0V_0}{\theta_0} = nR = \text{constant} \quad (83)$$

where, in our case, P_0 is taken to be atmospheric pressure at sea level (1 bar or 10^5 Pa or 10^6 barye), with V_0 being that alveolar volume whereat alveolar pressure and plural pressure are both atmospheric, while $\theta_0 = 37^\circ\text{C} = 310\text{ K}$ is assigned as body temperature. Parameter n is the molar content of gas within an alveolus, and R is the universal gas constant.

The material properties associated with an ideal gas contained within an adiabatic enclosure are

$$\alpha_t := \left. \frac{\theta}{L} \frac{\partial L}{\partial \theta} \right|_P = \left. \frac{\theta}{3V} \frac{\partial V}{\partial \theta} \right|_P = \frac{1}{3\theta_0} \frac{P_0V_0}{PV} \quad (84a)$$

and

$$K_t := -V \left. \frac{\partial P}{\partial V} \right|_\theta = P_0 \frac{V_0\theta}{\theta_0 V} \quad (84b)$$

with the other two material properties pertaining to moist air at body temperature* being its mass density ρ of $1.125 \times 10^{-3}\text{ g/cm}^3$ and its specific heat C_t of

*Physical properties for air were taken from the website www.peacesoftware.de hosted by Berndt Wischnewski.

1.007×10^7 erg/g.K at constant pressure, constrained by $K_t < K_{\max} = \rho C_t \theta / \alpha_t^2 \approx \rho C_t \theta_0 / 9 = 3.9 \times 10^5$ barye. An alveolar sac, when modeled as an adiabatic pressure vessel filled with an ideal gas, is described by

$$\begin{Bmatrix} d\eta \\ -3 dP \end{Bmatrix} = \begin{bmatrix} C_t - 9\alpha_t^2 K_t / \rho\theta & 9\alpha_t K_t / \rho\theta \\ -9\alpha_t K_t & 9K_t \end{bmatrix} \begin{Bmatrix} \theta^{-1} d\theta \\ d\Xi \end{Bmatrix} \quad (65c)$$

where the entropy within an alveolar sac is given by $S^a = \rho V \eta$ whose initial condition is $S_0^a = \rho V_0 \eta_0$ with $\rho \eta_0$ being the entropy per unit volume of humid air at body temperature and atmospheric pressure, viz., $\rho \eta_0 = 7.770 \times 10^4$ erg/cm³.K. Equation (65c) in conjunction with the physical properties describing an ideal gas (84) result in the following equation governing pressure

$$\frac{dP}{P} = \frac{P_0 V_0 \theta}{PV\theta_0} \left(\frac{P_0 V_0 \theta}{PV\theta_0} \frac{d\theta}{\theta} - \frac{dV}{V} \right)$$

where pressure, volume and temperature all appear as logarithmic rates.

Pressure P is mapped to nodal forces at the vertices of a dodecahedron in our alveolar model. This requires finite element technology, which is discussed in Part 6.

4.4.4.2 Alveoli Filled with Fluid

In lung tissues that are not healthy, fluids may fill alveolar volumes at various regions throughout a lung, e.g., as could have been caused by injury, pneumonia, etc. In such localities the mechanical response of the local parenchyma will be vastly stiffer than that of healthy tissue, and as such, it will respond very differently to a traveling shock wave. For example, the speed of a wave moving over alveoli filled with fluid will be several orders in magnitude faster than the speed of the same wave moving over healthy alveoli filled with air.

In the presence of a passing shock wave, we suppose that an unhealthy alveolar sac, like a healthy one, can be modeled as an adiabatic enclosure, but now the fluid within such an alveolus is considered to behave, momentarily, like an elastic solid.

The thermoelastic response of an alveolar volume, as described in Eqn. (78), is governed by three sets of uncoupled differential equations. The first set of ODEs

establishes the uniform response of Eqn. (78a) described by

$$\begin{Bmatrix} d\eta \\ d\Pi \end{Bmatrix} = \begin{bmatrix} C_t - 9\alpha_t^2 K/\rho\theta & 9\alpha_t K/\rho\theta \\ -9\alpha_t K & 9K \end{bmatrix} \begin{Bmatrix} \theta^{-1} d\theta \\ d\Xi \end{Bmatrix}, \quad K = K_t(\theta, \Pi, \Xi)$$

with the second set of ODEs in Eqn. (78b) governing the squeeze response

$$\begin{Bmatrix} d\sigma_1 \\ d\sigma_2 \end{Bmatrix} = \frac{3}{2} \begin{bmatrix} 2N_1 & -N_2 \\ -N_1 & 2N_2 \end{bmatrix} \begin{Bmatrix} d\varepsilon_1 \\ d\varepsilon_2 \end{Bmatrix}, \quad N_1 = N_t(\sigma_1, \varepsilon_1) \\ N_2 = N_t(\sigma_2, \varepsilon_2)$$

while the third set of ODEs in Eqn. (78c) governs the shear response

$$\begin{Bmatrix} d\tau_1 \\ d\tau_2 \\ d\tau_3 \end{Bmatrix} = \begin{bmatrix} G_1 & 0 & 0 \\ 0 & G_2 & 0 \\ 0 & 0 & G_3 \end{bmatrix} \begin{Bmatrix} d\gamma_1 \\ d\gamma_2 \\ d\gamma_3 \end{Bmatrix}, \quad G_1 = G_t(\tau_1, \gamma_1) \\ G_2 = G_t(\tau_2, \gamma_2) \\ G_3 = G_t(\tau_3, \gamma_3)$$

that, collectively, can be used to describe the thermoelastic response of a volume of material.

How these are to be parameterized will be addressed in next year's work.

4.5. Finite Element Implementation of Constitutive Equations

The above constitutive models are implemented into our finite element model as hypo-elastic material models⁶⁶ described by*

$$d\boldsymbol{\sigma} = \mathbf{M}(\boldsymbol{\sigma}, \boldsymbol{\epsilon}) d\boldsymbol{\epsilon} \quad \text{wherein} \quad d\boldsymbol{\epsilon} = \frac{d\boldsymbol{\varepsilon}(\boldsymbol{\lambda})}{d\boldsymbol{\lambda}} d\boldsymbol{\lambda} \quad (85)$$

where $\boldsymbol{\sigma}$, $\boldsymbol{\epsilon}$ and $\boldsymbol{\lambda}$ are arrays of stress, strain and stretch attributes, respectively, with matrix $\mathbf{M}(\boldsymbol{\sigma}, \boldsymbol{\epsilon})$ containing the constitutive tangent moduli, i.e., $d\boldsymbol{\sigma}/d\boldsymbol{\epsilon}$, that, in general, may depend upon both stress $\boldsymbol{\sigma}$ and strain $\boldsymbol{\epsilon}$, while strain depends solely upon stretch $\boldsymbol{\lambda}$.

The two-step PECE algorithm presented in Section 5.1 presumes the following in-

*Constitutive equation $d\boldsymbol{\sigma} = \mathbf{M}(\boldsymbol{\sigma}, \boldsymbol{\epsilon}) d\boldsymbol{\epsilon}$ is that of a hypo-elastic solid.⁶⁶ A reasonable visco-elastic constitutive equation that one could consider would be a Zener⁹² solid, which would look something like

$$\boldsymbol{\sigma} + \boldsymbol{\tau} d\boldsymbol{\sigma} = \mathbf{E}_\infty \boldsymbol{\epsilon} + \boldsymbol{\tau} \mathbf{E}_0 d\boldsymbol{\epsilon}$$

where \mathbf{E}_∞ is a matrix of rubbery moduli, \mathbf{E}_0 is a matrix of glassy moduli, and $\boldsymbol{\tau}$ is a matrix of characteristic relaxation times. This is a topic for future work.

formation. There is an initial condition for the thermodynamic stresses σ_0 . An initial far-field deformation gradient \mathbf{F}_0 is also known, from which initial conditions for the thermodynamic stretches λ_0 and strains ϵ_0 can be readily obtained. All nodes of integration are to be spaced uniformly in time with $dt > 0$ designating their separation in time.

A far-field deformation gradient is considered to be known at the end of the first integration step, i.e., \mathbf{F}_1 , from which the thermodynamic stretches λ_1 and strains ϵ_1 can be calculated, with differential rates $d\lambda_0$ and $d\lambda_1$ coming from finite difference formulæ, so that $d\epsilon_0 = [d\varepsilon(\lambda_0)/d\lambda_0] d\lambda_0$ and $d\epsilon_1 = [d\varepsilon(\lambda_1)/d\lambda_1] d\lambda_1$ follow. Consequently, an initial stress rate can be established, i.e., $d\sigma_0 = \mathbf{M}(\sigma_0, \epsilon_0) d\epsilon_0$. With this information, Heun's method (Eqn. 94) can be called upon to integrate Eqn. (85) to determine the thermodynamic stresses and their differential rates out to the end of the first integration step, viz., σ_1 after which one can determine $d\sigma_1 = \mathbf{M}(\sigma_1, \epsilon_1) d\epsilon_1$.

For the next step, and those that follow, a more stable two-step method in Eqn. (95) can be called upon to advance a solution for the thermodynamic stresses and their differential rates. What needs to be stored are variables from the previous step, viz., σ_{n-1} , λ_{n-1} and $d\sigma_{n-1}$, along with like variables from the current step, viz., σ_n , λ_n and $d\sigma_n$. Then, given a far-field deformation gradient for the next step, i.e., \mathbf{F}_{n+1} , one can determine λ_{n+1} and ϵ_{n+1} along with the differential rate $d\lambda_{n+1}$ obtained from finite difference formulæ, after which $d\epsilon_{n+1} = [d\varepsilon(\lambda_{n+1})/d\lambda_{n+1}] d\lambda_{n+1}$ can be established. With this information, the PECE method (Eqn. 95) can be called upon to integrate Eqn. (85) to determine the thermodynamic stresses and their differential rates out to the end of the next integration step, viz., σ_{n+1} along with $d\sigma_{n+1} = \mathbf{M}(\sigma_{n+1}, \epsilon_{n+1}) d\epsilon_{n+1}$.

4.5.1 1D Formulation

For any given alveolar chord, we know its reference length L_0 and its current length L from which chordal stretch is described by $\lambda := L/L_0$ and its strain is defined as $e := \ln \lambda$ whose differential rate of change is $de = L^{-1} dL$; consequently,

$$\begin{Bmatrix} \theta^{-1} d\theta \\ de \end{Bmatrix} = \begin{bmatrix} 1/\theta & 0 \\ 0 & 1/L \end{bmatrix} \begin{Bmatrix} d\theta \\ dL \end{Bmatrix} \quad (86)$$

where the above matrix establishes $d\varepsilon(\lambda)/d\lambda$ in Eqn. (85) for a chord, with $d\lambda$ being the vector to the right of this matrix, and $d\varepsilon$ being the vector on the left-hand side. Finite difference formulæ are used to quantify $d\theta$ and dL .

The matrix of tangent moduli $M(\sigma, \varepsilon)$ given in Eqn. (85) is Eqn. (65a) for the case of a chord, whose elastic tangent modulus is $E_t(\theta, s, e)$ with stress defined as $s := F/A = \lambda F/A_0$, where F is the force carried by the chord, and where A_0 and A are the chordal cross-sectional areas in its reference and current states, respectively. Here it is assumed that chordal volume is preserved, which is a reasonable assumption for soft biological structures. The vector being operated on by this matrix of tangent moduli is $d\varepsilon$ above, with the constitutive equation returning a vector $d\sigma = \{d\eta, ds\}^\top$. The numerical method presented in Section 5.1 can then be called upon to integrate this hypo-elastic constitutive equation for its thermodynamic stresses $\sigma = \{\eta, s\}^\top$.

4.5.2 2D Formulation

Consider an incoming deformation gradient $\mathbf{F} = \mathcal{F}_{ij} \vec{\mathbf{e}}_i \otimes \vec{\mathbf{e}}_j$, $i, j = 1, 2$, whose components \mathcal{F}_{ij} are evaluated in a co-ordinate system associated with a membrane whose base vectors $(\vec{\mathbf{e}}_1, \vec{\mathbf{e}}_2)$, cf. Fig. 10, have been re-indexed via an orthogonal matrix \mathbf{P} according to Section 3.3.6.3. It is in this co-ordinate system that the components \mathcal{U}_{ij} of Laplace stretch $\mathcal{U} = \mathcal{U}_{ij} \vec{\mathbf{e}}_i \otimes \vec{\mathbf{e}}_j$ and its inverse \mathcal{U}^{-1} are quantified, their physical attributes a, b, g are determined, and their associated thermodynamic strains ξ, ε, γ and differential strain rates $d\xi, d\varepsilon, d\gamma$ are established, cf. Section 3.3.6.3.

The differential rates of these physical attributes relate to the differential rates of their thermodynamic variables according to

$$\begin{Bmatrix} \theta^{-1} d\theta \\ d\xi \\ d\varepsilon \\ d\gamma \end{Bmatrix} = \begin{bmatrix} 1/\theta & 0 & 0 & 0 \\ 0 & 1/2a & 1/2b & 0 \\ 0 & 1/2a & -1/2b & 0 \\ 0 & 0 & 0 & 1 \end{bmatrix} \begin{Bmatrix} d\theta \\ da \\ db \\ dg \end{Bmatrix} \quad (87)$$

where the above matrix establishes $d\varepsilon(\lambda)/d\lambda$ in Eqn. (85) for a membrane, with $d\lambda$ being the vector to the right of this matrix, and $d\varepsilon$ being the vector on the left-hand side.

The matrix of tangent moduli $\mathbf{M}(\boldsymbol{\sigma}, \boldsymbol{\varepsilon})$ given in Eqn. (85) is Eqn. (71) for the case of a membrane, whose moduli are: an areal modulus $M_t(\theta, \pi, \xi)$, a squeeze modulus $N_t(\sigma, \varepsilon)$, and a shear modulus $G_t(\tau, \gamma)$. The vector being operated on by this matrix of tangent moduli is $d\boldsymbol{\varepsilon}$ above, with the constitutive equation returning a vector $d\boldsymbol{\sigma} = \{d\eta, d\pi, d\sigma, d\tau\}^\top$. The numerical method presented in Section 5.1 can then be called upon to integrate this hypo-elastic constitutive equation for its thermodynamic stresses $\boldsymbol{\sigma}$.

After this constitutive equation has been integrated, the ensuing thermodynamic stress attributes map into elements S_{ij} of a stress tensor $\mathbf{S} = S_{ij} \vec{\mathbf{e}}_i \otimes \vec{\mathbf{e}}_j$ evaluated in the basis $(\vec{\mathbf{e}}_1, \vec{\mathbf{e}}_2)$ of a membrane; specifically,

$$\begin{Bmatrix} \eta \\ S_{11} \\ S_{22} \\ S_{12} = S_{21} \end{Bmatrix} = \begin{bmatrix} 1 & 0 & 0 & 0 \\ 0 & 1/2 & 1/2 & 0 \\ 0 & 1/2 & -1/2 & 0 \\ 0 & 0 & 0 & b/a \end{bmatrix} \begin{Bmatrix} \eta \\ \pi \\ \sigma \\ \tau \end{Bmatrix}. \quad (88)$$

These physical stress components S_{ij} can be pulled back into components S_{ij} belonging to the Lagrangian, second, Piola-Kirchhoff stress $\mathbf{S} = S_{ij} \vec{\mathbf{e}}_i \otimes \vec{\mathbf{e}}_j$ or rotated into components s_{ij} belonging to the Eulerian Kirchhoff stress $\mathbf{s} = s_{ij} \vec{\mathbf{e}}_i \otimes \vec{\mathbf{e}}_j$ via

$$S_{ij} = \mathcal{U}_{ik}^{-1} S_{k\ell} \mathcal{U}_{j\ell}^{-1} \quad \text{or} \quad s_{ij} = \mathcal{F}_{ik} S_{k\ell} \mathcal{F}_{j\ell} = \mathcal{R}_{ik} S_{k\ell} \mathcal{R}_{j\ell} \quad (89)$$

where $\mathcal{R} = \mathbf{F}\mathcal{U}^{-1}$ is the Gram rotation that associates with Laplace stretch, viz., $\mathbf{F} = \mathcal{R}\mathcal{U}$.

Components S_{ij} belonging to the Lagrangian, second, Piola-Kirchhoff stress \mathbf{S} , while components s_{ij} belonging to the Eulerian Kirchhoff stress \mathbf{s} , as established in Eqn. (89). They are evaluated in a re-indexed co-ordinate system with base vectors $(\vec{\mathbf{e}}_1, \vec{\mathbf{e}}_2)$. To map these components back into the co-ordinate system of the ‘user’, one must apply the linear transformations

$$P_{ik} S_{k\ell} P_{j\ell} \quad \text{and} \quad P_{ik} s_{k\ell} P_{j\ell}$$

where \mathbf{P} is the orthogonal matrix defined in Eqn. (38).

4.5.3 3D Formulation

Consider an incoming deformation gradient $\mathbf{F} = \mathcal{F}_{ij} \vec{\mathbf{E}}_i \otimes \vec{\mathbf{E}}_j$, $i, j = 1, 2, 3$, whose components \mathcal{F}_{ij} are evaluated in a re-indexed co-ordinate system for the dodecahedron with base vectors $(\vec{\mathbf{E}}_1, \vec{\mathbf{E}}_2, \vec{\mathbf{E}}_3)$, as established in Section 2.1. It is in this co-ordinate system that the components \mathcal{U}_{ij} of Laplace stretch $\mathcal{U} = \mathcal{U}_{ij} \vec{\mathbf{E}}_i \otimes \vec{\mathbf{E}}_j$ and its inverse \mathcal{U}^{-1} are evaluated (described in Eqn. 50), their associated stretch attributes $a, b, c, \alpha, \beta, \gamma$ are determined, and their associated thermodynamic strains $\Xi, \varepsilon_1, \varepsilon_2, \gamma_1, \gamma_2, \gamma_3$ and differential strain rates $d\Xi, d\varepsilon_1, d\varepsilon_2, d\gamma_1, d\gamma_2, d\gamma_3$ are determined, cf. Section 3.4.1.1.

The differential rates of these physical attributes relate to the differential rates of their thermodynamic variables according to

$$\left\{ \begin{array}{l} \theta^{-1} d\theta \\ d\Xi \\ d\varepsilon_1 \\ d\varepsilon_2 \\ d\gamma_1 \\ d\gamma_2 \\ d\gamma_3 \end{array} \right\} = \left[\begin{array}{ccccccc} 1/\theta & 0 & 0 & 0 & 0 & 0 & 0 \\ 0 & 1/3a & 1/3b & 1/3c & 0 & 0 & 0 \\ 0 & 1/3a & -1/3b & 0 & 0 & 0 & 0 \\ 0 & 0 & 1/3b & -1/3c & 0 & 0 & 0 \\ 0 & 0 & 0 & 0 & 1 & 0 & 0 \\ 0 & 0 & 0 & 0 & 0 & 1 & 0 \\ 0 & 0 & 0 & 0 & 0 & 0 & 1 \end{array} \right] \left\{ \begin{array}{l} d\theta \\ da \\ db \\ dc \\ d\alpha \\ d\beta \\ d\gamma \end{array} \right\} \quad (90)$$

where the above matrix establishes $d\varepsilon(\lambda)/d\lambda$ in Eqn. (85), with $d\lambda$ being the vector at the right of this matrix, and $d\varepsilon$ being the vector on the left-hand side.

The matrix of tangent moduli $\mathbf{M}(\sigma, \varepsilon)$ given in Eqn. (85) is Eqn. (78) for the general case, whose tangent moduli are: a bulk modulus $K_t(\theta, \Pi, \Xi)$, two squeeze moduli $N_1 = N_t(\sigma_1, \varepsilon_1)$ and $N_2 = N_t(\sigma_2, \varepsilon_2)$, and three shear moduli $G_1 = G_t(\tau_1, \gamma_1)$, $G_2 = G_t(\tau_2, \gamma_2)$ and $G_3 = G_t(\tau_3, \gamma_3)$. The vector being operated on by this matrix of tangent moduli is $d\varepsilon$ above, with the constitutive equation returning a vector $d\sigma = \{d\eta, d\Pi, d\sigma_1, d\sigma_2, d\tau_1, d\tau_2, d\tau_3\}^\top$. The numerical method presented in Section 5.1 can be called upon to integrate this hypo-elastic constitutive equation.

After this constitutive equation has been integrated, the ensuing thermodynamic stress attributes can be mapped into components \mathcal{S}_{ij} belonging to a stress tensor $\mathcal{S} = \mathcal{S}_{ij} \vec{\mathbf{E}}_i \otimes \vec{\mathbf{E}}_j$, $i, j = 1, 2, 3$, evaluated in the re-indexed basis $(\vec{\mathbf{E}}_1, \vec{\mathbf{E}}_2, \vec{\mathbf{E}}_3)$ of our

dodecahedron; specifically,

$$\left\{ \begin{array}{l} \eta \\ \mathcal{S}_{11} \\ \mathcal{S}_{22} \\ \mathcal{S}_{33} \\ \mathcal{S}_{23} = \mathcal{S}_{32} \\ \mathcal{S}_{13} = \mathcal{S}_{31} \\ \mathcal{S}_{12} = \mathcal{S}_{21} \end{array} \right\} = \left[\begin{array}{ccccccc} 1 & 0 & 0 & 0 & 0 & 0 & 0 \\ 0 & 1/3 & 2/3 & 1/3 & 0 & 0 & 0 \\ 0 & 1/3 & -1/3 & 1/3 & 0 & 0 & 0 \\ 0 & 1/3 & -1/3 & -2/3 & 0 & 0 & 0 \\ 0 & 0 & 0 & 0 & c/b & 0 & 0 \\ 0 & 0 & 0 & 0 & 0 & c/a & 0 \\ 0 & 0 & 0 & 0 & 0 & ab/a & b/a \end{array} \right] \left\{ \begin{array}{l} \eta \\ \Pi \\ \sigma_1 \\ \sigma_2 \\ \tau_1 \\ \tau_2 \\ \tau_3 \end{array} \right\}. \quad (91)$$

These physical components \mathcal{S}_{ij} can be pulled back into components S_{ij} belonging to the Lagrangian, second, Piola-Kirchhoff stress $\mathbf{S} = S_{ij} \vec{\mathbf{E}}_i \otimes \vec{\mathbf{E}}_j$ or rotated into components s_{ij} belonging to the Eulerian Kirchhoff stress $\mathbf{s} = s_{ij} \vec{\mathbf{E}}_i \otimes \vec{\mathbf{E}}_j$ via

$$S_{ij} = \mathcal{U}_{ik}^{-1} \mathcal{S}_{kl} \mathcal{U}_{jl}^{-1} \quad \text{or} \quad s_{ij} = \mathcal{F}_{ik} S_{kl} \mathcal{F}_{jl} = \mathcal{R}_{ik} \mathcal{S}_{kl} \mathcal{R}_{jl} \quad (92)$$

where $\mathcal{R} = \mathbf{F}\mathcal{U}^{-1}$ is the Gram rotation that associates with Laplace stretch, viz., $\mathbf{F} = \mathcal{R}\mathcal{U}$.

Components S_{ij} belonging to the Lagrangian, second, Piola-Kirchhoff stress \mathbf{S} , and components s_{ij} belonging to the Eulerian Kirchhoff stress \mathbf{s} , as established in Eqn. (89), are evaluated in a re-indexed co-ordinate system with base vectors $(\vec{\mathbf{E}}_1, \vec{\mathbf{E}}_2, \vec{\mathbf{E}}_3)$. To map these components back into the co-ordinate system of the ‘user’, i.e., $(\vec{i}, \vec{j}, \vec{k})$, one must apply the linear transformations

$$P_{ik} S_{kl} P_{jl} \quad \text{and} \quad P_{ik} s_{kl} P_{jl}$$

where \mathbf{P} is an orthogonal matrix defined in Section 2.1.

4.6. Code Verification and Capabilities of the Constitutive Equations

Figure 28 illustrates what a typical thermo-mechanical response for a collagen fiber would be expected to look like *in vivo* (top row) and *ex vivo* (bottom row) for thirty typical fibers, as predicted by the Freed-Rajagopal⁹⁰ model derived in Section A.2.1 of this appendix. The *in vivo* response typifies how fibers are preloaded in the various alveolar structures of paraenchyma. The material properties for collagen used to create this figure came from Table 5. Stress/strain curves are shown in the left column, while entropy/strain curves are shown in the right column. The top row

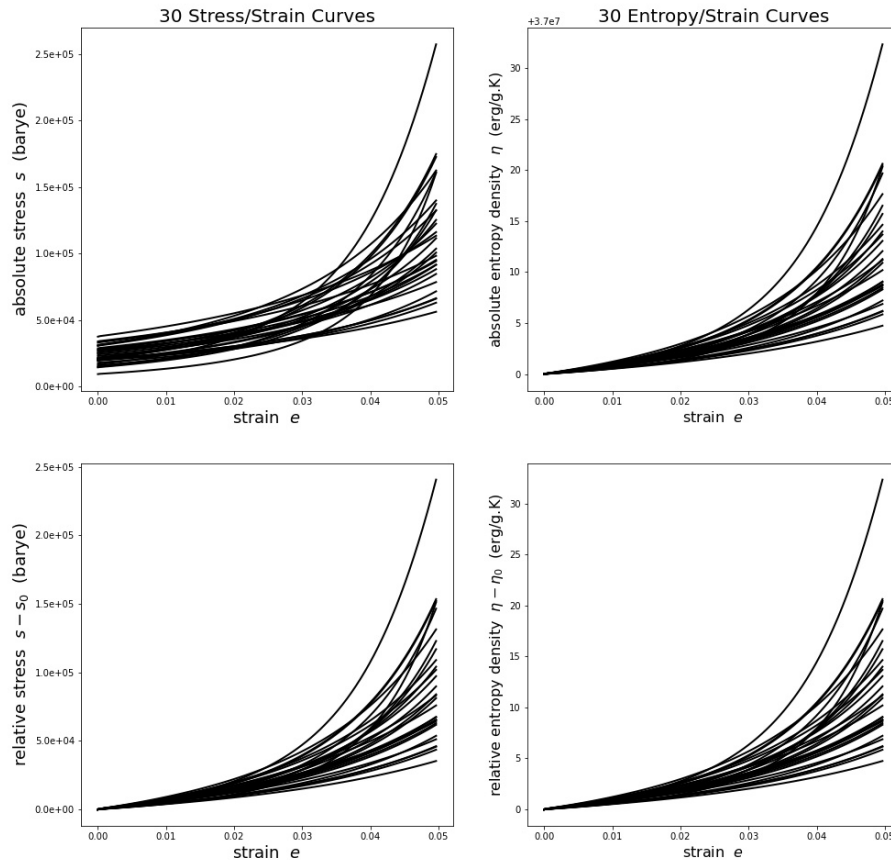


Fig. 28 Typical stress/strain (left column) and entropy/strain (right column) response curves for collagen fibers loaded *in vivo* to 5% strain. The top row presents their absolute responses, while the bottom row presents their relative responses. A reference fiber length, whereat strain is arbitrarily set to zero, has been selected to associate with half the available stretch that can be attributed to molecular reconfiguration.

provides their absolute responses, while the bottom row provides their relative responses. *In vivo*, biologic fibers do not associate with reference states that are void of stress. This is apparent in the upper-left graph (s vs. e), whose response is normalized in the lower-left graph ($s - s_0$ vs. e), and likewise for entropy. The graphs that follow will plot relative values.

Figure 28 presents stress/strain and entropy/strain response curves out to 5% strain. Figure 29 extends the deformation out to 10%, 20%, 30% and 40% strains. In both of these figures we observe that any additional contribution to the entropy caused by deformation can be neglected (it being less than 1 part out of 10^4). In addition to possessing a capability of having stressed fibers in their reference state, established via $s_0 := \frac{1}{2}E_1e_{1\max}$ and as seen in Fig. 28, our fiber model also accounts for fiber rupture, which is considered to be triggered at a maximum stress of $s_f := E_2e_f$. Ruptures start at around 30% strain for the specified material parameters. In these figures, material properties E_1 , E_2 and $e_{1\max}$ for collagen were all assigned random values according to their respective probabilistic distributions taken from Table 5. Employing 75 steps to integrate each response (sufficient for drawing nice curves) results in numerical errors of integration (right column in Fig. 29), specifically, in local truncation errors that were found to be on the order of the square root of machine precision, which is considered to be very good.

Like Figs. 28 & 29, material properties E_1 , E_2 and $e_{1\max}$ were each assigned random values for both elastin and collagen using parameters taken from Table 5 for the purpose of constructing the 30 curves presented in each plot of Fig. 30 for septal chords. Plus, their fiber lengths and diameters were likewise assigned random values according to their respective probabilistic distributions taken from Fig. (8), using formula (11), and the data from Table 4. Figure 30 presents realistic variability with what one should expect for chordal responses in the alveoli of lung. Both the chordal force and entropy (actual entropy, not entropy density) were calculated using the rule of mixtures based upon volume fractions of collagen vs. elastin. The change in chordal entropy was so small that variability caused by variation in volume fraction dominates this response; hence, relative changes in entropy ($S - S_0$) had to be plotted to visualize the effect. In the septal chords that failed during this analysis, it was collagen fibers that ruptured with elastin fibers continuing to carry load.

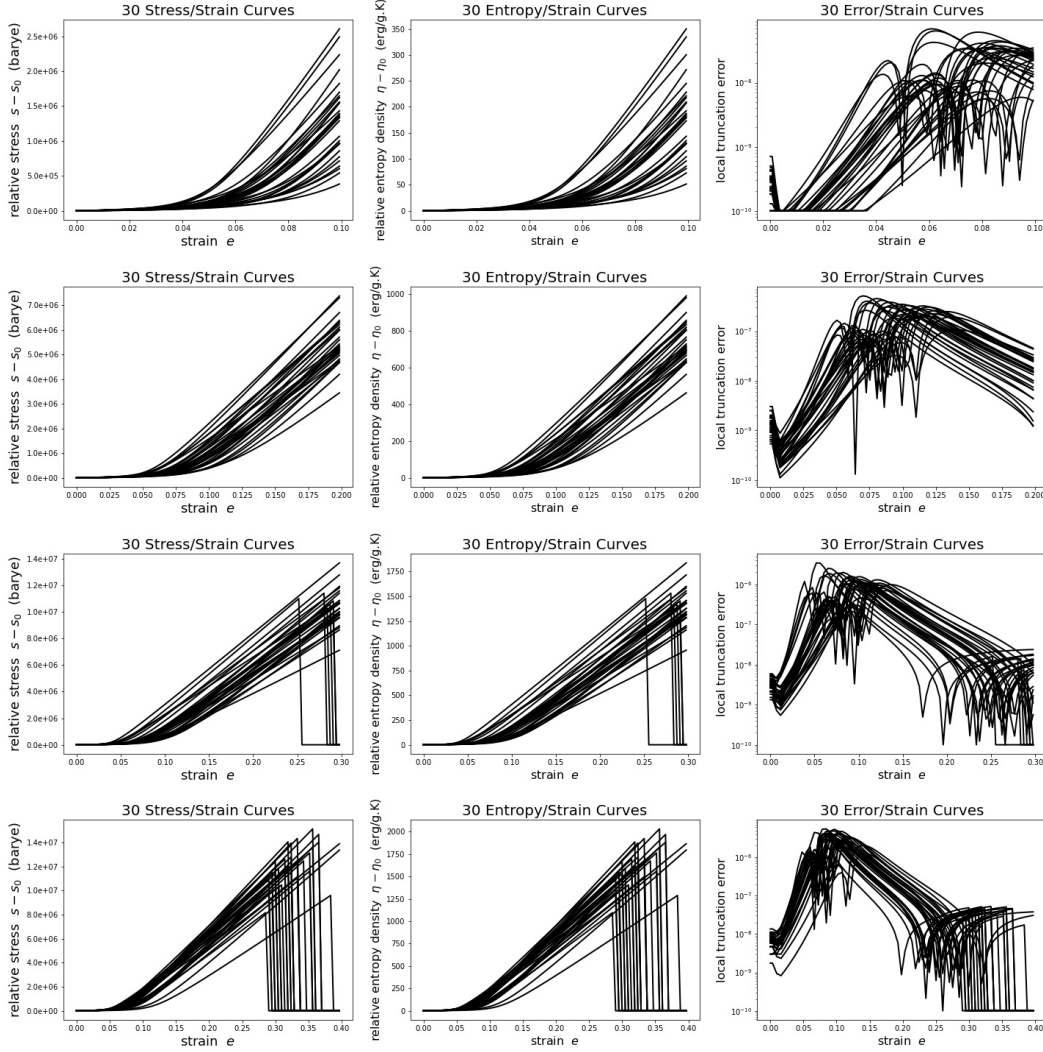


Fig. 29 Stress/strain (left column), entropy density/strain (center column), and local truncation error/strain (right column) curves for collagen using the material parameters listed in Table 5, which are described in terms of probability distributions. The top row is for strains out to 10%, the second row is for strains out to 20%, the third row is for strains out to 30%, and the fourth row is for strains out to 40%. There were no fiber failures in those that were stretched out to 10% and 20% strain. Six of the thirty fibers failed in those stretched out to 30% strain, while twenty eight of the thirty fibers failed for those stretched out to 40% strain. The local truncation errors plotted here associate with the PECE integrator presented in Eqn. (95) of Part 5 using 75 steps of integration, with errors less than 10^{-10} set at 10^{-10} . The reported truncation errors never exceeded 0.001%.

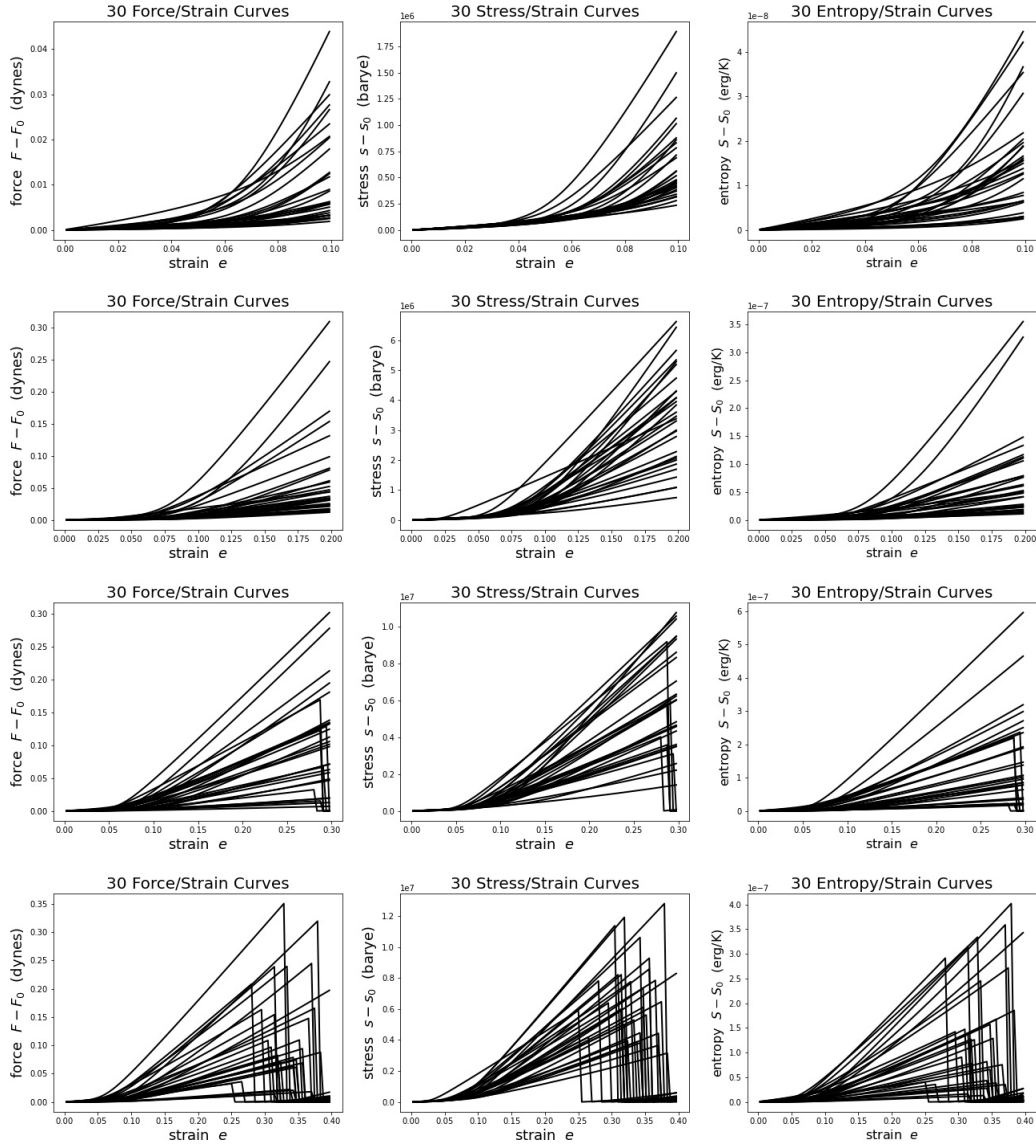


Fig. 30 Relative force/strain (left column), relative nominal stress/strain (center column), and relative entropy/strain (right column) curves for septal chords comprised of individual collagen and elastin fibers whose material parameters are listed in Table 5, which are described in terms of probability distributions. The top row is for strains out to 10%, the second row is for strains out to 20%, the third row is for strains out to 30%, and the fourth row is for strains out to 40%. There were no fiber failures in those that were stretched out to 10% and 20% strain. Six of the thirty collagen fibers failed in those stretched out to 30% strain with none of the elastin fibers failing, while twenty nine of the thirty collagen fibers failed for those stretched out to 40% strain, again, with none of the elastin fibers failing.

The three conjugate pairs that describe a membrane's response are presented as rows in Fig. 31—one row per experiment, with there being 30 curves per plot. These conjugate pairs describe: uniform dilation (s^π, ξ), non-uniform squeeze (s^σ, ε), and non-uniform (simple) shear (s^τ, γ). The three motions that we consider include: dilation

$$a = \lambda \quad b = \lambda \quad g - g_0 = 0 \quad (93a)$$

pure shear⁵¹

$$a = \frac{\sqrt{\lambda^2 + \lambda^{-2}}}{\sqrt{2}} \quad b = \frac{\sqrt{2}}{\sqrt{\lambda^2 + \lambda^{-2}}} \quad g - g_0 = \frac{\lambda^2 - \lambda^{-2}}{\lambda^2 + \lambda^{-2}} \quad (93b)$$

and simple shear

$$a = 1 \quad b = 1 \quad g - g_0 \neq 0 \quad (93c)$$

where λ denotes a stretch with $\lambda_0 = 1$. For dilation: $\xi = \ln \lambda$, $\varepsilon = 0$ & $\gamma = 0$; for pure shear: $\xi = 0$, $\varepsilon = \ln(\frac{1}{2}(\lambda^2 + \lambda^{-2}))$ & $\gamma = (\lambda^2 - \lambda^{-2})/(\lambda^2 + \lambda^{-2})$; and for simple shear: $\xi = 0$, $\varepsilon = 0$ & $\gamma = g - g_0$. The constitutive model is that of Eqns. (71 & 82), applying material parameters (and their variability) given in Table 6. In the dilation experiment (top row) there is only uniform (s^π, ξ) response. There are no non-uniform responses, neither (s^σ, ε) nor (s^τ, γ) in an uniform dilation, either theoretical or numerical. The conjugate pairs are uncoupled here. Likewise, in the simple shear experiment (bottom row) there is only a non-uniform (s^τ, γ) response. Theoretically, there is neither uniform (s^π, ξ) nor non-uniform (s^σ, ε) responses in a non-uniform simple shear. However, we observe some numerical error arising in the uniform response—on the order of 1 part in 10^{12} and, therefore, negligible. The pure shear experiment (middle row) is dominated by both a squeeze (s^σ, ε) and a shear (s^τ, γ) response, with there being a small, systematic, dilational coupling through pair (s^π, ξ) that is on the order of 1 part in 10^6 . This is the greatest numerical error in our implementation, but still it is sufficiently small so that it can be neglected without concern. Eight of the thirty dilation experiments presented here resulted in membrane rupture. As currently modeled, rupture only associates with the dilational response in septal membranes.

Recently, Birzle *et al.*⁹³ performed experiments on thin slices of rat parenchyma

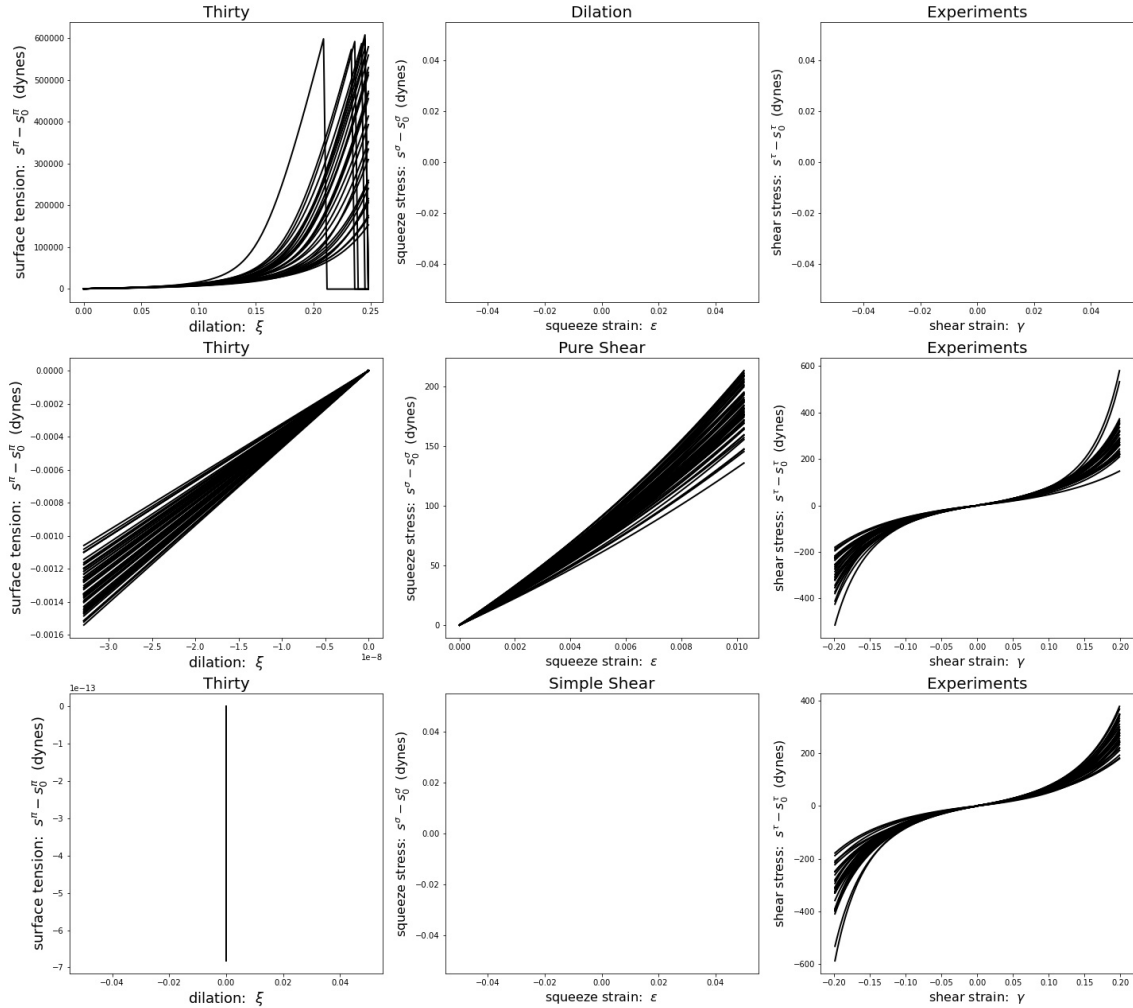


Fig. 31 Membrane response from thirty numerical experiments whose constitutive behavior is described by Eqns. (71 & 82) using the parameters listed in Table 6. The first column gives the $(s^\pi - s_0^\pi, \xi)$ conjugate pair response, the second column gives the $(s^\sigma - s_0^\sigma, \varepsilon)$ conjugate pair response, while the third column gives the $(s^\tau - s_0^\tau, \gamma)$ conjugate pair response. The first row represents a dilation experiment described by Eqn. (93a), the second row represents a pure shear experiment described by Eqn. (93b), while the third row represents a simple shear experiment described by Eqn. (93c). During these numerical experiments, eight membranes ruptured under dialation, while none ruptured during these pure and simple shear experiments.

DRAFT: UNCLASSIFIED

loaded in tension where they removed the collagen and/or elastin fiber content through collagenase and elastase treatment baths to study their individual behaviors and their interactions under load.

Part 5

Numerical Integrators

This analysis tool, which models alveolar geometry as a dodecahedron, requires numerical methods for the temporal integration of its constitutive equations (systems of first-order ODEs) and their governing equations of motion (systems of second-order ODEs), and for the spatial integrations of: length of line, area of surface, and volume of space that pertain to the various finite-element geometries required. Results obtained at the Gauss points need to be mapped out to their nodal locations, so extrapolation procedures that are consistent with the shape (interpolation) functions used are derived for the various elements and quadratures selected.

5.1. ODE Solvers

The constitutive equations used to describe our alveolar model present themselves as ordinary differential equations that need to be integrated, cf. Section 4.5. To this end, we employ the PECE (Predict, Evaluate, Correct, re-Evaluate) algorithms of Freed⁹⁴ suitable for solving stiff systems of first- and second-order differential equations. These methods are based upon Gear's well-known, second-order, backward, difference formula (BDF2) that appears in Eqns. (95c & 99e) below.

Time t is considered to be the independent variable, discretized over an interval in time $[t_0, t_N]$ for which N solutions are to be extracted at nodes $n = 1, 2, \dots, N$ spaced at uniform intervals in time with a common step size of $dt = (t_N - t_0)/N$ separating them, where time t_0 associates with the initial condition.

5.1.1 PECE Solver for First-Order ODEs

Let $\mathbf{x}(t)$ be a vector of independent control variables described in terms of time t , and let $\mathbf{y}(\mathbf{x})$ be a vector of dependent response variables obeying a differential equation of evolution $\dot{\mathbf{y}} = \mathbf{f}(\mathbf{x}, \mathbf{y}) \dot{\mathbf{x}}$, or equivalently $d\mathbf{y} = \mathbf{f}(\mathbf{x}, \mathbf{y}) \dot{\mathbf{x}} dt = \mathbf{f}(\mathbf{x}, \mathbf{y}) d\mathbf{x}$, subject to an initial condition $\mathbf{y}_0 = \mathbf{y}(\mathbf{x}_0)$ where $\mathbf{x}_0 = \mathbf{x}(t_0)$ with matrix $\mathbf{f}(\mathbf{x}, \mathbf{y})$ establishing the constitutive response for the system.

The two-step method put forward here incrementally solves such an ODE, returning

solutions associated with the next moment in time t_{n+1} , i.e., it acquires \mathbf{y}_{n+1} , given knowledge of the previous \mathbf{y}_{n-1} and current \mathbf{y}_n solutions plus their rates $\dot{\mathbf{y}}_{n-1}$ and $\dot{\mathbf{y}}_n$, with the corrector also depending upon $\dot{\mathbf{y}}_{n+1}$; consequently, the corrector is an implicit method, which is the source of the method's stability properties.

5.1.1.1 Start-Up Algorithm

Multi-step methods are not self starting. As such, Heun's method (a forward-Euler predictor with a trapezoidal corrector) is used to start this integrator; specifically,

$$\text{Predict} \quad \mathbf{y}_1^p = \mathbf{y}_0 + \dot{\mathbf{y}}_0 dt + \mathcal{O}((dt)^2) \quad (94a)$$

$$\text{Evaluate} \quad \dot{\mathbf{y}}_1^p = \mathbf{f}(\mathbf{x}_1, \mathbf{y}_1^p) \dot{\mathbf{x}}_1 \quad (94b)$$

$$\text{Correct} \quad \mathbf{y}_1 = \mathbf{y}_0 + \frac{1}{2}(\dot{\mathbf{y}}_1^p + \dot{\mathbf{y}}_0)dt + \mathcal{O}((dt)^3) \quad (94c)$$

$$\text{re-Evaluate} \quad \dot{\mathbf{y}}_1 = \mathbf{f}(\mathbf{x}_1, \mathbf{y}_1) \dot{\mathbf{x}}_1 \quad (94d)$$

wherein $\dot{\mathbf{y}}_0 = \mathbf{f}(\mathbf{x}_0, \mathbf{y}_0) \dot{\mathbf{x}}_0$. The predictor is the forward Euler method, while the corrector is the trapezoidal rule. The order of accuracy for a method (the exponent on dt in \mathcal{O}), as they appear in the above big \mathcal{O} operators, pertains to a single step of integration. The overall order of the method, when integrated over a sequence of steps, is one less than the exponent inside the \mathcal{O} operator. Therefore, Euler's method is first-order accurate, and Heun's method is second-order accurate.

5.1.1.2 Two-Step ODE Solver

The two-step method of Freed⁹⁴ for solving first-order ODEs is

$$\text{Predict} \quad \mathbf{y}_{n+1}^p = \frac{1}{3}(4\mathbf{y}_n - \mathbf{y}_{n-1}) + \frac{2}{3}(2\dot{\mathbf{y}}_n - \dot{\mathbf{y}}_{n-1})dt + \mathcal{O}((dt)^3) \quad (95a)$$

$$\text{Evaluate} \quad \dot{\mathbf{y}}_{n+1}^p = \mathbf{f}(\mathbf{x}_{n+1}, \mathbf{y}_{n+1}^p) \dot{\mathbf{x}}_{n+1} \quad (95b)$$

$$\text{Correct} \quad \mathbf{y}_{n+1} = \frac{1}{3}(4\mathbf{y}_n - \mathbf{y}_{n-1}) + \frac{2}{3}\dot{\mathbf{y}}_{n+1}^p dt + \mathcal{O}((dt)^3) \quad (95c)$$

$$\text{re-Evaluate} \quad \dot{\mathbf{y}}_{n+1} = \mathbf{f}(\mathbf{x}_{n+1}, \mathbf{y}_{n+1}) \dot{\mathbf{x}}_{n+1} \quad (95d)$$

whose corrector is the well-known BDF2 formula made popular by Gear, for which Freed has provided a predictor. This method is second-order accurate in both its predictor and corrector.

Both the predictor and corrector of this PECE scheme have a solution \mathbf{y} with a weight of 1, and a rate $\dot{\mathbf{y}}$ with a weight of $\frac{2}{3}dt$; hence, this predictor/corrector pair is internally consistent, i.e., the predictor and corrector will produce the same result

whenever they integrate over a constant $\dot{\gamma}$ field.

The correct/re-evaluate (CE) steps of a PECE method are often iterated over until a convergence criterion is satisfied. Such methods are typically denoted as PE(CE)^{*m*}, where *m* specifies the number of iterations imposed.

5.1.2 A Relevant Example

In our finite element implementation, a hypo-elastic material model⁶⁶ is introduced to describe the constitutive response of an alveolus whereby

$$\dot{\sigma} = M(\epsilon, \sigma) \dot{\epsilon} \quad \text{or equivalently}^{95} \quad d\sigma = M(\epsilon, \sigma) d\epsilon$$

where ϵ is a vector of thermodynamic strains, σ is a vector of thermodynamic stresses, and M is a square matrix comprised of their tangent moduli, which can depend upon both stress and strain in our application; specifically,

$$\sigma_{1D} = \{\eta, s\}^T, \quad \sigma_{2D} = \{\eta, s^\pi, s^\sigma, s^\tau\}^T, \quad \sigma_{3D} = \{\eta, \Pi, \sigma_1, \sigma_2, \tau_1, \tau_2, \tau_3\}^T$$

where η is entropy and the rest of its constituents are stress attributes. Their thermodynamic conjugates are the control variables

$$\epsilon_{1D} = \{\theta, e\}^T, \quad \epsilon_{2D} = \{\theta, \xi, \varepsilon, \gamma\}^T, \quad \epsilon_{3D} = \{\theta, \Xi, \varepsilon_1, \varepsilon_2, \gamma_1, \gamma_2, \gamma_3\}^T$$

where θ is temperature and the rest of its constituents are strain attributes. In the 2- and 3-D cases, these stress/strain attributes arise from Gram-Schmidt decompositions of their respective deformation gradients (cf. Sections 3.3.6.1, 4.4 and 4.5). Constructing tangent moduli $M(\epsilon, \sigma)$ is the topic of Part 4. Both σ and $d\sigma = M d\epsilon$ arise in the construction of our stiffness matrices, cf. Section 6.2.

Equation (94) is used to take the first step of integration; specifically,

Predict	$\sigma_1^p = \sigma_0 + \dot{\sigma}_0 dt$
Evaluate	$\dot{\sigma}_1^p = M(\epsilon, \sigma_1^p) \dot{\epsilon}_1$
Correct	$\sigma_1 = \sigma_0 + \frac{1}{2}(\dot{\sigma}_1^p + \dot{\sigma}_0)dt$
re-Evaluate	$\dot{\sigma}_1 = M(\epsilon_1, \sigma_1) \dot{\epsilon}_1$

where $\dot{\sigma}_0 = \mathbf{M}(\epsilon_0, \sigma_0) \dot{\epsilon}_0$. The remaining steps of integration follow according to Eqn. (95); specifically,

$$\begin{array}{ll} \text{Predict} & \sigma_{n+1}^p = \frac{1}{3}(4\sigma_n - \sigma_{n-1}) + \frac{2}{3}(2\dot{\sigma}_n - \dot{\sigma}_{n-1})dt \\ \text{Evaluate} & \dot{\sigma}_{n+1}^p = \mathbf{M}(\epsilon_{n+1}, \sigma_{n+1}^p) \dot{\epsilon}_{n+1} \\ \text{Correct} & \sigma_{n+1} = \frac{1}{3}(4\sigma_n - \sigma_{n-1}) + \frac{2}{3}\dot{\sigma}_{n+1}^p dt \\ \text{re-Evaluate} & \dot{\sigma}_{n+1} = \mathbf{M}(\epsilon_{n+1}, \sigma_{n+1}) \dot{\epsilon}_{n+1} \end{array}$$

whose strain rates $\dot{\epsilon}$ are computed according to Section 4.5.

5.1.3 PECE Solver for Second-Order ODEs

Now let \mathbf{u} denote a vector of dependent variables obeying a differential equation of evolution $d^2\mathbf{u}(t)/dt^2 = \ddot{\mathbf{u}} = \mathbf{f}(t, \mathbf{u}, \dot{\mathbf{u}})$ subjected to the pair of initial conditions $\mathbf{u}_0 = \mathbf{u}(t_0)$ and $\dot{\mathbf{u}}_0 = \dot{\mathbf{u}}(t_0)$. One may think of \mathbf{u} as being displacements whose rates $\dot{\mathbf{u}}$ are velocities \mathbf{v} , with $\ddot{\mathbf{u}} = \dot{\mathbf{v}}$ representing their accelerations \mathbf{a} .

The two-step method put forward here incrementally solves such an ODE, returning solutions associated with the next moment in time t_{n+1} for both displacement \mathbf{u}_{n+1} and velocity $\dot{\mathbf{u}}_{n+1}$. To update the displacement to \mathbf{u}_{n+1} , the predictor requires knowledge of the previous fields \mathbf{u}_{n-1} , $\dot{\mathbf{u}}_{n-1}$ and $\ddot{\mathbf{u}}_{n-1}$ plus the current fields \mathbf{u}_n , $\dot{\mathbf{u}}_n$ and $\ddot{\mathbf{u}}_n$, with the corrector also requiring knowledge of $\dot{\mathbf{u}}_{n+1}$ and $\ddot{\mathbf{u}}_{n+1}$. Likewise, to update the velocity to $\dot{\mathbf{u}}_{n+1}$, the predictor requires knowledge of the previous fields $\dot{\mathbf{u}}_{n-1}$ and $\ddot{\mathbf{u}}_{n-1}$ plus the current fields $\dot{\mathbf{u}}_n$ and $\ddot{\mathbf{u}}_n$, with the corrector also requiring knowledge of $\ddot{\mathbf{u}}_{n+1}$. Both predictors are explicit, and both correctors are implicit. It is this implicit quality that provides numeric stability for the integrator.

5.1.3.1 Start-Up Algorithm

Again, multi-step methods are not self starting, so a one-step method is needed to take the first step of integration; specifically, we employ

$$\text{Predict} \quad \mathbf{u}_1^p = \mathbf{u}_0 + \dot{\mathbf{u}}_0 dt + \frac{1}{2}\ddot{\mathbf{u}}_0(dt)^2 + \mathcal{O}((dt)^3) \quad (98a)$$

$$\dot{\mathbf{u}}_1^p = \dot{\mathbf{u}}_0 + \ddot{\mathbf{u}}_0 dt + \mathcal{O}((dt)^2) \quad (98b)$$

$$\text{Evaluate} \quad \ddot{\mathbf{u}}_1^p = \mathbf{f}(t_1, \mathbf{u}_1^p, \dot{\mathbf{u}}_1^p) \quad (98c)$$

$$\text{Correct} \quad \mathbf{u}_1 = \mathbf{u}_0 + \frac{1}{2}(\dot{\mathbf{u}}_1^p + \dot{\mathbf{u}}_0)dt - \frac{1}{12}(\ddot{\mathbf{u}}_1^p - \ddot{\mathbf{u}}_0)(dt)^2 + \mathcal{O}((dt)^4) \quad (98d)$$

$$\dot{\mathbf{u}}_1 = \dot{\mathbf{u}}_0 + \frac{1}{2}(\ddot{\mathbf{u}}_1^p + \ddot{\mathbf{u}}_0)dt + \mathcal{O}((dt)^3) \quad (98e)$$

$$\text{re-Evaluate} \quad \ddot{\mathbf{u}}_1 = \mathbf{f}(t_1, \mathbf{u}_1, \dot{\mathbf{u}}_1) \quad (98f)$$

wherein $\ddot{\mathbf{u}}_0 = \mathbf{f}(t_0, \mathbf{u}_0, \dot{\mathbf{u}}_0)$ and $t_1 = t_0 + dt$.

5.1.3.2 Two-Step ODE Solver

The two-step method of Freed⁹⁴ for solving second-order ODEs is

$$\begin{aligned} \text{Predict} \quad \mathbf{u}_{n+1}^p &= \frac{1}{3}(4\mathbf{u}_n - \mathbf{u}_{n-1}) + \frac{1}{6}(3\dot{\mathbf{u}}_n + \dot{\mathbf{u}}_{n-1})dt \\ &\quad + \frac{1}{36}(31\ddot{\mathbf{u}}_n - \ddot{\mathbf{u}}_{n-1})(dt)^2 + \mathcal{O}((dt)^4) \end{aligned} \quad (99a)$$

$$\dot{\mathbf{u}}_{n+1}^p = \frac{1}{3}(4\dot{\mathbf{u}}_n - \dot{\mathbf{u}}_{n-1}) + \frac{2}{3}(2\ddot{\mathbf{u}}_n - \ddot{\mathbf{u}}_{n-1})dt + \mathcal{O}((dt)^3) \quad (99b)$$

$$\text{Evaluate} \quad \ddot{\mathbf{u}}_{n+1}^p = \mathbf{f}(t_{n+1}, \mathbf{u}_{n+1}^p, \dot{\mathbf{u}}_{n+1}^p) \quad (99c)$$

$$\begin{aligned} \text{Correct} \quad \mathbf{u}_{n+1} &= \frac{1}{3}(4\mathbf{u}_n - \mathbf{u}_{n-1}) + \frac{1}{24}(\dot{\mathbf{u}}_{n+1}^p + 14\dot{\mathbf{u}}_n + \dot{\mathbf{u}}_{n-1})dt \\ &\quad + \frac{1}{72}(10\ddot{\mathbf{u}}_{n+1}^p + 51\ddot{\mathbf{u}}_n - \ddot{\mathbf{u}}_{n-1})(dt)^2 + \mathcal{O}((dt)^4) \end{aligned} \quad (99d)$$

$$\dot{\mathbf{u}}_{n+1} = \frac{1}{3}(4\dot{\mathbf{u}}_n - \dot{\mathbf{u}}_{n-1}) + \frac{2}{3}\ddot{\mathbf{u}}_{n+1}^p dt + \mathcal{O}((dt)^3) \quad (99e)$$

$$\text{re-Evaluate} \quad \ddot{\mathbf{u}}_{n+1} = \mathbf{f}(t_{n+1}, \mathbf{u}_{n+1}, \dot{\mathbf{u}}_{n+1}) \quad (99f)$$

which is a second-order method for integrating velocities $\dot{\mathbf{u}}$, and a third-order method for integrating displacements \mathbf{u} .

This PECE solver for velocity $\dot{\mathbf{u}}$ has a predictor and a corrector, i.e., Eqns. (99b & 99e), that are the same as those of method (95a & 95c), and as such, this predictor/corrector pair for integrating velocity is consistent. Likewise, in both the predictor and corrector for displacement \mathbf{u} , contributions from the solution \mathbf{u} have a weight of 1, contributions from the velocities $\dot{\mathbf{u}}$ have a weight of $\frac{2}{3}dt$, and contributions from the accelerations $\ddot{\mathbf{u}}$ have a weight of $\frac{5}{6}(dt)^2$; hence, this predictor/corrector pair is internally consistent, too.

5.1.4 A Relevant Example

The finite element problem that we consider here requires solutions for the second-order ODE*

$$\mathbf{M}\ddot{\mathbf{u}} + \mathbf{K}\mathbf{u} = \mathbf{f}(t)$$

where \mathbf{u} is a generalized displacement vector, $\ddot{\mathbf{u}}$ is its acceleration, \mathbf{M} and \mathbf{K} are mass and stiffness matrices, and $\mathbf{f}(t)$ is a forcing function evaluated at current time t . For this system of ODEs, the first step to be taken follows algorithm (98) and is implemented as

Predict	$\mathbf{u}_1^p = \mathbf{u}_0 + \dot{\mathbf{u}}_0 dt + \frac{1}{2}\ddot{\mathbf{u}}_0(dt)^2$
	$\dot{\mathbf{u}}_1^p = \dot{\mathbf{u}}_0 + \ddot{\mathbf{u}}_0 dt$
Evaluate	$\ddot{\mathbf{u}}_1^p = \mathbf{M}^{-1}(\mathbf{f}(t_1) - \mathbf{K}\mathbf{u}_1^p)$
Correct	$\mathbf{u}_1 = \mathbf{u}_0 + \frac{1}{2}(\dot{\mathbf{u}}_1^p + \dot{\mathbf{u}}_0)dt - \frac{1}{12}(\ddot{\mathbf{u}}_1^p - \ddot{\mathbf{u}}_0)(dt)^2$
	$\dot{\mathbf{u}}_1 = \dot{\mathbf{u}}_0 + \frac{1}{2}(\ddot{\mathbf{u}}_1^p + \ddot{\mathbf{u}}_0)dt$
re-Evaluate	$\ddot{\mathbf{u}}_1 = \mathbf{M}^{-1}(\mathbf{f}(t_1) - \mathbf{K}\mathbf{u}_1)$

with continued steps being governed by algorithm (99), which takes on the form of

Predict	$\mathbf{u}_{n+1}^p = \frac{1}{3}(4\mathbf{u}_n - \mathbf{u}_{n-1}) + \frac{1}{6}(3\dot{\mathbf{u}}_n + \dot{\mathbf{u}}_{n-1})dt$
	$+ \frac{1}{36}(31\ddot{\mathbf{u}}_n - \ddot{\mathbf{u}}_{n-1})(dt)^2$
	$\dot{\mathbf{u}}_{n+1}^p = \frac{1}{3}(4\dot{\mathbf{u}}_n - \dot{\mathbf{u}}_{n-1}) + \frac{2}{3}(2\ddot{\mathbf{u}}_n - \ddot{\mathbf{u}}_{n-1})dt$
Evaluate	$\ddot{\mathbf{u}}_{n+1}^p = \mathbf{M}^{-1}(\mathbf{f}(t_{n+1}) - \mathbf{K}\mathbf{u}_{n+1}^p)$
Correct	$\mathbf{u}_{n+1} = \frac{1}{3}(4\mathbf{u}_n - \mathbf{u}_{n-1}) + \frac{1}{24}(\dot{\mathbf{u}}_{n+1}^p + 14\dot{\mathbf{u}}_n + \dot{\mathbf{u}}_{n-1})dt$
	$+ \frac{1}{72}(10\ddot{\mathbf{u}}_{n+1}^p + 51\ddot{\mathbf{u}}_n - \ddot{\mathbf{u}}_{n-1})(dt)^2$
	$\dot{\mathbf{u}}_{n+1} = \frac{1}{3}(4\dot{\mathbf{u}}_n - \dot{\mathbf{u}}_{n-1}) + \frac{2}{3}\ddot{\mathbf{u}}_{n+1}^p dt$
re-Evaluate	$\ddot{\mathbf{u}}_{n+1} = \mathbf{M}^{-1}(\mathbf{f}(t_{n+1}) - \mathbf{K}\mathbf{u}_{n+1})$

where, in this example, velocity $\dot{\mathbf{u}}$ is not needed for the evaluation steps, but it is used by both the prediction and correction steps of integration.

We observe that the mass matrix must not be ill conditioned in order for this algo-

*This solver can also be used to get solutions for the system of equations $\mathbf{M}\ddot{\mathbf{u}} + \mathbf{C}\dot{\mathbf{u}} + \mathbf{K}\mathbf{u} = \mathbf{f}(t)$ wherein \mathbf{M} is a mass matrix, \mathbf{C} is a damping matrix, \mathbf{K} is a stiffness matrix, and \mathbf{f} is a forcing function.

rithm to work as intended. In those cases where the mass matrix does not change with time, it will only need to be evaluated and inverted once. This is an advantage over using the popular Newmark⁹⁶ integrator, where matrix evaluation and inversion is required at every step along its solution paths.

A small amount of damping is often introduced into finite element problems of this type, i.e., a damping matrix \mathbf{C} is introduced so that $\mathbf{M}\ddot{\mathbf{u}} + \mathbf{K}\mathbf{u} = \mathbf{f}(t)$ becomes $\mathbf{M}\ddot{\mathbf{u}} + \mathbf{C}\dot{\mathbf{u}} + \mathbf{K}\mathbf{u} = \mathbf{f}(t)$, where elements of the damping matrix \mathbf{C} are small compared to those of the stiffness matrix \mathbf{K} . This is done to enhance solution stability. Presently, it is not known if this gimmick will be required or not for our application.

5.2. Quadrature Rules for Spatial Integration

The quadrature rules of Gauss are usually selected to integrate over individual elements within a finite element model, because this class of methods have integrators with the smallest errors of approximation. All integrations occur in their natural co-ordinate systems. Four sets of Gauss quadrature rules are cataloged here: for 1D rods, for 2D triangles, for 2D pentagons, and for 3D tetrahedra. Formulae presented in the following tables integrate 1st, 3rd and 5th order polynomials exactly in their respective geometries. Formulae for the pentagon cannot be found elsewhere. Later, in Section 5.3, quadrature rules are presented where the number of Gauss points equals the number of nodal points, which are the integrators that we implement.

5.2.1 Gauss Integration Along a Rod

Quadrature rules that integrate a 1D chord in its natural co-ordinate system, which spans the interval $-1 \leq \xi \leq 1$, are presented in Table 7. These formulae are well known and can be found in any standard textbook on finite elements. Here the integral of some function $f(\xi)$ is approximated via the quadrature rule

$$\mathcal{I} = \int_{-1}^1 f(\xi) d\xi = \sum_{i=1}^n w_i f(\xi_i) + E \quad \text{with} \quad \int_{-1}^1 d\xi = \sum_{i=1}^n w_i = 2 \quad (102)$$

where ξ_i and w_i are the nodes and weights of integration, respectively, for which there are n pairs, with E denoting the error of approximation.

nodes	ξ co-ordinate	weight
Exact for Polynomials of Degree 1		
1	0.000000000000000	2.000000000000000
Exact for Polynomials of Degree 3		
1	-0.577350269189626	1.000000000000000
2	0.577350269189626	1.000000000000000
Exact for Polynomials of Degree 5		
1	-0.774596669241483	0.555555555555556
2	0.000000000000000	0.888888888888889
3	0.774596669241483	0.555555555555556

Table 7 Gauss quadrature weights and nodes for integrating over a line in its natural co-ordinate system ξ . These weights sum to 2, which is the span of its natural co-ordinate. We note that $\sqrt{3}/3 \approx 0.577350269189626$ and that $\sqrt{15}/25 \approx 0.774596669241483$.

5.2.2 Multi-Dimensional Integration

When integrating some function f over, say, a square, one often introduces tensor products of the 1D formulæ (102) whose quadratures are listed in Table 7; specifically, one might construct a quadrature rule that looks like

$$\begin{aligned} \mathcal{I} &= \int_{-1}^1 \int_{-1}^1 f(\xi, \eta) d\xi d\eta = \int_{-1}^1 \sum_{i=1}^n w_i f(\xi_i, \eta) d\eta + E \\ &= \sum_{i=1}^n \sum_{j=1}^n w_i w_j f(\xi_i, \eta_j) + E \quad \text{with} \quad \int_{-1}^1 \int_{-1}^1 d\xi d\eta = \sum_{i=1}^n \sum_{j=1}^n w_i w_j = 4 \end{aligned}$$

which is the integration scheme presented in most textbooks on finite elements. In this approach there is an $n \times n$ grid of nodes that associate with n^2 weights.

The above multi-dimensional formulæ are not optimal, as they require more function evaluations than are usually needed to secure a quadrature rule at some specified order of accuracy. It is more efficient to adopt non-tensor product quadrature rules where, e.g., when integrating over a square, one would have

$$\begin{aligned} \mathcal{I} &= \int_{-1}^1 \int_{-1}^1 f(\xi, \eta) d\xi d\eta = \sum_{i=1}^n w_i f(\xi_i, \eta_i) + E \\ &\quad \text{with} \quad \int_{-1}^1 \int_{-1}^1 d\xi d\eta = \sum_{i=1}^n w_i = 4 \end{aligned}$$

where co-ordinates ξ_i and η_i place the i^{th} node of integration inside a square of area

nodes	ξ co-ordinate	η co-ordinate	weight
Exact for Polynomials of Degree 1			
1	0.33333333333333	0.33333333333333	0.5000000000000000
Exact for Polynomials of Degree 3			
1	0.33333333333333	0.33333333333333	-0.2812500000000000
2	0.2000000000000000	0.6000000000000000	0.2604166666666667
3	0.2000000000000000	0.2000000000000000	0.2604166666666667
4	0.6000000000000000	0.2000000000000000	0.2604166666666667
Exact for Polynomials of Degree 5			
1	0.33333333333333	0.33333333333333	0.1125000000000000
2	0.101286507323456	0.797426985353087	0.062969590272413
3	0.101286507323456	0.101286507323456	0.062969590272413
4	0.797426985353087	0.101286507323456	0.062969590272413
5	0.470142064105115	0.059715871789770	0.066197076394253
6	0.470142064105115	0.470142064105115	0.066197076394253
7	0.059715871789770	0.470142064105115	0.066197076394253

Table 8 Symmetric weights and nodes for Gauss quadratures that integrate over a triangle in its natural co-ordinate system (ξ, η) , where $0 \leq \xi \leq 1$ and $0 \leq \eta \leq 1 - \xi$. These weights sum to $1/2$, which is the area of a triangle when evaluated in its natural co-ordinate system.

4 whose weights of integration are w_i , $i = 1, 2, \dots, n$. We employ such methods.

5.2.3 Gauss Integration of a Triangle

A triangle has natural co-ordinates (ξ, η) that span regions of $0 \leq \xi \leq 1$ and $0 \leq \eta \leq 1 - \xi$ so that an integral of $f(\xi, \eta)$ becomes

$$\mathcal{I} = \int_0^1 \int_{\eta=0}^{1-\xi} f(\xi, \eta) d\eta d\xi = \sum_{i=1}^n w_i f(\xi_i, \eta_i) + E$$

with $\int_0^1 \int_{\eta=0}^{1-\xi} d\eta d\xi = \sum_{i=1}^n w_i = \frac{1}{2}$ (103)

where co-ordinates ξ_i and η_i place the i^{th} node of integration inside a triangle, and whose corresponding weight of integration is w_i , with their being n pairs of nodes and weights. The sum of its weights must equal the area of this triangle, which is $1/2$. Table 8 provides a selection of quadrature rules for such triangles. This table can be found in some finite element textbooks.

node	ξ co-ordinate	η co-ordinate	weight
Exact for Polynomials of Degree 1			
1	0.0000000000000000	0.0000000000000000	2.3776412907378837
Exact for Polynomials of Degree 3			
1	-0.0349156305831802	0.6469731019095136	0.5449124407446143
2	-0.5951653065516678	-0.0321196846022659	0.6439082046243272
3	0.0349156305831798	-0.6469731019095134	0.5449124407446146
4	0.5951653065516677	0.0321196846022661	0.6439082046243275
Exact for Polynomials of Degree 5			
1	-0.0000000000000000	-0.0000000000000002	0.6257871064166934
2	-0.1351253857178451	0.7099621260052327	0.3016384608809768
3	-0.6970858746672087	0.1907259121533272	0.3169910433902452
4	-0.4651171392611024	-0.5531465782166917	0.3155445150066620
5	0.2842948078559476	-0.6644407817506509	0.2958801959111726
6	0.7117958231685716	-0.1251071394727008	0.2575426306970870
7	0.5337947578638855	0.4872045224587945	0.2642573384350463

Table 9 Gauss quadrature weights and nodes (a.k.a., cubature rules) for integrating over a regular pentagon in its natural co-ordinate system (ξ, η). These weights sum to the area of a pentagon inscribing an unit circle, the formula for which is given in Eqn. (6).

5.2.4 Gauss Integration of a Pentagon

Gauss quadrature rules for a regular pentagon described in its natural co-ordinate system, i.e., oriented according to Fig. 7, are presented in Table 9, which describe integrations of the type

$$\mathcal{I} = \iint_{\triangle} f(\xi, \eta) d\eta d\xi = \sum_{i=1}^n w_i f(\xi_i, \eta_i) + E$$

with $\iint_{\triangle} d\eta d\xi = \sum_{i=1}^n w_i = A^p = 2.3776412907378837$ (104)

where co-ordinates ξ_i and η_i place the i^{th} node inside a pentagon, and whose corresponding weight of integration is w_i , with their being n pairs of nodes and weights. The sum of these weights must equal the area of this pentagon $A^p = 5 \sin \omega \cos \omega$ where $2\omega = 108^\circ$ is an inside angle of a regular pentagon, here inscribing the unit circle.

The quadrature rules presented in Table 9 were supplied to the authors by Prof. N.

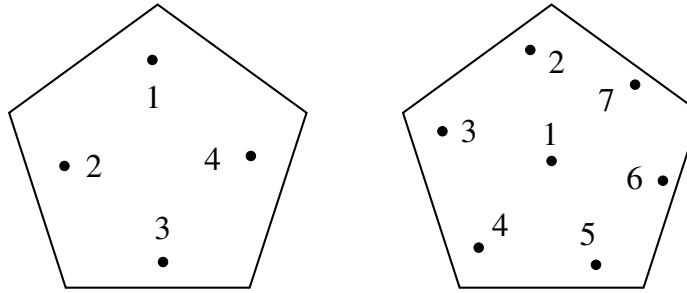


Fig. 32 Locations of generalized, Gaussian, quadrature nodes for the 3rd (left) and 5th (right) degree integration methods presented in Table 9. Vertex 1 is located at the top of the pentagon, cf. Fig. 7, while the coordinate origin is located at its centroid (node 1 in the right figure). It is readily apparent that these quadrature rules are not symmetric.

Sukumar from the University of California at Davis, which he derived for us at our request using a methodology that he had published.⁹⁷ In tabulated form, they cannot be found elsewhere in the literature. In their document, the authors derived non-symmetric cubature formulae for determining the nodes and weights of quadrature for a class of methods. They applied their technique to quadrilaterals, pentagons, hexagons, heptagons and octagons, of which they only published their nodes and weights of quadrature for the hexagon, as hexagons tile two space. The node for the 1st order method for integrating over the area of a pentagon is located at its centroid. Nodes for the 3rd and 5th order methods of Table 9 are displayed in Fig. 32.

The Gaussian quadrature rules of Mousavi, Xiao & Sukumar⁹⁷ presented in Table 9 are compatible with the shape functions of Wachspress^{44,45} and Dasgupta⁴⁸ presented in Section 3.3. More recently, Chakrabort *et al.*⁹⁸ have provided alternative quadrature schemes for pentagons that are also compatible with the Wachspress shape functions. Again, Table 9 cannot be found in the literature.

5.2.5 Gauss Integration of a Tetrahedron

Integrating over the volume of a tetrahedron, when expressed in its natural coordinates (ξ, η, ζ) , which span the ranges of $0 \leq \xi \leq 1$, $0 \leq \eta \leq 1 - \xi$, and

$0 \leq \zeta \leq 1 - \xi - \eta$, approximates an integral of some function $f(\xi, \eta, \zeta)$ as

$$\begin{aligned} \mathcal{I} &= \int_0^1 \int_{\eta=0}^{1-\xi} \int_{\zeta=0}^{1-\xi-\eta} f(\xi, \eta, \zeta) d\zeta d\eta d\xi = \sum_{i=1}^n w_i f(\xi_i, \eta_i, \zeta_i) + E \\ \text{with } &\int_0^1 \int_{\eta=0}^{1-\xi} \int_{\zeta=0}^{1-\xi-\eta} d\zeta d\eta d\xi = \sum_{i=1}^n w_i = \frac{1}{6} \end{aligned} \quad (105)$$

where co-ordinates ξ_i , η_i and ζ_i place the i^{th} node of integration inside a tetrahedron, and whose corresponding weight of integration is w_i , with there being n pairs of nodes and weights. The volume of this tetrahedron is $1/6$. Table 10 provides a selection of quadrature rules for tetrahedra when expressed in their natural co-ordinate system. This table can be found in some finite element textbooks.

5.3. Interpolation: Nodal Points \mapsto Gauss Points

Extrapolation: Gauss Points \mapsto Nodal Points

In a general finite element setting, information comes into the nodes of an element that then gets interpolated down to its Gauss points for their use there. In many applications, and in particular, in ours, one needs to also be able to take fields, in our case the stress and entropy that have been determined at the Gauss points of an element, and extrapolate this information out to the exterior nodes of the element.

Particular to our application, a suite of nodes is common betwixt three, separate, finite element models comprised of twenty common vertices that belong to a dodecahedron used as a geometric model for an alveolus. The resultant force at each vertex arises from: a finite element model of thirty 1D rods representing the alveolar chords, a finite element model of twelve 2D pentagons representing the alveolar membranes, and a finite element model of sixty 3D tetrahedra representing the alveolar sac. The microscopic forces coming from these three models are summed at these twenty common vertices. These resultant forces are then collectively homogenized to yield an averaged macroscopic state of stress for the parenchyma. Feasibility of this solution strategy hinges upon one's ability to *i*) extrapolate stresses evaluated at the Gauss points out to their nodal positions, and *ii*) the conversion of these nodal stresses into nodal forces. We address the first of these two issues in this section, and the second of these two issues in the next section.

Shape functions are introduced for interpolating within an element; specifically,

node	ξ co-ordinate	η co-ordinate	ζ co-ordinate	weight
Exact for Polynomials of Degree 1				
1	0.250000000000000	0.250000000000000	0.250000000000000	0.166666666666667
Exact for Polynomials of Degree 3				
1	0.250000000000000	0.250000000000000	0.250000000000000	-0.133333333333333
2	0.500000000000000	0.166666666666667	0.166666666666667	0.075000000000000
3	0.166666666666667	0.500000000000000	0.166666666666667	0.075000000000000
4	0.166666666666667	0.166666666666667	0.500000000000000	0.075000000000000
5	0.166666666666667	0.166666666666667	0.166666666666667	0.075000000000000
Exact for Polynomials of Degree 5				
1	0.250000000000000	0.250000000000000	0.250000000000000	0.030283678097089
2	0.000000000000000	0.333333333333333	0.333333333333333	0.006026785714286
3	0.333333333333333	0.000000000000000	0.333333333333333	0.006026785714286
4	0.333333333333333	0.333333333333333	0.000000000000000	0.006026785714286
5	0.333333333333333	0.333333333333333	0.333333333333333	0.006026785714286
6	0.727272727272727	0.090909090909091	0.090909090909091	0.011645249086029
7	0.090909090909091	0.727272727272727	0.090909090909091	0.011645249086029
8	0.090909090909091	0.090909090909091	0.727272727272727	0.011645249086029
9	0.090909090909091	0.090909090909091	0.090909090909091	0.011645249086029
10	0.066550153573664	0.433449846426336	0.433449846426336	0.010949141561386
11	0.433449846426336	0.066550153573664	0.433449846426336	0.010949141561386
12	0.433449846426336	0.433449846426336	0.066550153573664	0.010949141561386
13	0.433449846426336	0.066550153573664	0.066550153573664	0.010949141561386
14	0.066550153573664	0.433449846426336	0.066550153573664	0.010949141561386
15	0.066550153573664	0.066550153573664	0.433449846426336	0.010949141561386

Table 10 Symmetric weights and nodes for Gauss quadratures that integrate over a tetrahedron in its natural co-ordinate system (ξ, η, ζ) , where $0 \leq \xi \leq 1 - \eta - \zeta$, $0 \leq \eta \leq 1 - \zeta$ and $0 \leq \zeta \leq 1$. These weights sum to $1/6$, which is the volume of a tetrahedron measured in its natural co-ordinate system.

consider an arbitrary field, say f , whose values are known at the nodes, then

$$f(\boldsymbol{\xi}_k) = \sum_{i=1}^n N_i(\boldsymbol{\xi}_k) f(\boldsymbol{x}_i) \quad k = 1, 2, \dots, m \quad (106a)$$

where the \boldsymbol{x}_i are co-ordinates that locate one of the n vertices in an element of interest, and where the $\boldsymbol{\xi}_i$ are co-ordinates that locate one of its m Gauss points, both being evaluated in the natural co-ordinate system of the element. Functions N_i are the so-called shape (interpolation) functions. They obey $\sum_{i=1}^n N_i(\boldsymbol{\xi}) = 1$.

A corresponding extrapolation scheme can therefore be written down as

$$f(\boldsymbol{x}_k) = \sum_{i=1}^m M_i(\boldsymbol{x}_k) f(\boldsymbol{\xi}_i) \quad k = 1, 2, \dots, n \quad (106b)$$

where the M_i denote extrapolation functions, i.e., they take values of function f , now assumed to be known at all Gauss points $\boldsymbol{\xi}_i$, $i = 1, 2, \dots, m$, and extrapolate them out to their individual nodal points \boldsymbol{x}_k , $k \in \{1, 2, \dots, n\}$. They obey $\sum_{i=1}^m M_i(\boldsymbol{x}) = 1$.

These interpolation/extrapolation functions must also obey the following constraints: either

$$1 = \sum_{i=1}^n N_i(\boldsymbol{\xi}_j) M_j(\boldsymbol{x}_i) \quad j = 1, 2, \dots, m \quad (106c)$$

$$0 = \sum_{i=1}^n N_i(\boldsymbol{\xi}_j) M_k(\boldsymbol{x}_i) \quad j, k = 1, 2, \dots, m, \quad j \neq k \quad (106d)$$

or

$$1 = \sum_{i=1}^m M_i(\boldsymbol{x}_j) N_j(\boldsymbol{\xi}_i) \quad j = 1, 2, \dots, n \quad (106e)$$

$$0 = \sum_{i=1}^m M_i(\boldsymbol{x}_j) N_k(\boldsymbol{\xi}_i) \quad j, k = 1, 2, \dots, n, \quad j \neq k \quad (106f)$$

which follow upon substituting Eqn. (106b) into Eqn. (106a), or vice versa. In this regard, such a pair of interpolation/extrapolation functions are self consistent.

Specifically, whenever $m = n$, the matrices that come about from the interpolation and extrapolation coefficients are reciprocal to one another, with the 0's and 1's of

Eqns. (106c & 106d or 106e & 106f) associating with the individual components of an identity matrix. Consequently, our need to extrapolate information as-well-as interpolate it strongly suggests that the number of Gauss points selected ought to equal the number of nodal points for any given element geometry.

For example, in the case of a tetrahedron one interpolates via

$$\begin{Bmatrix} f(\xi_1) \\ f(\xi_2) \\ f(\xi_3) \\ f(\xi_4) \end{Bmatrix} = \begin{bmatrix} N_1(\xi_1) & N_2(\xi_1) & N_3(\xi_1) & N_4(\xi_1) \\ N_1(\xi_2) & N_2(\xi_2) & N_3(\xi_2) & N_4(\xi_2) \\ N_1(\xi_3) & N_2(\xi_3) & N_3(\xi_3) & N_4(\xi_3) \\ N_1(\xi_4) & N_2(\xi_4) & N_3(\xi_4) & N_4(\xi_4) \end{bmatrix} \begin{Bmatrix} f(x_1) \\ f(x_2) \\ f(x_3) \\ f(x_4) \end{Bmatrix}$$

and extrapolates via

$$\begin{Bmatrix} f(x_1) \\ f(x_2) \\ f(x_3) \\ f(x_4) \end{Bmatrix} = \begin{bmatrix} M_1(x_1) & M_2(x_1) & M_3(x_1) & M_4(x_1) \\ M_1(x_2) & M_2(x_2) & M_3(x_2) & M_4(x_2) \\ M_1(x_3) & M_2(x_3) & M_3(x_3) & M_4(x_3) \\ M_1(x_4) & M_2(x_4) & M_3(x_4) & M_4(x_4) \end{bmatrix} \begin{Bmatrix} f(\xi_1) \\ f(\xi_2) \\ f(\xi_3) \\ f(\xi_4) \end{Bmatrix}$$

where vectors x_1 , x_2 , x_3 and x_4 hold the co-ordinates of the nodal points, and where vectors ξ_1 , ξ_2 , ξ_3 and ξ_4 hold the co-ordinates of their Gauss points, all evaluated in the natural co-ordinate system of the element. The matrices in the above mappings are inverses of one another in this construction.

Our three-model finite element analysis of an alveolus requires the use of rods with two nodes, triangles with three nodes, tetrahedra with four nodes, and pentagons with five nodes. We now provide consistent interpolation/extrapolation procedures for these geometries. This requires the selection of a two-point quadrature rule for rods, a three-point quadrature rule for triangles, a four point quadrature rule for tetrahedra, and a five-point quadrature rule for pentagons. Our selections, and their associated interpolation/extrapolation pairs, are presented below.

5.3.1 Self-Consistent Interpolation/Extrapolation Procedures for Rods

Considering a rod with two Gauss points, the interpolation of an arbitrary field, say f , whose values are known at nodal points x_i , $i = 1, 2$, into approximated values located at Gauss points ξ_i , assigned according to Table 11, while selecting shape (interpolation) functions $N_1 = \frac{1}{2}(1 - \xi)$ and $N_2 = \frac{1}{2}(1 + \xi)$, where $-1 \leq \xi \leq 1$,

node	ξ co-ordinate	weight
1	$-\sqrt{3}/3$	1
2	$\sqrt{3}/3$	1

Table 11 A Gauss quadrature rule for integrating functions over the lengths of rods. It approximates $\int_{-1}^1 f(\xi) d\xi$ using two quadrature points. The weights of quadrature sum to its length because $L = \int_{-1}^1 d\xi = 2$. This quadrature rule is from Christoffel. It integrates polynomials along a line exactly up through second order.

results in an interpolation that maps values for a field from nodes to Gauss point via

$$\begin{Bmatrix} f(-\sqrt{3}/3) \\ f(\sqrt{3}/3) \end{Bmatrix} = \frac{1}{6} \begin{bmatrix} 3 + \sqrt{3} & 3 - \sqrt{3} \\ 3 - \sqrt{3} & 3 + \sqrt{3} \end{bmatrix} \begin{Bmatrix} f(-1) \\ f(1) \end{Bmatrix} \quad (107a)$$

that, upon applying the methodology put forward in Eqn. (106), leads to a straightforward extrapolation formula that maps values for the field from Gauss points to nodes via

$$\begin{Bmatrix} f(-1) \\ f(1) \end{Bmatrix} = \frac{1}{2\sqrt{3}} \begin{bmatrix} \sqrt{3} + 3 & \sqrt{3} - 3 \\ \sqrt{3} - 3 & \sqrt{3} + 3 \end{bmatrix} \begin{Bmatrix} f(-\sqrt{3}/3) \\ f(\sqrt{3}/3) \end{Bmatrix}. \quad (107b)$$

This extrapolation matrix can be found in Oñate [99, pg. 332]. As a check, each row in this matrix sums to 1. Furthermore, the matrices in Eqns. (107a & 107b) are reciprocals to one another, as they must be.

5.3.2 Self-Consistent Interpolation/Extrapolation Procedures for Triangles

Now, considering a triangle with three Gauss points, the interpolation of an arbitrary field f whose values are known at nodal points \mathbf{x}_i , $i = 1, 2, 3$, into approximated values located at Gauss points ξ , assigned according to Table 12, while selecting shape (interpolation) functions $N_1 = 1 - \xi - \eta$, $N_2 = \xi$, and $N_3 = \eta$, where $0 \leq \xi \leq 1$ and $0 \leq \eta \leq 1 - \xi$, results in an interpolation that maps according to

$$\begin{Bmatrix} f(1/6, 1/6) \\ f(2/3, 1/6) \\ f(1/6, 2/3) \end{Bmatrix} = \frac{1}{6} \begin{bmatrix} 4 & 1 & 1 \\ 1 & 4 & 1 \\ 1 & 1 & 4 \end{bmatrix} \begin{Bmatrix} f(0, 0) \\ f(1, 0) \\ f(0, 1) \end{Bmatrix} \quad (108a)$$

node	ξ co-ordinate	η co-ordinate	weight
1	1/6	1/6	1/6
2	2/3	1/6	1/6
3	1/6	2/3	1/6

Table 12 A Gauss quadrature rule for integrating functions over the areas of triangles. It approximates $\int_0^1 \int_0^{1-\xi} f(\xi, \eta) d\eta d\xi$ using three quadrature points. The weights of quadrature sum to its area because $A = \int_0^1 \int_0^{1-\xi} d\eta d\xi = 1/2$. This quadrature rule is from Strang. It integrates polynomials over a triangular region exactly up through second order.

that, upon applying the methodology put forward in Eqn. (106), which requires some algebra, leads to a simple extrapolation formula applicable for triangles when evaluated in their natural co-ordinate system, viz.,

$$\begin{Bmatrix} f(0, 0) \\ f(1, 0) \\ f(0, 1) \end{Bmatrix} = \frac{1}{3} \begin{bmatrix} 5 & -1 & -1 \\ -1 & 5 & -1 \\ -1 & -1 & 5 \end{bmatrix} \begin{Bmatrix} f(1/6, 1/6) \\ f(2/3, 1/6) \\ f(1/6, 2/3) \end{Bmatrix}. \quad (108b)$$

As a check, each row in both matrices sums to 1 and, as expected, plus these matrices are reciprocals to one another.

5.3.3 Self-Consistent Interpolation/Extrapolation Procedures for Tetrahedra

We now consider a tetrahedron with four Gauss points. Here the interpolation of an arbitrary field f whose values are known at nodal points x_i , $i = 1, 2, 3, 4$, into approximated values located at Gauss points ξ_i , assigned according to Table 13, while selecting shape functions $N_1 = 1 - \xi - \eta - \zeta$, $N_2 = \xi$, $N_3 = \eta$, and $N_4 = \zeta$, bounded by $0 \leq \xi \leq 1$, $0 \leq \eta \leq 1 - \xi$ and $0 \leq \zeta \leq 1 - \xi - \eta$, leads to the following interpolation formula

$$\begin{Bmatrix} f(a, a, a) \\ f(b, a, a) \\ f(a, b, a) \\ f(a, a, b) \end{Bmatrix} = \begin{bmatrix} 1 - 3a & a & a & a \\ 1 - 2a - b & b & a & a \\ 1 - 2a - b & a & b & a \\ 1 - 2a - b & a & a & b \end{bmatrix} \begin{Bmatrix} f(0, 0, 0) \\ f(1, 0, 0) \\ f(0, 1, 0) \\ f(0, 0, 1) \end{Bmatrix} \quad (109a)$$

node	ξ co-ordinate	η co-ordinate	ζ co-ordinate	weight
1	0.1381966011250105	0.1381966011250105	0.1381966011250105	1/24
2	0.5854101966249685	0.1381966011250105	0.1381966011250105	1/24
3	0.1381966011250105	0.5854101966249685	0.1381966011250105	1/24
4	0.1381966011250105	0.1381966011250105	0.5854101966249685	1/24

Table 13 A Gauss quadrature rule for integrating functions over the volumes of tetrahedra.
It approximates $\int_0^1 \int_0^{1-\xi} \int_0^{1-\xi-\eta} f(\xi, \eta, \zeta) d\zeta d\eta d\xi$ **using four quadrature points. The weights of quadrature sum to its volume because** $V = \int_0^1 \int_0^{1-\xi} \int_0^{1-\xi-\eta} d\zeta d\eta d\xi = 1/6$. **This quadrature rule is from Keast. It integrates polynomials over a tetrahedral region exactly up through second order. As a point of reference, the centroid has co-ordinates** $(1/4, 1/4, 1/4)$.

that, upon applying the methodology put forward in Eqn. (106), which now requires a good deal of algebra, results in the following extrapolation formula for tetrahedra

$$\begin{Bmatrix} f(0, 0, 0) \\ f(1, 0, 0) \\ f(0, 1, 0) \\ f(0, 0, 1) \end{Bmatrix} = \frac{1}{b-a} \begin{bmatrix} 2a+b & -a & -a & -a \\ 2a+b-1 & 1-a & -a & -a \\ 2a+b-1 & -a & 1-a & -a \\ 2a+b-1 & -a & -a & 1-a \end{bmatrix} \begin{Bmatrix} f(a, a, a) \\ f(b, a, a) \\ f(a, b, a) \\ f(a, a, b) \end{Bmatrix} \quad (109b)$$

where $a = 0.1381966011250105$ and $b = 0.5854101966249685$ from Table 13. As a check, each row in the above matrices sums to 1. Unlike the interpolation/extrapolation formulae for rods and triangles, whose matrices are symmetric, here these matrices of interpolation/extrapolation coefficients are not symmetric.

5.3.4 Self-Consistent Interpolation/Extrapolation Procedures for Pentagons

We only know of two papers where quadrature formulae have been created for integrating over the area of pentagons.^{97,98} Neither presents tables for their nodes and weights of quadrature, cf. Section 5.2 for such a table. Only mathematical methodologies from which one can numerically construct such tables are published. Also, neither of their strategies exploits the symmetry properties of a pentagon.

Because we seek a quadrature rule for regular pentagons that employs five Gauss points, and pentagons possess five radial lines of symmetry, it is reasonable to consider that the five nodes of quadrature that we seek lie along these five radial lines. Specifically, we seek a quadrature rule for a pentagon whose vertices are located at

$\boldsymbol{x}_i, i = 1, 2, \dots, 5$, and whose nodes of quadrature are located at ξ_i such that

$$\boldsymbol{x}_1 = (\cos(\pi/2), \sin(\pi/2)) \quad \xi_1 = \ell \boldsymbol{x}_1 \quad (110\text{a})$$

$$\boldsymbol{x}_2 = (\cos(9\pi/10), \sin(9\pi/10)) \quad \xi_2 = \ell \boldsymbol{x}_2 \quad (110\text{b})$$

$$\boldsymbol{x}_3 = (\cos(13\pi/10), \sin(13\pi/10)) \quad \xi_3 = \ell \boldsymbol{x}_3 \quad (110\text{c})$$

$$\boldsymbol{x}_4 = (\cos(17\pi/10), \sin(17\pi/10)) \quad \xi_4 = \ell \boldsymbol{x}_4 \quad (110\text{d})$$

$$\boldsymbol{x}_5 = (\cos(\pi/10), \sin(\pi/10)) \quad \xi_5 = \ell \boldsymbol{x}_5 \quad (110\text{e})$$

where lines radiating from the origin out to vertices \boldsymbol{x}_i each have unit length, while those that radiate out to the Gauss points ξ have a shorter length of ℓ .

Implementing the strategies that underlie Gauss quadrature, length ℓ represents a distance out to the centroid of an area. In our case, this area (one of five equivalent areas) is a four-sided polygon whose apex has an inside angle of 108° , whose shoulders have right angles, and whose inside angle at the origin is 72° . A little bit of geometry and algebra leads to the result that

$$\ell = \frac{1 + \sin(3\pi/10)}{3 \sin(3\pi/10)} \approx 0.7454 \quad (111\text{a})$$

whose associated area becomes the weight of quadrature

$$w = \sin(3\pi/10) \cos(3\pi/10) \approx 0.4755 \quad (111\text{b})$$

which is one-fifth the area of a pentagon, cf. Eqn. (6). To the best of our knowledge, the quadrature rule put forward in Eqns. (110 & 111) for regular pentagons is new to the literature.

Interpolation is described through shape functions. Adopting the shape functions of Wachspress, which were constructed in Section 3.3 for a pentagon, while using the quadrature rule of Eqns. (110 & 111), results in a symmetric interpolation map of

$$\begin{Bmatrix} f(\xi_1) \\ f(\xi_2) \\ f(\xi_3) \\ f(\xi_4) \\ f(\xi_5) \end{Bmatrix} = \begin{bmatrix} a & b & c & c & b \\ b & a & b & c & c \\ c & b & a & b & c \\ c & c & b & a & b \\ b & c & c & b & a \end{bmatrix} \begin{Bmatrix} f(\boldsymbol{x}_1) \\ f(\boldsymbol{x}_2) \\ f(\boldsymbol{x}_3) \\ f(\boldsymbol{x}_4) \\ f(\boldsymbol{x}_5) \end{Bmatrix} \quad (112\text{a})$$

with elements sized as $a = 0.6901471673508344$, $b = 0.1367959452017669$ and $c = 0.0181304711228159$, and an ensuing extrapolation map that is described by

$$\begin{Bmatrix} f(\boldsymbol{x}_1) \\ f(\boldsymbol{x}_2) \\ f(\boldsymbol{x}_3) \\ f(\boldsymbol{x}_4) \\ f(\boldsymbol{x}_5) \end{Bmatrix} = \frac{1}{\Delta} \begin{bmatrix} x & y & z & z & y \\ y & x & y & z & z \\ z & y & x & y & z \\ z & z & y & x & y \\ y & z & z & y & x \end{bmatrix} \begin{Bmatrix} f(\boldsymbol{\xi}_1) \\ f(\boldsymbol{\xi}_2) \\ f(\boldsymbol{\xi}_3) \\ f(\boldsymbol{\xi}_4) \\ f(\boldsymbol{\xi}_5) \end{Bmatrix} \quad (112b)$$

wherein

$$x = a^2 + (a - b)(b + c) - c^2 \quad (112c)$$

$$y = (b + c)c - (a + b)b \quad (112d)$$

$$z = b^2 - (a - b)c - c^2 \quad (112e)$$

$$\Delta = a^2 - (a + b)b - (a - 3b)c - c^2 \quad (112f)$$

where, as a check, $\sum_{i=1}^5 N_i(\boldsymbol{\xi}_j) = 1$ and $\sum_{i=1}^5 M_i(\boldsymbol{x}_j) = 1$ for $j = 1, 2, \dots, 5$, and therefore, $a + 2b + 2c = 1$ and $x + 2y + 2z = \Delta$. Furthermore, these coefficient matrices for interpolation and extrapolation are inverses to one another.

5.4. Converting Nodal Stresses into Nodal Forces

Part 6

Variational Formulation

The problem we have set up to solve takes on the general form of a second-order, hyperbolic, ordinary, differential equation; specifically,

$$\mathbf{M}\ddot{\mathbf{u}} + \mathbf{K}\mathbf{u} = \mathbf{f}(t) \quad (113)$$

where \mathbf{M} is a mass matrix, \mathbf{K} is a stiffness matrix, \mathbf{f} is a forcing function dependent upon time t , and \mathbf{u} is a displacement vector with $\ddot{\mathbf{u}}$ denoting acceleration. At present, a possible contribution arising from dissipation is not included, e.g., a $\mathbf{C}\dot{\mathbf{u}}$ term accounting for viscoelastic effects. The numerical solution strategy employed to solve this ODE is discussed in Section 5.1.3.2, which requires \mathbf{M} to be an invertible matrix.

A dodecahedron used to model an alveolar sac is our problem of interest. The shape of an irregular dodecahedron is described by a set of 20 vertices, each experiencing a displacement

$$\mathbf{u}_i = \{u_{xi}, u_{yi}, u_{zi}\}^\top := \{x_i - x_{0i}, y_i - y_{0i}, z_i - z_{0i}\}^\top, \quad i = 1, 2, \dots, 20 \quad (114)$$

that contains co-ordinate differences at a dodecahedral vertex evaluated in the physical co-ordinate frame of this dodecahedron ($\vec{\mathbf{E}}_1, \vec{\mathbf{E}}_2, \vec{\mathbf{E}}_3$), as established in Section 2.1, with each vertex i having reference co-ordinates denoted as $\{x_{0i}, y_{0i}, z_{0i}\}^\top$ and current co-ordinates denoted as $\{x_i, y_i, z_i\}^\top$. The 20 vertices of a dodecahedron uniquely establish its 30 alveolar chords, its 12 alveolar septa, and the alveolar sac that these chords and septa envelop, cf. Section 2.6.

When assembled, vectors \mathbf{f} , \mathbf{u} and $\ddot{\mathbf{u}}$ have lengths of 60 for the alveolar chord and septa models, and a length of 63 for the alveolar sac model, while matrices \mathbf{M} and \mathbf{K} have dimensions of 60×60 for the alveolar chord and septa models, and dimensions of 63×63 for the alveolar sac model. The model for alveolar volume has an extra node located at the centroid of the dodecahedron, which is a node in common betwixt the 60 tetrahedra needed to fill the volume of a dodecahedron in our modeling of an alveolus.

DRAFT: UNCLASSIFIED

As a modeling simplification, the alveolar chords, the alveolar septa, and the alveolar sac are each modeled separately. It is the nodal forces, i.e., forces at the vertices, resulting from these three, separate, finite-element models that are then summed. These are obtained by interpolating the stresses integrated at each model's Gauss points out to these common nodes, which belong to the set of dodecahedral vertices. These three sources for vertex force can be added, from which an uniform (homogenized) state of stress can then be calculated for return.

Consequently, we are constructing three, individual, finite-element models governed by the following systems of hyperbolic differential equations

$$\mathbf{M}_{1D}\ddot{\mathbf{u}} + \mathbf{K}_{1D}\mathbf{u} = \mathbf{f}_{1D}(t) \quad (115a)$$

$$\mathbf{M}_{2D}\ddot{\mathbf{u}} + \mathbf{K}_{2D}\mathbf{u} = \mathbf{f}_{2D}(t) \quad (115b)$$

$$\mathbf{M}_{3D}\ddot{\mathbf{u}} + \mathbf{K}_{3D}\mathbf{u} = \mathbf{f}_{3D}(t) \quad (115c)$$

where subscript ' $_{1D}$ ' designates alveolar chords, subscript ' $_{2D}$ ' designates alveolar septa, and subscript ' $_{3D}$ ' designates an alveolar sac. It is thought to be necessary to split the overall problem into these three subproblems due to the vast differences in their compliance moduli.

6.1. Mass Matrix

A consistent mass matrix¹⁰⁰ for an element, established in its natural co-ordinate system, is defined as

$$\mathbf{M}_C = \int_V \rho \mathbf{N}^T \mathbf{N} dV \quad (116)$$

wherein \mathbf{N} is the shape function matrix for an element of interest whose mass density is ρ . This mass matrix is said to be consistent in that it is calculated with the same shape functions that are used to create the stiffness matrix. Consistent mass matrices are symmetric. Unfortunately, they may be singular, too, which is not a desirable feature for our chosen numerical approach.

To construct a non-singular mass matrix, we introduce a lumped mass matrix. Specifically, a sum of all column elements for each row of a consistent mass matrix establishes the diagonal elements of a lumped mass matrix¹⁰¹ in that

$$\mathbf{M}_L = \sum_{i=1}^n M_{Li} \quad \text{where} \quad M_{Li} = \sum_{j=1}^n \int_V \rho N_i N_j dV \quad (117)$$

wherein $\sum_{j=1}^n N_j = 1$, with i being a Gauss point from the n Gauss points in an element.

A lumped-consistent (or weighted) mass matrix \mathbf{M}_W can be created as follows

$$\mathbf{M}_W = (1 - \mu) \mathbf{M}_C + \mu \mathbf{M}_L \quad (118)$$

wherein μ is a free scalar parameter for weighting the consistent and lumped mass matrices. The reason for mixing \mathbf{M}_C and \mathbf{M}_L is to ensure a nonsingular mass matrix. In this work, μ is taken to be a half, i.e., an averaged mass matrix is adopted, which has a nice property of minimizing low frequency dispersion; specifically,

$$\mathbf{M}_A := \frac{1}{2} (\mathbf{M}_C + \mathbf{M}_L) \quad (119)$$

is how we shall construct all of our mass matrices. The averaged mass matrix \mathbf{M}_A is invertible—a requirement of the selected numerical solution strategy presented in Section 5.1.3.2.

6.1.1 Mass Matrices for a Chord

A two-noded alveolar chord has shape functions N_i that, when evaluated in its natural co-ordinate system wherein $-1 \leq \xi \leq 1$, aggregate into a matrix of shape functions

$$\mathbf{N} = \begin{bmatrix} N_1 & N_2 \end{bmatrix} = \begin{bmatrix} \frac{1}{2}(1-\xi) & \frac{1}{2}(1+\xi) \end{bmatrix}$$

with $N_{1,\xi} = -\frac{1}{2}$ and $N_{2,\xi} = \frac{1}{2}$ (120)

where ξ is an abscissa associated with a specific Gauss quadrature rule, cf. Table 7.

The Jacobian matrix \mathbf{J} for a one-dimensional chord, which is also its Jacobian determinant $|\mathbf{J}|$, is used to transform the integrals in Eqns. (116 & 117) from their global co-ordinate system into their natural co-ordinate system. It has a value of

$$\mathbf{J} \equiv |\mathbf{J}| = \sum_{i=1}^2 N_{i,\xi}(\xi) x_i = -\frac{1}{2} \cdot -\frac{1}{2}L + \frac{1}{2} \cdot \frac{1}{2}L = \frac{1}{2}L \quad (121)$$

given nodal co-ordinates of $x_1 = -\frac{1}{2}L$ and $x_2 = \frac{1}{2}L$, where L is the length of our alveolar chord. The Jacobian matrix and its Jacobian determinant are equal in the case of a rod, because the space is one dimensional.

The consistent mass matrix for a 1D alveolar chord modeled as a two-noded rod, when evaluated in its natural co-ordinate system, becomes

$$\begin{aligned} \mathbf{M}_{1C} &= \int_0^L \rho \mathbf{N}^\top \mathbf{N} A dx = \int_{-1}^1 \rho \mathbf{N}^\top \mathbf{N} A |\mathbf{J}| d\xi \\ &= \sum_{i=1}^n \rho \mathbf{N}^\top(\xi_i) \mathbf{N}(\xi_i) A |\mathbf{J}| w_i \\ &= \sum_{i=1}^n \frac{\rho A L w_i}{8} \begin{bmatrix} 1 - 2\xi_i + \xi_i^2 & 1 - \xi_i^2 \\ 1 - \xi_i^2 & 1 + 2\xi_i + \xi_i^2 \end{bmatrix} \end{aligned} \quad (122)$$

with $\mathbf{N}(\xi_i)$ and w_i being the shape functions and weights of quadrature for a selected Gauss integration rule evaluated at its Gauss point i , while A is the cross-sectional area of our alveolar chord. Table 7 presents values for the abscissæ ξ_i and weights w_i of integration for schemes where there are $n = 1, 2$ or 3 nodes of integration along an alveolar chord.

The lumped mass matrix for a 1D alveolar chord in its natural co-ordinate system

is

$$\begin{aligned} \mathbf{M}_{1L} &= \sum_{\text{rows}} \sum_{i=1}^n \frac{\rho AL w_i}{8} \begin{bmatrix} 1 - 2\xi_i + \xi_i^2 & 1 - \xi_i^2 \\ 1 - \xi_i^2 & 1 + 2\xi_i + \xi_i^2 \end{bmatrix} \\ &= \sum_{i=1}^n \frac{\rho AL w_i}{4} \begin{bmatrix} 1 - \xi_i & 0 \\ 0 & 1 + \xi_i \end{bmatrix} \quad (123) \end{aligned}$$

where it is seen that the mass matrix in Eqn. (122) is singular at any given Gauss point, whereas the mass matrix in Eqn. (123) has a reciprocal, except when $\xi = \pm 1$.

Chordal mass matrices associated with the Gauss quadratures listed in Table 7 become: the consistent mass matrices for a chord are

$$\mathbf{M}_{1C} = \frac{\rho AL}{4} \begin{bmatrix} 1 & 1 \\ 1 & 1 \end{bmatrix} \quad \mathbf{M}_{1C} = \frac{\rho AL}{6} \begin{bmatrix} 2 & 1 \\ 1 & 2 \end{bmatrix} \quad \mathbf{M}_{1C} = \frac{\rho AL}{6} \begin{bmatrix} 2 & 1 \\ 1 & 2 \end{bmatrix} \quad (124a)$$

the lumped mass matrices for a chord are

$$\mathbf{M}_{1L} = \frac{\rho AL}{2} \begin{bmatrix} 1 & 0 \\ 0 & 1 \end{bmatrix} \quad \mathbf{M}_{1L} = \frac{\rho AL}{2} \begin{bmatrix} 1 & 0 \\ 0 & 1 \end{bmatrix} \quad \mathbf{M}_{1L} = \frac{\rho AL}{2} \begin{bmatrix} 1 & 0 \\ 0 & 1 \end{bmatrix} \quad (124b)$$

that when averaged become

$$\mathbf{M}_{1A} = \frac{\rho AL}{8} \begin{bmatrix} 3 & 1 \\ 1 & 3 \end{bmatrix} \quad \mathbf{M}_{1A} = \frac{\rho AL}{12} \begin{bmatrix} 5 & 1 \\ 1 & 5 \end{bmatrix} \quad \mathbf{M}_{1A} = \frac{\rho AL}{12} \begin{bmatrix} 5 & 1 \\ 1 & 5 \end{bmatrix} \quad (124c)$$

which are the mass matrices that we employ. This collection of mass matrices pertain to one Gauss point (left column of mass matrices), two Gauss points (center column of mass matrices), and three Gauss points (right column of mass matrices). For this element, there is no difference between the mass matrices for two and three Gauss points of integration. In the derivation of these matrices, it is assumed that the cross-sectional area and mass density are both uniform along the length of a septal chord. Furthermore, because septal chord volume V is considered to be preserved, i.e., $V = V_0$ where $V_0 = A_0 L_0$ and $V = AL$, it follows that these mass matrices are constant; hence, they only need to be inverted once.

6.1.1.1 Assemble Mass Matrices for the Septal Chords

6.1.2 Mass Matrices for a Pentagon

For an alveolar septa represented as an irregular pentagon, its matrix of shape functions \mathbf{N} takes on the form of

$$\mathbf{N} = \begin{bmatrix} N_1 & 0 & N_2 & 0 & N_3 & 0 & N_4 & 0 & N_5 & 0 \\ 0 & N_1 & 0 & N_2 & 0 & N_3 & 0 & N_4 & 0 & N_5 \end{bmatrix} \quad (125)$$

where N_i , $i = 1, \dots, 5$, are the five shape functions that correspond with the five vertices of a pentagon, as established in Eqn. (20).

A consistent mass matrix \mathbf{M}_{2C} is constructed by substituting the above matrix of shape functions into the following expression

$$\mathbf{M}_{2C} = \iint_{\triangle} \rho \mathbf{N}^T \mathbf{N} |\mathbf{J}| h d\xi d\eta \quad (126)$$

with h denoting membrane thickness, and where $|\mathbf{J}|$ specifies the determinant of its 2×2 Jacobian matrix \mathbf{J} . In areal derivations, the Jacobian of a two-dimensional transformation connects the physical x, y to the natural ξ, η co-ordinate systems involved. Components of this Jacobian matrix are calculated using derivatives of shape functions taken with respect to the local co-ordinates at the i^{th} vertex via

$$\mathbf{J} = \begin{bmatrix} \partial x / \partial \xi & \partial y / \partial \xi \\ \partial x / \partial \eta & \partial y / \partial \eta \end{bmatrix} = \begin{bmatrix} \sum_{i=1}^5 N_{i,\xi}(\xi, \eta) x_i & \sum_{i=1}^5 N_{i,\xi}(\xi, \eta) y_i \\ \sum_{i=1}^5 N_{i,\eta}(\xi, \eta) x_i & \sum_{i=1}^5 N_{i,\eta}(\xi, \eta) y_i \end{bmatrix} \quad (127)$$

where the shape function gradients $N_{i,\xi}$ and $N_{i,\eta}$ have been established in Eqn. (24), with

$$\mathbf{J}^{-1} = \frac{1}{|\mathbf{J}|} \begin{bmatrix} \partial y / \partial \eta & -\partial y / \partial \xi \\ -\partial x / \partial \eta & \partial x / \partial \xi \end{bmatrix} \quad \text{wherein} \quad |\mathbf{J}| = \frac{\partial x}{\partial \xi} \frac{\partial y}{\partial \eta} - \frac{\partial x}{\partial \eta} \frac{\partial y}{\partial \xi} \quad (128)$$

providing its inverse and Jacobian determinant. A numerical integration of Eqn. (126) results in

$$\mathbf{M}_{2C} = \rho h \sum_{i=1}^n \mathbf{N}^T(\xi_i, \eta_i) \mathbf{N}(\xi_i, \eta_i) |\mathbf{J}(\xi_i, \eta_i)| w_i \quad (129)$$

where co-ordinates ξ_i and η_i locate a Gauss point i within the pentagon whose associate weight of integration is w_i , which can be found in Table 9. Here it is assumed that the mass density ρ and membrane thickness h are uniform across the

alveolar septa.

A lumped mass matrix for a pentagon gets its diagonal elements as follows

$$M_{2Li} = \sum_{j=1}^n M_{2Cij} \quad (130)$$

because $\sum_{j=1}^n N_j = 1$.

For instance, the averaged lumped-consistent mass matrix for a pentagon with 1 Gauss point of integration located at its centroid is constructed by averaging its consistent and lumped mass matrices resulting in

$$\mathbf{M}_{2A} = \frac{\rho h A}{100} \begin{bmatrix} 6 & 0 & 1 & 0 & 1 & 0 & 1 & 0 & 1 & 0 \\ 0 & 6 & 0 & 1 & 0 & 1 & 0 & 1 & 0 & 1 \\ 1 & 0 & 6 & 0 & 1 & 0 & 1 & 0 & 1 & 0 \\ 0 & 1 & 0 & 6 & 0 & 1 & 0 & 1 & 0 & 1 \\ 1 & 0 & 1 & 0 & 6 & 0 & 1 & 0 & 1 & 0 \\ 0 & 1 & 0 & 1 & 0 & 6 & 0 & 1 & 0 & 1 \\ 1 & 0 & 1 & 0 & 1 & 0 & 6 & 0 & 1 & 0 \\ 0 & 1 & 0 & 1 & 0 & 1 & 0 & 6 & 0 & 1 \\ 1 & 0 & 1 & 0 & 1 & 0 & 1 & 0 & 6 & 0 \\ 0 & 1 & 0 & 1 & 0 & 1 & 0 & 1 & 0 & 6 \end{bmatrix} \quad (131)$$

where h and A are the thickness and area of the membrane. It just so happens that, in this case, the mass matrix turns out nice. Because septal volume V is considered to be preserved, i.e., $V = V_0$ where $V_0 = h_0 A_0$ and $V = hA$, it follows that this mass matrix is constant; hence, its inverse need only be determined once.

Three mass matrices have been constructed for a pentagon based upon the three, Gauss, quadrature rules presented in Table 9, which integrate polynomials of orders 1, 3 and 5 exactly, respectively.

6.1.2.1 Assemble Mass Matrices for the Alveolar Septa

6.1.3 Mass Matrices for a Tetrahedron

A dodecahedron has 60 individual tetrahedra contained within it, whose centroid is a common vertex to all 60 of these tetrahedra. Hence, an analysis to find the mass matrix of a tetrahedron is used as the building block needed to assemble the mass

matrix for an alveolar sac.

The matrix of shape functions \mathbf{N} for a tetrahedron has the form of

$$\mathbf{N} = \begin{bmatrix} N_1 & 0 & 0 & N_2 & 0 & 0 & N_3 & 0 & 0 & N_4 & 0 & 0 \\ 0 & N_1 & 0 & 0 & N_2 & 0 & 0 & N_3 & 0 & 0 & N_4 & 0 \\ 0 & 0 & N_1 & 0 & 0 & N_2 & 0 & 0 & N_3 & 0 & 0 & N_4 \end{bmatrix} \quad (132)$$

in which N_i , $i = 1, 2, 3, 4$, are the four shape functions corresponding to the four vertices of a tetrahedron that are defined as follows

$$N_1 = 1 - \xi - \eta - \zeta \quad (133a)$$

$$N_2 = \xi \quad (133b)$$

$$N_3 = \eta \quad (133c)$$

$$N_4 = \zeta. \quad (133d)$$

Numerical integration is used to obtain the mass matrix of a tetrahedron via

$$\begin{aligned} \mathbf{M}_{3C} &= \iiint_V \rho \mathbf{N}^T \mathbf{N} dx dy dz = \int_0^1 \int_0^1 \int_0^1 \rho \mathbf{N}^T \mathbf{N} |\mathbf{J}| d\xi d\eta d\zeta \\ &= \rho \sum_{i=1}^n \mathbf{N}^T(\xi_i, \eta_i, \zeta_i) \mathbf{N}(\xi_i, \eta_i, \zeta_i) |\mathbf{J}(\xi_i, \eta_i, \zeta_i)| w_i \end{aligned} \quad (134)$$

with $|\mathbf{J}|$ being the determinant of the Jacobian matrix, and n denoting the number of Gauss points used for integration. The Jacobian is calculated from derivatives of the shape functions taken with respect to its local co-ordinates (ξ, η, ζ) that associate with their current global co-ordinates (x_i, y_i, z_i) according to

$$\begin{aligned} \mathbf{J} &= \begin{bmatrix} \partial x / \partial \xi & \partial y / \partial \xi & \partial z / \partial \xi \\ \partial x / \partial \eta & \partial y / \partial \eta & \partial z / \partial \eta \\ \partial x / \partial \zeta & \partial y / \partial \zeta & \partial z / \partial \zeta \end{bmatrix} = \begin{bmatrix} x_{,\xi} & y_{,\xi} & z_{,\xi} \\ x_{,\eta} & y_{,\eta} & z_{,\eta} \\ x_{,\zeta} & y_{,\zeta} & z_{,\zeta} \end{bmatrix} \\ &= \begin{bmatrix} \sum_{i=1}^4 N_{i,\xi}(\xi, \eta, \zeta) x_i & \sum_{i=1}^4 N_{i,\xi}(\xi, \eta, \zeta) y_i & \sum_{i=1}^4 N_{i,\xi}(\xi, \eta, \zeta) z_i \\ \sum_{i=1}^4 N_{i,\eta}(\xi, \eta, \zeta) x_i & \sum_{i=1}^4 N_{i,\eta}(\xi, \eta, \zeta) y_i & \sum_{i=1}^4 N_{i,\eta}(\xi, \eta, \zeta) z_i \\ \sum_{i=1}^4 N_{i,\zeta}(\xi, \eta, \zeta) x_i & \sum_{i=1}^4 N_{i,\zeta}(\xi, \eta, \zeta) y_i & \sum_{i=1}^4 N_{i,\zeta}(\xi, \eta, \zeta) z_i \end{bmatrix} \end{aligned} \quad (135)$$

with

$$\mathbf{J}^{-1} = \frac{1}{|\mathbf{J}|} \begin{bmatrix} y_{,\eta} z_{,\zeta} - z_{,\eta} y_{,\zeta} & z_{,\xi} y_{,\zeta} - y_{,\xi} z_{,\zeta} & y_{,\xi} z_{,\eta} - y_{,\eta} z_{,\xi} \\ z_{,\eta} x_{,\zeta} - x_{,\eta} z_{,\zeta} & x_{,\xi} z_{,\zeta} - z_{,\xi} x_{,\zeta} & z_{,\xi} x_{,\eta} - x_{,\xi} z_{,\eta} \\ x_{,\eta} y_{,\zeta} - y_{,\eta} x_{,\zeta} & y_{,\xi} x_{,\zeta} - x_{,\xi} y_{,\zeta} & y_{,\eta} x_{,\xi} - y_{,\xi} x_{,\eta} \end{bmatrix} \quad (136)$$

establishing its inverse.

For instance, the averaged lumped-consistent mass matrix for a tetrahedron with 1 Gauss point of integration located at its centroid is

$$\mathbf{M}_{3A} = \frac{\rho V}{96} \begin{bmatrix} 5 & 0 & 0 & 1 & 0 & 0 & 1 & 0 & 0 & 1 & 0 & 0 \\ 0 & 5 & 0 & 0 & 1 & 0 & 0 & 1 & 0 & 0 & 1 & 0 \\ 0 & 0 & 5 & 0 & 0 & 1 & 0 & 0 & 1 & 0 & 0 & 1 \\ 1 & 0 & 0 & 5 & 0 & 0 & 1 & 0 & 0 & 1 & 0 & 0 \\ 0 & 1 & 0 & 0 & 5 & 0 & 0 & 1 & 0 & 0 & 1 & 0 \\ 0 & 0 & 1 & 0 & 0 & 5 & 0 & 0 & 1 & 0 & 0 & 1 \\ 1 & 0 & 0 & 1 & 0 & 0 & 5 & 0 & 0 & 1 & 0 & 0 \\ 0 & 1 & 0 & 0 & 1 & 0 & 0 & 5 & 0 & 0 & 1 & 0 \\ 0 & 0 & 1 & 0 & 0 & 1 & 0 & 0 & 5 & 0 & 0 & 1 \\ 1 & 0 & 0 & 1 & 0 & 0 & 1 & 0 & 0 & 5 & 0 & 0 \\ 0 & 1 & 0 & 0 & 1 & 0 & 0 & 1 & 0 & 0 & 5 & 0 \\ 0 & 0 & 1 & 0 & 0 & 1 & 0 & 0 & 1 & 0 & 0 & 5 \end{bmatrix} \quad (137)$$

where the volume V varies with deformation because air is compressible. The other cases are not as simple.

Three mass matrices for a tetrahedron are implemented based upon the three, Gauss, quadrature rules presented in Table 10. These quadratures integrate polynomials of order 1, 2 and 3, respectively.

6.1.3.1 Assemble Tetrahedral Mass Matrices to Get Mass Matrix for an Alveolar Sac

6.2. Stiffness Matrix

For a nonlinear elastic material, like a soft tissue, the stress-strain response generally becomes stiffer with increasing deformation. Consequently, the slope along their stress-strain curve changes with strain and, therefore, its instantaneous stiffness changes, too. Therefore, tangent stiffness matrices are required for our finite element simulations.

The total potential energy of a deformed body can be expressed as the difference between a variation in the potential energy of deformation δU and a variation in the potential energy of the external loading δW^{102}

$$\delta R = \delta U - \delta W \quad (138a)$$

with

$$\delta W = \mathbf{F} d\Delta \quad (138b)$$

$$\delta U = \int_V \bar{\mathbf{B}}^T \mathbf{T} dV d\Delta \quad (138c)$$

where \mathbf{F} is a vector of external forces, \mathbf{T} are the conjugate stresses to our strains, and $\bar{\mathbf{B}}$ is a matrix relation between strain \mathbf{E} and nodal displacements Δ such that

$$\mathbf{E} = \bar{\mathbf{B}} \Delta \quad \text{with} \quad d\mathbf{E} = \bar{\mathbf{B}} d\Delta \quad (139)$$

with displacement fields being interpolated as

$$\bar{\mathbf{u}} = \begin{Bmatrix} u \\ v \end{Bmatrix} = \begin{Bmatrix} \sum_{i=1}^n u_i N_i \\ \sum_{i=1}^n v_i N_i \end{Bmatrix} = \mathbf{N} \Delta. \quad (140)$$

In order to make our computation more systematic, the total strain-displacement matrix is additively decomposed into its linear and nonlinear components as

$$\bar{\mathbf{B}} = \mathbf{B}_L + \mathbf{B}_N. \quad (141)$$

Here \mathbf{B}_L is obtained from a linear analysis, i.e., $\mathbf{E}_L = \mathbf{B}_L \Delta$. Note that the linear strain-displacement matrix \mathbf{B}_L does not vary with the displacement whereas its nonlinear counterpart \mathbf{B}_N is a function of the displacement vector \mathbf{u} associated with the nonlinear part of strain, \mathbf{E}_N . This fact has a greater consequence in obtaining

stiffness matrices as this implies that $d\mathbf{B}_L = 0$ which allows one to write that $d\bar{\mathbf{B}} = d\mathbf{B}_N$.

The nonlinear part of strain \mathbf{E}_N is composed of products of different elements of the displacement gradient matrix. Thus, \mathbf{E}_N can be written as the product of two matrices \mathbf{A} and $\boldsymbol{\theta}$, i.e.,

$$\mathbf{E}_N = \frac{1}{2} \mathbf{A} \boldsymbol{\theta} \quad (142)$$

where \mathbf{A} is a matrix consisting of different elements of the displacement gradient, and $\boldsymbol{\theta}$ is a vector containing the derivatives of displacements. The elements of displacement gradient are placed in the matrix \mathbf{A} in a way such that its matrix multiplication with the vector $\boldsymbol{\theta}$ provides the required nonlinear strain matrix \mathbf{E}_N . To obtain the stiffness matrix, one needs to express the strain matrices in terms of nodal displacements. To achieve that, the vector $\boldsymbol{\theta}$ is further expressed as $\boldsymbol{\theta} = \mathbf{H} \Delta$, or in rate form as $d\boldsymbol{\theta} = \mathbf{H} d\Delta$, where \mathbf{H} is the derivative of shape functions taken with respect to the global co-ordinate system. Following the same argument as before, one can conclude that $d\mathbf{E}_L$ is also zero. Thus, the derivative of strain takes on the form of

$$d\mathbf{E} = d(\mathbf{E}_L + \mathbf{E}_N) = d\mathbf{E}_N = \frac{1}{2} (d\mathbf{A} \boldsymbol{\theta} + \mathbf{A} d\boldsymbol{\theta}) = \mathbf{A} \mathbf{H} d\Delta. \quad (143)$$

The last of Eqn. (143) is derived using the property $d\mathbf{A}\boldsymbol{\theta} = \mathbf{A}d\boldsymbol{\theta}$ which follows from the definitions of \mathbf{A} and $\boldsymbol{\theta}$.

Since $d\mathbf{E}_L = d\mathbf{B}_L = 0$, Eqn. (139) reduces to $d\mathbf{E}_N = \mathbf{B}_N d\Delta$. Now, expressing $d\mathbf{E}_N$ in terms of incremental nodal displacements in Eqn. (143), one can easily write that

$$\mathbf{B}_N = \mathbf{A} \mathbf{H} \quad \text{with} \quad d\mathbf{B}_N = d\mathbf{A} \mathbf{H}. \quad (144)$$

With the relationships between the strain; strain-displacement matrices and the displacements established, now we are ready to determine the stiffness matrix. In order to satisfy equilibrium, the internal and external forces must be balanced.¹⁰³ The difference between these two forces is called the residual force. If \mathbf{R} denotes the residual force vector, then for equilibrium, the following condition must be satisfied:

$$\mathbf{R} = \int_V \bar{\mathbf{B}}^T \mathbf{T} dV - \mathbf{F} = 0. \quad (145)$$

The total tangent stiffness matrix is defined as $\mathbf{K}_T := d\mathbf{R}/d\Delta$. Now derivative of Eqn. (145) yields

$$d\mathbf{R} = \int_V d\bar{\mathbf{B}}^T \mathbf{T} dV + \int_V \bar{\mathbf{B}}^T d\mathbf{T} dV \quad (146)$$

where $d\mathbf{T} = \mathbf{M} d\mathbf{E} = \mathbf{M} \bar{\mathbf{B}} d\Delta$, with \mathbf{M} being the matrix of elastic tangent moduli.

Substituting the definition of $d\mathbf{T}$ into Eq. (146), we obtain

$$d\mathbf{R} = \int_V dB_N^T \mathbf{T} dV + \int_V \bar{\mathbf{B}}^T \mathbf{M} \bar{\mathbf{B}} dV d\Delta \quad (147a)$$

$$= \int_V (\mathbf{H}^T d\mathbf{A}^T \mathbf{T}) dV + \int_V (\mathbf{B}_L + \mathbf{B}_N)^T \mathbf{M} (\mathbf{B}_L + \mathbf{B}_N) dV d\Delta \quad (147b)$$

Notice that the first term in $d\mathbf{R}$ does not include variation of the stress and hence, is associated with the initial stress applied on the body. Now we need to express the variation of residual force $d\mathbf{R}$ in terms of the variation of nodal displacements to compute the stiffness matrices.

$$= \mathbf{K}_S d\Delta + \underbrace{\int_V \mathbf{B}_L^T \mathbf{M} \mathbf{B}_L dV}_{\mathbf{K}_L} d\Delta \quad (147c)$$

$$+ \underbrace{\int_V (\mathbf{B}_L^T \mathbf{M} \mathbf{B}_N + \mathbf{B}_N^T \mathbf{M} \mathbf{B}_L + \mathbf{B}_N^T \mathbf{M} \mathbf{B}_N) dV}_{\mathbf{K}_N} d\Delta \quad (147d)$$

$$= (\mathbf{K}_S + \mathbf{K}_L + \mathbf{K}_N) d\Delta = \mathbf{K}_T d\Delta \quad (147e)$$

wherein \mathbf{K}_S is the stiffness matrix associated with the initial stress, \mathbf{K}_L is the conventional small displacement stiffness matrix*, and \mathbf{K}_N is the large displacement stiffness matrix. \mathbf{K}_T denotes the total tangent-stiffness matrix relating the residual force vector with nodal displacements.

6.2.1 Stiffness Matrix for Chord

The components of Laplace stretch \mathcal{U} can be obtained from a Cholesky factorization of the right Cauchy-Green tensor $\mathbf{C} = \mathbf{F}^T \mathbf{F} = \mathcal{U}^T \mathcal{U}$, which is a symmetric second-

*When expressed in terms of stress and strain, the small displacement stiffness matrix \mathbf{K}_L is nothing but the secant modulus, whereas the total stiffness matrix \mathbf{K}_T is the tangent modulus.

order tensor. For a 1-D chord, the only possible deformation is a stretch of the chord in axial direction. Therefore, in this case, the deformation gradient as well as the right Cauchy-Green tensor \mathbf{C} has only one component. Consequently, the Laplace stretch \mathcal{U} also consists of only one component which is denoted by a . If u denotes the axial displacement of the chord, then the axial stretch a can be written as

$$a = \mathcal{U}_{11} = \sqrt{C_{11}} \quad \text{with} \quad C_{11} = \left(\frac{\partial u}{\partial x} \right)^2 + 2 \frac{\partial u}{\partial x} + 1 \quad (148)$$

The chord is subjected to an axial strain defined as $e = \ln(a/a_0) \equiv \ln(L/L_0)$ where L is the length of the chord, and L_0 and a_0 are initial length of the chord and the initial stretch respectively. Here, without loss of generality, we assume that $a_0 = 1$. As before, we decompose the total strain into its linear and nonlinear components as

$$e = e_L + e_N. \quad (149)$$

The linear and nonlinear strain components can be obtained from a Taylor series expansion of $e = \ln \sqrt{C_{11}}$. Here, terms only up to second order have been considered. The strain components, thus obtained, are given as

$$e_L = \frac{\partial u}{\partial x} \quad (150a)$$

$$e_N = -\frac{1}{2} \frac{\partial u}{\partial x} \frac{\partial^2 u}{\partial x^2} \quad (150b)$$

The linear strain-displacement matrix \mathbf{B}_L can now be obtained by expressing the linear strain e_L in terms of the nodal displacements, viz.,

$$e_L = \partial u / \partial x = \sum_{i=1}^2 N_{i,x} u_i = [[\mathbf{b}_{L1}], [\mathbf{b}_{L2}]] \{\Delta\} = [\mathbf{B}_L] \{\Delta\} \quad (151a)$$

with

$$\mathbf{b}_{Li} = N_{i,x} \quad \text{and} \quad \Delta^T = \{u_1, u_2\} \quad (151b)$$

where u_1 and u_2 are the nodal displacements of the chord.

As discussed earlier, the nonlinear strain e_N can be written as a product of a matrix

A and $\boldsymbol{\theta}$. For a 1-D chord, both **A** and $\boldsymbol{\theta}$ consist of a single element, i.e.,

$$e_N = \frac{1}{2} [-\partial u / \partial x] \{\partial u / \partial x\} = \frac{1}{2} \mathbf{A} \boldsymbol{\theta}. \quad (152)$$

Furthermore, $\boldsymbol{\theta}$ can be expressed in terms of the nodal displacements as

$$\boldsymbol{\theta} = \left\{ \partial u / \partial x \right\} = \left\{ \sum_{i=1}^2 N_{i,x} u_i \right\} = \begin{bmatrix} [\mathbf{h}_1], & [\mathbf{h}_2] \end{bmatrix} \left\{ \boldsymbol{\Delta} \right\} = [\mathbf{H}] \left\{ \boldsymbol{\Delta} \right\}. \quad (153)$$

with $\mathbf{h}_i = N_{i,x}$

Hence, in view of Eqn. (144), the nonlinear strain-displacement matrix \mathbf{B}_N can be written as

$$\mathbf{B}_N = \mathbf{A} \mathbf{H} = \begin{bmatrix} [\mathbf{b}_{N1}], & [\mathbf{b}_{N2}] \end{bmatrix} \quad (154)$$

where

$$\mathbf{b}_{Ni} = [-\partial u / \partial x] \cdot N_{i,x} \quad (155)$$

Now we derive the stiffness matrix \mathbf{K}_S associated with initial stress as defined in Eqn. (147). Note that when expressed in terms of the nodal displacements, $d\mathbf{A}$ can be written as $d\mathbf{A} = \mathbf{H} d\boldsymbol{\Delta}$. Using this property, one can obtain \mathbf{K}_S as

$$\mathbf{K}_S = \int_{\Gamma} \mathbf{H}^T d\mathbf{A}^T \mathbf{T} A dx = \int_{-1}^1 \mathbf{H}^T \mathbf{T} \mathbf{H} \mathbf{J} A d\xi = \sum_{i=1}^n \mathbf{H}^T \mathbf{T} \mathbf{H} \mathbf{J} A w_i \quad (156)$$

wherein \mathbf{T} is the initial stress carried by collagen and elastin fibers, as discussed in Part 4. Note that the term \mathbf{K}_S does not contain any material property. This is due to the fact that the force component $\mathbf{K}_S d\boldsymbol{\Delta}$ exhibits the influence of the initial stress on the axial displacement of the chord. As before, \mathbf{H} can be expressed as follows

$$\mathbf{H} = \begin{bmatrix} N_{1,x} & N_{2,x} \end{bmatrix} = \begin{bmatrix} N_{1,\xi} & N_{2,\xi} \end{bmatrix} \mathbf{J}^{-1} \quad (157)$$

where the Jacobian \mathbf{J} is defined in Eqn. 121.

The small displacement stiffness matrix for a 1-D alveolar chord, that is transformed from global co-ordinate system to the natural coordinate system by using the determinant of the Jacobian matrix, (i.e., Eq. (121)) can be evaluated numerically as

$$\mathbf{K}_L = \int_{\Gamma} \mathbf{B}_L^T \mathbf{M} \mathbf{B}_L A dx = \int_{-1}^1 \mathbf{B}_L^T \mathbf{M} \mathbf{B}_L \mathbf{J} A d\xi = \sum_{i=1}^n \mathbf{B}_L^T \mathbf{M} \mathbf{B}_L \mathbf{J} A w_i \quad (158)$$

with w_i being the weighting coefficients of the Gauss integration rule, and A being the cross section area of alveolar chord. The values of ξ and w_i for $n = 1, 2$, and 3 Gauss integration points are demonstrated in Table 7.

In calculation of the stiffness matrix for an element, we need the linear strain-displacement matrix \mathbf{B}_L . \mathbf{B}_L contains the derivatives of the shape functions with respect to the global co-ordinate system and is given as

$$\mathbf{B}_L = \begin{bmatrix} N_{1,x} & N_{2,x} \end{bmatrix} = \begin{bmatrix} N_{1,\xi} & N_{2,\xi} \end{bmatrix} \mathbf{J}^{-1} \quad (159)$$

wherein ξ is abscissae of the Gauss integration rule.

The large displacement stiffness matrix for chord can be written as

$$\mathbf{K}_N = \int_{-1}^1 \mathbf{D} \mathbf{J} A d\xi = \sum_{i=1}^n \mathbf{D} \mathbf{J} A w_i \quad (160)$$

where \mathbf{D} takes on the form of

$$\mathbf{D} = \mathbf{B}_L^T \mathbf{M} \mathbf{B}_N + \mathbf{B}_N^T \mathbf{M} \mathbf{B}_L + \mathbf{B}_N^T \mathbf{M} \mathbf{B}_N \quad (161)$$

wherein \mathbf{B}_N can be expressed as

$$\mathbf{B}_N = \left[\partial \mathbf{u} / \partial \mathbf{x} \right] \begin{bmatrix} N_{1,x} & N_{2,x} \end{bmatrix} = \left[\sum_{i=1}^n N_{i,x} u_i \right] \begin{bmatrix} N_{1,\xi} & N_{2,\xi} \end{bmatrix} \mathbf{J}^{-1} \quad (162)$$

Thereby the total stiffness matrix \mathbf{K}_T can be obtained by summation of stress stiffness matrix, small and large displacement stiffness matrices.

6.2.2 Stiffness Matrix for Pentagon

For a planar member, the components of Laplace stretch \mathcal{U} , obtained from a Cholesky factorization of the right Cauchy-Green tensor $\mathbf{C} := \mathbf{F}^T \mathbf{F} = \mathcal{U}^T \mathcal{U}$, can be written as

$$\begin{aligned} \mathcal{U}_{11} &= a = \sqrt{C_{11}} & \mathcal{U}_{12} &= a g = C_{12}/\mathcal{U}_{11} \\ \mathcal{U}_{21} &= 0 & \mathcal{U}_{22} &= b = \sqrt{C_{22} - (\mathcal{U}_{12})^2} \end{aligned} \quad (163)$$

where C_{11} , $C_{12}=C_{21}$ and C_{22} are the components of the right Cauchy-Green tensor \mathbf{C} . Furthermore, these components of Cauchy-Green tensor can be expressed in

terms of the components of the deformation gradient \mathbf{F} as

$$C_{11} = \left(\frac{\partial u}{\partial x} \right)^2 + \left(\frac{\partial v}{\partial x} \right)^2 + 2 \frac{\partial u}{\partial x} + 1 \quad (164a)$$

$$C_{12} = \frac{\partial u}{\partial y} + \frac{\partial v}{\partial x} + \frac{\partial u}{\partial x} \cdot \frac{\partial u}{\partial y} + \frac{\partial v}{\partial x} \cdot \frac{\partial v}{\partial y} \quad (164b)$$

$$C_{22} = \left(\frac{\partial u}{\partial y} \right)^2 + \left(\frac{\partial v}{\partial y} \right)^2 + 2 \frac{\partial v}{\partial y} + 1 \quad (164c)$$

wherein

$$\mathbf{F} = \begin{bmatrix} 1 + \partial u / \partial x & \partial u / \partial y \\ \partial v / \partial x & 1 + \partial v / \partial y \end{bmatrix} \quad (164d)$$

Here, u and v are the displacements associated with the deformation of the planar member.

Now, the thermodynamic strain attributes, as defined earlier, can be expressed in terms of the components of Laplace stretch as

$$\xi = \ln \left(\sqrt{\frac{a b}{a_0 b_0}} \right); \quad \varepsilon = \ln \left(\sqrt{\frac{a b_0}{b a_0}} \right); \quad \gamma = g - g_0. \quad (165)$$

Without loss of generality, we can assume the membrane to be initially undeformed which allows us to assume a_0 and b_0 to be 1 whereas the initial shear g_0 is taken as zero. To gain computational advantage, we decompose the total strain increments, thus obtained, into their linear and two nonlinear components as

$$\xi = \xi_L + \xi_{N1} + \xi_{N2} \quad (166a)$$

$$\varepsilon = \varepsilon_L + \varepsilon_{N1} + \varepsilon_{N2} \quad (166b)$$

$$\gamma = \gamma_L + \gamma_{N1} + \gamma_{N2}. \quad (166c)$$

Traditionally, the total strain increment is decomposed into a linear and a non-linear components. However, in our case, further decomposition of the nonlinear strain component makes our computation much easier as will be realized later. The decomposition of total strain increment is achieved by using Taylor series expansion up to second-order terms. The linear and nonlinear components of total strain

increments, thus obtained, are given as

$$\xi_L = \frac{1}{2} \left(\frac{\partial u}{\partial x} + \frac{\partial v}{\partial y} \right) \quad (167a)$$

$$\xi_{N1} = \frac{1}{4} \left(-\frac{\partial v}{\partial y} \frac{\partial v}{\partial y} - \frac{\partial u}{\partial x} \frac{\partial u}{\partial x} \right) \quad (167b)$$

$$\xi_{N2} = -\frac{1}{2} \frac{\partial u}{\partial y} \frac{\partial v}{\partial x} \quad (167c)$$

$$\varepsilon_L = \frac{1}{2} \left(\frac{\partial u}{\partial x} - \frac{\partial v}{\partial y} \right) \quad (167d)$$

$$\varepsilon_{N1} = \frac{1}{4} \left(\frac{\partial v}{\partial y} \frac{\partial v}{\partial y} - \frac{\partial u}{\partial x} \frac{\partial u}{\partial x} \right) \quad (167e)$$

$$\varepsilon_{N2} = \frac{1}{2} \left(\frac{\partial v}{\partial x} \frac{\partial v}{\partial x} + \frac{\partial u}{\partial y} \frac{\partial v}{\partial x} \right) \quad (167f)$$

$$\gamma_L = \frac{\partial u}{\partial y} + \frac{\partial v}{\partial x} \quad (167g)$$

$$\gamma_{N1} = \frac{\partial v}{\partial x} \frac{\partial v}{\partial y} - \frac{\partial u}{\partial x} \frac{\partial u}{\partial y} \quad (167h)$$

$$\gamma_{N2} = -2 \frac{\partial u}{\partial x} \frac{\partial v}{\partial x}. \quad (167i)$$

The linear components of strain attributes consist of only first-order derivatives of the displacements whereas the nonlinear components contain the second-order terms. The nonlinear components of strains are arranged in a way such that when represented in a set of bases, they can be written as a product of matrix and a vector containing the derivatives of displacements. To achieve that, for the dilatation and squeeze strains, the first nonlinear components consist of the squares of derivatives whereas the second nonlinear components are made up of products between different derivatives of the displacements, e.g., the component ξ_{N1} contains terms of the form $\left(\frac{\partial u}{\partial x} \right)^2$ whereas its other counterpart, ξ_{N2} is made up of a cross term like $\frac{\partial u}{\partial y} \frac{\partial v}{\partial x}$. Note that the nonlinear part of the total shear strain contains only products of different derivatives of displacements, i.e., no square term is present in its expression. Therefore, we club together the terms containing the products of derivatives of the *same* displacement with respect to different spatial variables, e.g., $\frac{\partial v}{\partial x} \frac{\partial v}{\partial y}$ in γ_{N1} whereas γ_{N2} comprises the rest of the terms. This organization allows one to write the linear and the two nonlinear components of *all* the strain attributes in a matrix form. Moreover, this procedure helps us to write the strain-displacement

matrix corresponding to the linear and two nonlinear components of strain and thus, provides additional computational advantage.

To obtain the stiffness matrix for the planar membrane, first we need to compute the strain–displacement matrices as mentioned earlier. The strain–displacement matrices are obtained by expressing the corresponding strain components in terms of the five nodal displacements with the help of shape functions.

In terms of the nodal displacements the vector containing the linear strain attributes, \mathbf{E}_L can be written as

$$\begin{aligned} \mathbf{E}_L = \begin{Bmatrix} \xi_L \\ \varepsilon_L \\ \gamma_L \end{Bmatrix} &= \begin{Bmatrix} \frac{1}{2} u_{,x} + \frac{1}{2} v_{,y} \\ \frac{1}{2} u_{,x} - \frac{1}{2} v_{,y} \\ u_{,y} + v_{,x} \end{Bmatrix} = \begin{bmatrix} \frac{1}{2} \sum_{i=1}^5 N_{i,x} & \frac{1}{2} \sum_{i=1}^5 N_{i,y} \\ \frac{1}{2} \sum_{i=1}^5 N_{i,x} & -\frac{1}{2} \sum_{i=1}^5 N_{i,y} \\ \sum_{i=1}^5 N_{i,y} & \sum_{i=1}^5 N_{i,x} \end{bmatrix} \begin{Bmatrix} u_i \\ v_i \end{Bmatrix} \\ &= [[\mathbf{b}_{L1}], [\mathbf{b}_{L2}], [\mathbf{b}_{L3}], [\mathbf{b}_{L4}], [\mathbf{b}_{L5}]] \{\Delta\} = [\mathbf{B}_L] \{\Delta\} \end{aligned} \quad (168)$$

wherein the components of the linear strain–displacement matrix can be written in terms of the derivatives of the shape function as

$$\mathbf{b}_{Li} = \begin{bmatrix} \frac{1}{2} N_{i,x} & \frac{1}{2} N_{i,y} \\ \frac{1}{2} N_{i,x} & -\frac{1}{2} N_{i,y} \\ N_{i,y} & N_{i,x} \end{bmatrix} \quad (169a)$$

and

$$\Delta^T = \{u_1, v_1, u_2, v_2, \dots, u_n, v_n\}. \quad (169b)$$

The two nonlinear parts of strain are expressed as products of a matrix, \mathbf{A} containing the elements of the displacement gradient and a vector, $\boldsymbol{\theta}$ that contains the derivatives of displacements. Following this procedure, the first nonlinear strain can be written as

$$\begin{aligned} \mathbf{E}_{N1} = \begin{Bmatrix} \xi_{N1} \\ \varepsilon_{N1} \\ \gamma_{N1} \end{Bmatrix} &= \begin{Bmatrix} -\frac{1}{4} u_{,x}^2 - \frac{1}{4} v_{,y}^2 \\ -\frac{1}{4} u_{,x}^2 + \frac{1}{4} v_{,y}^2 \\ -u_{,y} u_{,x} + v_{,x} v_{,y} \end{Bmatrix} = \frac{1}{2} \begin{bmatrix} -\frac{1}{2} \partial u / \partial x & -\frac{1}{2} \partial v / \partial y \\ -\frac{1}{2} \partial u / \partial x & \frac{1}{2} \partial v / \partial y \\ -2 \partial u / \partial y & 2 \partial v / \partial x \end{bmatrix} \begin{Bmatrix} \partial u / \partial x \\ \partial v / \partial y \end{Bmatrix} = \frac{1}{2} [\mathbf{A}_{N1}] [\boldsymbol{\theta}_{N1}] \end{aligned} \quad (170)$$

To obtain the nonlinear strain–displacement matrix, we require the nonlinear strain to be expressed in terms of the nodal displacements. This is achieved by expressing

the elements of displacement gradient in terms of the nodal displacements by using the shape functions, specifically, the vector $\boldsymbol{\theta}_{N1}$ can be written as

$$[\boldsymbol{\theta}_{N1}] = \begin{Bmatrix} \partial u / \partial x \\ \partial v / \partial y \end{Bmatrix} = \begin{Bmatrix} \sum_{i=1}^5 N_{i,x} u_i \\ \sum_{i=1}^5 N_{i,y} v_i \end{Bmatrix} = [[\mathbf{h}_{N1}], [\mathbf{h}_{N2}], [\mathbf{h}_{N3}], [\mathbf{h}_{N4}], [\mathbf{h}_{N5}]] \{\Delta\} = [\mathbf{H}_{N1}] \{\Delta\} \quad (171)$$

where the components of \mathbf{H}_{N1} contains the derivatives of shape functions with respect to spatial variables, i.e.,

$$\mathbf{h}_{Ni} = \begin{bmatrix} N_{i,x} & 0 \\ 0 & N_{i,y} \end{bmatrix} \quad (172)$$

Therefore, the first nonlinear strain-displacement matrix \mathbf{B}_{N1} can be written as

$$\mathbf{B}_{N1} = [\mathbf{A}_{N1}] [\mathbf{H}_{N1}] = [[\mathbf{b}_{N1}], [\mathbf{b}_{N2}], [\mathbf{b}_{N3}], [\mathbf{b}_{N4}], [\mathbf{b}_{N5}]] \quad (173)$$

where the components of \mathbf{B}_{N1} are given as

$$\mathbf{b}_{Ni} = \begin{bmatrix} -\frac{1}{2} \partial u / \partial x & -\frac{1}{2} \partial v / \partial y \\ -\frac{1}{2} \partial u / \partial x & \frac{1}{2} \partial v / \partial y \\ -2 \partial u / \partial y & 2 \partial v / \partial x \end{bmatrix} \begin{bmatrix} N_{i,x} & 0 \\ 0 & N_{i,y} \end{bmatrix}. \quad (174)$$

In a similar manner, the second nonlinear strain terms can be written as

$$\mathbf{E}_{N2} = \begin{Bmatrix} \xi_{N2} \\ \varepsilon_{N2} \\ \gamma_{N2} \end{Bmatrix} = \begin{Bmatrix} -\frac{1}{2} u_{,y} v_{,x} \\ \frac{1}{2} u_{,y} v_{,x} + \frac{1}{2} v_{,x}^2 \\ -2 u_{,x} v_{,x} \end{Bmatrix} = \frac{1}{2} \begin{bmatrix} -\partial v / \partial x & 0 \\ \partial v / \partial x & \partial v / \partial x \\ 0 & -4 \partial u / \partial x \end{bmatrix} \begin{Bmatrix} \partial u / \partial y \\ \partial v / \partial x \end{Bmatrix} = \frac{1}{2} [\mathbf{A}_{N2}] [\boldsymbol{\theta}_{N2}] . \quad (175)$$

The vector $\boldsymbol{\theta}_{N2}$ is expressed in terms of the nodal displacements with the use of shape functions as

$$[\boldsymbol{\theta}_{N2}] = \begin{Bmatrix} \partial u / \partial y \\ \partial v / \partial x \end{Bmatrix} = \begin{Bmatrix} \sum_{i=1}^5 N_{i,y} u_i \\ \sum_{i=1}^5 N_{i,x} v_i \end{Bmatrix} = [[\mathbf{h}_{N1}], [\mathbf{h}_{N2}], [\mathbf{h}_{N3}], [\mathbf{h}_{N4}], [\mathbf{h}_{N5}]] \{\Delta\} = [\mathbf{H}_2] \{\Delta\} \quad (176)$$

where the elements of \mathbf{H}_{N2} are given as

$$\mathbf{h}_{Ni} = \begin{bmatrix} N_{i,y} & 0 \\ 0 & N_{i,x} \end{bmatrix}. \quad (177)$$

Hence, the second nonlinear strain–displacement matrix \mathbf{B}_{N2} becomes

$$\mathbf{B}_{N2} = [\mathbf{A}_{N2}] [\mathbf{H}_{N2}] = \left[[\mathbf{b}_{N1}], \quad [\mathbf{b}_{N2}], \quad [\mathbf{b}_{N3}], \quad [\mathbf{b}_{N4}], \quad [\mathbf{b}_{N5}] \right] \quad (178)$$

where its elements are given as

$$\mathbf{b}_{Ni} = \begin{bmatrix} -\partial v / \partial x & 0 \\ \partial v / \partial x & \partial v / \partial x \\ 0 & -4 \partial u / \partial x \end{bmatrix} \begin{bmatrix} N_{i,y} & 0 \\ 0 & N_{i,x} \end{bmatrix}. \quad (179)$$

The total nonlinear strain–displacement matrix is evaluated as the summation of its components \mathbf{B}_{N1} and \mathbf{B}_{N2} . Now, with all the strain–displacement matrices evaluated, we are ready to compute the stiffness matrix for a planar membrane.

The total stiffness matrix is additively decomposed into three components: the stiffness matrix associated with initial stress \mathbf{K}_S , the linear stiffness matrix \mathbf{K}_L and the nonlinear stiffness matrix \mathbf{K}_N . The initial stress stiffness matrix for a 2-D alveolar septa is given as

$$\mathbf{K}_S d\Delta = \int_{\triangle} \int_{\triangle} d\mathbf{B}_N^T \mathbf{T} |\mathbf{J}| h d\xi d\eta \quad (180)$$

From the expression of \mathbf{K}_S , it is easily understood that we need to express $d\mathbf{B}_N$ in terms of the incremental nodal displacements $d\Delta$. Using Eqn. (144), we get

$$d[\mathbf{B}_N]^T = [\mathbf{H}_{N1}^T] d[\mathbf{A}_{N1}^T] + [\mathbf{H}_{N2}^T] d[\mathbf{A}_{N2}^T] \quad (181)$$

which on substitution into Eq. (180) yields

$$\mathbf{K}_S d\Delta = \int_A ([\mathbf{H}_1^T] d[\mathbf{A}_1^T] + [\mathbf{H}_2^T] d[\mathbf{A}_2^T]) \begin{Bmatrix} s^\pi \\ s^\sigma \\ s^\tau \end{Bmatrix} dA \quad (182)$$

Furthermore, from the definition of \mathbf{A} , one can observe that

$$d[\mathbf{A}_1^T] \begin{Bmatrix} s^\pi \\ s^\sigma \\ s^\tau \end{Bmatrix} = \begin{bmatrix} s^\pi & s^\tau \\ s^\tau & s^\sigma \end{bmatrix} [\mathbf{H}_1] d\Delta \quad \text{and} \quad d[\mathbf{A}_2^T] \begin{Bmatrix} s^\pi \\ s^\sigma \\ s^\tau \end{Bmatrix} = \begin{bmatrix} s^\pi & s^\tau \\ s^\tau & s^\sigma \end{bmatrix} [\mathbf{H}_2] d\Delta \quad (183)$$

Using the above relation in Eqn. (182), finally we obtain the stiffness matrix asso-

ciated with initial stress as

$$\begin{aligned}\mathbf{K}_S &= \int_A [\mathbf{H}_1]^T \begin{bmatrix} s^\pi & s^\tau \\ s^\tau & s^\sigma \end{bmatrix} [\mathbf{H}_1] dA + \int_A [\mathbf{H}_2]^T \begin{bmatrix} s^\pi & s^\tau \\ s^\tau & s^\sigma \end{bmatrix} [\mathbf{H}_2] dA \\ &= \sum_{i=1}^n \sum_{j=1}^n \left([\mathbf{H}_1]^T \begin{bmatrix} s^\pi & s^\tau \\ s^\tau & s^\sigma \end{bmatrix} [\mathbf{H}_1] |\mathbf{J}| h + [\mathbf{H}_2]^T \begin{bmatrix} s^\pi & s^\tau \\ s^\tau & s^\sigma \end{bmatrix} [\mathbf{H}_2] |\mathbf{J}| h \right) w_i w_j\end{aligned}\quad (184)$$

where n denotes the number of Gauss points, w_i and w_j denote the natural weight of the element demonstrated in Table 9.

The linear and nonlinear stiffness matrices are rather easy to calculate from their definitions provided in Eqn. (147). For the sake of completeness their expressions are provided below.

The small/linear displacement stiffness matrix for the membrane is evaluated numerically as

$$\mathbf{K}_L = \int_{\triangle} \int_{\triangle} \mathbf{B}_L^T \mathbf{M} \mathbf{B}_L |\mathbf{J}| h d\xi d\eta = \sum_{i=1}^n \sum_{j=1}^n \mathbf{B}_L^T \mathbf{M} \mathbf{B}_L |\mathbf{J}| h w_i w_j \quad (185)$$

whereas the large/nonlinear displacement stiffness matrix takes the form of

$$\mathbf{K}_N = \int_{\triangle} \int_{\triangle} \mathbf{D} |\mathbf{J}| h d\xi d\eta = \sum_{i=1}^n \sum_{j=1}^n \mathbf{D} |\mathbf{J}| h w_i w_j \quad (186)$$

where \mathbf{D} contains the products of linear and nonlinear strain–displacement matrices and is given as

$$\mathbf{D} = \mathbf{B}_L^T \mathbf{M} \mathbf{B}_N + \mathbf{B}_N^T \mathbf{M} \mathbf{B}_L + \mathbf{B}_N^T \mathbf{M} \mathbf{B}_N. \quad (187)$$

Once the number of Gauss points and their corresponding weights have been selected, one can numerically evaluate all the components of stiffness matrices, addition of which yields the total stiffness matrix for the pentagonal membrane.

6.2.3 Stiffness Matrix for a tetrahedron

The Laplace stretch associated with a alveolar volume has geometric interpretations

that one can assign⁵¹

$$\mathcal{U}_{ij} = \begin{bmatrix} a & a\gamma & a\beta \\ 0 & b & b\alpha \\ 0 & 0 & c \end{bmatrix} \quad (188a)$$

The components of Laplace stretch \mathbf{U} has a Cholesky factorization expressed in terms of the right Cauchy-Green deformation tensor $\mathbf{C} := \mathbf{F}^T \mathbf{F} = \mathbf{U}^T \mathbf{U}$, which is a symmetric second-order tensor.

$$\begin{aligned} \mathcal{U}_{11} &= \sqrt{C_{11}} & \mathcal{U}_{12} &= C_{12}/\mathcal{U}_{11} & \mathcal{U}_{13} &= C_{13}/\mathcal{U}_{11} \\ \mathcal{U}_{21} &= 0 & \mathcal{U}_{22} &= \sqrt{C_{22} - \mathcal{U}_{12}^2} & \mathcal{U}_{23} &= (C_{23} - \mathcal{U}_{12}\mathcal{U}_{13})/\mathcal{U}_{22} \\ \mathcal{U}_{31} &= 0 & \mathcal{U}_{32} &= 0 & \mathcal{U}_{33} &= \sqrt{C_{33} - \mathcal{U}_{13}^2 - \mathcal{U}_{23}^2} \end{aligned} \quad (189)$$

where C_{11} , C_{12} , C_{21} and C_{22} are components of the Green deformation matrix \mathbf{C} wherein \mathbf{F} is the deformation gradient.

$$\mathbf{C} = \mathbf{F}^T \mathbf{F} = \begin{bmatrix} C_{11} & C_{12} & C_{13} \\ C_{21} & C_{22} & C_{23} \\ C_{31} & C_{32} & C_{33} \end{bmatrix}, \quad \mathbf{F} = \begin{bmatrix} 1 + \partial u/\partial x & \partial u/\partial y & \partial u/\partial z \\ \partial v/\partial x & 1 + \partial v/\partial y & \partial v/\partial z \\ \partial w/\partial x & \partial w/\partial y & 1 + \partial w/\partial z \end{bmatrix} \quad (190a)$$

with

$$C_{11} = \left(\frac{\partial u}{\partial x} \right)^2 + \left(\frac{\partial v}{\partial x} \right)^2 + \left(\frac{\partial w}{\partial x} \right)^2 + 2 \frac{\partial u}{\partial x} + 1 \quad (190b)$$

$$C_{22} = \left(\frac{\partial u}{\partial y} \right)^2 + \left(\frac{\partial v}{\partial y} \right)^2 + \left(\frac{\partial w}{\partial y} \right)^2 + 2 \frac{\partial v}{\partial y} + 1 \quad (190c)$$

$$C_{33} = \left(\frac{\partial u}{\partial z} \right)^2 + \left(\frac{\partial v}{\partial z} \right)^2 + \left(\frac{\partial w}{\partial z} \right)^2 + 2 \frac{\partial w}{\partial z} + 1 \quad (190d)$$

$$C_{12} = C_{21} = \frac{\partial u}{\partial y} + \frac{\partial v}{\partial x} + \frac{\partial u}{\partial x} \cdot \frac{\partial u}{\partial y} + \frac{\partial v}{\partial x} \cdot \frac{\partial v}{\partial y} + \frac{\partial w}{\partial x} \cdot \frac{\partial w}{\partial y} \quad (190e)$$

$$C_{13} = C_{31} = \frac{\partial u}{\partial z} + \frac{\partial w}{\partial x} + \frac{\partial u}{\partial x} \cdot \frac{\partial u}{\partial z} + \frac{\partial v}{\partial x} \cdot \frac{\partial v}{\partial z} + \frac{\partial w}{\partial x} \cdot \frac{\partial w}{\partial z} \quad (190f)$$

$$C_{23} = C_{32} = \frac{\partial v}{\partial z} + \frac{\partial w}{\partial y} + \frac{\partial u}{\partial y} \cdot \frac{\partial u}{\partial z} + \frac{\partial v}{\partial y} \cdot \frac{\partial v}{\partial z} + \frac{\partial w}{\partial y} \cdot \frac{\partial w}{\partial z} \quad (190g)$$

the dilatation δ for the alveolar volume is

$$\xi := \ln \sqrt[3]{\frac{a}{a_0} \frac{b}{b_0} \frac{c}{c_0}} \quad (191a)$$

and the squeezes ε_i and the shear strains γ_i are defined accordingly

$$\varepsilon_1 := \ln \sqrt[3]{\frac{a}{a_0} \frac{b_0}{b}} \quad \gamma_1 := \alpha - \alpha_0 \quad (191b)$$

$$\varepsilon_2 := \ln \sqrt[3]{\frac{b}{b_0} \frac{c_0}{c}} \quad \gamma_2 := \beta - \beta_0 \quad (191c)$$

$$\varepsilon_3 := \ln \sqrt[3]{\frac{c}{c_0} \frac{a_0}{a}} \quad \gamma_3 := \gamma - \gamma_0 \quad (191d)$$

wherein a_0 , b_0 and c_0 are their initial elongation ratios, and where α_0 , β_0 and γ_0 are their initial shears. It is useful to define the above strains in terms of linear and nonlinear incremental strains as follow

$$\xi = \xi_L + \xi_{N1} + \xi_{N2} + \xi_{N3} \quad (192a)$$

$$\varepsilon_i = \varepsilon_{iL} + \varepsilon_{iN1} + \varepsilon_{iN2} + \varepsilon_{iN3} \quad (192b)$$

$$\gamma_i = \gamma_{iL} + \gamma_{iN1} + \gamma_{iN2} + \gamma_{iN3} \quad (192c)$$

DRAFT: UNCLASSIFIED

Taylor series are used here to obtain the linear and nonlinear part of displacements

$$\xi_L = \frac{1}{3} \left(\frac{\partial u}{\partial x} + \frac{\partial v}{\partial y} + \frac{\partial w}{\partial z} \right) \quad (193a)$$

$$\begin{aligned} \xi_N = & \frac{1}{6} \left(- \frac{\partial u}{\partial x} \frac{\partial u}{\partial x} + \frac{\partial u}{\partial z} \frac{\partial u}{\partial z} - \frac{\partial v}{\partial y} \frac{\partial v}{\partial y} - \frac{\partial v}{\partial z} \frac{\partial v}{\partial z} + \frac{\partial w}{\partial x} \frac{\partial w}{\partial x} - \frac{\partial w}{\partial y} \frac{\partial w}{\partial y} - \frac{\partial w}{\partial z} \frac{\partial w}{\partial z} \right. \\ & \left. - 2 \frac{\partial u}{\partial y} \frac{\partial v}{\partial x} - 4 \frac{\partial v}{\partial z} \frac{\partial w}{\partial y} \right) \end{aligned} \quad (193b)$$

$$\varepsilon_{1L} = \frac{1}{3} \left(\frac{\partial u}{\partial x} - \frac{\partial v}{\partial y} \right) \quad (193c)$$

$$\varepsilon_{1N} = \frac{1}{6} \left(2 \frac{\partial v}{\partial x} \frac{\partial v}{\partial x} + \frac{\partial v}{\partial y} \frac{\partial v}{\partial y} - \frac{\partial u}{\partial x} \frac{\partial u}{\partial x} + \frac{\partial w}{\partial x} \frac{\partial w}{\partial x} - \frac{\partial w}{\partial y} \frac{\partial w}{\partial y} + 2 \frac{\partial u}{\partial y} \frac{\partial v}{\partial x} \right) \quad (193d)$$

$$\varepsilon_{2L} = \frac{1}{3} \left(\frac{\partial v}{\partial y} - \frac{\partial w}{\partial z} \right) \quad (193e)$$

$$\begin{aligned} \varepsilon_{2N} = & \frac{1}{6} \left(- \frac{\partial v}{\partial x} \frac{\partial v}{\partial x} - \frac{\partial v}{\partial y} \frac{\partial v}{\partial y} - \frac{\partial u}{\partial z} \frac{\partial u}{\partial z} + \frac{\partial v}{\partial z} \frac{\partial v}{\partial z} + 3 \frac{\partial w}{\partial y} \frac{\partial w}{\partial y} + \frac{\partial w}{\partial z} \frac{\partial w}{\partial z} \right. \\ & \left. - 2 \frac{\partial u}{\partial y} \frac{\partial v}{\partial x} + 4 \frac{\partial v}{\partial z} \frac{\partial w}{\partial y} \right) \end{aligned} \quad (193f)$$

$$\varepsilon_{3L} = \frac{1}{3} \left(- \frac{\partial u}{\partial x} + \frac{\partial w}{\partial z} \right) \quad (193g)$$

$$\begin{aligned} \varepsilon_{3N} = & \frac{1}{6} \left(- \frac{\partial v}{\partial x} \frac{\partial v}{\partial x} + \frac{\partial u}{\partial x} \frac{\partial u}{\partial x} + \frac{\partial u}{\partial z} \frac{\partial u}{\partial z} - \frac{\partial v}{\partial z} \frac{\partial v}{\partial z} - \frac{\partial w}{\partial x} \frac{\partial w}{\partial x} - 2 \frac{\partial w}{\partial y} \frac{\partial w}{\partial y} \right. \\ & \left. - \frac{\partial w}{\partial z} \frac{\partial w}{\partial z} - 4 \frac{\partial v}{\partial z} \frac{\partial w}{\partial y} \right) \end{aligned} \quad (193h)$$

$$\gamma_{1L} = \frac{\partial v}{\partial z} + \frac{\partial w}{\partial y} \quad (193i)$$

$$\begin{aligned} \gamma_{1N} = & 2 \frac{\partial u}{\partial x} \frac{\partial v}{\partial z} - \frac{\partial u}{\partial z} \frac{\partial v}{\partial x} + 2 \frac{\partial u}{\partial x} \frac{\partial w}{\partial y} - \frac{\partial u}{\partial y} \frac{\partial w}{\partial x} - \frac{\partial v}{\partial y} \frac{\partial v}{\partial z} - \frac{\partial v}{\partial x} \frac{\partial w}{\partial x} \\ & - 2 \frac{\partial v}{\partial y} \frac{\partial w}{\partial y} + \frac{\partial w}{\partial y} \frac{\partial w}{\partial z} \end{aligned} \quad (193j)$$

$$\gamma_{2L} = \frac{\partial v}{\partial z} + \frac{\partial w}{\partial y} \quad (193k)$$

$$\gamma_{2N} = \frac{\partial u}{\partial y} \frac{\partial u}{\partial z} - 2 \frac{\partial u}{\partial x} \frac{\partial v}{\partial z} - 2 \frac{\partial u}{\partial x} \frac{\partial w}{\partial y} + \frac{\partial v}{\partial y} \frac{\partial v}{\partial z} + \frac{\partial w}{\partial y} \frac{\partial w}{\partial z} \quad (193l)$$

$$\gamma_{3L} = \frac{\partial u}{\partial y} + \frac{\partial v}{\partial x} \quad (193m)$$

$$\gamma_{3N} = - \frac{\partial u}{\partial x} \frac{\partial u}{\partial y} - 2 \frac{\partial u}{\partial x} \frac{\partial v}{\partial x} + \frac{\partial v}{\partial x} \frac{\partial v}{\partial y} + \frac{\partial w}{\partial x} \frac{\partial w}{\partial y} \quad (193n)$$

The linear strain displacement matrix \mathbf{B}_L can be obtained by differentiation of displacements expressed through the nodal displacements and shape functions from

infinitesimal linear strain vector that take the form of

$$\mathbf{E}_L = \begin{Bmatrix} \xi_L \\ \varepsilon_{1L} \\ \varepsilon_{2L} \\ \varepsilon_{3L} \\ \gamma_{1L} \\ \gamma_{2L} \\ \gamma_{3L} \end{Bmatrix} = \begin{Bmatrix} \frac{1}{3} u_{,x} + \frac{1}{3} v_{,y} + \frac{1}{3} w_{,z} \\ \frac{1}{3} u_{,x} - \frac{1}{3} v_{,y} \\ \frac{1}{3} v_{,y} - \frac{1}{3} w_{,z} \\ -\frac{1}{3} u_{,x} + \frac{1}{3} w_{,z} \\ v_{,z} + w_{,y} \\ v_{,z} + w_{,y} \\ u_{,y} + v_{,x} \end{Bmatrix} = \begin{Bmatrix} \frac{1}{3} \sum_{i=1}^4 N_{i,x} & \frac{1}{3} \sum_{i=1}^4 N_{i,y} & \frac{1}{3} \sum_{i=1}^4 N_{i,z} \\ \frac{1}{3} \sum_{i=1}^4 N_{i,x} & \frac{-1}{3} \sum_{i=1}^4 N_{i,y} & 0 \\ 0 & \frac{1}{3} \sum_{i=1}^4 N_{i,y} & \frac{-1}{3} \sum_{i=1}^4 N_{i,z} \\ -\frac{1}{3} \sum_{i=1}^4 N_{i,x} & 0 & \frac{1}{3} \sum_{i=1}^4 N_{i,z} \\ 0 & \sum_{i=1}^4 N_{i,z} & \sum_{i=1}^4 N_{i,y} \\ 0 & \sum_{i=1}^4 N_{i,z} & \sum_{i=1}^4 N_{i,y} \\ \sum_{i=1}^4 N_{i,y} & \sum_{i=1}^4 N_{i,x} & 0 \end{Bmatrix} \begin{Bmatrix} u_i \\ v_i \\ w_i \end{Bmatrix}$$

$$= [[\mathbf{b}_{L1}], [\mathbf{b}_{L2}], [\mathbf{b}_{L3}], [\mathbf{b}_{L4}]] \{\Delta\} = [\mathbf{B}_L] \{\Delta\} \quad (194)$$

wherein

$$\mathbf{b}_{Li} = \begin{bmatrix} \frac{1}{3} N_{i,x} & \frac{1}{3} N_{i,y} & \frac{1}{3} N_{i,z} \\ \frac{1}{3} N_{i,x} & -\frac{1}{3} N_{i,y} & 0 \\ 0 & \frac{1}{3} N_{i,y} & -\frac{1}{3} N_{i,z} \\ -\frac{1}{3} N_{i,x} & 0 & \frac{1}{3} N_{i,z} \\ 0 & N_{i,z} & N_{i,y} \\ 0 & N_{i,z} & N_{i,y} \\ N_{i,y} & N_{i,x} & 0 \end{bmatrix} \quad (195a)$$

and

$$\Delta^T = \{u_1, v_1, w_1, u_2, v_2, w_2, \dots, u_n, v_n, w_n\} \quad (195b)$$

The first nonlinear strain terms can be written as

$$\begin{aligned}
 \mathbf{E}_{N1} &= \begin{Bmatrix} \xi_L \\ \varepsilon_{1N} \\ \varepsilon_{2N} \\ \varepsilon_{3N} \\ \gamma_{1N} \\ \gamma_{2N} \\ \gamma_{3N} \end{Bmatrix} = \begin{Bmatrix} \frac{1}{6} (-u_{,x}^2 - 2u_{,y}v_{,x} + w_{,x}^2) \\ \frac{1}{6} (-u_{,x}^2 + 2v_{,x}^2 + w_{,x}^2) \\ \frac{1}{6} (-v_{,x}^2) \\ \frac{1}{6} (u_{,x}^2 - v_{,x}^2 - w_{,x}^2) \\ 2u_{,x}v_{,z} - u_{,z}v_{,x} - v_{,x}w_{,x} \\ -2u_{,x}v_{,z} \\ -u_{,x}u_{,y} - 2u_{,x}v_{,x} \end{Bmatrix} \\
 &= \frac{1}{2} \begin{bmatrix} -\frac{1}{3}\partial u/\partial x & -\frac{2}{3}\partial u/\partial y & \frac{1}{3}\partial w/\partial x \\ -\frac{1}{3}\partial u/\partial x & \frac{2}{3}\partial v/\partial x & \frac{1}{3}\partial w/\partial x \\ 0 & -\frac{1}{3}\partial v/\partial x & 0 \\ \frac{1}{3}\partial u/\partial x & -\frac{1}{3}\partial v/\partial x & -\frac{1}{3}\partial w/\partial x \\ 4\partial v/\partial z & -2\partial u/\partial z & -2\partial v/\partial x \\ -4\partial v/\partial z & 0 & 0 \\ -2\partial u/\partial y & -4\partial u/\partial x & 0 \end{bmatrix} \begin{Bmatrix} \partial u/\partial x \\ \partial v/\partial x \\ \partial w/\partial x \end{Bmatrix} = \frac{1}{2} [\mathbf{A}_{N1}] [\boldsymbol{\theta}_{N1}]
 \end{aligned} \tag{196}$$

the derivative of displacement can be related to the nodal parameters via

$$[\boldsymbol{\theta}_{N1}] = \begin{Bmatrix} \partial u/\partial x \\ \partial v/\partial x \\ \partial w/\partial x \end{Bmatrix} = \begin{Bmatrix} \sum_{i=1}^5 N_{i,x} u_i \\ \sum_{i=1}^5 N_{i,x} v_i \\ \sum_{i=1}^5 N_{i,x} w_i \end{Bmatrix} = [[\mathbf{h}_{N1}], [\mathbf{h}_{N2}], [\mathbf{h}_{N3}], [\mathbf{h}_{N4}]] \{\boldsymbol{\Delta}\} = [\mathbf{H}_{N1}] \{\boldsymbol{\Delta}\} \tag{197}$$

where

$$\mathbf{h}_{Ni} = \begin{bmatrix} N_{i,x} & 0 & 0 \\ 0 & N_{i,x} & 0 \\ 0 & 0 & N_{i,x} \end{bmatrix} \tag{198}$$

hence \mathbf{B}_{N1} become

$$\mathbf{B}_{N1} = [\mathbf{A}_{N1}] [\mathbf{H}_{N1}] = [[\mathbf{b}_{N1}], [\mathbf{b}_{N2}], [\mathbf{b}_{N3}], [\mathbf{b}_{N4}]] \tag{199}$$

where

$$\mathbf{b}_i = \begin{bmatrix} -\frac{1}{3} \partial u / \partial x & -\frac{2}{3} \partial u / \partial y & \frac{1}{3} \partial w / \partial x \\ -\frac{1}{3} \partial u / \partial x & \frac{2}{3} \partial v / \partial x & \frac{1}{3} \partial w / \partial x \\ 0 & -\frac{1}{3} \partial v / \partial x & 0 \\ \frac{1}{3} \partial u / \partial x & -\frac{1}{3} \partial v / \partial x & -\frac{1}{3} \partial w / \partial x \\ 4 \partial v / \partial z & -2 \partial u / \partial z & -2 \partial v / \partial x \\ -4 \partial v / \partial z & 0 & 0 \\ -2 \partial u / \partial y & -4 \partial u / \partial x & 0 \end{bmatrix} \begin{bmatrix} N_{i,x} & 0 & 0 \\ 0 & N_{i,x} & 0 \\ 0 & 0 & N_{i,x} \end{bmatrix} \quad (200)$$

The second nonlinear strain terms can be written as

$$\begin{aligned} \mathbf{E}_{N2} &= \begin{Bmatrix} \xi_L \\ \varepsilon_{1N} \\ \varepsilon_{2N} \\ \varepsilon_{3N} \\ \gamma_{1N} \\ \gamma_{2N} \\ \gamma_{3N} \end{Bmatrix} = \begin{Bmatrix} \frac{1}{6} (-v_{,y}^2 - w_{,y}^2) \\ \frac{1}{6} (2u_{,y}v_{,x} + 2v_{,y}^2 - w_{,y}^2) \\ \frac{1}{6} (-2u_{,y}v_{,x} - v_{,y}^2 + 3w_{,y}^2) \\ \frac{1}{6} (-2w_{,y}^2) \\ -u_{,y}w_{,x} - 2v_{,y}w_{,y} + w_{,y}w_{,z} \\ u_{,y}u_{,z} - 2u_{,x}w_{,y} \\ v_{,x}v_{,y} + w_{,x}w_{,y} \end{Bmatrix} \\ &= \frac{1}{2} \begin{bmatrix} 0 & -\frac{1}{3} \partial v / \partial y & \frac{1}{3} \partial w / \partial y \\ \frac{2}{3} \partial v / \partial x & \frac{2}{3} \partial v / \partial y & -\frac{1}{3} \partial w / \partial y \\ -\frac{2}{3} \partial v / \partial x & -\frac{1}{3} \partial v / \partial y & \partial w / \partial y \\ 0 & 0 & -\frac{2}{3} \partial w / \partial y \\ -2 \partial w / \partial x & -4 \partial w / \partial y & 2 \partial w / \partial z \\ 2 \partial u / \partial z & 0 & -4 \partial u / \partial x \\ 0 & 2 \partial v / \partial x & 2 \partial w / \partial x \end{bmatrix} \begin{Bmatrix} \partial u / \partial y \\ \partial v / \partial y \\ \partial w / \partial y \end{Bmatrix} = \frac{1}{2} [\mathbf{A}_{N2}] [\boldsymbol{\theta}_{N2}] \end{aligned} \quad (201)$$

the derivative of displacement can be related to the nodal parameters via

$$[\boldsymbol{\theta}_{N2}] = \begin{Bmatrix} \partial u / \partial y \\ \partial v / \partial y \\ \partial w / \partial y \end{Bmatrix} = \begin{Bmatrix} \sum_{i=1}^5 N_{i,y} u_i \\ \sum_{i=1}^5 N_{i,y} v_i \\ \sum_{i=1}^5 N_{i,y} w_i \end{Bmatrix} = [[\mathbf{h}_{N1}], [\mathbf{h}_{N2}], [\mathbf{h}_{N3}], [\mathbf{h}_{N4}]] \{\Delta\} = [\mathbf{H}_{N2}] \{\Delta\} \quad (202)$$

where

$$\mathbf{h}_{Ni} = \begin{bmatrix} N_{i,y} & 0 & 0 \\ 0 & N_{i,y} & 0 \\ 0 & 0 & N_{i,y} \end{bmatrix} \quad (203)$$

hence \mathbf{B}_{N2} become

$$\mathbf{B}_{N2} = [\mathbf{A}_{N2}] [\mathbf{H}_{N2}] = \left[[\mathbf{b}_{N1}], \quad [\mathbf{b}_{N2}], \quad [\mathbf{b}_{N3}], \quad [\mathbf{b}_{N4}] \right] \quad (204)$$

where

$$\mathbf{b}_{Ni} = \begin{bmatrix} 0 & -\frac{1}{3} \partial v / \partial y & \frac{1}{3} \partial w / \partial y \\ \frac{2}{3} \partial v / \partial x & \frac{2}{3} \partial v / \partial y & -\frac{1}{3} \partial w / \partial y \\ -\frac{2}{3} \partial v / \partial x & -\frac{1}{3} \partial v / \partial y & \partial w / \partial y \\ 0 & 0 & -\frac{2}{3} \partial w / \partial y \\ -2 \partial w / \partial x & -4 \partial w / \partial y & 2 \partial w / \partial z \\ 2 \partial u / \partial z & 0 & -4 \partial u / \partial x \\ 0 & 2 \partial v / \partial x & 2 \partial w / \partial x \end{bmatrix} \begin{bmatrix} N_{i,y} & 0 & 0 \\ 0 & N_{i,y} & 0 \\ 0 & 0 & N_{i,y} \end{bmatrix} \quad (205)$$

The third nonlinear strain terms can be written as

$$\begin{aligned} \mathbf{E}_{N3} &= \begin{Bmatrix} \xi_L \\ \varepsilon_{1N} \\ \varepsilon_{2N} \\ \varepsilon_{3N} \\ \gamma_{1N} \\ \gamma_{2N} \\ \gamma_{3N} \end{Bmatrix} = \begin{Bmatrix} \frac{1}{6} (u_{,z}^2 - v_{,z}^2 - 4 v_{,z} w_{,y} - w_{,z}^2) \\ 0 \\ \frac{1}{6} (-u_{,z}^2 + v_{,z}^2 + 4 v_{,z} w_{,y} + w_{,z}^2) \\ \frac{1}{6} (u_{,z}^2 - v_{,z}^2 - w_{,z}^2 - 4 v_{,z} w_{,y}) \\ -v_{,y} v_{,z} \\ v_{,y} v_{,z} + w_{,y} w_{,z} \\ 0 \end{Bmatrix} \\ &= \frac{1}{2} \begin{bmatrix} \frac{1}{3} \partial u / \partial z & -\frac{1}{3} \partial v / \partial z - \frac{4}{3} \partial w / \partial y & -\frac{1}{3} \partial w / \partial z \\ 0 & 0 & 0 \\ -\frac{1}{3} \partial u / \partial z & \frac{1}{3} \partial v / \partial z + \frac{4}{3} \partial w / \partial y & \frac{1}{3} \partial w / \partial z \\ \frac{1}{3} \partial u / \partial z & -\frac{1}{3} \partial v / \partial z - \frac{4}{3} \partial w / \partial y & -\frac{1}{3} \partial w / \partial z \\ 0 & -2 \partial v / \partial y & 0 \\ 0 & 2 \partial v / \partial y & 2 \partial w / \partial y \\ 0 & 0 & 0 \end{bmatrix} \begin{Bmatrix} \partial u / \partial z \\ \partial v / \partial z \\ \partial w / \partial z \end{Bmatrix} = \frac{1}{2} [\mathbf{A}_{N3}] [\boldsymbol{\theta}_{N3}] \end{aligned} \quad (206)$$

the derivative of displacement can be related to the nodal parameters via

$$[\boldsymbol{\theta}_{N3}] = \begin{Bmatrix} \partial u / \partial z \\ \partial v / \partial z \\ \partial w / \partial z \end{Bmatrix} = \begin{Bmatrix} \sum_{i=1}^5 N_{i,z} u_i \\ \sum_{i=1}^5 N_{i,z} v_i \\ \sum_{i=1}^5 N_{i,z} w_i \end{Bmatrix} = [[\mathbf{h}_{N1}], \quad [\mathbf{h}_{N2}], \quad [\mathbf{h}_{N3}], \quad [\mathbf{h}_{N4}]] \{\boldsymbol{\Delta}\} = [\mathbf{H}_{N3}] \{\boldsymbol{\Delta}\} \quad (207)$$

where

$$\mathbf{h}_{Ni} = \begin{bmatrix} N_{i,z} & 0 & 0 \\ 0 & N_{i,z} & 0 \\ 0 & 0 & N_{i,z} \end{bmatrix} \quad (208)$$

hence \mathbf{B}_{N3} become

$$\mathbf{B}_{N3} = [\mathbf{A}_{N3}] [\mathbf{H}_{N3}] = [[\mathbf{b}_{N1}], [\mathbf{b}_{N2}], [\mathbf{b}_{N3}], [\mathbf{b}_{N4}]] \quad (209)$$

where

$$\mathbf{b}_{Ni} = \begin{bmatrix} \frac{1}{3} \partial u / \partial z & -\frac{1}{3} \partial v / \partial z - \frac{4}{3} \partial w / \partial y & -\frac{1}{3} \partial w / \partial z \\ 0 & 0 & 0 \\ -\frac{1}{3} \partial u / \partial z & \frac{1}{3} \partial v / \partial z + \frac{4}{3} \partial w / \partial y & \frac{1}{3} \partial w / \partial z \\ \frac{1}{3} \partial u / \partial z & -\frac{1}{3} \partial v / \partial z - \frac{4}{3} \partial w / \partial y & -\frac{1}{3} \partial w / \partial z \\ 0 & -2 \partial v / \partial y & 0 \\ 0 & 2 \partial v / \partial y & 2 \partial w / \partial y \\ 0 & 0 & 0 \end{bmatrix} \begin{bmatrix} N_{i,z} & 0 & 0 \\ 0 & N_{i,z} & 0 \\ 0 & 0 & N_{i,z} \end{bmatrix} \quad (210)$$

In order to be able to evaluate the nonlinear stiffness matrix, $[\bar{\mathbf{B}}]$ should be established as the summation of \mathbf{B}_{N1} , \mathbf{B}_{N2} and \mathbf{B}_{N3} . Hence, the stress stiffness matrix for a 3-D alveolar volume take the form of

$$\mathbf{K}_S = \int_V d\mathbf{B}_N^T \mathbf{T} |\mathbf{J}| d\xi d\eta d\zeta = \sum_{i=1}^n \sum_{j=1}^n \sum_{k=1}^n d\mathbf{B}_N^T \mathbf{T} |\mathbf{J}| w_i w_j w_k \quad (211)$$

where n stands for number of Gauss points. Table 10 By taking the variation of Eq. (141) and substituting the definition of first and second nonlinear strain displacement matrices, the total nonlinear strain displacement matrix becomes

$$d[\mathbf{B}_N]^T = [\mathbf{H}_1^T]d[\mathbf{A}_1^T] + [\mathbf{H}_2^T]d[\mathbf{A}_2^T] + [\mathbf{H}_3^T]d[\mathbf{A}_3^T] \quad (212)$$

which on substituting into Eq. (211) gives

$$\mathbf{K}_S d\Delta = \int_A ([\mathbf{H}_1^T] d[\mathbf{A}_1^T] + [\mathbf{H}_2^T] d[\mathbf{A}_2^T] + [\mathbf{H}_3^T] d[\mathbf{A}_3^T]) \begin{Bmatrix} s^\pi \\ s^{\sigma_1} \\ s^{\sigma_2} \\ s^{\tau_1} \\ s^{\tau_2} \\ s^{\tau_3} \end{Bmatrix} dA \quad (213)$$

However, using the mathematical properties of the matrix \mathbf{A} , the following expression will appear

$$\begin{aligned} d[\mathbf{A}_1^T] \begin{Bmatrix} s^\pi \\ s^{\sigma_1} \\ s^{\sigma_2} \\ s^{\tau_1} \\ s^{\tau_2} \\ s^{\tau_3} \end{Bmatrix} &= \begin{bmatrix} s^\pi & s^{\tau_1} & s^{\tau_3} \\ s^{\tau_1} & s^{\sigma_1} & s^{\tau_2} \\ s^{\tau_3} & s^{\tau_2} & s^{\sigma_2} \end{bmatrix} [\mathbf{H}_1] d\Delta \\ d[\mathbf{A}_2^T] \begin{Bmatrix} s^\pi \\ s^{\sigma_1} \\ s^{\sigma_2} \\ s^{\tau_1} \\ s^{\tau_2} \\ s^{\tau_3} \end{Bmatrix} &= \begin{bmatrix} s^\pi & s^{\tau_1} & s^{\tau_3} \\ s^{\tau_1} & s^{\sigma_1} & s^{\tau_2} \\ s^{\tau_3} & s^{\tau_2} & s^{\sigma_2} \end{bmatrix} [\mathbf{H}_2] d\Delta \\ d[\mathbf{A}_3^T] \begin{Bmatrix} s^\pi \\ s^{\sigma_1} \\ s^{\sigma_2} \\ s^{\tau_1} \\ s^{\tau_2} \\ s^{\tau_3} \end{Bmatrix} &= \begin{bmatrix} s^\pi & s^{\tau_1} & s^{\tau_3} \\ s^{\tau_1} & s^{\sigma_1} & s^{\tau_2} \\ s^{\tau_3} & s^{\tau_2} & s^{\sigma_3} \end{bmatrix} [\mathbf{H}_3] d\Delta \end{aligned} \quad (214)$$

and finally the stress/geometric stiffness matrix can be expressed as follow

$$\begin{aligned} \mathbf{K}_S &= \sum_{i=1}^n \sum_{j=1}^n \sum_{k=1}^n [\mathbf{H}_1]^T \begin{bmatrix} s^\pi & s^{\tau_1} & s^{\tau_3} \\ s^{\tau_1} & s^{\sigma_1} & s^{\tau_2} \\ s^{\tau_3} & s^{\tau_2} & s^{\sigma_2} \end{bmatrix} [\mathbf{H}_1] |J| w_i w_j w_k \\ &+ \sum_{i=1}^n \sum_{j=1}^n \sum_{k=1}^n [\mathbf{H}_2]^T \begin{bmatrix} s^\pi & s^{\tau_1} & s^{\tau_3} \\ s^{\tau_1} & s^{\sigma_1} & s^{\tau_2} \\ s^{\tau_3} & s^{\tau_2} & s^{\sigma_2} \end{bmatrix} [\mathbf{H}_2] |J| w_i w_j w_k \\ &+ \sum_{i=1}^n \sum_{j=1}^n \sum_{k=1}^n [\mathbf{H}_3]^T \begin{bmatrix} s^\pi & s^{\tau_1} & s^{\tau_3} \\ s^{\tau_1} & s^{\sigma_1} & s^{\tau_2} \\ s^{\tau_3} & s^{\tau_2} & s^{\sigma_2} \end{bmatrix} [\mathbf{H}_3] |J| w_i w_j w_k \end{aligned} \quad (215)$$

The small/linear displacement stiffness matrix for tetrahedron is evaluated numerically as

$$\mathbf{K}_L = \int_V \mathbf{B}_L^T \mathbf{M} \mathbf{B}_L |J| d\xi d\eta d\zeta = \sum_{i=1}^n \sum_{j=1}^n \sum_{k=1}^n \mathbf{B}_L^T \mathbf{M} \mathbf{B}_L |J| w_i w_j w_k \quad (216)$$

The large/nonlinear displacement stiffness matrix for chord can be presented as follow

$$\mathbf{K}_N = \int_V \mathbf{D} |J| d\xi d\eta d\zeta = \sum_{i=1}^n \sum_{j=1}^n \sum_{k=1}^n \mathbf{D} |J| w_i w_j w_k \quad (217)$$

where \mathbf{D} have the expression

$$\mathbf{D} = \mathbf{B}_L^T \mathbf{M} \mathbf{B}_N + \mathbf{B}_N^T \mathbf{M} \mathbf{B}_L + \mathbf{B}_N^T \mathbf{M} \mathbf{B}_N \quad (218)$$

6.3. Force Vector

The principle of stationary potential energy with the Rayleigh-Ritz approach, i.e., Eqn. (138), determines the basis of finite element stress analysis. The internal strain energy is balanced with the potential energy of applied internal and external loads on the body.

The virtual work done by external forces δW in Eq. (138) can be expressed as follow

$$\delta W = \int_S \mathbf{t} \delta \mathbf{u} dS = \int_S \mathbf{t} \mathbf{N} d\Delta dS = \left(\int_S \mathbf{N}^T \mathbf{t} dS \right) d\Delta \quad (219)$$

where dS denotes the surface element and \mathbf{t} is the surface traction vector (per unit surface area) at current time. Hence, the external FE force vectors are

$$\mathbf{F} = \int_S \mathbf{N}^T \mathbf{t} dS \quad (220)$$

with \mathbf{F} being the deformation gradient.

6.3.1 Force Vector for a Chord

The force vector of the 1-D alveolar chord that is evaluated numerically in its natural co-ordinate system can be described as

$$\mathbf{F}_{1D} = \int_{\Gamma} \mathbf{N}^T \mathbf{t} dx = \int_{-1}^1 \mathbf{N}^T \mathbf{t} \mathbf{J} d\xi = \sum_{i=1}^n \mathbf{N}^T \mathbf{t} \mathbf{J} w_i \quad (221)$$

where w_i being the weighting coefficients of the Gauss integration rule, \mathbf{N} is the shape function matrix for chord, and \mathbf{t} is the traction on the septal chord that is selected so that $\mathbf{t} = \mathbf{t}^c + \mathbf{t}^e$ as established in part 4 via engineering stress carried by collagen and elastin fibers. Table 7 demonstrates the values of ξ and w_i for $n = 1, 2$, and 3 Gauss integration points.

6.3.2 Force Vector for a Pentagon

The boundary of a two dimensional pentagon consist of line segments, which can be considered as one-dimensional chord. Hence, the evaluation of the boundary integrals on pentagon amounts to evaluating line integrals. Once the interpolation function for a pentagon are evaluated on the boundary of pentagon, we obtain the corresponding chordal interpolation functions.¹⁰¹ Thus, the force vector \mathbf{F}_{2D} for a

pentagon can be obtained by integral over all sides of pentagon as follow

$$\begin{aligned}
 \mathbf{F}_{2D} = \oint_{\Gamma} \mathbf{N}^T \mathbf{t} dS &= \int_{\Gamma_{12}} \mathbf{N}^T \mathbf{t}_{12} |\mathbf{J}| d\xi + \int_{\Gamma_{23}} \mathbf{N}^T \mathbf{t}_{23} |\mathbf{J}| d\xi + \int_{\Gamma_{34}} \mathbf{N}^T \mathbf{t}_{34} |\mathbf{J}| d\xi \\
 &\quad + \int_{\Gamma_{45}} \mathbf{N}^T \mathbf{t}_{45} |\mathbf{J}| d\xi + \int_{\Gamma_{51}} \mathbf{N}^T \mathbf{t}_{51} |\mathbf{J}| d\xi \\
 &= \sum_{i=1}^n \mathbf{N}^T \mathbf{t}_{12} |\mathbf{J}| w_i + \sum_{i=1}^n \mathbf{N}^T \mathbf{t}_{23} |\mathbf{J}| w_i + \sum_{i=1}^n \mathbf{N}^T \mathbf{t}_{34} |\mathbf{J}| w_i \\
 &\quad + \sum_{i=1}^n \mathbf{N}^T \mathbf{t}_{45} |\mathbf{J}| w_i + \sum_{i=1}^n \mathbf{N}^T \mathbf{t}_{51} |\mathbf{J}| w_i
 \end{aligned} \tag{222}$$

wherein \mathbf{N} being the shape function matrix of a chord with the matrix dimension of a pentagon, $|\mathbf{J}|$ being the determinant of the Jacobian for a 1-D chord, w_i denotes the natural weight of the chord, dS is the arc-length of an infinitesimal line element along the boundary, and \mathbf{t} is the traction vector on each edge of the pentagon as follow

$$\mathbf{t} = \boldsymbol{\sigma}^T \cdot \mathbf{n} \tag{223}$$

where \mathbf{n} is the normal vector to each sides of pentagon on which the traction acts and $\boldsymbol{\sigma}$ is the Cauchy stress as established in part 4.

6.3.3 Force Vector for a Tetrahedron

The analysis to find the force vector of a tetrahedron is used to reach the force vector of whole alveolar volume. The matrix of shape functions Eq. (132) is used to obtain the force vector for tetrahedron. The force vector \mathbf{F}_{3D} can be specified as follow

$$\begin{aligned}
 \mathbf{F}_{3D} = \oint_A \mathbf{N}^T \mathbf{t} dA &= \int_{\Delta_1} \int_{\Delta_1} \mathbf{N}^T \mathbf{t}_{\Delta_1} |\mathbf{J}| d\xi d\eta + \int_{\Delta_2} \int_{\Delta_2} \mathbf{N}^T \mathbf{t}_{\Delta_2} |\mathbf{J}| d\xi d\eta \\
 &\quad + \int_{\Delta_3} \int_{\Delta_3} \mathbf{N}^T \mathbf{t}_{\Delta_3} |\mathbf{J}| d\xi d\eta + \int_{\Delta_4} \int_{\Delta_4} \mathbf{N}^T \mathbf{t}_{\Delta_4} |\mathbf{J}| d\xi d\eta \\
 &= \sum_{i=1}^n \sum_{j=1}^n \mathbf{N}^T \mathbf{t}_{\Delta_1} |\mathbf{J}| w_i w_j + \sum_{i=1}^n \sum_{j=1}^n \mathbf{N}^T \mathbf{t}_{\Delta_2} |\mathbf{J}| w_i w_j \\
 &\quad + \sum_{i=1}^n \sum_{j=1}^n \mathbf{N}^T \mathbf{t}_{\Delta_3} |\mathbf{J}| w_i w_j + \sum_{i=1}^n \sum_{j=1}^n \mathbf{N}^T \mathbf{t}_{\Delta_4} |\mathbf{J}| w_i w_j
 \end{aligned} \tag{224}$$

wherein \mathbf{N} being the shape function matrix for a triangle with the matrix dimension

DRAFT: UNCLASSIFIED

node	ξ co-ordinate	η co-ordinate	weight
Exact for Polynomials of Degree 1			
1	1/3	1/3	1.0
Exact for Polynomials of Degree 2			
1	2/3	1/6	1/3
2	1/6	1/6	1/3
3	1/6	2/3	1/3
Exact for Polynomials of Degree 3			
1	1/3	1/3	-27/48
2	3/5	1/5	25/48
3	1/5	1/5	25/48
4	1/5	3/5	25/48

Table 14 Generalized, Gaussian, weights and nodes for integrating over a triangle in its natural co-ordinate system.

of a tetrahedron, $|J|$ being the determinant of the Jacobian for triangle, n stands for number of Gauss points, w_i and w_j are the natural weight of the triangle from Table 14, and t is the surface traction on the triangle surface. $\oint\int$ denotes the integral over the surface boundary of the tetrahedron. We compute the integral over one of the tetrahedrone's surfaces on which makes one triangles of a pentagon because by internal stress equilibrium, those portions cancel with like contributions from the neighboring elements in the assembled force vector of the structure. Hence, the force vector for a tetrahedron takes the form of

$$\mathbf{F}_{3D} = \sum_{i=1}^n \sum_{j=1}^n \mathbf{N}^T \mathbf{t}_{\Delta_1} |J| w_i w_j \quad (225)$$

7.1. References

1. Clayton JD, Freed AD. Viscoelastic-damage theory based on a QR decomposition of deformation gradient. Aberdeen, MD: Army Research Laboratory; 2019 October. Report No.: ARL-TR-8840.
2. Clayton JD, Freed AD. A constitutive model for lung mechanics and injury applicable to static, dynamic, and shock loading. *Mechanics of Soft Materials*. 2020;2:3.
3. Josey T. Investigation of Blast Load Characteristics on Lung Injury [master's thesis]. [Waterloo, Ontario, Canada]: University of Waterloo; 2010.
4. Stuhmiller JH. Blast injury: Translating research into operational medicine. Borden Institute, Walter Reed Army Medical Center, U.S. Army Medical Department Center & School: TMM Publications; 2008. (Borden Institute Monograph Series).
5. Stitzel JD, Gayzik FS, Hoth JJ, Mercier J, Gage HD, Morton KA, Duma SM, Payne RM. Development of a finite element-based injury metric for pulmonary contusion, Part I: Model development and validation. *Stapp Car Crash Journal*. 2005;49:271–289.
6. Stuhmiller JH, Chuong CJ, Phillips YY, Dodd KT. Computer modeling of thoracic response to blast. *Journal of Trauma*. 1988;28:S132–S139.
7. Vlessis AA, Trunkey DD. Non-penetrating injury of the thorax. In: Scientific Foundations of Trauma; Cooper GJ, Dudley HAF, Gann DS, Little RA, Maynard RL, editors. Oxford, UK: Butterworth Heinemann; 1997; p. 127–143.
8. Fung YC, Patitucci P, Tong P. Stress and strain in the lung. *ASCE Journal of Engineering Mechanics*. 1978;104:201–223.
9. Vawter DL, Fung YC, West JB. Constitutive equation of lung tissue elasticity. *Journal of Biomechanical Engineering*. 1979;101:38–45.
10. Vawter DL. A finite element model for macroscopic deformation of the lung. *Journal of Biomechanical Engineering*. 1980;102:1–7.
11. Gayzik FS, Hoth JJ, Daly M, Meredith JW, Stitzel JD. A finite element based injury metric for pulmonary contusion: investigation of candidate metrics through correlation with computed tomography. *Stapp Car Crash Journal*. 2007;51:189–209.
12. Gayzik FS, Hoth JJ, Stitzel J. Finite element-based injury metrics for pulmonary contusion via concurrent model optimization. *Biomechanics and Modeling in Mechanobiology*. 2011;10:505–520.

DRAFT: UNCLASSIFIED

13. Yuen K, Cronin DS, Deng YC. Lung response and injury in side impact conditions. In: Proceedings of the 2008 International Research Council on Biomechanics of Injury (IRCOBI) Conference;.
14. Freed AD, Einstein DR, Carson JP, Jacob RE. Viscoelastic model for lung parenchyma for multi-scale modeling of respiratory system, Phase II: Dodecahedral micro-model. Richland, WA: Pacific Northwest National Laboratory; 2012 March. Report No.: PNNL-21287.
15. Tsokos M, Paulsen F, Petri S, Madea B, Püschel K, Türk EE. Histologic, immunohistochemical, and ultrastructural findings in human blast lung injury. *American Journal of Respiratory and Critical Care Medicine*. 2003;168:549–555.
16. Butler JP, Miki H, Squarcia S, Rogers RA, Lehr JL. Effect of macroscopic deformation on lung microstructure. *Journal of Applied Physiology*. 1996;81:1792–1799.
17. Roan E, Waters CM. What do we know about mechanical strain in lung alveoli?. *American Journal of Physiology—Lung Cellular and Molecular Physiology*. 2011;301:L625–L635.
18. Fung YC. Biomechanics: Motion, flow, stress, and growth. New York: Springer-Verlag; 1990.
19. Fung YC. Stress, deformation, and atelectasis of the lung. *Circulation Research*. 1975;37:481–496.
20. Fung YC. A model of the lung structure and its validation. *Journal of Applied Physiology*. 1988;64:2132–2141.
21. Hoppin, Jr. FG, Hildebrandt J. Mechanical properties of the lung. In: Bioengineering Aspects of the Lung; Vol. 3; West JB, editor. New York: Marcel Dekker; 1977; p. 83–162.
22. Frankus A, Lee GC. A theory for distortion studies of lung parenchyma based on alveolar membrane properties. *Journal of Biomechanics*. 1974;7:101–107.
23. de Ryk J, Thiesse J, Namati E, McLennan G. Stress distribution in a three dimensional, geometric alveolar sac under normal and emphysematous conditions. *International Journal of COPD*. 2007;2:81–91.
24. Dale PJ, Matthews FL, Schroter RC. Finite element analysis of lung alveolus. *Journal of Biomechanics*. 1980;13:865–873.

DRAFT: UNCLASSIFIED

25. Denny E, Schroter RC. The mechanical behavior of a mammalian lung alveolar duct model. *Journal of Biomechanical Engineering*. 1995;117:254–261.
26. Denny E, Schroter RC. Relationships between alveolar size and fibre distribution in mammalian lung alveolar duct model. *Journal of Biomechanical Engineering*. 1997;119:289–297.
27. Denny E, Schroter RC. Viscoelastic behavior of a lung alveolar duct model. *Journal of Biomechanical Engineering*. 2000;122:143–151.
28. Kowe R, Schroter RC, Matthews FL, Hitchings D. Analysis of elastic and surface tension effects in the lung alveolus using finite element methods. *Journal of Biomechanics*. 1986;19(7):541–549.
29. Chen G, Zhang ZS, Mei YH, Li X, Yu DJ, Wang L, Chen X. Applying viscoplastic constitutive models to predict ratcheting behavior of sintered nanosilver lap-shear joint. *Mechanics of Materials*. 2014;2014:61–71.
30. Kimmel E, Kamm RD, Shapiro AH. A cellular model of lung elasticity. *Journal of Biomechanical Engineering*. 1987;109:126–131.
31. Budiansky B, Kimmel E. Elastic moduli of lungs. *Journal of Applied Mechanics*. 1987;54:351–358.
32. Kimmel E, Budiansky B. Surface tension and the dodecahedron model for lung elasticity. *Journal of Biomechanical Engineering*. 1990;112:160–167.
33. Weed B, Patnaik S, Rougeau-Browning M, Brazile B, Liao J, Prabhu R, Williams LN. Experimental evidence of mechanical isotropy in porcine lung parenchyma. *Materials*. 2015;8:2454–2466.
34. Hughes JMB, Hoppin, Jr. FG, Mead J. Effect of lung inflation on bronchial length and diameter in excised lungs. *Journal of Applied Physiology*. 1972;32(1):25–35.
35. Mead J. Respiration: pulmonary mechanics. *Annual Review of Physiology*. 1973;35:169–192.
36. West JB. *Respiratory physiology: The essentials*. eighth ed. Philadelphia: Lippincott Williams & Wilkins; 2007.
37. Denny E, Schroter RC. A model of non-uniform lung parenchyma distortion. *Journal of Biomechanics*. 2006;39:652–663.
38. McLellan AG. *The classical thermodynamics of deformable materials*. Cambridge: Cambridge University Press; 1980. (Cambridge Monographs in Physics).

DRAFT: UNCLASSIFIED

39. Freed AD, Zamani S. On the use of convected coordinate systems in the mechanics of continuous media derived from a **QR** factorization of **F**. International Journal of Engineering Science. 2018;127:145–161.
40. Paul S, Rajagopal KR, Freed AD. On coordinate indexing when using Laplace stretch. 2020;; In review.
41. Sabin SS, Fung YC, Tremper HM. Collagen and elastin fibers in human pulmonary alveolar walls. Journal of Applied Physiology. 1988;64(4):1659–1675.
42. Freed AD, Zamani S, Szabó L, Clayton JD. Laplace stretch: Eulerian and Lagrangian formulations. 2020;; In review.
43. Freed AD, le Graverend JB, Rajagopal KR. A decomposition of Laplace stretch with applications in inelasticity. Acta Mechanica. 2019;230:3423–3429.
44. Wachspress EL. A rational finite element basis. New York: Academic Press; 1975.
45. Wachspress E. Rational bases and generalized barycentrics: Applications to finite elements and graphics. Cham: Springer; 2016.
46. Hughes TJR. The finite element method: Linear static and dynamic finite element analysis. Englewood Cliffs, N.J.: Prentice-Hall; 1987.
47. Sukumar N, Malsch EA. Recent advances in the construction of polygonal finite element interpolants. Archives of Computational Methods in Engineering. 2006;13:129–163.
48. Dasgupta G. Interpolants within convex polygons: Wachspress' shape functions. Journal of Aerospace Engineering. 2003;16:1–8.
49. Clayton JD. Differential geometry and kinematics of continua. New York: World Scientific; 2015.
50. R. A Srinivasa. On the use of the upper triangle (or **QR**) decomposition for developing constitutive equations for Green-elastic materials. International Journal of Engineering Science. 2012;60:1–12.
51. Freed AD, R. A Srinivasa. Logarithmic strain and its material derivative for a **QR** decomposition of the deformation gradient. ACTA Mechanica. 2015;226:2645–2670.
52. Freed AD, Erel V, Moreno MR. Conjugate stress/strain base pairs for planar analysis of biological tissues. Journal of Mechanics of Materials and Structures. 2017;12:219–247.

DRAFT: UNCLASSIFIED

53. Freed AD, Zamani S. Elastic Kelvin-Poisson-Poynting solids described through scalar conjugate stress/strain pairs derived from a **QR** factorization of **F**. Journal of the Mechanics and Physics of Solids. 2019;;
54. McLellan AG. Finite strain coordinate and the stability of solid phases. Journal of Physics C: Solid State Physics. 1976;9:4083–4094.
55. Rosakis P. Ellipticity and deformations with discontinuous gradients in finite elasto-statics. Archives for Rational Mechanics and Analysis. 1990;109:1–37.
56. Souchet R. Concerning the polar decomposition of the deformation gradient. International Journal of Engineering Science. 1993;31:1499–1506.
57. Leon SJ, Björck Å, Gander W. Gram-Schmidt orthogonalization: 100 years and more. Numerical Linear Algebra with Applications. 2013;20:492–532.
58. Freed AD. A note on stress/strain conjugate pairs: explicit and implicit theories of thermoelasticity for anisotropic materials. International Journal of Engineering Science. 2017;120:155–171.
59. Carathéodory C. Untersuchungen über die Grundlagen der Thermodynamik. Mathematische Annalen. 1909;67:355–386; Translated in: J. Kestin (ed.), *The Second Law of Thermodynamics*, Dowden, Hutchinson and Ross, Stroudsberg, PA, 1976, pp. 229–256.
60. Perlman CE, Bhattacharya J. Alveolar expansion imaged by optical sectioning microscopy. Journal of Applied Physiology. 2007;103:1037–1044.
61. Treloar LRG. The physics of rubber elasticity. third ed. Oxford: Clarendon Press; 1975.
62. Suki B, Ito S, Stamenović D, Lutchen KR, Ingenito EP. Biomechanics of the lung parenchyma: critical roles of collagen and mechanical forces. Journal of Applied Physiology. 2005;98:1892–1899.
63. Suki B, Stamenović D, Hubmayr R. Lung parenchymal mechanics. Comprehensive Physiology. 2011;1:1317–1351.
64. Weinhold F. Metric geometry of equilibrium thermodynamics. III. Elementary formal structure of a vector-algebraic representation of equilibrium thermodynamics. The Journal of Chemical Physics. 1975;63:2488–2495.
65. Gilmore R. Length and curvature in the geometry of thermodynamics. Physical Review A. 1984;30:1994–1997.

DRAFT: UNCLASSIFIED

66. Truesdell C. Hypoelasticity. *Journal of Rational Mechanics and Analysis*. 1955;4:83–133.
67. Lai-Fook SJ. Elastic properties of lung parenchyma: the effect of pressure-volume hysteresis on the behavior of large blood vessels. *Journal of Biomechanics*. 1979;12:757–764.
68. Jahed M, Lai-Fook SJ, Bhagat PK. Effect of vascular volume and edema on wave propagation in canine lungs. *Journal of Applied Physiology*. 1990;68:2171–2176.
69. Saraf H, Ramesh KT, Lennon AM, Merkle AC, Roberts JC. Mechanical properties of soft human tissues under dynamic loading. *Journal of Biomechanics*. 2007;40:1960–1967.
70. Hajji MA, Wilson TA, Lai-Fook SJ. Improved measurements of shear modulus and pleural membrane tension of the lung. *Journal of Applied Physiology*. 1979;47:175–181.
71. Hildebrandt J. Comparison of mathematical models for cat lung and viscoelastic balloon derived by Laplace transform methods from pressure-volume data. *Bulletin of Mathematical Biophysics*. 1969;31(651-667).
72. Ames Research Staff. Equations, tables, and charts for compressible flow. National Advisory Committee for Aeronautics; 1953. Report No.: NACA 1135.
73. Stamenović D. Micromechanical foundations of pulmonary elasticity. *Physiological Reviews*. 1990;70(4):1117–1134.
74. Hills BA. An alternative view of the role(s) of surfactant and the alveolar model. *Journal of Applied Physiology*. 1999;87:1567–1583.
75. Bates JHT. A recruitment model of quasi-linear power-law stress adaptation in lung tissue. *Annals of Biomedical Engineering*. 2007;35:1165–1174.
76. Matsuda M, Fung YC, Sabin SS. Collagen and elastin fibers in human pulmonary alveolar mouths and ducts. *Journal of Applied Physiology*. 1987;63(3):1185–1194.
77. Kastelic J, Galeski A, Baer E. The multicomposite structure of tendon. *Connective Tissue Research*. 1978;6:11–23.
78. Freed AD, Doehring TC. Elastic model for crimped collagen fibrils. *Journal of Biomechanical Engineering*. 2005;127:587–593.
79. Aaron BB, Gosline JM. Elastin as a random-network elastomer: a mechanical and optical analysis of single elastin fibers. *Biopolymers*. 1981;20:1247–1260.

DRAFT: UNCLASSIFIED

80. Urry DW. Physicochemical properties of elastin and constituent peptides. In: Physicochemical properties of elastin and constituent peptides; Vol. 1; Boca Raton: CRC Press; 1989. Chapter 10, p. 141–173.
81. Fels IG. Hydration and density of collagen and gelatin. *Journal of Applied Polymer Science*. 1964;8:1813–1824.
82. Kanagy JR. Specific heats of collagen and leather. *Journal of Research of the National Bureau of Standards*. 1955;55:191–195.
83. Weir CE. Effect of temperature on the volume of leather and collagen in water. *Journal of Research of the National Bureau of Standards*. 1948;41:279–285.
84. Lillie MA, Gosline JM. Unusual swelling of elastin. *Biopolymers*. 2002;64:115–126.
85. Shadwick RE, Gosline JM. Physical and chemical properties of rubber-like elastic fibres from the octopus aorta. *Journal of Experimental Biology*. 1985;114:239–257.
86. Kakivaya SR, Hoeve CAJ. The glass point of elastin. *Proceedings of the National Academy of Sciences, USA*. 1975;72:3505–3507.
87. Lillie MA, Gosline JM. Mechanical properties of elastin along the thoracic aorta in the pig. *Journal of Biomechanics*. 2007;40:2214–2221.
88. Hörmann H, Schlebusch H. Reversible and irreversible denaturation of collagen fibers. *Biochemistry*. 1971;10(6):932–937.
89. Svensson RB, Hassenkam T, Grant CA, Magnusson SP. Tensile properties of human collagen fibrils and fascicles are insensitive to environmental salts. *Biophysical Journal*. 2010;99:4020–4027.
90. Freed AD, Rajagopal KR. A promising approach for modeling biological fibers. *ACTA Mechanica*. 2016;227:1609–1619; Errata: **229** (2018), pg. 3573.
91. Davison L. Fundamentals of shock wave propagation in solids. Berlin: Springer; 2008. (Shock Wave and High Pressure Phenomena).
92. Zener C. Elasticity and Anelasticity of Metals. Chicago: University of Chicago Press; 1948.
93. Birzle AM, Hobruck SMK, Martin C, Uhlig S, Wall WA. Constituent-specific material behavior of soft biological tissue: experimental quantification and numerical identification for lung parenchyma. *Biomechanics and Modeling in Mechanobiology*. 2019;18:1383–1400.

DRAFT: UNCLASSIFIED

94. Freed AD. A technical note: Two-step PECE methods for approximating solutions to first- and second-order ODEs. Texas A&M University; 2017. Report No.: arXiv:1707.02125 [cs.NA].
95. Noll W. On the continuity of the solid and fluid states. *Journal of Rational Mechanics and Analysis*. 1955;4:3–81.
96. Newmark NM. A method of computation for structural dynamics. *Journal of the Engineering Mechanics Division, Proceedings of the American Society of Civil Engineers*. 1959;EM 3:67–94.
97. Mousavi SE, Xiao H, Sukumar N. Generalized Gaussian quadrature rules on arbitrary polygons. *International Journal for Numerical Methods in Engineering*. 2010;82:99–113.
98. Chakraborty S, Natarajan S, Singh S, Mahapatra DR, Bordas SPA. Optimal numerical integration schemes for a family of polygonal finite elements with Schwarz-Christoffel conformal mapping. *International Journal for Computational Methods in Engineering Science and Mechanics*. 2018;19:283–304.
99. Oñate E. Structural analysis with the finite element method. linear statics. Barcelona: Springer; 2009. (Lecture Notes on Numerical Methods in Engineering and Sciences; vol. 1. Basis and Solids).
100. Archer JS. Consistent matrix formulations for structural analysis using finite-element techniques. *AIAA Journal*. 1965;3:1910–1918.
101. Reddy JN. An introduction to the finite element method. 2nd ed. McGraw-Hill, Inc.: McGraw.Hill series in mechanical engineering; 1993.
102. Y. Xiu-ying GJ Z. Jin-ch. Stiffness matrix derivation of space beam element at elevated temperature. *J. Shanghai Jiaotong Univ*. 2010;4:492–497.
103. Elseifi M. A new scheme for the optimum design of stiffened composite panels with geometric imperfections [thesis]. Virginia Polytechnic Institute and State University; 1998.
104. Green G. On the propagation of light in crystallized media. *Transactions of the Cambridge Philosophical Society*. 1841;7:121–140.
105. Rajagopal KR. On implicit constitutive theories. *Applications of Mathematics*. 2003;48(4):279–319.

DRAFT: UNCLASSIFIED

106. Akintunde AR, Miller KS. Evaluation of microstructurally motivated constitutive models to describe age-dependent tendon healing. *Biomechanics and Modeling in Mechanobiology*. 2018;17:793–814.
107. Robbins AB, Freed AD, Moreno MR. Characterizing the non-linear mechanical behavior of native and biomimetic engineered tissues in 1d with physically meaningful parameters. *Journal of the Mechanical Behavior of Biomedical Materials*. 2020;102:103509.
108. Freed AD, Rajagopal KR. A viscoelastic model for describing the response of biological fibers. *ACTA Mechanica*. 2016;227:3367–3380.

Appendix A. Implicit Elasticity

DRAFT: UNCLASSIFIED

Both explicit (i.e., Green¹⁰⁴) and implicit (i.e., Rajagopal¹⁰⁵) elastic material models are put forward in this appendix for one's consideration when choosing a material model to represent biologic fibers and membranes. We discuss thermoelastic fibers first, and then thermoelastic membranes. We have no need to address thermoelastic bodies in 3D for our application, beyond what has been presented in Section 4.4. In this appendix, we employ Gibbs free-energy potential \mathcal{G} instead of the internal energy potential U , which we employ in the body of this report. These potentials relate to one another through a well-known Legendre transformation. A Gibbs energy approach implies that a change in the intensive variables (thermodynamic forces) will cause a response in the extensive variables (thermodynamic displacements), which is the exact opposite cause-and-effect arising from an internal energy approach. Causality is correct whenever one uses a Gibbs approach, from a physics perspective. Nevertheless, applications often find other approaches to be more useful, especially that of Helmholtz. Here we present both secant and tangent moduli formulations for biologic fibers and membranes, as both are required by our variational formulation.

A.1 Alveolar Chords as Green (Explicit) Thermoelastic Fibers

For a 1D fiber with a mass density of ρ per unit length, the thermodynamic conjugate fields are: temperature θ and entropy η , plus force F and length L , whose initial values in some reference configuration are denoted as θ_0 , η_0 , F_0 and L_0 . In our construction, it is insightful to use $\ln(\theta/\theta_0)$ and $\ln(L/L_0)$ as measures for change in temperature and length, with the former changing how we interpret thermal strain, but not specific heat, while the latter is commonly referred to as mechanical strain, viz., $e := \ln(L/L_0)$.

A Green thermoelastic fiber has a Gibbs free-energy potential described by an explicit function of state, viz., $\mathcal{G}(\theta, F)$ where $d\mathcal{G} = -\eta d\theta - \frac{1}{\rho}e dF$ (cf. Eqn. 56a), out of which one derives the governing thermoelastic constitutive equations, viz., for entropy

$$\eta = -\partial_\theta \mathcal{G}(\theta, F), \quad (\text{A-1a})$$

and for strain

$$e := \ln(L/L_0) = -\rho \partial_F \mathcal{G}(\theta, F). \quad (\text{A-1b})$$

Providing an energy function establishes a material model.

A.1.1 Hookean Fibers

Herein we consider a Gibbs free-energy potential suitable for describing a Hookean fiber, i.e.,

$$\begin{aligned} \mathcal{G}(\theta, F) = & -\eta_0(\theta - \theta_0) - C \left(\theta \ln \left(\frac{\theta}{\theta_0} \right) - (\theta - \theta_0) \right) \\ & - \frac{F - F_0}{\rho} \left(\alpha \ln \left(\frac{\theta}{\theta_0} \right) + \frac{F - F_0}{2E} \right) \end{aligned} \quad (\text{A-2})$$

normalized so that $\mathcal{G}(\theta_0, F_0) = 0$ with initial conditions of $\eta_0 = -\partial_\theta \mathcal{G}(\theta_0, F_0)$ and $e_0 = -\rho \partial_F \mathcal{G}(\theta_0, F_0) = 0$ in our reference state associated with fields θ_0 and F_0 . Introducing $\ln(\theta/\theta_0)$ presumes that temperature θ is absolute, i.e., it is measured in Kelvin, not centigrade, so in our application $\theta_0 = 310$ K is body temperature.

The model's material properties are: a specific heat C , a thermal strain coefficient α , and an elastic compliance $1/E$ or modulus E . These properties are interpreted from the perspective of both secant and tangent functions of state in this appendix.

In vivo, biologic fibers operate under cyclic loading conditions where, typically, $0 < F_{\min} < F < F_{\max} < F_{\text{ult}}$ that, under normal physiologic conditions, finds force F traversing between F_{\min} and F_{\max} with F_{ult} designating ultimate rupture strength. Here we take F_0 to associate with F_{\min} . Consequently, strain is assigned to be zero in this reference state of $F_0 > 0$. Similarly, physicians will reference against some physiologic state of relevance; however, their reference states usually associate with F_{\max} , not F_{\min} , e.g., total lung capacity for pulmonary applications, and max systole for cardiac applications. *Ex vivo*, one typically selects $F_0 = 0$ for biologic fibers.

A.1.2 Secant Material Properties

Upon substituting the Gibbs free-energy function (A-2) into the constitutive equations (A-1a & A-1b) governing entropy and strain, respectively, results in the matrix

expression

$$\begin{Bmatrix} \eta - \eta_0 \\ \ln(L/L_0) \end{Bmatrix} = \begin{bmatrix} C_s & \alpha_s/\rho\theta \\ \alpha_s & 1/E_s \end{bmatrix} \begin{Bmatrix} \ln(\theta/\theta_0) \\ F - F_0 \end{Bmatrix}$$

which rearranges into a form that is more suitable for our needs, specifically

$$\begin{Bmatrix} \eta - \eta_0 \\ F - F_0 \end{Bmatrix} = \begin{bmatrix} C_s - \alpha_s^2 E_s / \rho\theta & \alpha_s E_s / \rho\theta \\ -\alpha_s E_s & E_s \end{bmatrix} \begin{Bmatrix} \ln(\theta/\theta_0) \\ \ln(L/L_0) \end{Bmatrix} \quad (\text{A-3a})$$

with material properties: a specific heat (evaluated at some reference force F_0) of

$$C_s := \left. \frac{\eta - \eta_0}{\ln(\theta/\theta_0)} \right|_{F=F_0} \quad (\text{A-3b})$$

with $C_s - \alpha_s^2 E_s / \rho\theta$ being a heat capacity (evaluated at some reference length L_0), plus a thermal strain coefficient (evaluated at some reference force F_0) of

$$\alpha_s := \left. \frac{\ln(L/L_0)}{\ln(\theta/\theta_0)} \right|_{F=F_0}, \quad (\text{A-3c})$$

and an elastic compliance (evaluated at some reference temperature θ_0) of

$$\frac{1}{E_s} := \left. \frac{\ln(L/L_0)}{F - F_0} \right|_{\theta=\theta_0}. \quad (\text{A-3d})$$

These are *secant* material properties, hence the subscript ‘ s ’, which can be measured through appropriate experiments. The curves that they trace through state space are then to be approximated via a model.

Note: Thermal elongation is typically modeled as $\alpha(\theta - \theta_0)$, wherein α is referred to as the coefficient for thermal expansion. Our thermal strain coefficient α_s , which is dimensionless, and the coefficient for thermal expansion α , which has dimensions of reciprocal temperature, relate via $\alpha_s = \alpha\theta_0 + \mathcal{O}\left(((\theta - \theta_0)/\theta_0)^2\right)$ because $\ln(\theta/\theta_0) = (\theta - \theta_0)/\theta_0 - (\theta - \theta_0)^2/\theta_0^2 + (\theta - \theta_0)^3/\theta_0^3 - \dots$.

A.1.3 Tangent Material Properties

Upon differentiating the constitutive equations for entropy and strain found in Eqns. (A-1a & A-1b), respectively, assuming that they are both sufficiently differentiable functions of state, while adopting the expression for Gibbs free energy found in

DRAFT: UNCLASSIFIED

Eqn. (A-2), results in the following constitutive equation

$$\begin{Bmatrix} d\eta \\ L^{-1} dL \end{Bmatrix} = - \begin{bmatrix} \partial_{\theta\theta} \mathcal{G} & \partial_{\theta F} \mathcal{G} \\ \rho \partial_{F\theta} \mathcal{G} & \rho \partial_{FF} \mathcal{G} \end{bmatrix} \begin{Bmatrix} d\theta \\ dF \end{Bmatrix} = \begin{bmatrix} C_t & \alpha_t/\rho\theta \\ \alpha_t & 1/E_t \end{bmatrix} \begin{Bmatrix} \theta^{-1} d\theta \\ dF \end{Bmatrix}$$

where we observe that the intensive and extensive variables now appear in rate or differential form; hence, this formulation is hypo-elastic.⁶⁶ This matrix equation can be rearranged into an expression that is more suitable for our needs, viz.,,

$$\begin{Bmatrix} d\eta \\ dF \end{Bmatrix} = \begin{bmatrix} C_t - \alpha_t^2 E_t / \rho\theta & \alpha_t E_t / \rho\theta \\ -\alpha_t E_t & E_t \end{bmatrix} \begin{Bmatrix} \theta^{-1} d\theta \\ L^{-1} dL \end{Bmatrix} \quad (\text{A-4a})$$

whose material properties are: a specific heat (at constant force) of

$$C_t := \frac{d\eta}{\theta^{-1} d\theta} \Big|_{dF=0} = C_s - \frac{\alpha_s(F - F_0)}{\rho\theta} = -\theta \partial_{\theta\theta} \mathcal{G}(\theta, F) \quad (\text{A-4b})$$

where the tangent response for specific heat C_t relates to the secant response for specific heat C_s via $C_t = C_s - \alpha_s(F - F_0)/\rho\theta$, with $C_t - \alpha_t^2 E_t / \rho\theta$ being a heat capacity (at constant strain), plus a thermal strain coefficient (at constant force) of

$$\alpha_t := \frac{L^{-1} dL}{\theta^{-1} d\theta} \Big|_{dF=0} = -\rho\theta \partial_{F\theta} \mathcal{G}(\theta, F) = -\rho\theta \partial_{\theta F} \mathcal{G}(\theta, F) \quad (\text{A-4c})$$

where, typically, $\alpha_t \equiv \alpha_s$, and an elastic compliance (at constant temperature) of

$$\frac{1}{E_t} := \frac{L^{-1} dL}{dF} \Big|_{d\theta=0} = -\rho \partial_{FF} \mathcal{G}(\theta, F) \quad (\text{A-4d})$$

which is distinct from its secant compliance for the biologic fiber model that follows. These are *tangent* material properties, hence the subscript ‘*t*’, whose values can be measured through appropriate experiments.

Matrix equation (A-4a) is expressed in terms of Helmholtz causality, but is derived out of Gibbs causality to ensure that Maxwell’s condition (present in Eqns. A-4a & A-4c) is satisfied.

It turns out that these tangent material properties correspond directly with components acquired from the Laplacian of one’s Gibbs free-energy potential.

A.2 Alveolar Chords as Rajagopal (Implicit) Thermoelastic Fibers

In 2003, Rajagopal¹⁰⁵ introduced the idea of an implicit elastic solid. In 2016, Freed & Rajagopal⁹⁰ constructed an elastic fiber model that convolves an explicit energy with an implicit energy. In their approach, they decomposed fiber strain $e := \ln(L/L_0)$ into a sum of two strains, viz., $e = e_1 + e_2$ wherein $e_1 := \ln(L_1/L_0)$ and $e_2 := \ln(L/L_1)$. Length L_0 is a reference fiber length, viz., its length whereat $F = F_0$. Length L_1 can be thought of as the fiber's length caused solely by a molecular reconfiguration under an applied load of F (e.g., an unraveling of crimp in collagen, a network reorientation in elastin, a reconformation in structural proteins, etc.). The state associated with length L_1 is non-physical in that one cannot unravel molecules without also stretching some of their bonds to a certain extent. Final length L is the actual fiber length under an applied load F caused by both a reconfiguration and a stretching of its molecular network. Here we present their ideas in terms of a Gibbs free-energy function, which leads naturally to additive compliances, instead of working with moduli, which do not add.*

Let the Gibbs free-energy potential be described by a function of the form[†]

$$\mathcal{G}(\theta, e, F) := \mathcal{G}_1(e_1, F) + \mathcal{G}_2(\theta, F) \quad \text{with} \quad d\mathcal{G} = -\eta d\theta - \frac{1}{\rho} e dF \quad (\text{A-5})$$

where \mathcal{G}_1 is an implicit potential (a configuration energy) and \mathcal{G}_2 is an explicit potential (a strain energy). This energy function leads to the same constitutive equation displayed in Eqn. (A-4a), but whose material properties from Eqns. (A-4b–A-4d) are now interpreted according to the following formulæ

$$C_t := \left. \frac{d\eta}{\theta^{-1} d\theta} \right|_{dF=0} = -\theta \partial_{\theta\theta} \mathcal{G}(\theta, e, F) = -\theta \partial_{\theta\theta} \mathcal{G}_2(\theta, F) \quad (\text{A-6a})$$

$$\alpha_t := \left. \frac{L^{-1} dL}{\theta^{-1} d\theta} \right|_{dF=0} = -\rho \theta \partial_{F\theta} \mathcal{G}(\theta, e, F) = -\rho \theta \partial_{F\theta} \mathcal{G}_2(\theta, F) \quad (\text{A-6b})$$

$$\begin{aligned} \frac{1}{E_t} := \left. \frac{L^{-1} dL}{dF} \right|_{d\theta=0} &= -(\rho \partial_{e_1} \mathcal{G}_1(e_1, F))^{-1} (e + \rho \partial_F \mathcal{G}(\theta, e, F)) \\ &\quad - \rho \partial_{FF} \mathcal{G}_2(\theta, F) \end{aligned} \quad (\text{A-6c})$$

*Freed & Rajagopal⁹⁰ originally used a Helmholtz free-energy function.

[†]One might be tempted to consider an implicit energy function of the form $\mathcal{G} = \mathcal{G}_1(\theta, e, F) + \mathcal{G}_2(\theta, F)$, but this would lead to a non-symmetric susceptibility matrix. Consequently, it would not satisfy Maxwell's thermodynamic constraint, a.k.a. Sylvester's condition for integrability of a Pfaffian form. Hence, it is an inadmissible functional dependence for a Gibbs potential.

where mass density ρ is a mass per unit length of line. Elastic compliance $1/E_t$ is now found to be a sum of two compliances, independent of the functional forms that one might select for $\mathcal{G}_1(e_1, F)$ and $\mathcal{G}_2(\theta, F)$. One compliance is explicit in origin, i.e., $e_2 = -\rho \partial_F \mathcal{G}_2$ with rate $de_2 = -\rho \partial_{F\theta} \mathcal{G}_2 d\theta - \rho \partial_{FF} \mathcal{G}_2 dF$. It comprises the second row in Eqn. (A-6c). The other compliance is implicit in origin, viz., $de_1 = -(\rho \partial_{e_1} \mathcal{G}_1)^{-1}(e_1 + \rho \partial_F \mathcal{G}_1) dF \equiv -(\rho \partial_{e_1} \mathcal{G}_1)^{-1}(e + \rho \partial_F \mathcal{G}) dF$. It comprises the first row in Eqn. (A-6c). Also, $\partial_{F\theta} \mathcal{G} = \partial_{\theta F} \mathcal{G}$ because of Maxwell's thermodynamic constraint.

The material properties of Eqn. (A-6) apply to matrix equation (A-4a), just as those for a Hookean material do, viz., Eqns. A-4b–A-4d). The specific heat C_t and thermal strain coefficient α_t have the same interpretations for both explicit and implicit fiber theories. It is with respect to their compliances through which they differ.

Derivation: Because Gibbs free energy is a state function, its differential describes a Pfaffian form, and as such, the left-hand side of the thermodynamic expression $d\mathcal{G} = -\eta d\theta - \frac{1}{\rho} e dF$ becomes $d\mathcal{G} = \partial_{e_1} \mathcal{G}_1 de_1 + \partial_F \mathcal{G}_1 dF + \partial_\theta \mathcal{G}_2 d\theta + \partial_F \mathcal{G}_2 dF$. Recalling that $e = e_1 + e_2$, the explicit (hyper-elastic like) terms combine to produce constitutive equations

$$\eta = -\partial_\theta \mathcal{G}_2(\theta, F) \quad \text{and} \quad e_2 = -\rho \partial_F \mathcal{G}_2(\theta, F)$$

while the remaining implicit terms collect to yield a differential constitutive equation of the form

$$\rho \partial_{e_1} \mathcal{G}_1(e_1, F) de_1 = -\left(e_1 + \rho \partial_F \mathcal{G}_1(e_1, F)\right) dF.$$

Differentiating the constitutive equation for entropy with respect to state leads directly to expressions for the specific heat C_t and the thermal expansion coefficient α_t stated in Eqns. (A-6a & A-6b). Recalling that the strains add, i.e., $e = e_1 + e_2$, and therefore so do their rates, viz., $de = de_1 + de_2$, a direct consequence of them being logarithmic in construction, it follows that upon rearranging the implicit constitutive equation to solve for de_1 , while differentiating the explicit constitutive equation for e_2 , and finally adding these strain increments to get de , one obtains the elastic compliance function stated in Eqn. (A-6c). \square

A.2.1 Biologic Fibers with Tangent Material Properties

The fiber model of Freed & Rajagopal⁹⁰ imposes a limiting constraint $e_{1\max}$ onto the internal strain of reconfiguration e_1 , viz., $e_1 \leq e_{1\max}$. Their model, when cast in terms of a Gibbs free-energy function in the form of Eqn. (A-5), is described by an implicit energy contribution of*

$$\mathcal{G}_1(e_1, F) = -\frac{1}{\rho} \left(e_{1\max} (E_1 e_1 - (F - F_0)) + 2e_1(F - F_0) \right) \quad (\text{A-7a})$$

and an explicit energy contribution of

$$\begin{aligned} \mathcal{G}_2(\theta, F) = & -\eta_0(\theta - \theta_0) - C \left(\theta \ln \left(\frac{\theta}{\theta_0} \right) - (\theta - \theta_0) \right) \\ & - \frac{F - F_0}{\rho} \left(\alpha \ln \left(\frac{\theta}{\theta_0} \right) + \frac{F - F_0}{2E_2} \right) \end{aligned} \quad (\text{A-7b})$$

that, collectively, depend upon temperature θ , force F , and an internal strain e_1 , whose free energy is normalized so that $\mathcal{G}_1(e_{1,0}, F_0) = 0$ and $\mathcal{G}_2(\theta_0, F_0) = 0$ with initial conditions $e_{1,0} = 0$, $e_{2,0} = -\rho \partial_F \mathcal{G}_2(\theta_0, F_0) = 0$ and $\eta_0 = -\partial_\theta \mathcal{G}_2(\theta_0, F_0)$. In fact, the explicit contribution to the free energy adopted here is Hookean, cf. Eqn. (A-2). The resulting constitutive responses for entropy η and force F are therefore described by the following differential matrix equation

$$\begin{Bmatrix} d\eta \\ dF \end{Bmatrix} = \begin{bmatrix} C_t - \alpha_t^2 E_t / \rho \theta & \alpha_t E_t / \rho \theta \\ -\alpha_t E_t & E_t \end{bmatrix} \begin{Bmatrix} \theta^{-1} d\theta \\ L^{-1} dL \end{Bmatrix} \quad (\text{A-4a})$$

whose elastic tangent compliance is now described by

$$\frac{1}{E_t(\theta, e, F)} = \frac{e_{1\max} - e_1}{E_1 e_{1\max} + 2(F - F_0)} + \frac{1}{E_2} \quad (\text{A-7c})$$

wherein

$$e_1 = e - \alpha \ln \left(\frac{\theta}{\theta_0} \right) - \frac{F - F_0}{E_2} \quad (\text{A-7d})$$

*In the paper of Freed & Rajagopal,⁹⁰ they adopted a Helmholtz free-energy potential of the form $Ee_1 - F + \beta e_1 F$ where β is a material parameter that relates to a limiting state of strain. Here we adopt a Gibbs free-energy potential of like form, specifically $e_{1\max}(Ee_1 - F) + 2e_1 F$ where $e_{1\max}$ is this limiting state of internal strain e_1 . We point out that an exponential response akin to Fung's material models will result whenever the energy of reconfiguration takes on a form of $Ee_1 - F$.

DRAFT: UNCLASSIFIED

and whose initial tangent modulus $E_t(\theta_0, e_0, F_0)$ is $E_1 E_2 / (E_1 + E_2)$ ($\approx E_1$ whenever $E_2 \gg E_1 > 0$) while its terminal tangent modulus $E_t(e_1 = e_{1\max})$ is E_2 . A transition strain occurs at $e_{1\max} (> 0)$, which establishes the limiting state for internal strain e_1 , i.e., $e_1 \leq e_{1\max}$. This is a strain whereat the fiber's molecular configuration becomes completely unraveled. The 2 in term $2e_1(F - F_0)$ of Eqn. (A-7a) leads to the desired numerator for the implicit contribution to compliance established in Eqn. (A-7c), viz., $e_{1\max} - e_1$, which is the source of the strain limiting quality of the model. This fiber model has been found to be superior to other models commonly employed in the literature for modeling biologic fibers.^{106,107}

Both the explicit and implicit models have the same hypo-elastic structure, viz., Eqn. (A-4a). Furthermore, their thermal properties C_t and α_t have the same physical interpretations. Only their elastic compliances/moduli are interpreted differently. Even so, they are related because $1/E_s = \int_{F_0}^F (1/E_t) dF$.

The sum of implicit and explicit fiber compliances, as established in Eqn. (A-7c), was originally a conjecture by Freed & Rajagopal.⁹⁰ Here it is shown to be a thermodynamic consequence, provided that $\mathcal{G}(\theta, e, F) = \mathcal{G}_1(e_1, F) + \mathcal{G}_2(\theta, F)$ and that $e = e_1 + e_2$ with $e_2 = -\rho \partial_F \mathcal{G}_2$. This follows because a Gibbs free energy is used here; whereas, Freed & Rajagopal employed a Helmholtz free energy.

Biologic fibers, per our application, are long and slender. Consequently, they will buckle under compression. Buckling is not accounted for in our modeling of alveolar chords. Rather, it is assumed that the compliant response at F_0 , with a modulus of $E_1 E_2 / (E_1 + E_2)$, continues over the non-physiologic loading range of $0 < F \leq F_{\min} = F_0$, which is the body's way of ensuring structural integrity of its biologic fibers.

The above methodology would allow us to construct a suite of thermodynamically admissible, elastic, compliance functions, but we will only have need for the simple fiber model put forward in Eqn. (A-7).

A.2.2 Biologic Fibers with Secant Material Properties

Material properties C_t , α_t and E_t for the above model, viz., those of Eqn. (A-7), describe tangents to material response functions. For the thermal properties, their secant counterparts C_s and α_s relate to their tangent properties C_t and α_t just as they do for a Green elastic fiber. Only the elastic compliance needs to be addressed.

DRAFT: UNCLASSIFIED

The tangent modulus E_t is established through the relationship

$$\frac{1}{E_t} := \left. \frac{de}{dF} \right|_{d\theta=0} = \left. \frac{de_1}{dF} \right|_{d\theta=0} + \left. \frac{de_2}{dF} \right|_{d\theta=0} =: \frac{1}{E_{1t}} + \frac{1}{E_{2t}} \quad (\text{A-8a})$$

so that a fiber's elastic compliance is described by

$$de = \frac{dF}{E_t} \quad \text{where} \quad \frac{1}{E_t} = \frac{1}{E_{1t}} + \frac{1}{E_{2t}} \quad (\text{A-8b})$$

and, consequently, its elastic modulus is described by

$$dF = E_t de \quad \text{where} \quad E_t = \frac{E_{1t}E_{2t}}{E_{1t} + E_{2t}}. \quad (\text{A-8c})$$

The implicit free-energy function introduced through Eqn. (A-7) produces a tangent compliance of

$$\frac{1}{E_t} = \frac{e_{1\max} - e_1}{E_1 e_{1\max} + 2(F - F_0)} + \frac{1}{E_2} \quad (\text{A-8d})$$

whose internal strain caused by molecular reconfiguration comes from

$$e_1 = e - \alpha_t \ln \left(\frac{\theta}{\theta_0} \right) - \frac{F - F_0}{E_2}. \quad (\text{A-8e})$$

The material properties of this model are: $E_1 E_2 / (E_1 + E_2)$ (> 0) is the initial tangent modulus, E_2 ($\gg E_1 > 0$) is the terminal tangent modulus, $e_{1\max}$ is the maximum strain that can arise from a molecular reconfiguration, and α_t is the thermal strain coefficient, all quantified against a reference state described by θ_0 and F_0 .

It follows then that its associated secant compliance obeys

$$\frac{1}{E_s} := \left. \frac{e}{F - F_0} \right|_{\theta=\theta_0} = \left. \frac{e_1}{F - F_0} \right|_{\theta=\theta_0} + \left. \frac{e_2}{F - F_0} \right|_{\theta=\theta_0} =: \frac{1}{E_{1s}} + \frac{1}{E_{2s}} \quad (\text{A-9a})$$

so the fiber's compliance representation is described by

$$e = \frac{F - F_0}{E_s} \quad \text{where} \quad \frac{1}{E_s} = \frac{1}{E_{1s}} + \frac{1}{E_{2s}} \quad (\text{A-9b})$$

and, therefore, its modulus representation is described by

$$F = F_0 + E_s e \quad \text{where} \quad E_s = \frac{E_{1s} E_{2s}}{E_{1s} + E_{2s}}. \quad (\text{A-9c})$$

where, upon integrating Eqn. (A-8d) by parts, one arrives at a secant compliance comprised of a sum between

$$\frac{1}{E_{1s}} = \frac{e_{1\max}}{F - F_0} \left(1 - \frac{\sqrt{E_1 e_{1\max}}}{\sqrt{E_1 e_{1\max} + 2(F - F_0)}} \right) \quad (\text{A-9d})$$

and

$$\frac{1}{E_{2s}} = \frac{1}{E_2} \quad (\text{A-9e})$$

with $E_s(F \leq F_0) = E_1 E_2 / (E_1 + E_2)$.

A.2.3 Viscoelastic Biologic Fibers

Freed & Rajagopal¹⁰⁸ have shown that realistic viscoelastic responses for biologic fibers can be based upon the above thermoelastic fiber model by retaining the implicit contribution to the compliance, i.e., $1/E_1$, as elastic, while only extending the explicit contribution to the compliance, viz., $1/E_2$, into the viscoelastic domain. This finding is significant! It allows one to model the viscoelastic response of non-linear biologic fibers by employing a *linear* theory for viscoelasticity. Effectively, elastic compliance $1/E_2$ in Eqn. (A-7c) becomes a viscoelastic function of state. This is a topic for future work.

A.3 Alveolar Septa as Green (Explicit) Thermoelastic Membranes

For a 2D membrane with a mass density of ρ per unit area, its response is comprised of uniform and non-uniform contributions. The thermodynamic conjugate fields pertaining to uniform behaviors are: temperature θ and entropy η , and surface tension π and dilation ξ , cf. Eqn. (69a). While the conjugate fields pertaining to non-uniform behaviors are: normal stress difference σ and squeeze strain ε , and shear stress τ and shear strain γ , cf. Eqn. (69b).

We observed in Section 4.2 that the uniform and non-uniform contributions of an alveolar membrane are not coupled. Consequently, their Gibbs free energies add in

DRAFT: UNCLASSIFIED

such a manner that $\mathcal{G}(\theta, \pi, \sigma, \tau) = \mathcal{G}_u(\theta, \pi) + \mathcal{G}_n(\sigma, \tau)$, with \mathcal{G}_u being the uniform contribution of \mathcal{G} , and \mathcal{G}_n being the non-uniform contribution of \mathcal{G} .

A Green thermoelastic membrane has a Gibbs free-energy potential described by $\mathcal{G}(\theta, \pi, \sigma, \tau) = \mathcal{G}_u(\theta, \pi) + \mathcal{G}_n(\sigma, \tau)$ where $d\mathcal{G} = -\eta d\theta - \frac{1}{\rho}(\xi d\pi + \varepsilon d\sigma + \gamma d\tau)$ from which one derives its governing thermoelastic constitutive equations; specifically, for entropy

$$\eta = -\partial_\theta \mathcal{G}(\theta, \pi, \sigma, \tau) = -\partial_\theta \mathcal{G}_u(\theta, \pi), \quad (\text{A-10a})$$

for dilation

$$\xi = -\rho \partial_\pi \mathcal{G}(\theta, \pi, \sigma, \tau) = -\rho \partial_\pi \mathcal{G}_u(\theta, \pi), \quad (\text{A-10b})$$

for squeeze

$$\varepsilon = -\rho \partial_\sigma \mathcal{G}(\theta, \pi, \sigma, \tau) = -\rho \partial_\sigma \mathcal{G}_n(\sigma, \tau), \quad (\text{A-10c})$$

and for shear

$$\gamma = -\rho \partial_\tau \mathcal{G}(\theta, \pi, \sigma, \tau) = -\rho \partial_\tau \mathcal{G}_n(\sigma, \tau) \quad (\text{A-10d})$$

whereby specifying energies \mathcal{G}_u and \mathcal{G}_n produces a material model for membranes.

A.3.1 Hookean Membranes

In this appendix, we consider a function for the Gibbs free-energy potential that is suitable for describing biologic Hookean membranes; specifically: for governing their uniform response, let

$$\begin{aligned} \mathcal{G}_u(\theta, \pi) &= -\eta_0(\theta - \theta_0) - C \left(\theta \ln \left(\frac{\theta}{\theta_0} \right) - (\theta - \theta_0) \right) \\ &\quad - \frac{\pi - \pi_0}{2\rho} \left(2\alpha \ln \left(\frac{\theta}{\theta_0} \right) + \frac{\pi - \pi_0}{4M} \right) \end{aligned} \quad (\text{A-11a})$$

and for governing their non-uniform response, let

$$\mathcal{G}_n(\sigma, \tau) = -\frac{1}{2\rho} \left(\frac{\sigma^2}{2N} + \frac{\tau^2}{G} \right) \quad (\text{A-11b})$$

where symmetries $\mathcal{G}_n(\sigma, \tau) = \mathcal{G}_n(-\sigma, \tau) = \mathcal{G}_n(\sigma, -\tau) = \mathcal{G}_n(-\sigma, -\tau)$ must hold because the squeeze and shear variables can take on either sign. These free energies are normalized so that $\mathcal{G}_u(\theta_0, \pi_0) = 0$ and $\mathcal{G}_n(\sigma_0, \tau_0) = 0$ with initial conditions of $\eta_0 = -\partial_\theta \mathcal{G}_u(\theta_0, \pi_0)$, $\xi_0 = -\rho \partial_\pi \mathcal{G}_u(\theta_0, \pi_0) = 0$, $\varepsilon_0 = -\rho \partial_\sigma \mathcal{G}_n(0, 0) = 0$ and $\gamma_0 = -\rho \partial_\tau \mathcal{G}_n(0, 0) = 0$ for a reference state with fields $\theta_0, \pi_0, \sigma_0 = 0$ and $\tau_0 = 0$.

Here we presume that the reference values for the non-uniform stresses, viz., σ_0 and τ_0 , are both zero, i.e., $\sigma_0 = 0$ and $\tau_0 = 0$. This follows because these fields can be either positive or negative in their values; whereas, surface tension π is a positive only field, and as such, the notion of a non-zero reference value π_0 is physiologically sound; it is nature's way of helping to stabilize a membrane.

A.3.2 Secant Material Properties

A.3.2.1 Uniform Response

Substituting the Gibbs free-energy function of Eqn. (A-11a) into the constitutive equations governing entropy (A-10a) and dilation (A-10b) results in a matrix expression of

$$\begin{Bmatrix} \eta - \eta_0 \\ \ln \sqrt{A/A_0} \end{Bmatrix} = \begin{bmatrix} C_s & \alpha_s/\rho\theta \\ \alpha_s & 1/4M_s \end{bmatrix} \begin{Bmatrix} \ln(\theta/\theta_0) \\ \pi - \pi_0 \end{Bmatrix}$$

where $\xi := \ln \sqrt{A/A_0}$. This matrix equation can be rearranged into a form that is more suitable for our needs, viz.,

$$\begin{Bmatrix} \eta - \eta_0 \\ \pi - \pi_0 \end{Bmatrix} = \begin{bmatrix} C_s - 4\alpha_s^2 M_s / \rho\theta & 4\alpha_s M_s / \rho\theta \\ -4\alpha_s M_s & 4M_s \end{bmatrix} \begin{Bmatrix} \ln(\theta/\theta_0) \\ \ln \sqrt{A/A_0} \end{Bmatrix} \quad (\text{A-12a})$$

whose material properties are: a specific heat (evaluated at a reference surface tension π_0) of

$$C_s := \left. \frac{\eta - \eta_0}{\ln(\theta/\theta_0)} \right|_{\pi=\pi_0} \quad (\text{A-12b})$$

with $C_s - 4\alpha_s^2 M_s / \rho\theta$ being a heat capacity in an absence of dilation, plus a thermal strain coefficient (evaluated at a reference surface tension π_0) of

$$\alpha_s := \left. \frac{\ln(L/L_0)}{\ln(\theta/\theta_0)} \right|_{\pi=\pi_0} = \frac{1}{2} \left. \frac{\ln(A/A_0)}{\ln(\theta/\theta_0)} \right|_{\pi=\pi_0}, \quad (\text{A-12c})$$

DRAFT: UNCLASSIFIED

where $\ln(A/A_0) = 2\ln(L/L_0)$ is the surface dilation, with L/L_0 being the stretch between any two points on its surface, plus an elastic membrane compliance (evaluated at a reference temperature θ_0) of

$$\frac{1}{M_s} := \left. \frac{\ln(A/A_0)}{T - T_0} \right|_{\theta=\theta_0} = 4 \left. \frac{\xi}{\pi - \pi_0} \right|_{\theta=\theta_0}, \quad (\text{A-12d})$$

where $T := \frac{1}{2}(\sigma_{11} + \sigma_{22}) =: \frac{1}{2}\pi$ is the surface tension, with σ_{ij} being components of the Cauchy stress in this two-dimensional space. These are *secant* material properties, hence the subscript ‘*s*’, whose values can be measured in experiments.

Note: Thermal strain is typically modeled as $\alpha(\theta - \theta_0)$, wherein α is referred to as the coefficient for lineal thermal expansion. Our thermal strain coefficient α_s and the coefficient for lineal thermal expansion α relate via $\alpha_s = \alpha\theta_0 + \mathcal{O}(((\theta - \theta_0)/\theta_0)^2)$ because $\ln(\theta/\theta_0) = (\theta - \theta_0)/\theta_0 - (\theta - \theta_0)^2/\theta_0^2 + (\theta - \theta_0)^3/\theta_0^3 - \dots$.

A.3.2.2 Non-Uniform Response

Substituting the Gibbs free-energy function of Eqn. (A-11b) into the constitutive equations governing squeeze (A-10c) and shear (A-10d) leads to the following matrix equation

$$\begin{Bmatrix} \varepsilon \\ \gamma \end{Bmatrix} = \begin{bmatrix} 1/2N_s & 0 \\ 0 & 1/G_s \end{bmatrix} \begin{Bmatrix} \sigma \\ \tau \end{Bmatrix}$$

that when inverted becomes

$$\begin{Bmatrix} \sigma \\ \tau \end{Bmatrix} = \begin{bmatrix} 2N_s & 0 \\ 0 & G_s \end{bmatrix} \begin{Bmatrix} \varepsilon \\ \gamma \end{Bmatrix} \quad (\text{A-13a})$$

whose material properties are: a squeeze compliance (in an absence of shear γ) of

$$\frac{1}{N_s} := \left. \frac{\ln(\Gamma/\Gamma_0)}{\sigma_{11} - \sigma_{22}} \right|_{g=g_0} = 2 \left. \frac{\varepsilon}{\sigma} \right|_{\gamma=0} \quad (\text{A-13b})$$

where $\Gamma := a/b$ and $\Gamma_0 = a_0/b_0$ are the current and reference stretches of squeeze, with $\varepsilon := \ln \sqrt{\Gamma/\Gamma_0}$ being the squeeze strain, and where $\sigma := \sigma_{11} - \sigma_{22}$ establishes a normal stress difference, plus a shear compliance (in an absence of squeeze ε) of

$$\frac{1}{G_s} := \left. \frac{g - g_0}{\Gamma \sigma_{21}} \right|_{\Gamma=\Gamma_0} = \left. \frac{\gamma}{\tau} \right|_{\varepsilon=0} \quad (\text{A-13c})$$

where g and g_0 are the current and reference magnitudes of shear, with $\gamma := g - g_0$ denoting shear strain, and where $\tau := \Gamma\sigma_{21}$ establishes the thermodynamic shear stress. These are *secant* material properties, hence the subscript ‘ s ’, whose values can be measured in experiments.

A.3.3 Tangent Material Properties

A.3.3.1 Uniform Response

Upon differentiating the constitutive equations for entropy and dilation found in Eqns. (A-10a & A-10b), respectively, assuming they are both sufficiently differentiable functions of state, while adopting the Gibbs free energy from Eqn. (A-11a), results in the following matrix constitutive equation

$$\begin{Bmatrix} d\eta \\ d\xi \end{Bmatrix} = - \begin{bmatrix} \partial_{\theta\theta} \mathcal{G}_u & \partial_{\theta\pi} \mathcal{G}_u \\ \rho \partial_{\pi\theta} \mathcal{G}_u & \rho \partial_{\pi\pi} \mathcal{G}_u \end{bmatrix} \begin{Bmatrix} d\theta \\ d\pi \end{Bmatrix} = \begin{bmatrix} C_t & \alpha_t/\rho\theta \\ \alpha_t & 1/4M_t \end{bmatrix} \begin{Bmatrix} \theta^{-1} d\theta \\ d\pi \end{Bmatrix}$$

which is hypo-elastic in its construction.⁶⁶ This expression can be rearranged into

$$\begin{Bmatrix} d\eta \\ d\pi \end{Bmatrix} = \begin{bmatrix} C_t - 4\alpha_t^2 M_t / \rho\theta & 4\alpha_t M_t / \rho\theta \\ -4\alpha_t M_t & 4M_t \end{bmatrix} \begin{Bmatrix} \theta^{-1} d\theta \\ \frac{1}{2} A^{-1} dA \end{Bmatrix} \quad (\text{A-14a})$$

recalling that $d\xi = dA/2A$, and with material properties defined accordingly: a specific heat (at constant surface tension) of

$$C_t := \left. \frac{d\eta}{\theta^{-1} d\theta} \right|_{d\pi=0} = C_s - \alpha_s(\pi - \pi_0)/\rho\theta = -\theta \partial_{\theta\theta} \mathcal{G}_u \quad (\text{A-14b})$$

with $C_t - 4\alpha_t^2 M_t / \rho\theta$ denoting a heat capacity at constant dilation, and a lineal thermal strain coefficient (at constant surface tension) of

$$\alpha_t := \left. \frac{L^{-1} dL}{\theta^{-1} d\theta} \right|_{d\pi=0} = \frac{1}{2} \left. \frac{A^{-1} dA}{\theta^{-1} d\theta} \right|_{d\pi=0} = \begin{cases} -\rho\theta \partial_{\pi\theta} \mathcal{G}_u \\ -\rho\theta \partial_{\theta\pi} \mathcal{G}_u \end{cases} \quad (\text{A-14c})$$

plus a compliance (at constant temperature) of

$$\frac{1}{M_t} := \left. \frac{A^{-1} dA}{dT} \right|_{d\theta=0} = 4 \left. \frac{d\xi}{d\pi} \right|_{d\theta=0} = -4\rho \partial_{\pi\pi} \mathcal{G}_u. \quad (\text{A-14d})$$

These are *tangent* material properties, hence the subscript ‘ t ’, whose values can be measured in experiments.

A.3.3.2 Non-Uniform Response

From $d\mathcal{G} = d\mathcal{G}_u + d\mathcal{G}_n$ with $d\mathcal{G}_u = -\eta d\theta - \frac{1}{\rho}\xi d\pi$ comes $d\mathcal{G}_n = -\frac{1}{\rho}(\varepsilon d\sigma + \gamma d\tau)$ out of which one obtains the constitutive equations governing non-uniform responses in a Green elastic membrane, viz., $\varepsilon = -\rho \partial_\sigma \mathcal{G}_n$ and $\gamma = -\rho \partial_\tau \mathcal{G}_n$, that, assuming they are continuous and differentiable functions of state, can be expressed as the matrix differential equation

$$\begin{Bmatrix} d\varepsilon \\ d\gamma \end{Bmatrix} = -\rho \begin{bmatrix} \partial_{\sigma\sigma} \mathcal{G}_n & \partial_{\sigma\tau} \mathcal{G}_n \\ \partial_{\tau\sigma} \mathcal{G}_n & \partial_{\tau\tau} \mathcal{G}_n \end{bmatrix} \begin{Bmatrix} d\sigma \\ d\tau \end{Bmatrix} = \begin{bmatrix} 1/2N_t & 0 \\ 0 & 1/G_t \end{bmatrix} \begin{Bmatrix} d\sigma \\ d\tau \end{Bmatrix}$$

where $\partial_{\sigma\tau} \mathcal{G}_n = \partial_{\tau\sigma} \mathcal{G}_n = 0$, because the modes of squeeze and shear are taken to be decoupled. The resulting matrix is readily inverted into a form that is more useful for us, namely

$$\begin{Bmatrix} d\sigma \\ d\tau \end{Bmatrix} = \begin{bmatrix} 2N_t & 0 \\ 0 & G_t \end{bmatrix} \begin{Bmatrix} d\varepsilon \\ d\gamma \end{Bmatrix} \quad (\text{A-15a})$$

whose associated material properties are established via

$$\frac{1}{N_t} := \left. \frac{\Gamma^{-1} d\Gamma}{d(\sigma_{11} - \sigma_{22})} \right|_{d\gamma=0} = 2 \left. \frac{d\varepsilon}{d\sigma} \right|_{d\gamma=0} = -2\rho \partial_{\sigma\sigma} \mathcal{G}_n \quad (\text{A-15b})$$

and

$$\frac{1}{G_t} := \left. \frac{1}{\Gamma} \frac{dg}{d\sigma_{21}} \right|_{d\Gamma=0} = \left. \frac{d\gamma}{d\tau} \right|_{d\varepsilon=0} = -\rho \partial_{\tau\tau} \mathcal{G}_n \quad (\text{A-15c})$$

where the conjugate stresses are defined as $\sigma := \sigma_{11} - \sigma_{22}$ and $\tau := \Gamma \sigma_{21}$ with $\Gamma := a/b$ being the stretch of squeeze from which it follows that $\Gamma^{-1} d\Gamma = 2 d\varepsilon$ because the strain of squeeze is given by $\varepsilon = \ln \sqrt{\Gamma/\Gamma_0}$. The squeeze compliance $1/N_t = 2 d\varepsilon/d\sigma|_\gamma$ is evaluated at a constant shear γ , while the shear compliance $1/G_t = d\gamma/d\tau|_\varepsilon$ is evaluated at a constant squeeze ε .

A.4 Alveolar Septa as Rajagopal (Implicit) Thermoelastic Membranes

We employ implicit elasticity here to derive a constitutive theory suitable for describing biologic membranes.

DRAFT: UNCLASSIFIED

A.4.1 Tangent Material Properties

A.4.1.1 Uniform Response

Like the implicit elastic fiber introduced in Eqn. (A-7), the uniform response of an implicit elastic membrane with a strain-limiting dilation can be modeled using a Gibbs free energy of the form $\mathcal{G}_u(\theta, \xi, \pi) := \mathcal{G}_1(\xi_1, \pi) + \mathcal{G}_2(\theta, \pi)$ where our definition for dilation $\xi := \ln \sqrt{A/A_0}$ decomposes into a sum of two dilations: $\xi_1 := \ln \sqrt{A_1/A_0}$ and $\xi_2 := \ln \sqrt{A/A_1}$ so that $\xi = \xi_1 + \xi_2$, with like interpretations as those from their 1D fiber counterparts, viz., e , e_1 and e_2 . Such a membrane's tangent material properties are then given by

$$C_t := -\theta \partial_{\theta\theta} \mathcal{G}_u(\theta, \xi, \pi) = -\theta \partial_{\theta\theta} \mathcal{G}_2(\theta, \pi) \quad (\text{A-16a})$$

$$\alpha_t := -\rho\theta \partial_{\pi\theta} \mathcal{G}_u(\theta, \xi, \pi) = -\rho\theta \partial_{\pi\theta} \mathcal{G}_2(\theta, \pi) = -\rho\theta \partial_{\theta\pi} \mathcal{G}_2(\theta, \pi) \quad (\text{A-16b})$$

$$1/4M_t := -(\rho \partial_{\xi_1} \mathcal{G}_1(\xi_1, \pi))^{-1} (\xi + \rho \partial_\pi \mathcal{G}_u(\theta, \xi, \pi)) - \rho \partial_{\pi\pi} \mathcal{G}_2(\theta, \pi) \quad (\text{A-16c})$$

whose derivations are analogous to those for the implicit fiber derived in Eqn. (A-6).

A.4.1.2 Uniform Biologic Membrane Model

Like our model for a biologic fiber, we consider a Gibbs free-energy function for describing the uniform response of a biologic membrane whose implicit energy function takes on the form of

$$\mathcal{G}_1(\xi_1, \pi) = -\frac{1}{\rho} \left(\xi_{1\max} (4M_1 \xi_1 - (\pi - \pi_0)) + 2\xi_1 (\pi - \pi_0) \right) \quad (\text{A-17a})$$

and whose explicit energy function is

$$\begin{aligned} \mathcal{G}_2(\theta, \pi) &= -\eta_0(\theta - \theta_0) - C_t \left(\theta \ln \left(\frac{\theta}{\theta_0} \right) - (\theta - \theta_0) \right) \\ &\quad - \frac{\pi - \pi_0}{2\rho} \left(2\alpha_t \ln \left(\frac{\theta}{\theta_0} \right) + \frac{\pi - \pi_0}{4M_2} \right) \end{aligned} \quad (\text{A-17b})$$

thereby resulting an elastic tangent compliance, as established in Eqn. (A-16c), of

$$\frac{1}{4M_t(\theta, \xi, \pi)} = \frac{\xi_{1\max} - \xi_1}{4M_1 \xi_{1\max} + 2(\pi - \pi_0)} + \frac{1}{4M_2} \quad (\text{A-17c})$$

wherein

$$\xi_1 = \xi - \alpha_t \ln \left(\frac{\theta}{\theta_0} \right) - \frac{\pi - \pi_0}{4M_2} \quad (\text{A-17d})$$

with $\xi_{1\max} > 0$ being an upper bound on strain ξ_1 , i.e., $\xi_1 \leq \xi_{\max}$. Such a membrane has an initial tangent stiffness $M_t(\theta_0, \xi_0, \pi_0)$ of $M_1 M_2 / (M_1 + M_2)$ ($\approx M_1$ whenever $M_2 \gg M_1 > 0$) and it has a terminal tangent stiffness $M_t(\xi_1 = \xi_{1\max})$ of M_2 .

Membranes will wrinkle under states of negative surface tension (or dilation). In alveolar mechanics, surfactant helps to prevent this, and a possible ensuing alveolar collapse. Wrinkling is not accounted for in our modeling of alveolar septa. Rather, like fibers, it is assumed that the compliant response at π_0 , with modulus $M_1 M_2 / (M_1 + M_2)$, continues over the non-physiologic regime of loading $0 < \pi \leq \pi_0$, which is a body's way of ensuring structural stability in its membranes.

The difference between a Green and Rajagopal thermoelastic membrane undergoing a dilation is in their definitions for elastic compliance. There is no difference in their properties for the specific heat or the thermal strain coefficient. The above model has been successfully applied to a visceral pleura membrane.⁵²

A.4.1.3 Non-Uniform Response

We seek an energetic construction that is consistent with the Freed & Rajagopal⁹⁰ fiber model, but which is applicable to the non-uniform responses that planar membranes can support. A Rajagopal elastic solid is implicit. Therefore, we choose a Gibbs free-energy function for governing non-uniform behavior that looks like

$$\mathcal{G}_n(\varepsilon, \gamma, \sigma, \tau) = \mathcal{G}_1(\varepsilon_1, \sigma) + \mathcal{G}_2(\sigma) + \mathcal{G}_3(\gamma_1, \tau) + \mathcal{G}_4(\tau) \quad (\text{A-18})$$

which depend upon three squeeze strains $\varepsilon := \ln \sqrt{\Gamma/\Gamma_0}$, $\varepsilon_1 := \ln \sqrt{\Gamma_1/\Gamma_0}$ and $\varepsilon_2 := \ln \sqrt{\Gamma/\Gamma_1}$, and three shear strains $\gamma := g - g_0$, $\gamma_1 := g_1 - g_0$ and $\gamma_2 := g - g_1$, both of which are additive in the sense that $\varepsilon = \varepsilon_1 + \varepsilon_2$ and $\gamma = \gamma_1 + \gamma_2$, and as such, so are their differential rates of change $d\varepsilon = d\varepsilon_1 + d\varepsilon_2$ and $d\gamma = d\gamma_1 + d\gamma_2$. Strains ε_1 and γ_1 may be thought of as describing an unraveling of molecular configuration, analogous to e_1 in the fiber model of Eqn. (A-7), and ξ_1 in the uniform membrane model of Eqn. (A-17). No coupling between squeeze and shear is assumed in this energy function. Energies \mathcal{G}_1 and \mathcal{G}_3 are Rajagopal elastic (they have implicit dependencies upon state), while energies \mathcal{G}_2 and \mathcal{G}_4 are Green elastic (they have explicit dependencies upon state).

From the thermodynamic expression $-\rho d\mathcal{G}_n = \varepsilon d\sigma + \gamma d\tau$, the non-uniform Gibbs

DRAFT: UNCLASSIFIED

free energy \mathcal{G}_n , when expressed in the form of Eqn. (A-18), and given the definitions for squeeze $1/N$ and shear $1/G$ compliances put forward in Eqns. (A-15b & A-15c), one determines that the tangent squeeze compliance is described by

$$\frac{1}{2N_t} := \frac{d\varepsilon}{d\sigma} = -(\rho \partial_{\varepsilon_1} \mathcal{G}_1)^{-1} (\varepsilon + \rho \partial_\sigma (\mathcal{G}_1 + \mathcal{G}_2)) - \rho \partial_{\sigma\sigma} \mathcal{G}_2 \quad (\text{A-19a})$$

and that the tangent shear compliance is described by

$$\frac{1}{G_t} := \frac{d\gamma}{d\tau} = -(\rho \partial_{\gamma_1} \mathcal{G}_3)^{-1} (\gamma + \rho \partial_\tau (\mathcal{G}_3 + \mathcal{G}_4)) - \rho \partial_{\tau\tau} \mathcal{G}_4 \quad (\text{A-19b})$$

whose mathematical structure is similar to that of the Freed-Rajagopal fiber model presented in Eqn. (A-7). The first collection of terms on the right-hand side of both formulæ is Rajagopal elastic; the second is Green elastic.

Derivation: The First and Second Laws of Thermodynamics, as they pertain to non-uniform contributions of stress power, have energetic components described in Eqn. (A-18) so that $\rho d\mathcal{G}_n = \rho \partial_{\varepsilon_1} \mathcal{G}_1(\varepsilon_1, \sigma) d\varepsilon_1 + \rho \partial_\sigma \mathcal{G}_1(\varepsilon_1, \sigma) d\sigma + \rho \partial_\sigma \mathcal{G}_2(\sigma) d\sigma + \rho \partial_{\gamma_1} \mathcal{G}_3(\gamma_1, \tau) d\gamma_1 + \rho \partial_\tau \mathcal{G}_3(\gamma_1, \tau) d\tau + \rho \partial_\tau \mathcal{G}_4(\tau) d\tau$ that associate with the conjugate pairings $-\varepsilon_1 d\sigma - \varepsilon_2 d\sigma - \gamma_1 d\tau - \gamma_2 d\tau$ because of the prescribed additivity in strains. These follow from a Legendre transformation of the internal energy. Gathering like terms result in a pair of Green elastic formulæ that describe two of the four internal strains

$$\varepsilon_2 = -\rho \partial_\sigma \mathcal{G}_2(\sigma) \quad \text{and} \quad \gamma_2 = -\rho \partial_\tau \mathcal{G}_4(\tau)$$

and two Rajagopal elastic formulæ whose ODEs describe the other internal strains

$$\begin{aligned} d\varepsilon_1 &= -(\rho \partial_{\varepsilon_1} \mathcal{G}_1(\varepsilon_1, \sigma))^{-1} (\varepsilon_1 + \rho \partial_\sigma \mathcal{G}_1(\varepsilon_1, \sigma)) d\sigma \\ d\gamma_1 &= -(\rho \partial_{\gamma_1} \mathcal{G}_3(\gamma_1, \tau))^{-1} (\gamma_1 + \rho \partial_\tau \mathcal{G}_3(\gamma_1, \tau)) d\tau \end{aligned}$$

that when combined as rates become the constitutive formulæ in Eqn. (A-19). \square

A.4.1.4 Non-Uniform Biologic Membrane Model

We now specify the Gibbs free-energy functions of Eqn. (A-18) such that they produce tangent compliances $1/N_t$ and $1/G_t$ with like mathematical structure to Eqn. (A-17c) for dilation, viz., $1/M_t$. Specifically, we consider Gibbs free-energy

DRAFT: UNCLASSIFIED

functions of the form

$$-\rho \mathcal{G}_1(\varepsilon_1, \sigma) = \operatorname{sgn}(\varepsilon_1) \varepsilon_{1\max} (2N_1\varepsilon_1 - \sigma) + 2\varepsilon_1\sigma \quad (\text{A-20a})$$

$$-\rho \mathcal{G}_2(\sigma) = \sigma^2/4N_2 \quad (\text{A-20b})$$

$$-\rho \mathcal{G}_3(\gamma_1, \tau) = \operatorname{sgn}(\gamma_1) \gamma_{1\max} (G_1\gamma_1 - \tau) + 2\gamma_1\tau \quad (\text{A-20c})$$

$$-\rho \mathcal{G}_4(\tau) = \tau^2/2G_2 \quad (\text{A-20d})$$

where these energy functions have the same mathematical structure as the energies for biologic fibers (Eqn. A-7) and uniform membranes (Eqn. A-17), less their temperature dependence, and less their states of pre-stress, i.e., $\sigma_0 = 0$ and $\tau_0 = 0$.

The sign functions, viz., $\operatorname{sgn}(\varepsilon_1)$ and $\operatorname{sgn}(\gamma_1)$, account for the fact that squeeze and shear strains can be of either sign, but the Gibbs energy must remain negative. In effect, the sign functions flip the limiting state between tension and compression, i.e., they change the signs of $\varepsilon_{1\max}$ and $\gamma_{1\max}$ depending upon the respective signs of ε_1 and γ_1 . As a consequence, $\mathcal{G}_1(\varepsilon_1, \sigma) = \mathcal{G}_1(-\varepsilon_1, -\sigma)$, $\mathcal{G}_2(\sigma) = \mathcal{G}_2(-\sigma)$, $\mathcal{G}_3(\gamma_1, \tau) = \mathcal{G}_3(-\gamma_1, -\tau)$ and $\mathcal{G}_4(\tau) = \mathcal{G}_4(-\tau)$.

When substituted into Eqn. (A-19), these energy functions produce the following thermoelastic compliances

$$\frac{1}{2N(\varepsilon, \sigma)} = \frac{\operatorname{sgn}(\varepsilon_1) \varepsilon_{1\max} - \varepsilon_1}{2N_1 \operatorname{sgn}(\varepsilon_1) \varepsilon_{1\max} + 2\sigma} + \frac{1}{2N_2} \quad \varepsilon_1 = \varepsilon - \frac{\sigma}{2N_2} \quad (\text{A-21a})$$

$$\frac{1}{G(\gamma, \tau)} = \frac{\operatorname{sgn}(\gamma_1) \gamma_{1\max} - \gamma_1}{G_1 \operatorname{sgn}(\gamma_1) \gamma_{1\max} + 2\tau} + \frac{1}{G_2} \quad \gamma_1 = \gamma - \frac{\tau}{G_2} \quad (\text{A-21b})$$

which provide the tangent operators that we will use to describe the non-uniform behavior of a biologic membrane.

Like our other biologic models, the tangent squeeze compliance $1/N_t$ is described by three material properties: an asymptotic modulus at the reference state of $N_1 N_2 / (N_1 + N_2)$ ($\approx N_1$ whenever $N_2 \gg N_1 > 0$) where N_1 may be thought of as the stiffness of an unstretched molecular network, and a terminal modulus N_2 designating a stiffness after its molecular network has been stretched out at a limiting state of configurational squeeze $\varepsilon_{1\max}$. The tangent shear compliance $1/G_t$ is also described by three material properties: an asymptotic modulus at the reference state of $G_1 G_2 / (G_1 + G_2)$ ($\approx G_1$ whenever $G_2 \gg G_1 > 0$), a terminal modulus G_2 , and a limiting state of configurational shear $\gamma_{1\max}$.

DRAFT: UNCLASSIFIED

In soft biological tissues, the shear moduli G_1 and G_2 will be several orders in magnitude smaller than their respective squeeze moduli N_1 and N_2 . Classical theories cannot make such a distinction.

A.4.2 Secant Material Properties

A.4.2.1 Uniform Response

Integrating by parts the tangent compliance governing dilation found in Eqn. (A-17c) results in a secant compliance of

$$\frac{1}{4M_s(\pi)} = \frac{\xi_{1\max}}{\pi - \pi_0} \left(1 - \frac{\sqrt{M_1 \xi_{1\max}}}{\sqrt{M_1 \xi_{1\max} + \frac{1}{2}(\pi - \pi_0)}} \right) + \frac{1}{4M_2} \quad (\text{A-22})$$

where $M_s(\pi \leq \pi_0) = M_1 M_2 / (M_1 + M_2)$. This compliance applies to the thermodynamic equations governing the uniform secant response of our membranes, as established in Eqn. (A-12a).

A.4.2.2 Non-Uniform Response

Integrating by parts the tangent compliance governing squeeze in Eqn. (A-21a) provides its secant compliance of

$$\frac{1}{2N_s(\sigma)} = \frac{\varepsilon_{1\max}}{|\sigma|} \left(1 - \frac{\sqrt{N_1 \varepsilon_{1\max}}}{\sqrt{N_1 \varepsilon_{1\max} + |\sigma|}} \right) + \frac{1}{2N_2} \quad (\text{A-23})$$

where $N_s(\sigma = 0) = N_1 N_2 / (N_1 + N_2)$, while integrating by parts the tangent compliance governing shear in Eqn. (A-21b) results in its secant compliance of

$$\frac{1}{G_s(\tau)} = \frac{\gamma_{1\max}}{|\tau|} \left(1 - \frac{\sqrt{G_1 \gamma_{1\max}}}{\sqrt{G_1 \gamma_{1\max} + 2|\tau|}} \right) + \frac{1}{G_2} \quad (\text{A-24})$$

where $G_s(\tau = 0) = G_1 G_2 / (G_1 + G_2)$. These compliances apply to the thermodynamic equations governing the non-uniform secant response of our membranes, as established in Eqn. (A-13a).